

https://dspace.org/

Investigating the corrosion resistance of copper-ruthenium coatings

Zaba, Winnie

2018

https://hdl.handle.net/10539/26995

Zaba, Winnie (2018) Investigating the corrosion resistance of copper-ruthenium coatings, University of the Witwatersrand, Johannesburg, https://hdl.handle.net/10539/26995

Downloaded from a DSpace repository. https://dspace.org/



Investigating the corrosion resistance of copper-ruthenium coatings

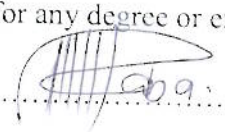
Winnie Zaba

A dissertation submitted to the Faculty of Engineering and the Built Environment, University of the Witwatersrand, in fulfilment of the requirements for the degree of Masters of Science in Engineering

Johannesburg, 2018

Declaration

I Winnie Zaba declare that this dissertation is my own unaided work except where references were made and were properly acknowledged. It is being submitted to the Degree of Masters of Science to the University of the Witwatersrand, Johannesburg. It has not been submitted before for any degree or examination to any other University.



.....30.....day of ...August.....year.2018.....

Abstract

Copper has been widely used, and its increased application in different industries resulted in high demands. With more applications, it has increased the need to improve the mechanical, and corrosion properties to improve its life span during operation. Pure copper has been used in many aqueous environments (e.g. pipe lines, storage tanks, and electro-winning) because of its good conductivity and corrosion resistivity. However, when it is exposed to harsh environmental conditions with high acidity it experiences corrosion. This research focuses on these corrosion characteristics. Appropriate surface chemistry is very important in many of the copper applications. Surface engineering techniques have been applied to improve the corrosion property of many materials like stainless steel, but only a few scientific investigations and developments have been done on copper. This development has been carried out by introducing ruthenium to the copper surface to improve the corrosion resistance and serviceability of copper in general. The ruthenium was added to the copper surface using thermal spray coating high velocity oxygen fuel spray coating, cold spray coating, spark plasma sintering, and electroplating.

One should note that the nature of the surface coating and arrangement of the powder particles determines the overall protection that can be achieved/induced. For the different coatings and alloys, ruthenium was added in 0.5, 1, and 2 weight percent. This research found that in many cases, the corrosion resistance increased with increase in ruthenium content. The HVOF and SPS experienced the same trend. The CSC coating did not achieve any corrosion resistance improvement when compared to as-received copper. The electroplating of a copper substrate successfully decreased the corrosion rate in sulphuric acid at 65°C. The electroplated powders had contaminations that affected the corrosion characteristics of the coating and the alloy.

Other properties of the material were also affected after the ruthenium addition. These also include the hardness of the materials which was increased with the increase in ruthenium content. The research limitations encountered was the shortage of equipment to perform other tests like the scratch adhesion test which would have validated the adhesion property of the coatings.

Dedication

I dedicate my dissertation work to God almighty, who gave me life, sustained me, and equipped me with all the knowledge, wisdom, and understanding to accomplish this work, and to my dearest loving son, Kgosi blessing Tapala, and my beautiful mother, Thifhelimbilu Jane Mphohoni, the greatest women in my world, with so much love that overflows throughout my life, and in memory of my father, the handsome Stephen Republic Zaba. I also dedicate it to my grandparents, Vho-Wilson Mphohoni and Vho-Kutama Mmbadaliga Mphohoni, and the rest of my family and friends. Your love, support, and prayers got me where I am today, I'm eternally grateful to have all of you in my life; you're just the reflection of God's love to me. I am indebted to you for all you have done for me.

Acknowledgements

I would like to acknowledge the University of the Witwatersrand for enrolling me in their engineering faculty and allowing me access in their facilities to carry out this research. The support of the DST-NRF Centre of Excellence in Strong Materials (CoE-SM) towards this research is hereby acknowledged. Opinions expressed and conclusions arrived at, are those of the author and are not necessarily to be attributed to the CoE-SM. I also would like to acknowledge my supervisor Prof. Josias van der Merwe who contributed a lot in making this work possible by supervising me. I also acknowledge Mr Nelwalani B.N. for helping with the SEM operation, Mr Nichael L. for assisting the cold spray facilities, Mr Rokebrand P. for assisting with the spark plasma sintering facilities, Mr Mahole D and Mr Monga J. for his assistance equipment connections. I would also like to acknowledge Thermalspray Company for allowing me to use their facilities in applying thermal spray coatings. Many thanks to all the people not mentioned above who supported and contributed directly and indirectly to my work.

Contents

Declaration i
Abstract ii
Dedication iii
Acknowledgements iv
List of figures viii
List of tables xiii
Nomenclature xiv
Abbreviations xiv
Symbols xiv
Chapter 1 1
1.1 Introduction 1
1.2 RESEARCH OBJECTIVES 4
Chapter 2 : Literature review 5
2.1 History of copper 5
2.2 History of ruthenium 10
2.3 Improved corrosion resistance through ruthenium additions 13
2.3.1 Ru in austenitic-stainless steels 13
2.3.2 Ru in Duplex stainless steels 14
2.3.3 Ru in titanium 16
2.3.4 Ru in tungsten carbide 17
2.4 Methods used to mitigate copper corrosion 19
2.4.1 Coating processes 19
2.4.2 Metal alloying 26
2.4.3 Electroplating 29
2.5 Corrosion theory used to explain corrosion chemistry/predicting the corrosion behaviour 33
2.5.1 Polarisation 33
2.5.2 Passivity 35
Chapter 3 : Methodology 37
3.1 Introduction 37
3.2 Powder mixing 37
3.3 High velocity oxygen fuel (HVOF) Coating 38

3.4 Cold spray Coating 39
3.5 Alloy sintering 40
3.6 Electroplating 41
3.6.1 Electrolyte preparation 41
3.6.2 Electroplating process 41
3.7 Metallography Sample preparation 42
3.8 Metallography analysis 43
3.8.1 Light optical microscopy 43
3.8.2 SEM 43
3.9 Hardness measurements 44
3.10 Corrosion measurements 45
3.10.1 The electrochemical cell 45
3.10.2 Electrochemical measurements 46
3.10.3 Potentiodynamic polarisation 46
3.10.4 Corrosion rate calculations 46
Chapter 4 : Results 49
4.1 Introduction 49
4.2 As-received copper 49
4.2.1 Micrographs 49
4.2.2 Electrochemical results 50
4.2.3 Average hardness 51
4.3 HVOF 51
4.3.1 Optical microscopy images 52
4.3.2 SEM EDS results 53
4.3.3 Hardness results 63
4.3.4 Electrochemical results 63
4.4 CSC 66
4.4.1 Optical micrographs 66
4.4.2 SEM EDS results 67
4.4.3 Hardness results 76
4.4.4 Electrochemical results 76
4.5 SPS 79
4.5.1 Optical micrographs 79

4.5.2 SEM EDS results 80
4.5.3 Hardness results 84
4.5.4 Electrochemical results 85
4.6 Electroplating (Electroplated samples-EPS) 95
4.6.1 Experimental design 96
4.6.2 Microscopic visual examination Results 96
4.6.3 SEM EDS results 98
4.6.4 Hardness results 103
4.6.5 Electrochemical results 104
4.7 EPP (Electroplated powders) 107
4.7.1 Ruthenium powder 107
4.8 EPP-HVOF 111
4.8.1 SEM EDS results 111
4.8.3 Hardness results 112
4.8.4 Electrochemical results 113
4.9 EP-SPS 114
4.9.1 SEM EDS results 115
4.9.3 Average hardness results 116
4.9.4 Electrochemical results 116
4.10 Summary of results 118
Chapter 5 : Discussions 119
5.1 Introduction 119
5.2 As-received copper 119
5.3 High velocity oxygen-fuel spray coating 119
5.4 Cold spray coating 121
5.5 Spark plasma sintered alloys 123
5.6 Electroplating 125
5.7 Electroplated copper powder used in EPP-HVOF and EP-SPS 126
Chapter 6 : Conclusions 127
Chapter 7 : References 129
Appendices 139

List of figures

Figure 2.1: Historical copper prices and charts [http://www.infomine.com/investment/copper/] 5
Figure 2.2: Corrosion rate of copper and carbon steel with increase in (a) exposure time and (b) temperature [Al-Zubidy & Hummza, 2014]. 7
Figure 2.3: Pourbaix diagram of Cu-H_2O at 25˚C [Lu, 2005]. 9
Figure 2.4: Major producers and suppliers of PGMs [Conradic, 2003]. 10
Figure 2.5: Ruthenium prices and charts [http://www.infomine.com/investment/ruthenium/, 2017]. 11
Figure 2.6: Demand of ruthenium from the year 2010 to 2016. [https://www.statista.com/statistics/592893/demand-for-ruthenium-worldwide-by-application/, 2015] 12
Figure 2.7: The potentiodyanic polarisation curve for Ru-alloyed stainless steel [Lekala et al., 2012]. 14
Figure 2.8: Corrosion rates for duplex stainless steel alloys with ruthenium [Sherif et al. 2009]. 15
Figure 2.9: Corrosion resistance of titanium in reducing environments improved by micro alloying with ruthenium [Van der Lingen & Sandenbergh, 2005]. 17
Figure 2.10: The effect of ruthenium additions on corrosion rate of the alloys in 1 M H_2SO_4 [Thanjekwayo, 2009]. 19
Figure 2.11: A schematic diagram of cold spraying process [Champagne, 2007] 21
Figure 2.12: The experimental results of individual deposited Cu particle on polished Cu substrate: a surface and b cross-section morphologies at incident angle of 90º [Li et al., 2014]. 22
Figure 2.13: Microstructures (cross-section) of cold-sprayed Cu-powder on Cu-substrate using (a) nitrogen and (b) helium process gas [Stoltenhoff et al., 2006]. 23
Figure 2.14: The cross-sections show microstructures of HVOF sprayed Cu-coatings on a substrate [Stoltenhoff et al., 2006]. 26
Figure 2.15: Schematic of the SPS process [Munir and Anselmi-Tamburini, 2006]. 27
Figure 2.16: The microstructures of copper discs produced by SPS using a (high oxygen) and b (low oxygen content) powders [Menapace et al., 2016]. 29
Figure 2.17: The setting of the electroplating process of copper [McCarthy, 2012]. 31
Figure 2.18: Typical distribution of deposit on various shapes of surface during electroplating , (a) thickening of deposit at edge of flat sheet, (b) Ovality of deposit on circular section, and (c) Build-up on corners of square section [Edwards 1983]. 32
Figure 2.19: Typical pulse-current waveform [Chandrasekar & Pushpavanam, 2008]. 33
Figure 2.20: Increase in corrosion rate with increasing potential E and anodic polarisation ^{e}a (Jones, 1996) 35
Figure 2.21: The effect of oxidizer concentration on corrosion of an active-passive alloy [Jones, 1996] 36
Figure 3.1: Experimental flow sheet. 37
Figure 3.2: The SEM images of (a) copper and (b) ruthenium powder. 38
Figure 3.3: High velocity oxy fuel spray [flame spray technologies, FST, October 2012] 39
Figure 3.4: Cold spray equipment [https://www.wits.ac.za/mecheng/research/research-units/cold-spray-research/facilities/ Access date: 5 June 2017]. 40
Figure 3.5: The coating deposition pattern. 40
Figure 3.6: Electroplating process setting 42
Figure 3.7: Carl Zeiss FESEM. 44

Figure 3.8: Vickers micro-hardness tester. 44
Figure 3.9: The electrochemical cell. 45
Figure 3.10: The overall setting for the experiment and the equipment used. 46
Figure 4.1: The optical micrograph of as-received copper (oxygen free), etched with Beraha's lead sulfide (PbS) reagent. 49
Figure 4.2: Potentiodynamic polarisation curves of as-received copper exposed to 2M sulphuric acid solution at 25, 45, and 65°C. 50
Figure 4.3: The average hardness of the as-received copper. 51
Figure 4.4: The collection of HVOF optical micrographs where (a) is HVOF-0%Ru, (b) HVOF-0.5%Ru, (c) HVOF-1%Ru, and (d) HVOF-2%Ru. 52
Figure 4.5: The SEM micrograph taken with a back-scattered electron detector (a) and the EDS spectrum with elemental weight percentages (b) of the HVOF-0%Ru coated sample. 54
Figure 4.6: SEM micrograph of the cross-section of HVOF-0%Ru coating, (a) measurements of the coating thickness, and (b) the etched coating interface at higher magnification. 55
Figure 4.7: SEM micrograph taken with a back-scattered electron detector (a) of the top surface of the coating, and (b) the EDS spectrum of the coating with elemental weight percentages. 56
Figure 4.8: SEM micrograph of the cross section of HVOF-0.5%Ru coating and estimated measurements of the coating thickness. 57
Figure 4.9: (a) The SEM image of the top surface of the HVOF-1%Ru coating, and (b) results of the EDS analysis with average compositions of the elements. 58
Figure 4.10: The SEM images showing (a) Cross section image with estimated coating height, (b) the coating at a higher magnification, and (c) the EDS of the ruthenium in the coating. ..59
Figure 4.11: The SEM micrograph of (a) the top surface of the HVOF-2%Ru coating, and (b) the results of the EDS analysis performed on the coating surface in (a) and the averaged elemental compositions detected. 60
Figure 4.12: SEM micrograph of the cross-section of the HVOF-2%Ru coating, showing measurements of the coating thickness. 61
Figure 4.13: The SEM EDS elemental maps (copper (green) and ruthenium (yellow)) of the HVOF coating surfaces. 62
Figure 4.14: Hardness profile of all the HVOF coated samples compared to that of as-received copper. 63
Figure 4.15: Linear polarisation potentiodynamic curves of HVOF coated copper and the as-received copper exposed to 2M H_2SO_4 at 45˚C. 64
Figure 4.16: Linear polarisation potentiodynamic curves of HVOF coated copper and the as-received copper exposed to 2M H_2SO_4 at 65˚C. 64
Figure 4.17: Corrosion rate as a function of ruthenium concentration in the HVOF coatings exposed to 2M H_2SO_4. 66
Figure 4.18: Optical micrographs of (a) CSC-0%Ru, (b) CSC-0.5%Ru, (c) CSC-1%Ru, and (d) CSC-2%Ru. 67
Figure 4.19: The SEM micrograph taken with a back-scattered electron detector (a) and the EDS spectrum with elemental weight percentages (b) of the CSC-0%Ru coating. 68
Figure 4.20: SEM micrograph of the cross section of CSC-0%Ru coated coating taken using a backscattered detector. 69
Figure 4.21: SEM micrograph taken with a back-scattered electron detector (a) of the top surface of the CSC-0.5%Ru coating, and (b) the EDS spectrum of the coating with elemental weight percentages. 70
Figure 4.22: the back-scattered SEM micrograph of the cross section of CSC-0.5%Ru coating which was not etched. 70
Figure 4.23: (a) SEM image of the top surface of the CSC-1%Ru coating, and (b) results of the EDS analysis over the area with averaged elemental compositions. 71

Figure 4.24: SEM micrograph of the cross section of CSC-1%Ru coating taken by the back-scattered detector. 72
Figure 4.25: SEM micrograph taken with a back-scattered electron detector (a) of the top surface of the CSC-2%Ru coating, and (b) the EDS spectrum of the CSC-2%Ru coating with elemental weight percentages. 73
Figure 4.26: SEM micrograph of the cross section of CSC-2%Ru coating and estimated measurements of the coating thickness. 74
Figure 4.27: SEM EDS elemental maps of the CSC coating surfaces representing copper (green) and ruthenium (yellow). 75
Figure 4.28: The average Vickers hardness of all the CSC coating compared to that of as-received copper. 76
Figure 4.29: Potentiodynamic polarisation curves of CSC coating and as-received copper exposed to 2M H_2SO_4 at 45˚C. 77
Figure 4.30: Potentiodynamic polarisation curves of CSC coating and as-received copper exposed to 2M H_2SO_4 at 65˚C. 77
Figure 4.31: Corrosion rate as a function of ruthenium concentration in the CSC coatings exposed to in 2M H_2SO_4. 79
Figure 4.32: Optical micrographs of (a) SPS-0%Ru, (b) SPS-0.5%Ru, (c) SPS-1%Ru, and (d) SPS-1%Ru etched with Beraha's lead sulfide (PbS). 80
Figure 4.33: SEM micrograph of the SPS-0%Ru alloy taken with a backscattered electron detector (a), and (b) is showing the alloy at higher magnification, and (c) is the results of the EDS analysis of the alloy. 81
Figure 4.34: SEM micrograph of (a) the SPS-0.5%Ru alloy, (b) the alloy at higher magnification, and (c) the EDS results of the analysis shown as a spectrum. 82
Figure 4.35: EDS spectrum of the SPS-0.5%Ru alloy showing the chemical compositions. ..82
Figure 4.36: SEM image, taken with a back-scattered detector, of (a) the SPS-1%Ru alloy, and (b) the same alloy at higher magnification, with(c) the EDS spectrum of the SPS-1%Ru alloy with elemental weight percentages. 83
Figure 4.37: SEM image, taken with a back-scattered detector, of (a) the SPS-2%Ru alloy, and (b) the same alloy at higher magnification. 84
Figure 4.38: EDS spectrum of the SPS-2%Ru alloy with elemental weight percentages. 84
Figure 4.39: The average Vickers hardness of all the SPS alloys compared to that of as-received copper. 85
Figure 4.40: Linear polarisation potentiodynamic curves for SPS alloys and as-received copper in 2M H_2SO_4 at 45˚C. 86
Figure 4.41: Linear polarisation potentiodynamic curves for SPS alloys and as-received copper in 2M H_2SO_4 at 65˚C. 86
Figure 4.42: Linear polarisation potentiodynamic curve of SPS alloys exposed in 2M H_2SO_4 at 65˚C for 1hr30min. 87
Figure 4.43: Corrosion rate as a function of ruthenium concentration in the SPS alloys exposed to 2M sulphuric acid. 89
Figure 4.44: Comparison of corrosion rates of the SPS alloys that were exposed for different durations (45 min and 90 min) in 2M H_2SO_4 at 65°C. 89
Figure 4.45: SEM micrograph of corroded SPS-0%Ru alloy analyzed after ultrasonic cleaning. 90
Figure 4.46: The SEM images taken by BSD and SE detectors showing the pits that formed by corrosion 91
Figure 4.47: SEM micrograph of corroded SPS-0.5%Ru alloy taken by the secondary electron detector. 91

Figure 4.48: The SEM micrographs of SPS-0.5%Ru alloy taken by the BSD and SE detectors under different magnifications.....92
Figure 4.49: the SEM micrograph of SPS-0.5%Ru alloying showing the area with ruthenium which was not corroded. 92
Figure 4.50: SEM image of the corroded SPS-1%Ru alloy after cleaning in acetone using an ultrasonic cleaner. 93
Figure 4.51: SEM micrographs of the corroded SPS-1%Ru alloying at different magnifications showing the area around ruthenium and the pits that had formed on the alloy. 94
Figure 4.52: SEM image of the corroded SPS-2%Ru alloy after cleaning in acetone using an ultrasonic cleaner. 94
Figure 4.53: BSD and SE SEM micrographs of the SPS-2%Ru alloy showing the pits growing around the grain boundaries.....95
Figure 4.54: SEM micrographs showing the results of the preliminary study conducted to chose the best plating parameters.....97
Figure 4.55: The SEM micrographs of 1.5 A plated copper, comparing the surface appearance before and after corrosion and their respective EDS spectrum scanned from each surface. ...98
Figure 4.56: The magnified SEM micrograph showing the corroded EP-1.5 A ruthenium electroplated copper, and (b) is the results of EDS analysis made on the crack of the coating after corrosion. 99
Figure 4.57: The cross section micrograph of 1.5 A plated copper and the EDS spectrum scanned on the coating. 100
Figure 4.58: The 2.0 A plated copper sample, before and after corrosion in 2M sulphuric acid, with their EDS spectrum scanned on the surface of the sample. 101
Figure 4.59: SEM micrograph of the corroded EP-2A copper sample showing different phases which were analyzed by EDS producing EDS spectrum in a, b, and c. 102
Figure 4.60: SEM image taken by BSD electron detector showing cross sections of the EP-2A ruthenium plated copper. 103
Figure 4.61: Average Vickers hardness for all ruthenium electroplated copper samples compared to as-received Cu.....104
Figure 4.62: Potentiodynamic polarisation curves of all EP copper samples and as-received copper exposed to 2M H_2SO_4 at 45°C.....105
Figure 4.63: Potentiodynamic polarisation curves of all EP copper samples and as-received copper exposed to 2M H_2SO_4 at 65°C.....105
Figure 4.64: Corrosion rate as a function of plating current.....106
Figure 4.65: SEM micrograph of the cross-section of copper powder.....107
Figure 4.66: SEM micrograph of the electroplated copper powder using 1.5 A plating current, and (b) is the EDS spectrum obtained after the EDS analysis over the selected area in (a)..108
Figure 4.67: SEM micrographs showing the film around the cross section of the plated copper powder which was analyzed and the results are shown by the EDS spectrum alongside the micrograph. 109
Figure 4.68: SEM micrograph of the electroplated copper powder using 2 A plating current, and (b) is the EDS spectrum obtained after the EDS analysis over the selected area in (a)..109
Figure 4.69: SEM micrographs showing the film around the cross section of the plated copper powder which was analyzed and the results are shown by the respective EDS spectrum alongside the micrograph.....111
Figure 4.70: SEM micrograph showing the cross section of the EPP-HVOF coated copper, and the EDS spectrum of the analysis made from the selected areas in the micrograph. 112
Figure 4.71: Vickers hardness profile for the EPP-HVOF coated copper.....113
Figure 4.72: Potentiodynamic polarisation curves of EPP-HVOF coated copper and as-received copper exposed to 2M H_2SO_4 at 45 and 65°C. 113

Figure 4.73: Comparison of the corrosion rates between as-received copper and EPP-HVOF coated copper at 45 and 65°C. 114
Figure 4.74: SEM micrograph of the EP-SPS alloy, (b) is the magnified alloy micrograph showing the EDS spectrum of particular futures of interest in the alloy. 115
Figure 4.75: Average Vickers hardness for EP-SPS alloy compared to as-received copper.116
Figure 4.76: Polarisation curve for EP-SPS alloy exposed in 2M sulphuric acid at 45 and 65°C. 116
Figure 4.77: Corrosion rate as a function of temperature. 117

List of tables

Table 2.1: Electrochemical data for duplex stainless steel alloy with 0.15 Ru [Olaseinde et al., 2012]. 16
Table 2.2: Benefits of HVOF [Sidhu et al. 2005] 25
Table 3.1: The composition of powders (copper and ruthenium) added to make different alloys (mixing composition). 38
Table 3.2: The compositions, preparation, and use of the etchant. 43
Table 4.1: Calculated corrosion rate of as-received copper at 25, 45, and 65°C respectively. 51
Table 4.2: The corrosion rate calculations for the HVOF coated samples measured at 45°C in 2M H_2SO_4. 65
Table 4.3: The corrosion rate calculations for the HVOF coated samples measured at 65°C in 2M H_2SO_4. 65
Table 4.4: Calculated corrosion rates for the CSC coatings at 45°C in 2M H_2SO_4 78
Table 4.5: Calculated corrosion rates for the CSC coatings at 65°C in 2M H_2SO_4 78
Table 4.6: The corrosion rate calculations for the SPS alloys and as-received copper measured in 2M H_2SO_4 at 45°C. 87
Table 4.7: The corrosion rate calculations for the SPS alloys and as-received copper measured in 2M H_2SO_4 at 65°C. 88
Table 4.8: The corrosion rate calculations for the SPS alloys exposed for 1hr30min and the as-received copper measured in 2M H_2SO_4 at 65°C. 88
Table 4.9: The presentation of the parameters (current and time) that were changed for the experimental design. 96
Table 4.10: Calculated corrosion rates for the ruthenium electroplated and as-received copper at 45°C. 106
Table 4.11: Calculated corrosion rates for the ruthenium electroplated and as-received copper at 65°C. 106
Table 4.12: Calculated corrosion rates of EPP-HVOF coated copper compared to as-received copper at 45 and 65°C in 2M sulphuric acid. 114
Table 4.13: Corrosion rate calculations for the EP-SPS alloy and as-received copper at 45 and 65°C. 117

Nomenclature

Abbreviations

CSC – Cold spray coating

Cu – Copper

EP – Electroplating

EPP – Electroplated powder

HVOF – High velocity oxygen fuel

Min - Minutes

PGMs – Platinum group metals

Ru – Ruthenium

SPS – Spark plasma sintering

Symbols

°C – Degree Celsius

A – Area (cm^2)

CR – Corrosion rate (mmpy)

E – Potential (v)

E_w – Equivalent weight

i_{corr} – Corrosion current density ($\mu A/cm^2$)

mm – Millimetre

Rp – Polarisation resistance

Wt.% - Weight percent

ρ – Density (g/cm^3)

Chapter 1

1.1 Introduction

Corrosion is a major challenge worldwide. Corrosion costs world-wide are more than $1.8 trillion every year; a contribution of about 3 to 4 percent of the gross domestic product of industrialised countries [Lieser & Xu, 2010]. This is from the direct cost for prevention, repair and replacement of corrosion. Furthermore, costs are increased by overdesigning equipment to allow for corrosion damage. Moreover, the efficiency of processes is compromised as the result of corrosion. In addition there could be contamination of product, which can even lead to the shutdown of processes where equipment has failed [Shaw & Kelly, 2006]. Preventive measures to avoid and slow down corrosion, such as coating of equipment, are implemented to reduce costs [Wilmot, 2007].

Corrosion is the deterioration and destruction of the material as a result of the reaction between a material and its environment [Shaw & Kelly, 2006]. Corrosion, whether in the atmosphere, underwater or underground, is electrochemical in nature and caused by the flow of electrons, from one metal to another, or from one area of the surface to another [Jones, 1996]. The rate of corrosion can be very rapid or extend over thousands of years depending on the type of materials involved and the environment they are exposed to. It occurs as general/uniform and localised corrosion in various forms, such as galvanic, crevice, pitting, intergranular, erosion, and stress corrosion [Fontana, 1987]. Numerous prevention and protection methods have been implemented for different materials to combat corrosion. The most common prevention methods are coatings, addition of inhibitors to the environment, cathodic and anodic protection, alloying, and component design [Fontana, 1987].

The focus of this work will be on copper metal. Copper is a metal that has received a wide range of applications in many industries such as electrical connectors, cables, power generation equipment, in aircrafts, space structures, and energy conversion systems [Wan et al. 2012]. Copper is being used in many applications, because of its desirable properties, such as electrical conductivity, high thermal conductivity, and good workability [Fontana, 1987]. For a material with so manyapplications, it is important to improve its service life. Especially

in acidic environments at elevated temperatures [Cohen, 2005] where it is more prone to corrosion.

One of the processes where copper has shown significant corrosion is the electro-winning process in hydrometallurgy. This process employs copper cathodes that are connected to copper hanger bars and busbars [Eastwood & Whebell, 2015]. The copper hanger bars and the busbars show severe corrosion that affect the overall production efficiency. Once these units have been corroded, the current flow and distribution over the unit is compromised. In addition, production time is lost during replacement of these corroded copper hanger and busbars, which leads to increased costs and maintenance [Aslin et al. 2007].

Copper is susceptible to corrosion in oxidizing acids, sulphuric acid and ammonia [Cohen, 2005]. In copper production, copper is leached out of the ore with sulphuric acid [Vracar et al, 2003]. The humidity, bubbles, and mist from the electro-winning tank reaches the busbars and hanger bars, and since the electrolyte has high acidity levels, it causes them to corrode. The acid is a product of the pregnant leach solution, and both hydrochloric and sulphuric acid can be present. The pregnant leach solution contains dissolved copper, which was leached from the ore [Dunbar, 2012]. The acid is introduced during the leaching, solvent extraction and stripping stages prior to electro-winning [Kordosky, 2002].

The present work intends to improve the life span of the copper hanger bars and busbars by increasing its corrosion resistance to prolong the life of the equipment. This will be investigated by the corrosion testing of applied metallic coatings and alloys. Coating is a process of applying a layer to the surface of an object or metal, the substrate [Flink et al. 2011]. Coatings are applied to protect and improve the corrosion resistance of the substrate [Saeed, 2014]. In this instance, the coating and the alloy also has to have good electrical conductivity. When the coatings have been applied , it has to be assured that the substrate is still a functional bar.

The success of this work will also benefit other industries that use copper components in their processes. This could be any industry that uses heat exchangers, steam power plants, electrical wires, cables and connectors, circuit boards, and chemical process applications.

To investigate the improvement of corrosion resistance of the copper surface , copper and ruthenium powders will be used to coat samples. The addition of ruthenium will not negatively affect the electro-winning process [Sandoval et al. 2010]. Copper and ruthenium should function well together, because copper has an excellent conductivity, and sometimes poor corrosion resistance, whereas ruthenium has an excellent corrosion resistance, and an acceptable electrical conductivity. Various concentrations of copper and ruthenium will be used to determine the corrosion resistance of the alloyed coating. It is expected that an optimum ruthenium level in the surface coating exists, as well as in the alloys, which might depend on the processing method used to produce the specific coating or the alloy.

Conductivity in the electro-winning process is essential to electroplating. This is because the plating quality and efficiency is affected by the conductivity of the cathodes and this influences the resultant current flowing between the solution and the electrode [Beukes & Badenhorst, 2009]. Copper has a very high electrical conductivity with acceptable strength and formability [Powel & Webster, 2012], which makes it the best metal to use as the hanger and busbars in the copper electro-winning process. Ruthenium has excellent properties in both corrosion resistance and conductivity relative to copper [Chan et al. 2004]. The electrical conductivity of copper and ruthenium are 5.9×10^7 S/m and 1.4×10^7 S/m respectively. The two metals combined could still achieve the same conductivity required in the electro-winning process.

Ruthenium is the least expensive of the platinum group metals [Hilliard, 2000]. It is readily available in South Africa, and it is a by-product of the platinum group metals [Crundwell et al. 2011]. It therefore would make financial sense to beneficiate and process this by-product for economical gain. This will utilize local resources and create more stable income for companies producing it, resulting in job security for their employees [Hilliard, 2002].

Improvement of copper corrosion resistance will increase the suitability for its use in the harsh acidic electro-winning conditions. It will be of significant impact to the electro-winning processes to use hanger bars and busbars with improved corrosion resistance. Therefore, theywill only be replaced with the rest of the units during routine maintenance. With copper-ruthenium coatings such improvements might become possible.

1.2 RESEARCH OBJECTIVES

The aim of this project is to develop a corrosion resistant of copper-ruthenium coating applied to a copper substrate when exposed to simulated electro-winning conditions.

The objectives will be to:

- Find the best copper coating procedure to produce various Cu-Ru coatings.
- Characterise the mechanical properties of coatings
- Characterise microstructure of coated samples
- Characterise the corrosion of copper and coated samples under simulated conditions.

Chapter 2 : Literature review

This chapter reviews the material characteristics of about copper and ruthenium. It includes their corrosion properties and ways that have been used to improve corrosion resistance of other metals through the additions of ruthenium. It also considers methods used to mitigate copper corrosion.

2.1 History of copper

Copper has been used for over 10 000 years as pure copper and in alloy form [Beatty, 2001]. It is usually mined as a copper sulphide mineral such as chalcocite (Cu_2S) and covellite (CuS) [Ayres et al., 2002]. In certain geological formations, copper exists in its pure metallic state. Copper is very versatile and is widely used in many industrial and house hold applications such as heat exchangers, valves, pumps, circuit boards, desalination plants, electro winning plants, power stations and as piping material [Al Kharafi et al., 2013]. The copper metal and its alloys possess a combination of acceptable corrosion resistance, excellent electrical and heat conductivity; with good formability, acceptable machinability and mechanical properties [Fontana, 1987].

Considering the price of copper over the last decade, as presented in Figure 2.1, it has been steadily increasing. This is due to, amongst many factors, the increase in copper demand, and pressure in the commodity markets [Kabwe & Yiming, 2015]. This is disadvantageous for the consumers because it cost them more to access the copper that they need in their processes.



Figure 2.1: Historical copper prices and charts [http://www.infomine.com/investment/copper/]

This will force the consumers to consider other alternatives for copper in their processes [Kabwe & Yiming, 2015]. However, that is not always possible in some processes, like in electrical cables and the copper hanger and busbars. For such processes the only option is to find ways to improve the lifespan of the copper material while in application.

Even with its apparent exceptional corrosion resistance, copper is still susceptible to certain forms of corrosion that can be performance limiting. Copper corrosion is the result of the loss of solid copper metal into solution. Here the base metal (copper) loses electrons and its solid phase is transformed into a soluble state and dissolves [Darren et al. 2010]. Corrosion rate is directly proportional to solubility of oxygen in the acid in the environment[Hinds, 1996]. Therefore, when a component is exposed to the atmosphere with excess oxygen, the corrosion rate is increased.

Copper has an acceptable corrosion resistance when exposed to water. However, pitting or other forms of corrosion can occur in environmental conditions containing oxidizing acids, such as oxidizing heavy-metal salts, sulphur, ammonia as well as their compounds [King 2009]. Environments that cause pitting corrosion usually contain species such as: chloride, nitrate, or sulphate [Duthil et al. 1996]. These species produce pitting at varying levels of aggressiveness. Nitrate is the most aggressive, followed by sulphate, and lastly chloride [Duthil et al. 1996]. The occurrence of corrosion is greatly affected by the dissolved oxygen content in the solution, or environment [Damon & Cross, 1936].

Corrosion of copper in sulphuric acid has been studied and it was discovered that the process involved the following electron stages [Baeshow et al. 2014]:

$$Cu \rightarrow Cu^{+} + e^{-} \quad \text{.....1}$$

$$Cu^{+} \rightarrow Cu^{2+} + e^{-} \quad \text{.....2}$$

In a concentrated sulphuric acid solution, the copper can passivate by forming a Cu_2O, CuO, or $CuSO_4$ layer on the surface [Wagner, 1996]. This is achieved under certain conditions. When copper is placed in an environment containing sulphuric acid it reacts to form copper sulfate [Kear et al. 2004] as indicated in Equation 3

$$Cu + H_2SO_4 \rightarrow CuSO_4 + SO_2 + H_2O \quad \text{.....3}$$

Based on the chemical composition of the surface films that forms on copper, it was concluded that Cu_2O and CuO oxides formed by solid phase mechanics, and that they were responsible

for copper passivation [Grishina et al. 2002]. It is assumed a level of $CuSO_4$ in the surface film resulted from interaction of the surface oxides with the sulfuric acid by means of the following reactions [Grishina et al. 2002].

$$Cu_2O + H_2SO_4 \rightarrow CuSO_4 + H_2O + Cu \quad \text{.....4}$$

$$CuO + H_2SO_4 \rightarrow CuSO_4 + H_2O \quad \text{.....5}$$

The tendency of copper to corrode in sulphuric acid depends on factors such as temperature, concentration, presence of oxidising and reducing contaminants [Jehn and Zielonka, ASM handbook]. Al-Zubidy & Hummza (2014) found that copper corrodes in a 1M H_2SO_4 solution. Some of the findings of this research are presented in Figure 2.2. This was confirmed by the consistent increase of the corrosion rate of the material with exposure time and temperature. With increasing temperature, the corrosion rate increased as oxygen diffusion to the metal surface improved and this increased the overall reaction kinetics.

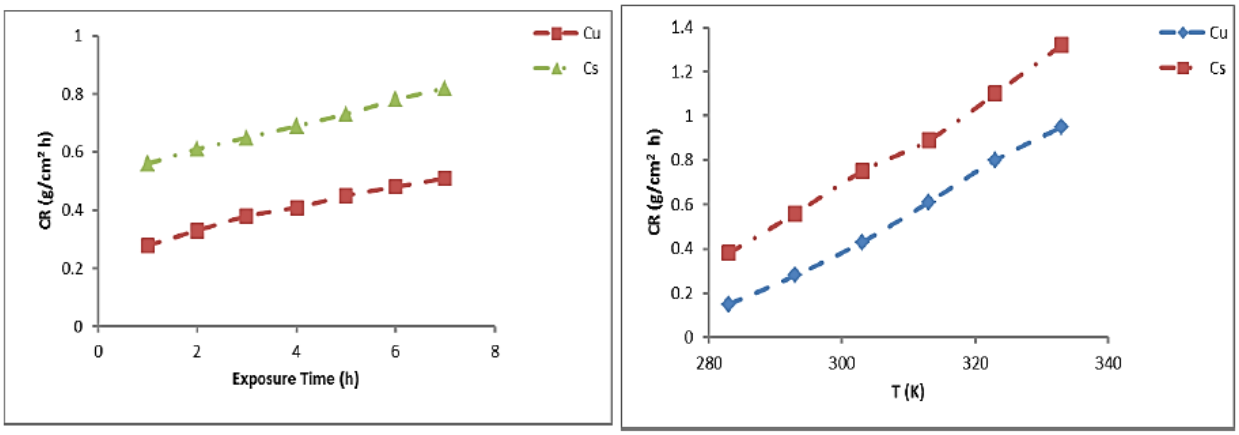


Figure 2.2: Corrosion rate of copper and carbon steel with increase in (a) exposure time and (b) temperature [Al-Zubidy & Hummza, 2014].

In an acidic aqueous environment with chloride copper dissolves and forms Cl^- copper complexes [Lu, 2005]. These corrosion products do not form a protective film to improve corrosion resistance, since passivation layers usually form as a result of surface oxides that adhere to the surface [Mak, 2013].

As mentioned, the occurrence of corrosion and resultant corrosion products has a negative effect on the functioning of copper hanger bars and busbars for conductivity [Sherif, 2012]. Localized corrosion of copper depends on the composition of the metal surface, pH, and the media concentration [King & Liljia, 2014]. In cases where the copper surface is at a different

temperature than that of the medium, the corrosion rate can be accelerated [Bartonicek, 1979]. Copper and copper alloys can show increased corrosion rates due to the presence of certain pollutants in the corrosive environment such as sulphide ions and dissolved oxygen in the chloride media [Rahmouni et al., 2005].

Another condition that leads to copper corrosion in copper electrowinning process is the acid mist. Acid mists are generated by bubbles bursting at the electrolyte-air interface [McGinnity et al. 2014]. The formations of acid mist not only result in hazardous environment for the operators, but it also results in severe structural and equipment corrosion [Liow et al. 2007]. The resultant amount of acid mist that is generated is dependent on the solution temperature and mist suppression chemical used. Al Shakarji et al. 2011 found that acid mist increase with increase in temperature and current density.

As mentioned before, copper is susceptible to corrosion in oxidizing acids, sulphur and ammonia solutions. There are certain surface modifications and corrosion protection techniques that can be applied to copper to protect the metal from corroding. These are anodic oxidation, chemical etching, inhibitors, electrochemical deposition, sol-gel method, coating and wet chemical reaction [Chen et al. 2012].

Inhibitors are compounds that control, reduce, or prevent corrosion of a metal and its surroundings when added to the environment in small quantities [Al-Zubidy & Hummza, 2014]. The use of inhibitors has been found to be one of the most practical methods for protection against corrosion, especially in acidic media. Most corrosion inhibitors are organic compounds containing electronegative atoms such as nitrogen, sulphur, phosphorus and tetraoxygen [Behpour & Mohammad, 2012]. Inhibitors can be used to protect copper from corroding, but can lose their efficiency when the medium is contaminated.

The environment will define the type of corrosion and the reaction products. A thermodynamic E-pH (Pourbaix) diagram is designed to help define the reaction that takes place at a specific temperature, electrolyte condition, electrode potential (E), and the corrosion product that will form [Protopopoff & Marcus, 2003]. The thermodynamics of copper corrosion resistance is characterised by the Pourbaix diagram shown in Figure 2.3, with an indication of the stable phases which form at different pH and potential levels. It shows phase fields where immunity can be expected as well as where corrosion and passivation are possible. The information provided on the behaviour of a system as the pH and potential vary, offers valuable interpretation for experimental work analysis and teaching.

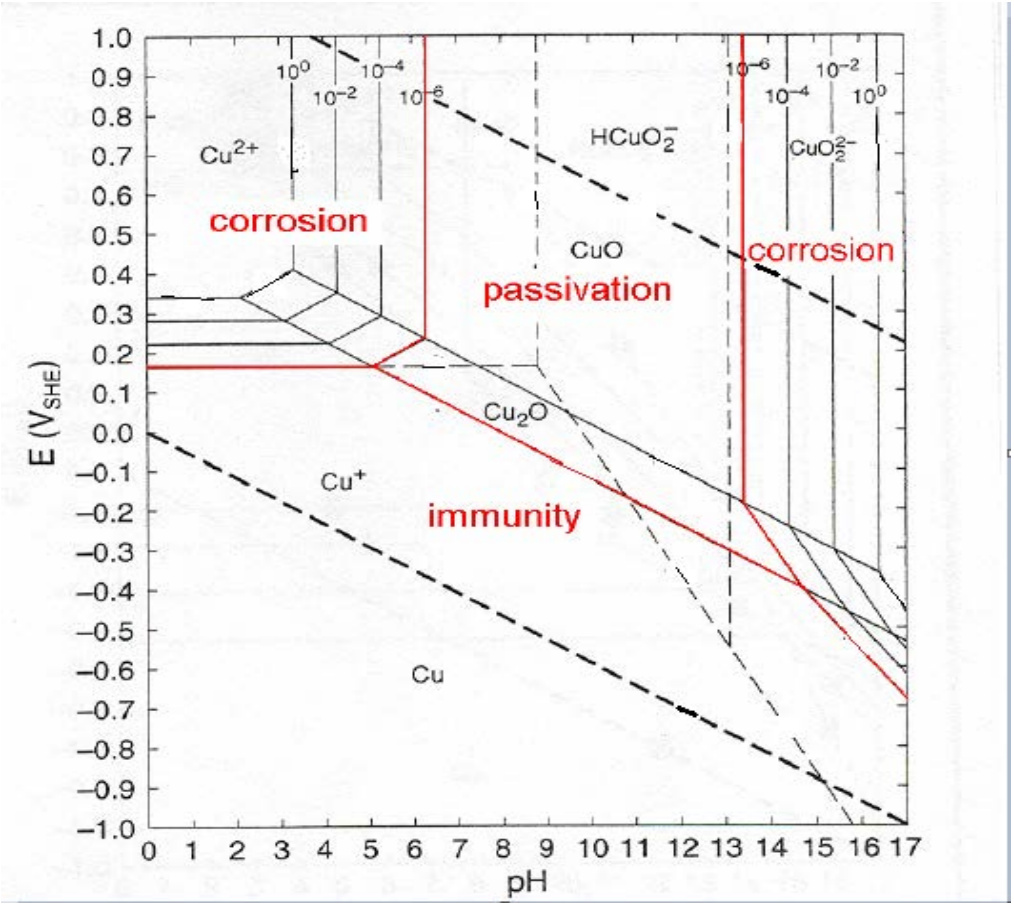


Figure 2.3: Pourbaix diagram of Cu-H_2O at 25°C [Lu, **2005].**

As indicated in Figure 2.3, copper will be susceptible to corrosion in regions with potentials above 0.2 and pH less than 6.5, and also at potentials above -0.6 V and pH greater than 13.5. At the other regions it will either be immune to corrosion, or it will passivate.

Corrosion resistance of copper in aqueous environments is different from the other alloys and metals in that it does not form a completely passive corrosion product on thesurface. It produces a cuprous oxide (Cu_2O) film which is predominantly responsible for its protection [Molina et al. 2015]. The Cu_2O film is adherent to the surface and follows parabolic growth kinetics [Dodek et al. 2011]. Cu_2O is a p-type semiconductor. Equation 6 and 7 shows how it is formed by electro chemical processes.

$4Cu + 2H_2O \rightarrow 2Cu_2O + 4H^+ + 4e^- \ (anode)$ 6

$O_2 + 2H_2O + 4e^- \rightarrow 4(OH)^- \ (cathode)$ 7

Net reaction: $4Cu + O_2 \rightarrow 2Cu_2O$.....8

The transformation from this state to having corrosion occur requires that Cu ions and electrons migrate through the Cu_2O film. However, this results in reduced conductivity of the film. Addition of alloying metals like ruthenium is done to dope the corrosion product film, which results in significant reductions in corrosion rates [Chen et al. 2017].

Depending on the conditions of the environment pitting, crevice, galvanic and other types of corrosion can occur to copper. Ruthenium is considered as one of the noble metals. When it is added to materials and metals, it tends to elevate the corrosion potential, and also stabilizes the passive film [Chen et al. 2017].

2.2 History of ruthenium

Ruthenium is a platinum group metal. The platinum group metals (PGMs) constitute a family of six chemically similar elements: platinum, rhodium, palladium, iridium, osmium and ruthenium. Platinum, osmium, and iridium are denser compared to rhodium, palladium, and ruthenium [Conradic, 2003]. PGMs have excellent catalytic qualities, chemical inertness, resistance to corrosion, and high melting points [Swanson, 2006].

South Africa and Russia are the world's largest producers of the PGMs [Wilburn & Bleiwas, 2004]. In South Africa PGMs occur in economic concentrations in three separate extensive layered reefs associated with the mafic rocks of the Rustenburg Layered Suite of the Bushveld Complex [Kinnaird 2005].

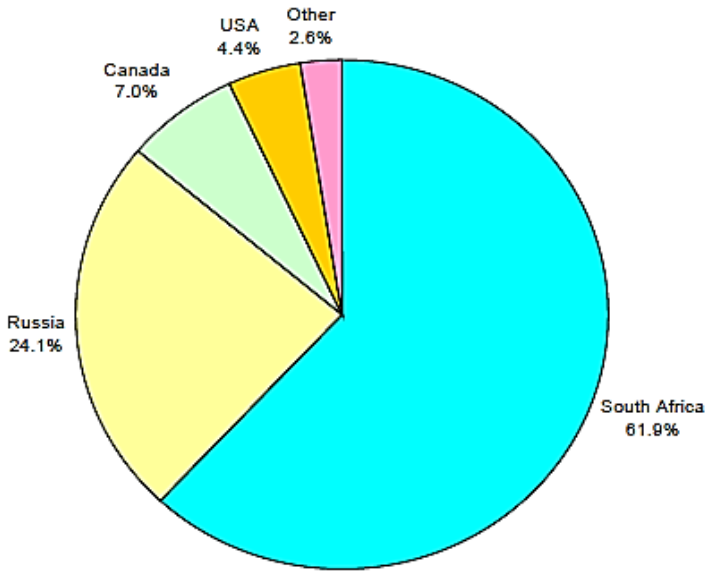


Figure 2.4: Major producers and suppliers of PGMs [Conradic, 2003].

South Africa is one of the major producers and suppliers of the PGMs. Figure 2.4 shows South Africa's contribution to world PGM supply in 2002 [Conradic, 2003].

The demand of ruthenium has been increasing over the years due to the new use of the metal in different sectors. This includes the electrochemical and chemical industry, electronic sector, development of super alloys in the aerospace sector, jewelry sector, and the corrosion sector [Hilliard, 2000]. In the electronics sector ruthenium paste is used in the manufacturing of resistor components [George, 2007]. Resistors are found in all electronic devices such as phones, laptops, television, and video games [Wilburn et al., 2004].

In the electrochemical industry and processes, ruthenium is used to coat the electrodes. The most important amongst the electrochemical industry is the chlor-alkali process which is used to produce caustic soda and chlorine from brine [Zahedipoor et al., 2013]. The chemical processors use ruthenium to manufacture acetic acid and polymers [George, 2007]. In jewelry applications, ruthenium is used as one of the alloying components. Adding ruthenium to platinum-palladium alloys increases their hardness while maintaining their oxidation resistance [Wilburn et al., 2004].



Figure 2.5: Ruthenium prices and charts [http://www.infomine.com/investment/ruthenium/, 2017].

The good news that comes with the increasing uses of ruthenium is that its price has been decreasing over the years as shown in Figure 2.5 above. This should open the possibility for more applications, thereby increasing the demand of the metal. The current market is still lacking new applications and with this research new new areas will be investigated.

In the aerospace sector, the demand for higher inlet temperatures of turbines has been the main reason for super alloy development, and ruthenium is used as one of the alloying elements. It has excellent properties that can withstand high temperatures while maintaining good mechanical properties. It is used as a substitute to rhenium, because it is approximately half the density of rhenium [Caron et al., 2000]. It also acts as a solid solution strengthener in ɣ precipitates for super alloys. At very high temperatures ruthenium-containing alloys show improved in creep resistance [Neumeier et al., 2008].

The demand for ruthenium in the electrical, chemical and electrochemical industries from the year 2010 to 2016 is shown in Figure 2.6.

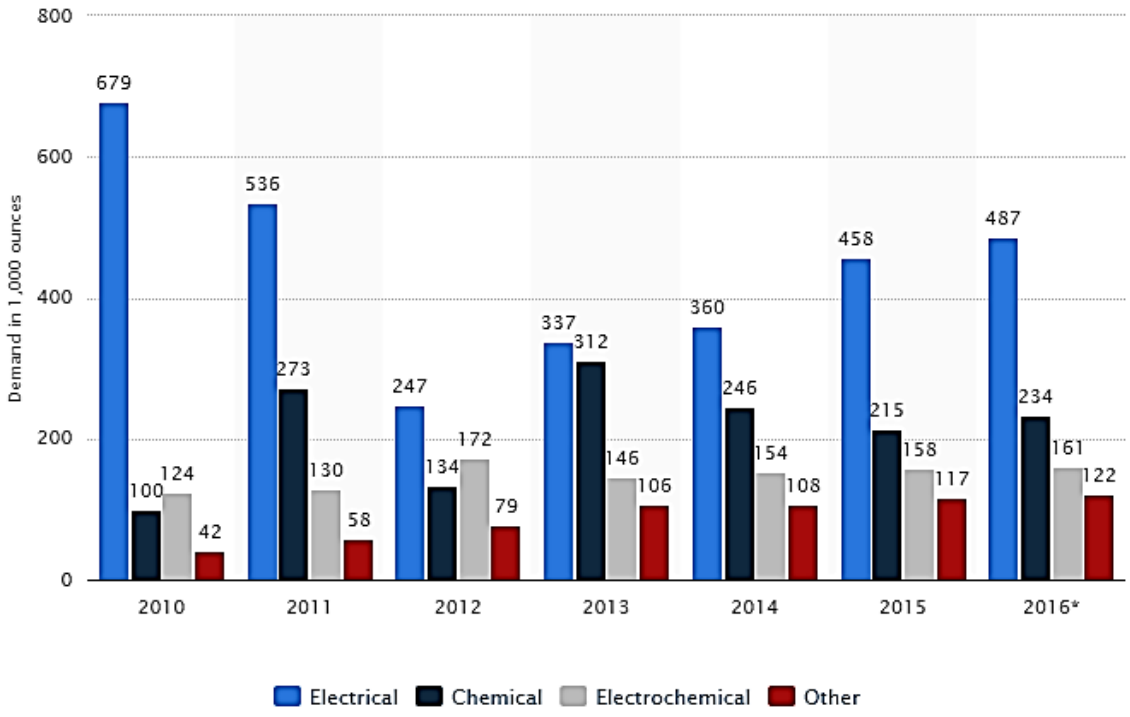


Figure 2.6: Demand of ruthenium from the year 2010 to 2016. [https://www.statista.com/statistics/592893/demand-for-ruthenium-worldwide-by-application/, 2015]

2.3 Improved corrosion resistance through ruthenium additions

Ruthenium has proved its usefulness in many cases that have been studied over the years [Zandra and O'Hara, 2006]. It has been added to different steels including, 304, duplex, austenitic and ferritic stainless steels [Govender et al., 2012]. In addition it has been added to tungsten carbide and titanium and other materials [Potgieter et al., 2014]. This has been done to improve the mechanical, physical and corrosion resistance properties. However, due to the cost associated with ruthenium, alloying with ruthenium limits its applications, and to make it economically feasiblesurface treatments instead of bulk alloying has been investigated, since corrosion is a surface phenomenon [Lekala et al., 2012].

2.3.1 Ru in austenitic-stainless steels

The use of ruthenium in 304L stainless steel (SS304L) has been investigated in the welding industry for both bulk and surface alloying. The welding industry fabricates 304L stainless steel structures that have to maintain suitable mechanical and corrosion properties during its application. This has to be achieved by ensuring that the corrosion potential of the welds is slightly higher than the corrosion potential of the 304L stainless steel [Liang et al., 2010]. The stated condition help minimize the galvanic attack of the weld metal. Until now, welds in SS304L were made with Ni-Cu-Pd welding consumables [Liang et al., 2010]. The addition of palladium (Pd) was beneficial for the corrosion resistance. The problem faced in the welding industry was that Pd is substantially more expensive than 304L. Replacing it with ruthenium, the least expensive of the PGMs, presented a sound economic approach. Alloying with ruthenium was found to increase the corrosion resistance of the welds in various acidic solutions.

Lekala et al. (2012) studied the corrosion characteristics of laser surface alloyed AISI 316L stainless steel and on alloyed AISI 316L stainless steel with 5.6 and 9.6 wt. % Ru in 80% sulphuric acid at 60℃. Figure 2.7 presents the potentiodyanic polarisation curve for Ru-alloyed stainless steel of the conducted study. Although all samples exhibited passivation, the AISI 316L stainless steel base alloys had some instability associated with the passive layer that had formed. However, the alloy with 9.6% Ru surface and the AISI 316L corroded at similar potentials, whereas the 5.6% Ru showed significant change in the corrosion potential. It presented more favourable conditions resulting in the lowest corrosion current density. Overall, the 5.6% Ru alloy showed the best corrosion resistance properties.

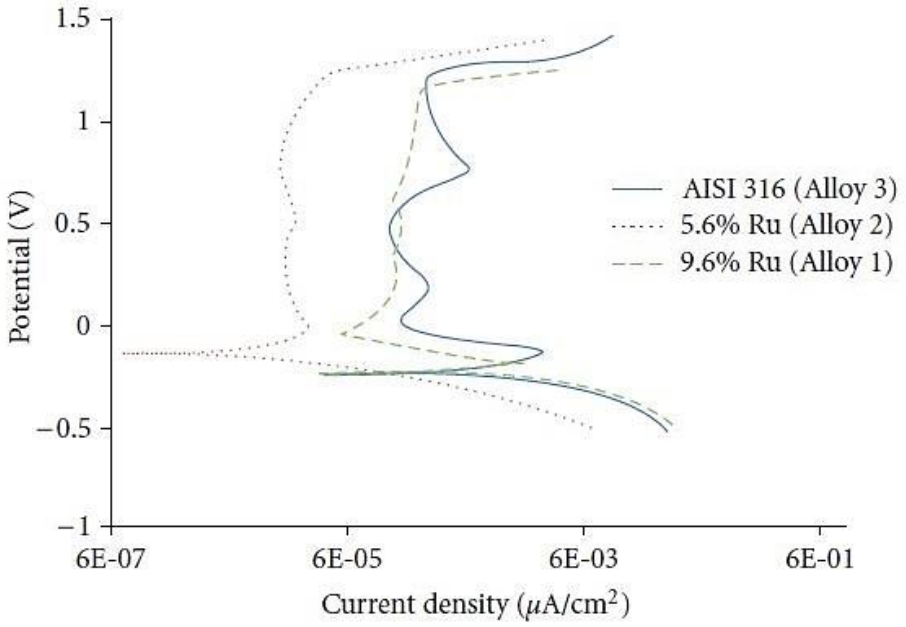


Figure 2.7: The potentiodyanic polarisation curve for Ru-alloyed stainless steel [Lekala et al., 2012].

Research was performed on Ru additions which were added to stainless steel cladding in a non-porous and well adhered layer of uniform thickness through a laser surface cladding method [Van der Merwe et al., 2014]. The work showed that the corrosion resistance of the stainless steel improved in 1M H_2SO_4 as well as 1M H_2SO_4 with 1 wt. % NaCl [Van der Merwe & Tharandt, 2015]. This conclusion was reached based on results from polarisation curves: corrosion rate calculated, corrosion potential, and passivation exchange current density, as well as open-circuit potential tests.

2.3.2 Ru in Duplex stainless steels

Duplex stainless steels (DSS) have a number of admirable basic properties like high strength and weldability. The research conducted by Sherif et al. (2009) showed that minor additions of PGMs to stainless steels increase the corrosion resistance remarkably. Their research particularly focused on the effect of ruthenium additions, 0.00, 0.14, 0.22 and 0.28%, on the passivation of 22%Cr-9%Ni-3%Mo duplex stainless steel immersed in a 3.5%NaCl solution.. The corrosion rates are presented in Figure 2.8.

Alloy	Ru content (%)
Alloy I	0.00
Alloy II	0.14
Alloy III	0.22
Alloy IV	0.28

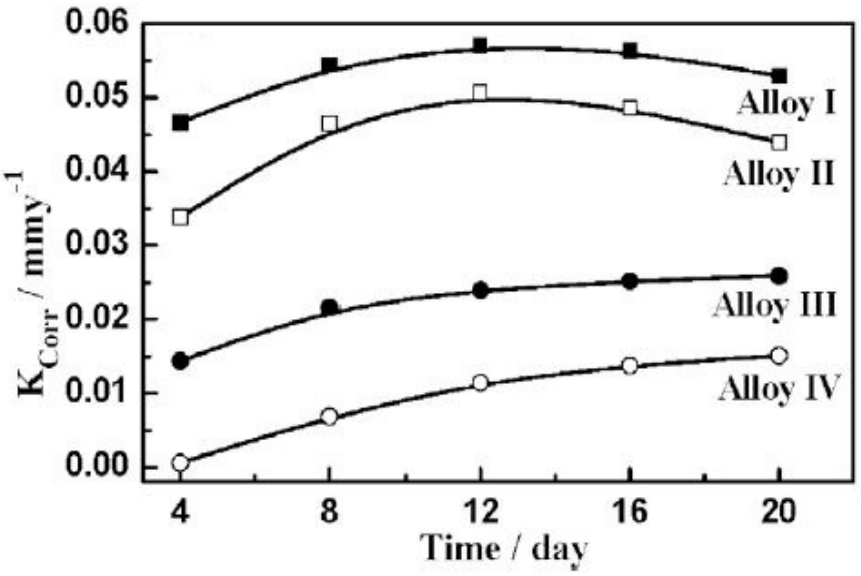


Figure 2.8: Corrosion rates for duplex stainless steel alloys with ruthenium [Sherif et al. 2009].

Although all the alloys showed an increase in the corrosion rate with time, alloying with ruthenium showed an improved corrosion resistance in the presence of chlorides. This effect had appeared to be more dominant on the 0.22 and 0.28% Ru alloys.

Furthermore, Sherif (2012) studied the corrosion of a DSS alloy 2209 with 0.3%Ru in 2M HCL and 0.6M NaCl. Based on the corrosion rates and the corrosion potentials recorded, the presence of ruthenium had a positive shift in the corrosion potential. This condition was observed in both the environments (2M HCl and 0.6M NaCl). For the 2M HCL environment, the corrosion rate had decreased by almost half of the original unalloyed duplex stainless steel, moving from 0.660 to 0.330 mmpy. The corrosion rate of the DSS decreased by a factor of about 3, in the 0.6M NaCl solution, changing from 0.022 to 0.007 mmpy. These results

suggested that the presence of ruthenium in that alloy causes the increase in surface resistance of the alloy against general and pitting corrosion [Sherif, 2012].

Most of studies conducted relating to ruthenium additions to duplex stainless steels are all in agreement that ruthenium improves the corrosion resistance by moving the corrosion potential to a more positive value. Olaseinde et al. (2012) studied the effect of ruthenium additions in 1M H_2SO_4 at different temperatures, ranging from 25 to 80°C. Even at varying temperatures, the potentiodynamic measurements showed the same trend. Alloying with ruthenium moved the corrosion potential to more positive values [Olaseinde et al., 2012]. Table 2.1 presents the results with the shift in the corrosion potential of the alloy.

Table 2.1: Electrochemical data for duplex stainless steel alloy with 0.15 Ru [Olaseinde et al., 2012].

Electrochemical data for samples in 1M H_2SO_4		
Alloy	T (°C)	E_{corr} (V)
2101	25	-0.404
2101LDX + 0.15Ru	25	-0.155
2101	40	0.006
2101LDX + 0.15Ru	40	0.194
2101	60	0.141
2101LDX + 0.15Ru	60	-0.363
2101	80	0.0007
2101LDX + 0.15Ru	80	0.149

2.3.3 Ru in titanium

In oxidizing environments, titanium exhibits excellent corrosion resistance. This results from the passivation film that forms at relatively negative potentials. The protective passive film formed is stable over a large range of potentials, but in strong reducing acids such as hydrochloric acid, the film is destroyed [Van der Lingen & Sandenbergh, 2005].

Corrosion resistance of titanium (Ti) in reducing environments was altered and improved by micro alloying with ruthenium. Van der Lingen and Sandenbergh (2005) conducted a study which compared the separate effect of alloying with ruthenium or palladium (Pd). The ruthenium alloys had compositions of 0.16% Ru and 0.20% Ru. The palladium alloys had compositions of 0.15% Pd and 0.25% Pd. These alloys were exposed to a 25wt% HCl aqueous environment at 25°C. The corrosion rates were calculated and compared with the unalloyed titanium, as shown in Figure 2.9.

The addition of the Ru and Pd only offered improved corrosion resistance to the titanium when added at a slightly higher level. An undesirable effect was observed at low concentrations of Ru and Pd. The corrosion resistance of the 0.16% Ru and 0.15% Pd alloys did not improve. However, an increase inruthenium content to 0.20% Ru resulted in substantially lower corrosion rates compared with the unalloyed titanium. Palladium (0.25% Pd) had a similar effect, but the corrosion rate was even lower.

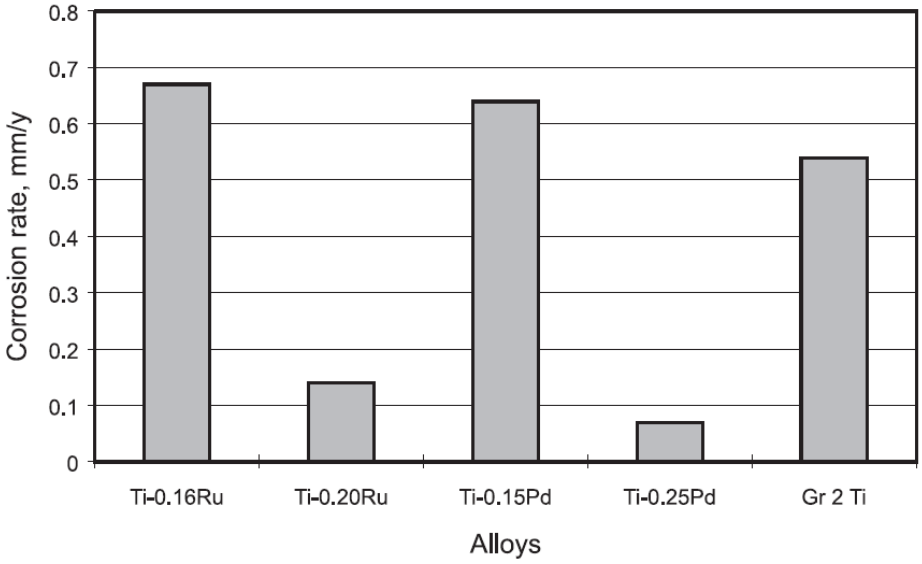


Figure 2.9: Corrosion resistance of titanium in reducing environments improved by micro alloying with ruthenium [Van der Lingen & Sandenbergh, 2005].

Sandenbergh & Van der Lingen (2005) found that ruthenium stimulated the cathodic reaction of the Ti-Ru alloy, but the anodic behaviour of titanium was unchanged. Biesiekierski et al. (2014) found that ruthenium additions to an as-cast Ti-Nb alloy improved the corrosion resistance. These two studies are in agreement that ruthenium improves corrosion resistance of materials.

2.3.4 Ru in tungsten carbide

Tungsten carbide is one of the hardest metals and possesses an excellent wear resistance. It has several industrial applications, especially in the mining industry. This application encounters difficulties in corrosive environments [Potgieter et al., 2014]. In the mining industry the tungsten carbide metal is used in applications such as conveyor belt scrapers, seal rings, jet nozzles, valves, linings and fluid mixers [Wentzel, 1995]. Often these units are in contact with corrosive environments. This can result in aggravated surface degradation and accelerating the wear process significantly.

Conventional tungsten carbide hard metals are composed of tungsten carbide particles and a cobalt binder matrix. It is produced during a liquid phase sintering process where the tungsten carbide is embedded the in a ductile binder phase. These tungsten carbide hardmetals are mainly composed of tungsten carbide, 88–95%, with cobalt as binder or various combinations of copper, chromium, iron and nickel [Potgieter et al., 2011]. According to Thanjekwayo (2009) and Potgieter et al. (2014) the cobalt binder phase is susceptible to corrosion in neutral and acidic environments. Ruthenium is added to improve the corrosion resistance of the cobalt. The binder metal showed localized corrosion, where the media preferentially attacked the binders first and then thereafter the tungsten carbide.

An experiment was conducted in synthetic mine water by Thanjekwayo (2009) and Potgieter et al., (2014). The experiment performed added ruthenium to the cobalt binder phase. The ruthenium was added at different proportions which where: 0.0, 0.4, 1.0, 1.5, 2.0, and 3.0wt%Ru. The results obtained from this research indicate that the presence of ruthenium in the binder decreased the corrosion rate significantly. The extent of corrosion resistance increased with the increase in the ruthenium content added to the binders. The corrosion rate decreased from 7.79 mmpya for the tungsten carbide without ruthenium to 0.004 mmpy for the 3.0 wt% Ru additions. Even the smallest addition of ruthenium had a great effect in the corrosion rate. The 0.4 wt% Ru achieved a corrosion rate of 1.79 mmpy. It was concluded from this work that ruthenium additions of up to 3 wt% Ru increased the corrosion resistance of the WC-Co alloys in acidic media.

A similar potentiodynamic test was performed in 1M H_2SO_4, using the same alloy composition (0.0, 0.4, 1.0, 1.5, 2.0, and 3.0 wt% Ru.). The results were recorded in a graph presented in Figure 2.10. The corrosion rate decreased with increasing ruthenium content in the alloy as expected.

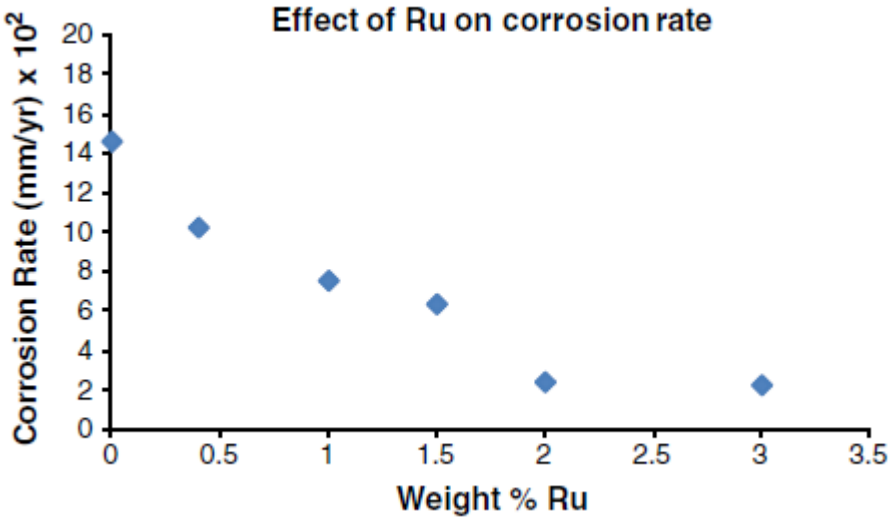


Figure 2.10: The effect of ruthenium additions on corrosion rate of the alloys in 1 M H_2SO_4 [Thanjekwayo, 2009].

These improvements were achieved because ruthenium is nobler than cobalt, and it therefore can resist chemical attack better. When there is accumulation of the ruthenium atoms on the surface of the alloy after corrosion of the cobalt has occurred, it promotes the efficiency for hydrogen evolution. With this condition met, the corrosion potential is bound to move towards the noble direction.

2.4 Methods used to mitigate copper corrosion

2.4.1 Coating processes

The corrosion protection mechanism associated to coating depends on the electrochemical nobility of the coating. Anodic coatings are less noble than the substrate. The protection mechanism is based on cathodic protection where the coating corrodes sacrificially to protect the substrate. Cathodic coatings are more noble than the substrate and forms a physical barrier between the corrosive environment and the substrate [Schiefler Filho et al., 2004].

The different coating application methods, such as cold spray, flame spray, electrical arc and thermal spray are used. Thermal spray processes use a combination of kinetic and thermal energy to form the coating [Davis, 2013]. The choice of the spraying process determines the amount and distribution of defects (e.g. oxides, pores, and cracks), and coating properties, such as hardness, thickness, and adhesion. The quality of the coating is strongly related to the spray parameters: oxygen pressure, fuel gas type, particle velocity and spray distance [Schiefler Filho

et al., 2004]. Selecting the correct spraying process will enhance the service life of a component.

The different coating processes were considered in order to select one for the project. The flame spray process could not be used because its coatings exhibit lower bond strength, higher porosity, and narrower working temperature ranges [Faunchais & Vardelle, 2012]. Porosity in coatings breaks the cohesion between the substrate and the coating. Therefore, electrical arc spray process could not be used because it produces coatings with higher porosity [Robert & Tucker, 1994].Two coating processes were selected for this research: The cold spraying (CS) process and the high velocity oxygen fuel (HVOF) thermal spray process. This will allow for the comparison to see the better coating process.

2.4.1.1 Cold spray coating process

The cold spray process utilises a supersonic jet of compressed gas to accelerate powder particles to ultra-high velocities and consolidate on impact with the substrate to create a coating [Faunchais et al., 2014]. This is achieved when the solid particles, exiting the nozzle, impact the substrate and plastically deform, and create both a mechanical and metallurgical bond with the surrounding material [Villafuerte, 2015].

Figure 2.11 shows a schematic diagram of the cold spray process. The powder is fed and travels with a supersonic gas jet and exits through the nozzle to the substrate, forming a coating. This process relies on the critical velocity of the feed powder particles. It can achieve a deposition efficiency of 0.5-0.8 of the powder. This process is influenced by a number of parameters, including powder size, feed rate, critical velocity, gas temperature and pressure, as well as stand-off distance. The particle size of the powder used in the cold spraying process range from 5 to 100 µm [Champagne, 2007].

The velocity of the powder particles range from 200 to 1000 m/s [Li et al., 2014]. Pressures range from 2 to 2.5 MPa for a typical nozzle throat with an internal diameter ranging from 2-3 mm. The processing gases used are nitrogen, helium or a mixture of the two, and air. For standard conditions, typical gas flow rate must be 10 times that of the powder entrained [Fauchais el al., 2014].

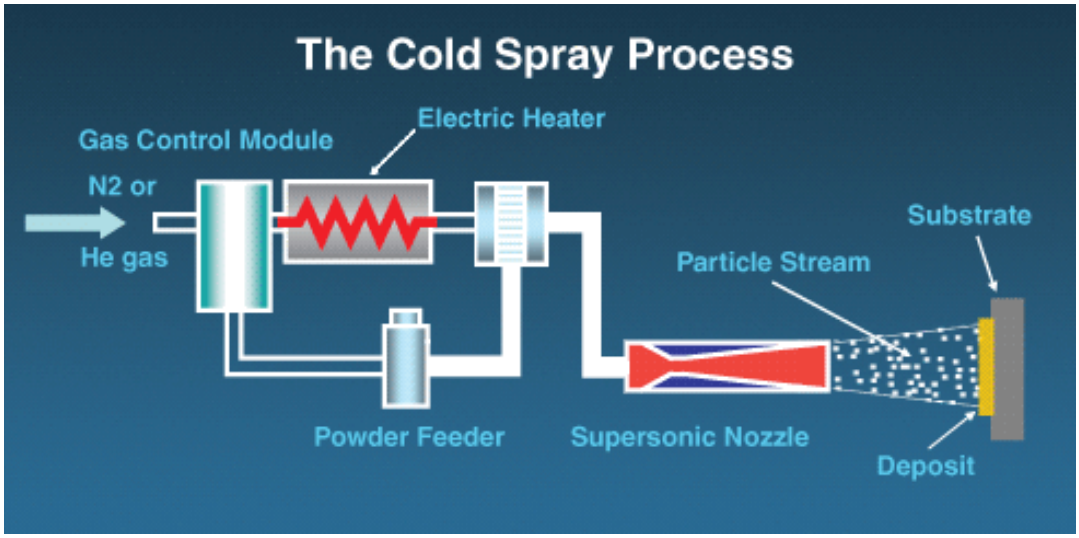


Figure 2.11: A schematic diagram of cold spraying process [Champagne, 2007]

The cold spray process is able to produce a large range of coating thicknesses [Villafuerte, 2015]. This method has achieved very high coating deposition rates, and it deposits a wide variety of materials such as metallic alloys, composites polymers and pure metals, onto various substrates [Conto, 2011].

Cold spraying has been considered because it achieves the coating formation without the use of very high temperatures. With other thermal coating processes the coating is formed by both the kinetic as well as thermal energies of the sprayed particles, whereas the cold spray process mostly relies on their kinetic energy . The kinetic energy is sufficient to produce plastic deformation and high interfacial pressures, as well as increasing the temperature required to form the coatings [Conto, 2011]. Despite the lower temperatures used the cold spraying method can achieve low porosity and very high density in the coating [Conto, 2011]. The high velocity impact in cold spray process enables the formation of a low oxidation coating because it can induce intensive plastic deformation of the powder particles and the substrate [Li et al., 2014]. During the cold spraying process, there is no melting and splashing of the powder particles as they reach the substrate surface [Champagne, 2007]. This process is a solid state process. Low temperatures greatly reduce or eliminate the possibility of any oxidation reactions of the metal powder to form during deposition. It also prevents vaporization of volatile powders. These result in improved thermal, mechanical and electrical properties of the coating [Champagne, 2007]. Cold spray can also be applied to temperature sensitive substrates.

One of the desirable qualities of using the cold spraying process is that it retains and preserves the grain structure and phase composition of the feed powder, even in the final coating

[Fauchais el al., 2014]. The initial powder will have the exact same properties as the final product.

The cold spray process is limited to a narrow set of materials, which are strain rate sensitive, within much defined limits [Robert & Tucker, 1994]. It requires that depositing materials have good ductility to produce quality bonds between the coating and the substrate [Davis, 2013]. Since the powder particles do not melt before impacting the surface, and only rely on the ductility of the powder to deform and form a coating, only certain substrates can be used. The substrate material should be harder than the particles being sprayed, to allow the ductile particles to deform upon impact. Softer materials cannot be used as a substrate, and the harder and more brittle materials cannot be used as coating material [Conto, 2011]. The cold spray coating process consumes a lot more processing gas compared to thermal spray coating processes. Some of these gases, like helium, are very expensive.

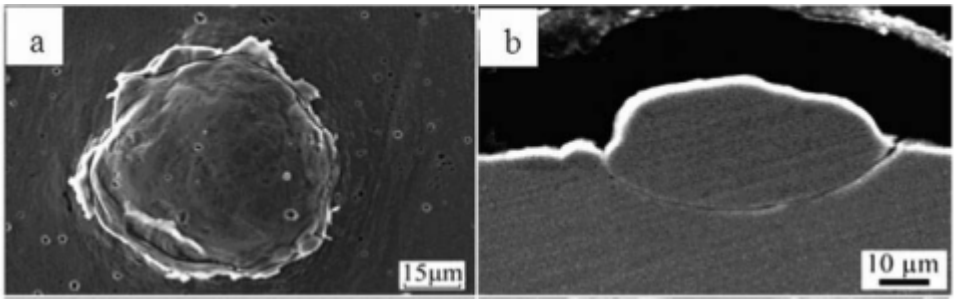


Figure 2.12: The experimental results of an individually deposited Cu particle on a polished Cu substrate. (a) surface and (b) cross-section morphologies at incident angle of 90º [Li et al., 2014].

Copper powder has been done successfully coated onto a copper substrate. Work done by Li et al. (2014) considered the effect of impacting velocity, preheating and oxidation state, and impacting angle on the coating properties. The micrographs in Figure 2.12 show the surface and the cross section of an individual copper particle that was deposited on a polished copper surface.

The impact angles of 90, 70, 50, and 30º were considered. As the impact angle decreased, the deposition efficiency of the coatings also decreased. The other noticeable effect was that with a greater deviation from 90º increased porosity in the coatings were found. At 30º no particles adhered to the substrate, but instead the substrate was eroded. It was shown that 90º is the best impacting angle for coatings [Li et al. 2014].

The research by Stoltenhoff et al. (2006) indicated that the cold spraying of copper powder on the copper substrate produced coatings with well bonded particle-particle and particle-substrate interfaces. The coatings had a smooth surface morphology, with low porosity and few oxides. The oxygen content was recorded to range from 0.04 to 0.09wt% which was comparable to the oxygen content of the initial feed material. The particles appeared much more flattened and the microstructure of the coatings revealed almost no defects.

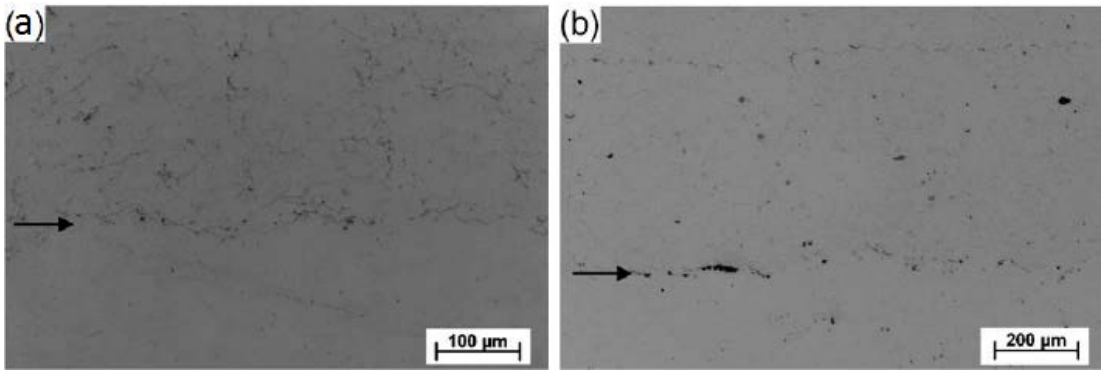


Figure 2.13: Microstructures (cross-section) of cold-sprayed Cu-powder on Cu-substrate using (a) nitrogen and (b) helium process gas [Stoltenhoff et al., 2006].

The use of different process gases resulted in different coating qualities. As mentioned, the most commonly used gases are nitrogen and helium. The cross sectional microstructures of the copper coating produced with nitrogen and helium are compared in Figure 2.13 [Stoltenhoff et al., 2006]. The coatings produced revealed almost no defect. These coatings could only be distinguished from the substrate material by the residue from the grid blasting in the bond zone. Compared to nitrogen sprayed coatings (Figure 2.13a), helium sprayed coatings (Figure 2.13b) were well bonded and showed a very smooth surface morphology [Stoltenhoff et al., 2006].

2.4.1.2 High Velocity Oxygen Fuel spray coating process

The HVOF spray, a thermal spray process, will be used in this study for coating the copper metal. Thermal spraying is a method in which the coating is formed from molten metal droplets that are sprayed onto the metal surface [Pawlowski, 2008]. The feed can be in the form of powder or wire. Feed particles have to plastically deform at impact with the substrate. Thermal spray processes are able to apply the coating to the substrate without significant heat input [Davis, 2013]. Therefore, there is little or no change to the properties of the substrate with no thermal distortion [Davis, 2004]. In the coating process, velocity and temperature of the flame has a strong effect on the material being sprayed. Good adhesion and low porosity of the coating is important since coating is applied to improve corrosion and wear resistance.

The HVOF spray process obtains coatings with low porosity, good adhesion, and uniform coating thickness [Schmid et al., 2004]. It has the ability to produce dense coatings with little degradation, oxidation of metallic materials, and phase transformation [Oksa et al., 2011]. There are several parameters that can be controlled and monitored during the HVOF process for acceptable coatings. These include particle state, temperature, velocity, and molten state of the powder in the feed [Faunchais & Vaedelle, 2012]. During the HVOF spray process accurate control over the powder feed rate is possible, because it is sensitive to the volume of powder injection [Davis et al., 2004]. The coating properties depend on coating microstructure, density and thickness. Coating microstructure is influenced by the phases formed, the porosity, and non-melted powders [Wang et al., 2006].

The most important coating properties are: hardness, strength of bonding, elastic modulus and residual stresses [Faunchais et al., 2014]. These properties determine the function of the coated material, and its suitability for the desired job.

According to Mott (1956), “hardness is a measure of resistance to permanent deformation and damage”. When coatings are applied on a hard base, it causes the hardness to increase with decreasing layer thickness with all other factors remaining unchanged. Practically the resultant coating is harder and more suitable [Fink-Jensen, 1964].

The bonding strength of the coating to the substrate and the cohesion between consecutive splats is affected by: the residual stresses within the coating, melting and localized alloying at the contact surfaces between particles and substrate and adjoining particles, diffusion of elemental species across splat boundaries, and mechanical interlocking [Davis, 2004].

The residual stresses in coatings, which could be either beneficial or detrimental, result from individual particle stress. It will be detrimental if the tensile stress exceeds the elastic limit. This will cause cracking at the interface between the coat and the substrate and also in the coating surface. However, the beneficial part is that the compressive residual stresses can increase the number of cycles before crack initiation begins [Montay et al., 2004]. When the coating is complete, the coating performance can be investigated. The investigation looks at the wear resistance, corrosion resistance, and electrical insulation.

The advantage of the HVOF process is that it produces coatings with low porosity. The percentage porosity can be as low as 1 % [Oksa et al., 2011]. This is because the particles move at very high velocities and minimises the time for particles to cool down. It produces

more uniform and efficient particle heating as a result of high turbulence in the combustion chamber [Stokes, 2003]. The particles are exposed to the high temperatures for shorter times which leads to less surface oxidation [Hasan, 2005]. The main benefits of using HVOF are summarised in Table 2.2.

Table 2.2: Benefits of HVOF process [Sidhu et al. 2005].

Coating benefits	**Main reason for this benefit**
Higher density (Lower porosity)	Higher impact energy
Improved corrosion barrier	Less porosity
Higher hardness ratings	Better bonding, less degradation, denser coatings
Improved wear resistance	Harder, tougher coating
Higher bond and cohesive strength	Improved particle bonding
Lower oxide content	Less in flight exposure tine to air
Fewer unmelted particle content	Better particle heating
Greater chemistry and phase retention	Reduces time at higher temperature
Thicker coatings	Less residual stress
Smoother as sprayed surface	Higher impact energies

The HVOF spraying method is performed with an additional cooling system, to cool the substrate so that it does not overheat. Liquid CO_2 can be used for the cooling system [Hasan, 2005]. The disadvantage of the HVOF process is that there is a possibility of cracks forming in the coating. These cracks can originate from the stresses induced at the coating-substrate interface. It can also be the result of thermal expansion mismatch between the coating and the substrate [Heath et al., 1997]. The cracks allow the corrosive environment to reach the substrate that has to be protected.

Post-coating procedures can be used to improve the coating microstructure, dimensions, relaxation of residual stresses, closure and porosity reduction, homogeneity, etc. [Davis, 2004]. These improvements are achieved by chemical, physical, , thermal, and/or mechanical treatments. The heat treatment process during hot isostatic pressing (HIP) can be used to reduce residual stresses and increase of inter-particle cohesion [Davis, 2004].

HVOF spraying of copper powder has been done successfully. The photograph presented in Figure 2.14 shows the cross section of a copper coating on a substrate using the HVOF spraying technique [Stoltenhoff et al., 2006]. The cross section of the coating shows quite a non-uniform microstructure. The microstructure had some oxidized lamellar regions in particle-particle interfaces. There also are spheriodized oxides within the copper matrix resulting from the presence of oxides in the coatings. The oxygen content for this coating was approximately 0.8wt% [Stoltenhoff et al., 2006].

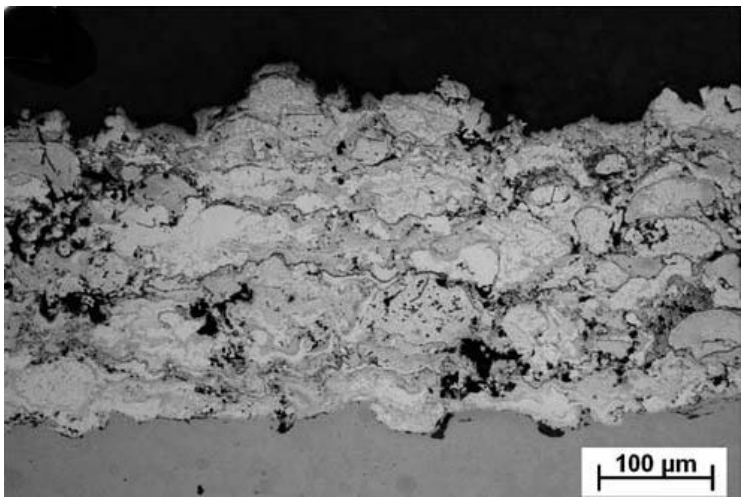


Figure 2.14: Cross-section of a HVOF sprayed Cu-coating [Stoltenhoff et al., 2006].

2.4.2 Metal alloying

Spark plasma sintering (SPS) is a high speed powder consolidation process. It is based on the simultaneous application of a low-voltage, high-energy pulse current and uniaxial pressure [Menapace et al., 2006]. The schematic drawing of this process is shown in Figure 2.15. SPS is characterised by fast heating, a short isothermal holding time and a relatively low sintering temperature. This is a great advantage since it results in low heat input limiting chemical interaction between the constituents [Diouf et al., 2013].

Material processing is completed in short periods of approximately 5 to 25 minutes. The relatively low temperatures combined with fast processing times ensure tight control over grain growth and microstructure [Aulund 2008]. Spark plasma sintering is capable of processing conductive and nonconductive materials. When compared with conventional sintering methods, the spark plasma sintering is found to save energy and time, and also improve the equipment efficiency. Materials made by SPS have grains within narrow size ranges and excellent mechanical properties [Lianga et al., 2015].

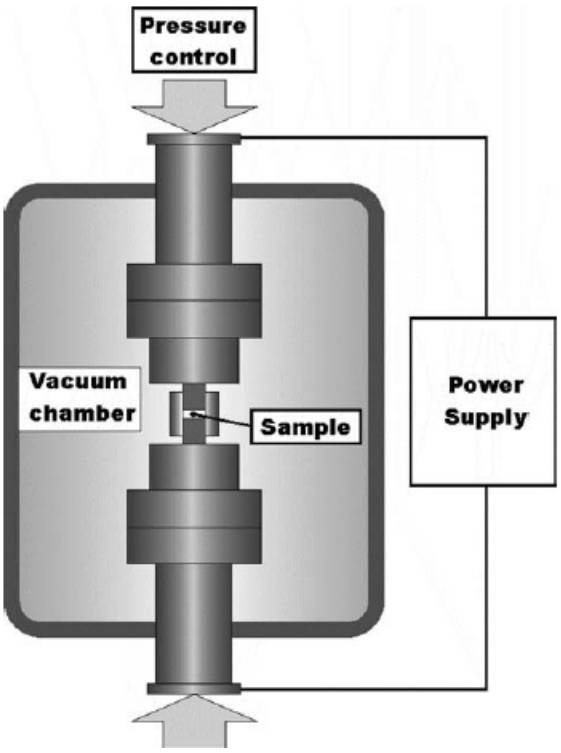


Figure 2.15: Schematic drawing of the SPS process [Munir and Anselmi-Tamburini, 2006].

A lot of work has been done in powder metallurgy using the SPS to sinter copper powder. The following Table 2.3 entails some of the work, recording the parameters they used for sintering, with temperatures between 700 to 950℃.

Table 2.3: The SPS experiments conducted and the main parameters used.

Material	Parameters (Heating profile)				Reference
	Temperature (℃)	Pressure (MPa)	Hold time (min)	Heating and cooling rate (℃/min)	
Copper-diamond powder	900	50	10	100	Niazi et al. (2016)
Copper-ruthenium-tantalum	850	30	30	20	Sule et al. (2012)
Copper powder	950	30	1	100	Menapace et al. (2016)
Cu-CNT powder	700	50	5	80	Sule et al. (2014)
Copper powder	800	50	10	-	Lianga et al. (2015)

Some of the work done in sintering copper powder using SPS was by Menapace et al. (2016). Their research focused on the effect particle size and the initial oxygen content of the powders had on the outcome of the sintered bulk copper. The finer particles lead to a faster and better densification during sintering. Higher oxygen content in the initial powder decreased the ability of the powders to be sintered. This also lead to higher electrical resistance for the powders due to higher particle-particle contact area and the oxide content.

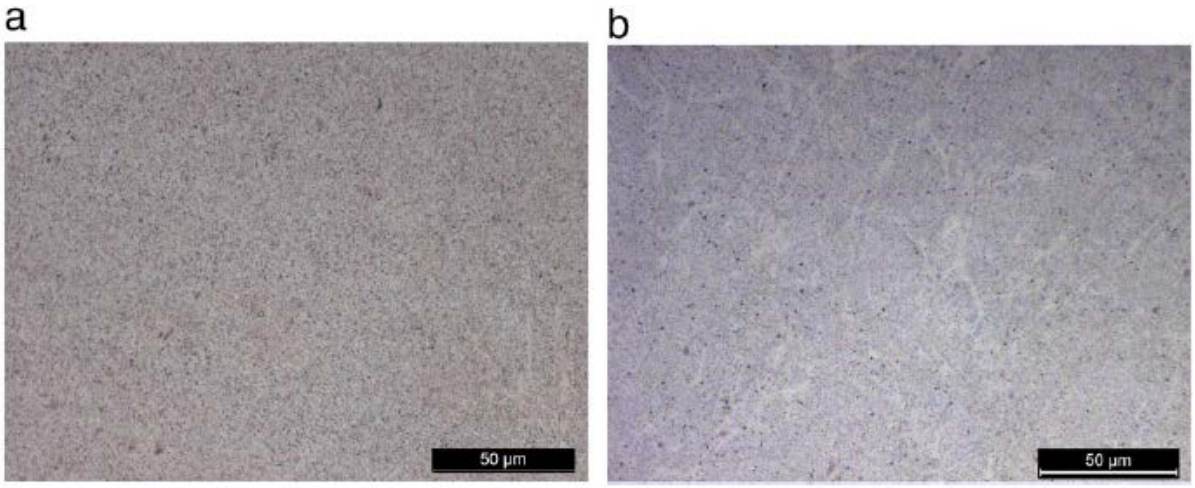


Figure 2.16: The microstructures of copper discs produced by SPS using a (high oxygen) and b (low oxygen content) powders [Menapace et al., 2016].

Both the microstructure presents fine grains with no resolved grain boundaries. The microstructure of the copper disc produced using high oxygen content powder had larger grain sizes, together with a lower dislocation density compared to the one produced using low oxygen content powder. The total porosity of sample (a) was also higher than that of sample (b) [Menapace et al., 2016].

The benefit of using sintering is that it allows for freedom to choose the proportions of the charged materials that will be of great benefit to the final product [Besta et al., 2012]. Fedrizzi et al. (1991) and Velasco et al. (1996) showed that it allows for a good combination of mechanical and corrosion resistance as found in sintered stainless steels. However, sometimes when these components are exposed to sulphuric acid environments they do behave differently from the wrought material. It is suggested that the sintered components will entrap electrolyte in their pores and form hydrogen ion concentration cells [Raghu et al., 1988].

2.4.3 Electroplating

Electroplating is an electrochemical process that can produce a coherent metal coating on the surface of an electrode [Jaganraj et al., 2016]. This method has received considerable attention over the years, because it can be feasible, inexpensive and economically viable [Rashidi & Amadeh, 2010]. The electroplating method has been used to coat many different materials including zinc, copper, silver, nickel, gold and platinum. These coatings are applied for various reasons, such as improvement in abrasion, corrosion and contact resistance [Edwards, 1983].

The electroplating process that focuses on resistance to or protection against corrosion in materials accomplishes this in one of two ways. The coating either shields the substrate from the corrosive environment or acts as a sacrificial anode [Edwards, 1983].

Electroplating is carried out in an electrolyte cell filled with a suitable salt solution, electrolyte, of the metal being deposited [Palanna, 2009]. The electrolyte cell contains electrically equivalent amounts of dissolved cations (positively charged particles) and anions (negatively charged particles) in a solvent. A direct electric current is passed through the solution between the anode and the cathode to perform the electroplating process [Jaganraj et al., 2016]. The anode is the pure metal plate or rod and the cathode is the object being plated. Upon electrolysis the anode metal M dissolves as M^{n+} ions and the cathodic reduction of M^{n+} from electrolyte and deposition of metal on the substrate takes place. These reactions can be presented in the following equations:

$M_{anode} \rightarrow M_{solution}^{n+} + ne^{-}$…..(anodic dissolution of the metal-oxidation)

$M_{solution}^{n+} + ne^{-} \rightarrow M$…..(cathodic reduction of M^{n+})

This reaction is accompanied by the transfer of n electrons from an external electron source to the electron gas in the metal M [Kanani, 2004]. Ideally, both reactions are assumed to be taking place at the same rate and the concentration of M^{n+} in the solution remains the same [Palanna, 2009]. Some of the electroplating processes make use of an inert anode like platinum. For such cases, the main anodic reaction is the evolution of oxygen and M^{n+} concentration get decreased during the main electrolysis. The electrolyte has to be added from time to time in order to maintain the concentration of M^{n+} ions [Palanna, 2009].

The mechanism of electroplating can be presented in 3 steps [Palanna, 2009]. The first step is the diffusion of metal ion from bulk electrolyte to the cathodic surface.

$M_{anode} \rightarrow M_{solution}^{n+}$ (Bulk diffusion)

The second step is the reduction of the metal ions on the substrate surface to form adsorbed atom layer.

$M^{n+} \rightarrow ne^{-} \rightarrow M_{ad\ substrate}$ (Formation of atomic layer)

The third stage is the growth of deposition resulting in thickening of layer into macroscopic deposit.

$$M_{ad\ atom} + M_{atoms} \rightarrow M_{substrate} \rightarrow thickening$$

A schematic of the electroplating process of copper is shown in Figure 2.17 [McCarthy 2012].

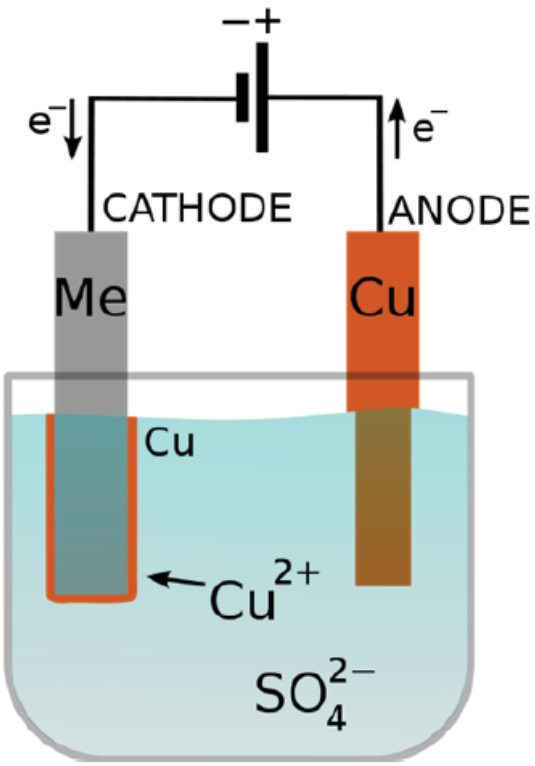


Figure 2.17: Schematic of the electroplating process of copper [McCarthy, 2012].

In this case (Figure 2.17) the metal ions (Cu^{2+}) moved from the anode (the source metal) through the sulphate bath to the substrate Me. The quality of the coating formed is determined by certain factors, the distance between the electrodes, the applied voltage and current, and the geometry of the part being plated [McCarthy, 2012]. Table 2.4 lists the characteristics of good and poor deposits during an electroplating process.

Table 2.4: Characteristics of good and poor deposits during an electroplating process [Palanna, 2009], [Kanani, 2004], and [Stoltenhoff et al., 2006].

Good characteristics of electroplating coatings	Poor characteristics of electroplating coatings
Should have good adhesion to the substrate and should be uniform	Has poor adhesion with the substrate and is non uniform

The deposit should be non-porous, dense and with a fine grained structure	The coatings are porous and have coarsely crystalline structure
It should be hard with sufficient ductility	The deposit has a powdery structure and is brittle
The coatings must be bright and shiny	They appear dull

Good adhesion ensures that there is no necking and the coating remain on the substrate and will not be easily removed in application [Stoltenhoff et al., 2006]. Porous coatings are avoided in order to prevent corrosion from occuring since porosity affects the corrosion resistance of the material [Kanani, 2009].

During electroplating, coating thickness distribution varies and depends on the shape of the material being coated. Figure 2.18 shows the typical distribution deposit for 3 common shapes [Edwards 1983].

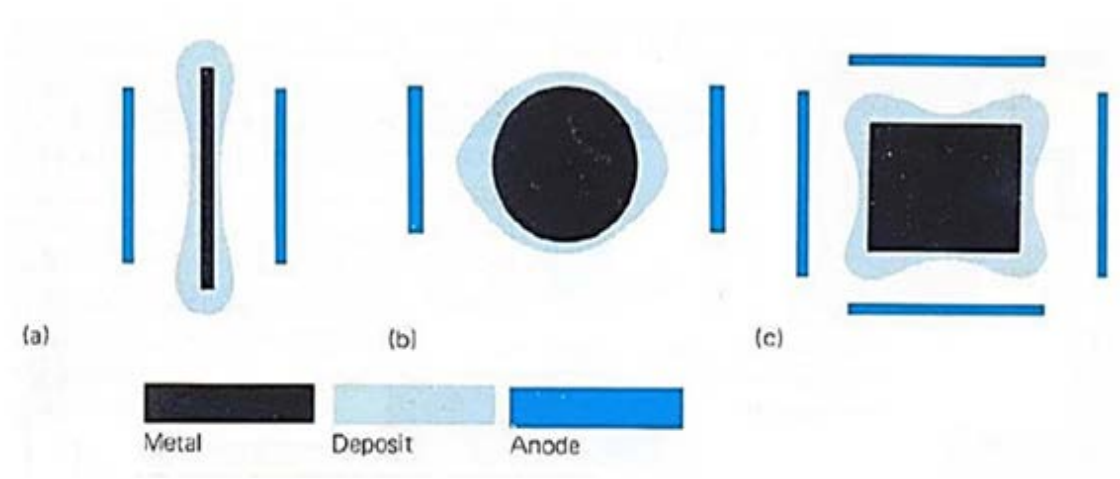


Figure 2.18: Typical distribution of deposit on various shapes of surfaces during electroplating , (a) thickening of deposit at edge of flat sheet, (b) Ovality of deposit on circular section, and (c) Build-up on corners of square section [Edwards 1983].

There are factors that influence the nature of electrodeposits that result. These include current density, pH, power, plating bath, and temperature [Palanna, 2009]. Two electrodeposition methods can be used during electroplating. The pulse electrodeposition or continuous electrodeposition method. During pulse electrodeposition the current or potential is alternated swiftly. The resultant to these actions is a series of pulses of equal amplitude, polarity and duration, separated by zero current as shown in Figure 2.19. Each pulse consist of an ON time

(T_{ON}) and an OFF time (T_{OFF}). During T_{ON} the potential and/current is applied, and during T_{OFF} there is zero current applied [Chandrasekar & Pushpavanam, 2008].

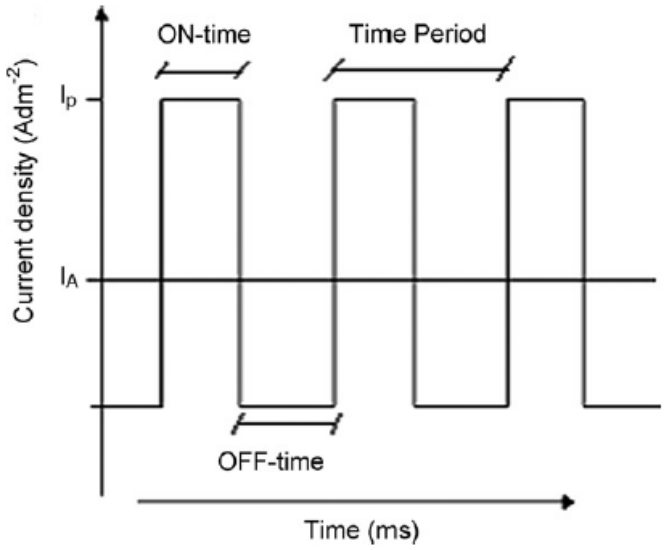


Figure 2.19: Typical pulse-current waveform [Chandrasekar & Pushpavanam, 2008].

By controlling the pulse amplitude and width, one can actually control the deposited film thickness, composition and grain size. The pulse plating method can produce layers with a fine grain size (less than 10 nm) and better porosity compared to conventionally plated coatings. The grain size decreases with an increase in current density [Melciu & Maidee, 2015]. During the T_{ON} period, ions in the bath become depleted around the high density areas. During the T_{OFF} period, the ions are evenly distributed and become available for deposition during the next cycle. This process allows for better levelling of deposit, grain size control and minimizes porosity [Chandrasekar & Pushpavanam, 2008].

2.5 Corrosion theory used to explain corrosion chemistry/predicting the corrosion behaviour

2.5.1 Polarisation

Polarisation is the potential change from the equilibrium half-cell reaction. There are various chemical and physical factors that limit the electrochemical reaction rate [Fontana, 1987]. Electrochemical reactions (anodic and cathodic reactions) proceed only at limited rates. When the electrons are produced at the cathode, and excess negatively charged electrons accumulate at the metal-solution interface, the potential at the surface becomes more negative [Jones, 1996]. As an example the corrosion of zinc in sulphuric acid is as follows:

$Zn \rightarrow Zn^{2+} + 2e^{-}$ $(anodic\ reaction)$ ……...9

$2H^{+} + 2e^{-} \rightarrow H_2$ $(cathodic\ reaction)$ ……10

When the sample is negatively charged, it is cathodically polarised. A deficiency of electrons in the metal liberated by equation 1 at the interface produces a positive potential change, or anodically polarised (Jones, 1996). As seen in Figure 2.20, as the polarisation increases, the tendency for anodic dissolution increases. The anodic polarisation represents a driving force for corrosion by the anodic reaction presented in equation 9. When the surface potential measures more positive, the anodic polarisation becomes greater, and the corrosive power of the solution increases [Fontana, 1986]. The relationship between polarisation and the rate of the reaction represented by current density is:

$\eta_a = \beta_a log\left(\frac{i_a}{i_o}\right)$ ……...11

$\eta_c = \beta_c log\left(\frac{i_c}{i_o}\right)$ ……12

$\beta_a$and β_c are Tafel constants (which are assumed as ±0.1V per decade of current) for the half-cell reaction.

The corrosion rate generally increases as the surface potential increases above E_{corr} (steady state potential) to E. According to Figure 2.20, the anodic polarisation is given by $\varepsilon_a = E - E_{corr}$.

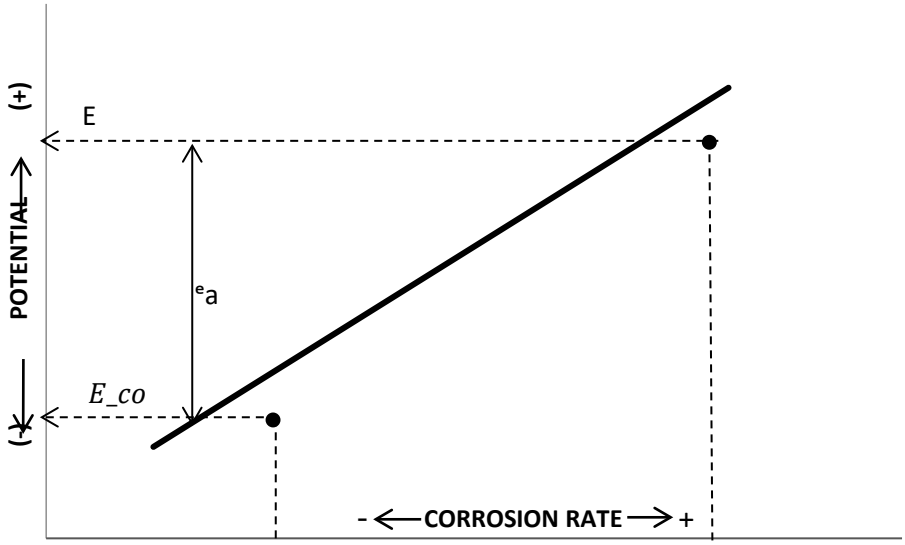


Figure 2.20: Increase in corrosion rate with increasing potential E and anodic polarisation ᵉa (Jones, 1996)

2.5.2 Passivity

Passivity is when alloys and metals in a corrosive solution form an oxide layer, which can be very thin and protect the surface [Jones, 1996]. It is a condition where there is loss of chemical reactivity experienced by certain alloys and metals under distinct environmental conditions.

Metals and alloys display distinctive behaviour as anodic polarisation increases, illustrated in Figure 2.21. At low over potentials characteristic of deaerated acid solutions, corrosion rates measured by anodic current densities are high and increase further with potential in the active region. At high over potentials, in the passive region, the corrosion rates falls and the passive film become stable. This condition changes at even higher over potentials (transpassive region), where the passive film breaks down and the anodic rate increases [Fontana, 1987]. In cases where there is an oxidizer, increasing the oxidizer concentration increases the potential of the half reaction. Ideally you want to increase the oxidizer concentration until it reaches the passive region (point 4 in the graph) where the corrosion rate drops. Any other points (1 to 3) tend to increase the corrosion rate and the corrosion potential.

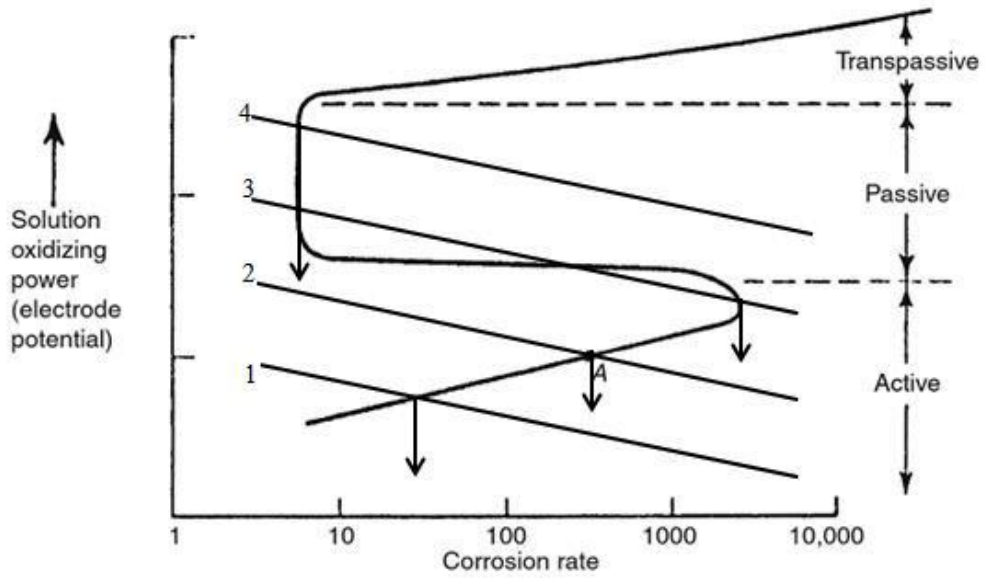


Figure 2.21: The effect of oxidizer concentration on corrosion of an active-passive alloy [Jones, 1996]

According to Babic et al. (2001) copper metal forms a thin passive layer in neutral and alkaline solutions. The passivation corresponds to the formation of a duplex oxide film Cu_2O. This is different for acidic solutions since copper does not form a passive layer [Vastag et al., 2013]. In some cases it can only form a transpassive layer as shown by Schneider et al. (2012).

Chapter 3 : Methodology

3.1 Introduction

This chapter gives details on how the experiments were set-up and performed, the material and equipment used, and procedure. Copper and ruthenium powders were mixed, and were either formed into alloys, or applied as coatings. Thereafter the microstructure, composition, and hardness of the samples were analysed. The corrosion behaviour of the different samples was investigated. Figure 3.1 shows the graphical experimental flow sheet.

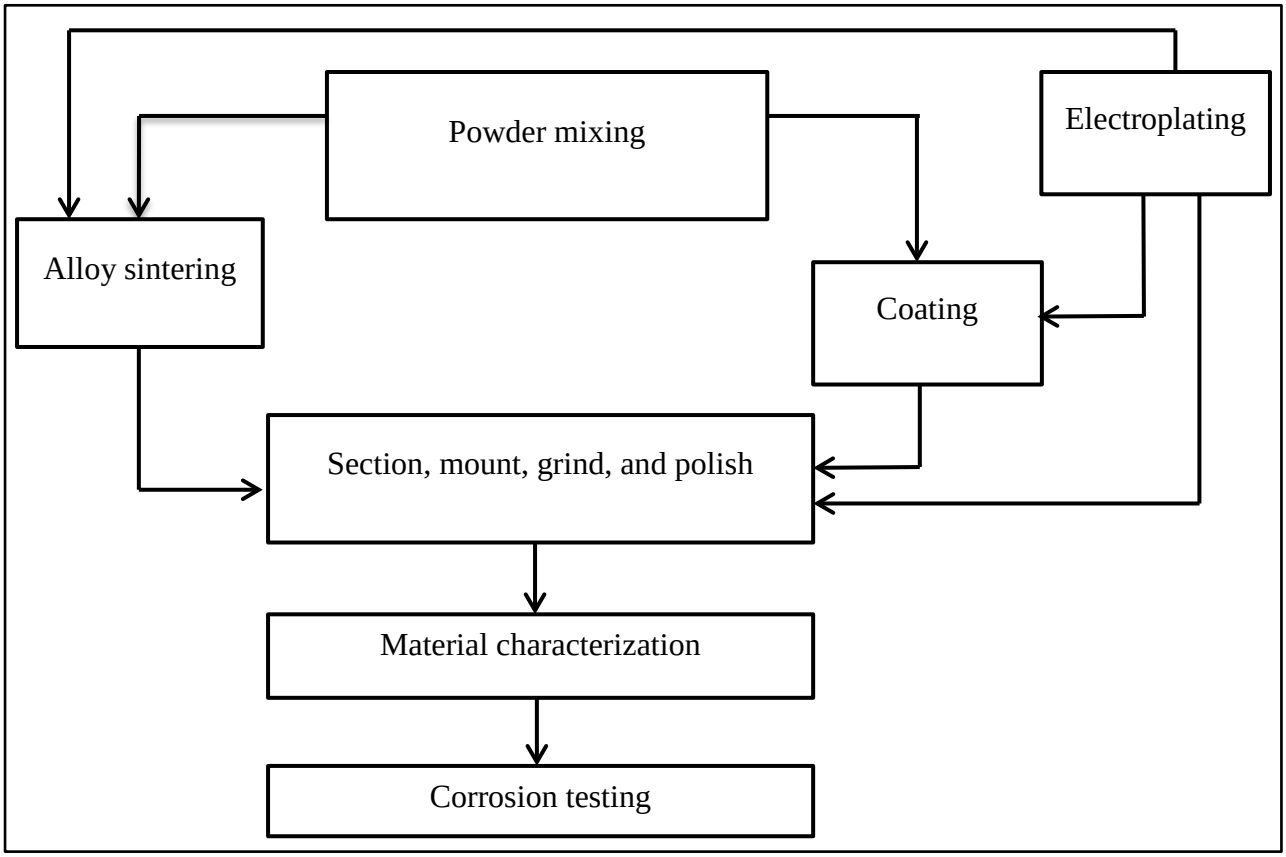


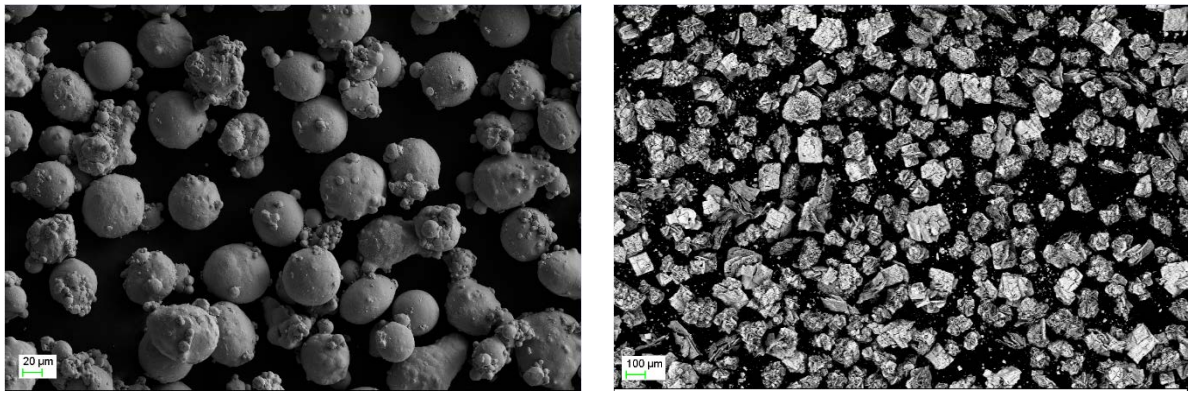
Figure 3.1: Experimental flow sheet.

3.2 Powder mixing

The copper and ruthenium powders were supplied by Wear Minerals Company. The copper and the ruthenium powders had a purity of 99.9 %. These powders had a size range between 10 and 45 µm. A copper substrate was used with a purity of 99.9% and dimensions of 0.5x120x60 mm. The powders were mixed using a turbula shaker mixer. The mixing was to ensure a homogeneous distribution of the powders. The proportions of the ruthenium powder added are tabulated in Table 3.1.

Table 3.1: The composition of powders (copper and ruthenium) added to make different alloys (mixing composition).

Alloy	Wt.% Copper	Wt.% Ruthenium
1	100	0
2	99.5	0.5
3	99	1
4	98	2



(a) (b)

Figure 3.2: The SEM images of (a) copper and (b) ruthenium powder.

The mixed powders, presented in Figure 3.2 (a) and (b), were used to make copper coatings and alloys using HVOF, cold spray coating (CSC), and SPS. Some of the copper powders were electroplated using ruthenium salt [the process is detailed in Section 3.6] and also used to create the coatings and the alloy.

3.3 High velocity oxygen fuel (HVOF) Coating

A sheet of copper with a purity of 99.99 % was used as a substrate. The HVOF method was used to apply the copper and ruthenium powder mixture on top of the copper substrate. The substrate was sand blasted first for better adhesion of the coatings. The spray powders used in the experiments were from the powder mixing stage and the electroplating stage mentioned previously. A schematic diagram of the HVOF process is shown below in Figure 3.3. The HVOF coating was done at Thermaspray (Pty) SA. The optimum spraying parameters that were selected are:

HVOF gun position - horizontally
Supersonic flame speed -2000 m/s
Powder feed rate - 35 g/min

Particle velocity - 1000 m/s

Stand-off distance - 20cm

Temperature - 2500ºC

The coating thickness was fixed at (>300 µm). Small specimens were cut from the coating for further experimental use.

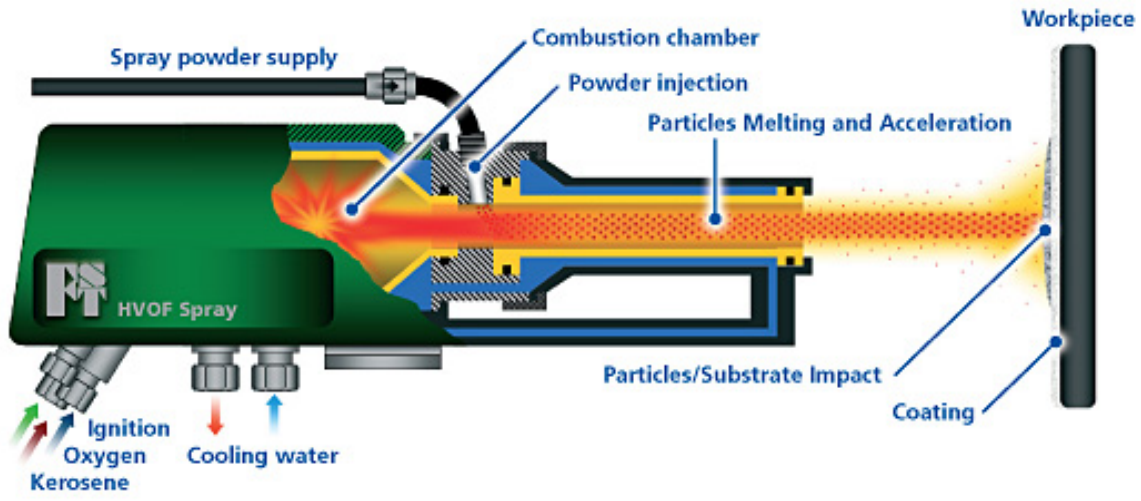


Figure 3.3: High velocity oxy fuel spray [flame spray technologies, FST, October 2012]

3.4 Cold Spray Coating

The substrate used was the same as that used for thermal spray process, a copper sheet with the purity of 99%. The substrate was sand blasted prior to coating. The cold spray equipment used is presented in Figure 3.4. The spray powders used for coating were from the powder mixing stage and the electroplating stage.

The parameters that we set for the experiment are as follows:

Operating gas - Air

Operating pressure - 130 psi

Operating temperature - 400 ºC

Standoff distance - 20 mm

Transverse speed - 10 mm/s

Powder feed rate - 15 %

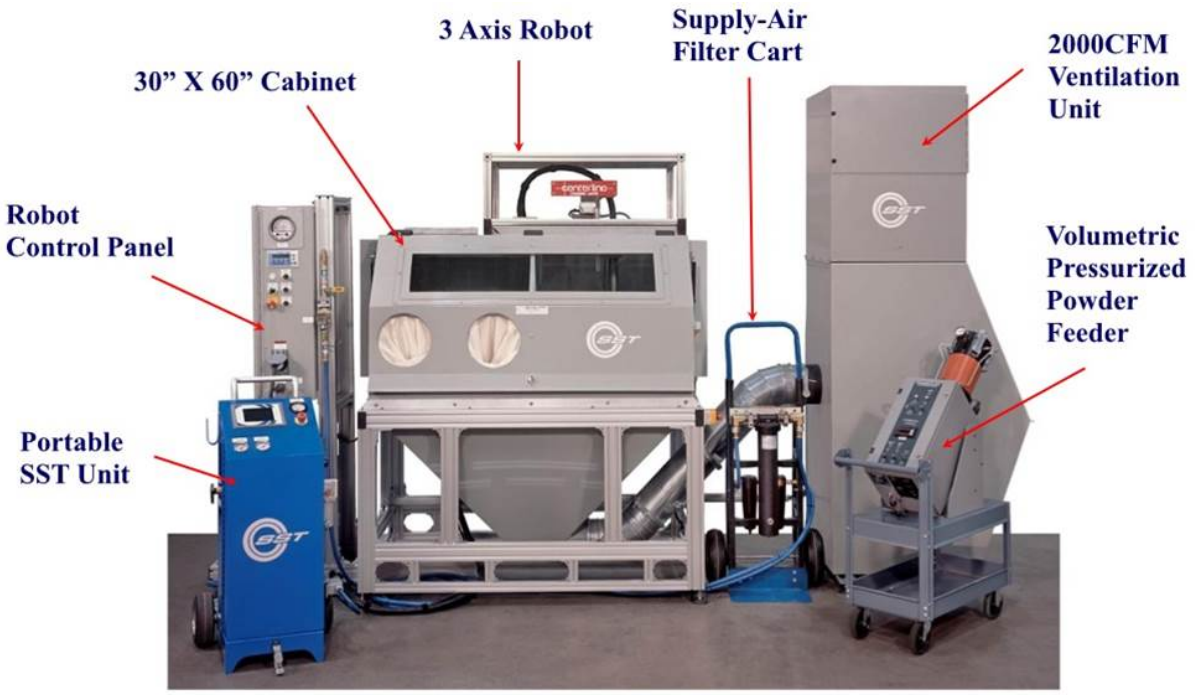


Figure 3.4: Cold spray equipment [https://www.wits.ac.za/mecheng/research/research-units/cold-spray-research/facilities/ Access date: 5 June 2017].

The cold spray coating thickness was expected to be very thin (>13 µm). The coating applied had three layers to allow for the desired thickness without having to increase the powder feed rate. The zig-zag deposition pattern (Figure 3.5) was used to apply the coating on the substrate.

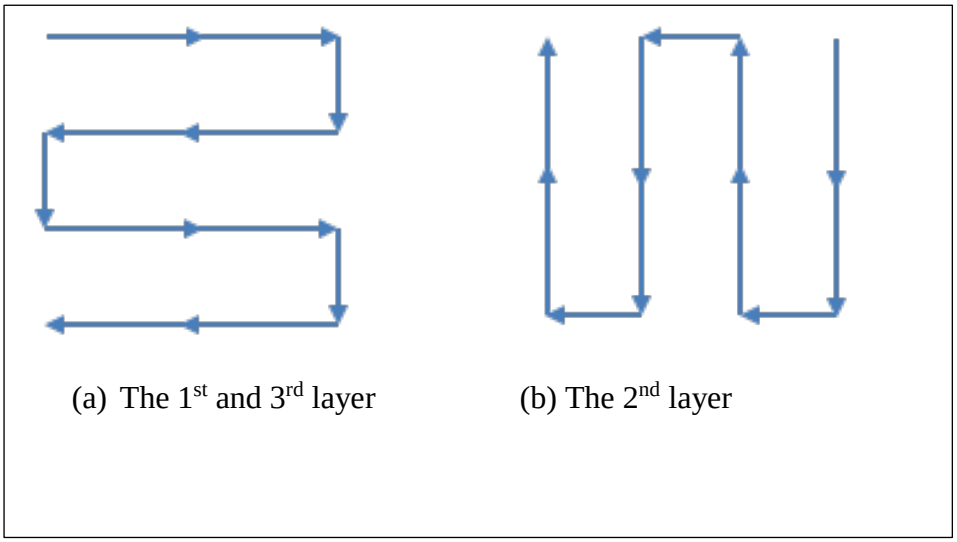


Figure 3.5: The coating deposition pattern.

3.5 Alloy sintering

Copper metal powder with a purity of 99.9% and a particle size ranging from 10-45 µm was used. The spark plasma sintering process was used to produce the alloys using a FCT HP-D5

furnace. The pulse time was 10 minutes with a pause of 5 minutes, and the vacuum pressure use was 2 hPa. The furnace settings were as follows:

Sintering temperature: 850℃
Pressure: 50 MPa
Hold time: 10 minutes
Heating rate: 200℃/minute
Cooling rate: 200℃/minute
Disks of 20 mm diameter and 4 mm height were produced using graphite die and punches.

3.6 Electroplating

3.6.1 Electrolyte preparation

The electrolyte contained containing 6.2 g/l of ruthenium nitrosyl salt and 80 g/l of oxalic acid. The ruthenium salt used was ammonium hexachlororuthenate (IV) ($(NH_4)_2RuCl_6$), with 24.07% ruthenium metal content. The ruthenium had the purity of 99.9 %. The oxalic acid was used to stabilize the ruthenium in the solution. The solution was stirred and heated for a period of 24 hours to ensure the dissolution of the salt and metal ions into the solution. The solution was then filtered to avoid solids in the bath, which alter and interfere with the plating process.

3.6.2 Electroplating process

Nova software (version 1.11) connected to the PGSTAT302 Autolab potentiostat was used to perform the electroplating experiment. Copper powder was used as the cathode. The powders, with the size range of 50 µm, were placed in a filter bag with dimensions of 50×50 mm and connected to a conducting wire. The graphical illustration of this setting is in Figure 3.6 (a) and the overall electroplating setting is in Figure 3.6 (b). Graphite was used as an anode electrode.

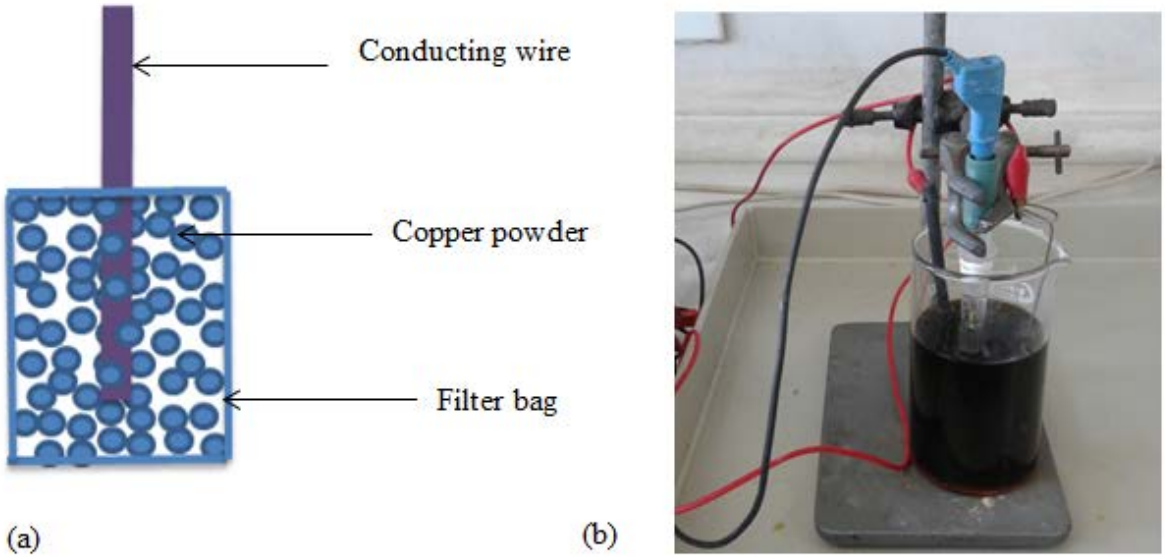


Figure 3.6: Electroplating process setting

The copper powder was electroplated using the pulse electrodeposition method. During the electroplating process the current was varied. The highest current range was 2 A and the lowest current range was 1.5 A. The total duration was 2704 seconds. The T_{ON} lasted for 10 s and T_{OFF} lasted for 3. After electroplating the powder was rinsed in distilled water and then dried in the oven.

3.7 Metallographic Sample Preparation

The ASM handbook volume 9 [Aliya, 2004] was used as a guide on performing the metallography and microstructure preparation and analysis. The samples produced from the coating and alloying processes were sectioned to get a representative sample for analysing the metallography, measuring the hardness, and performing the corrosion test. A cross section of the coatings was cut for metallography and hardness testing. Some representative samples were also sectioned for use in performing the corrosion test.

After sectioning samples for metallography and hardness testing, they were mounted using an ATA Opal 410 hot mounting press. These samples were then ground from 220, 350, 500, 800 and finally 1200 grit paper. The samples were rinsed with water to remove loose particles. They were polished using the 1 µm polishing cloth using ATA Saphir 520 automatic polisher for 5 minutes to obtain a mirror like finish. The polished samples were etched with Beraha's lead sulfide (PbS) reagent for copper and copper alloys for optical image analysis. After etching, the samples were rinsed distilled water and in ethanol and then dried using a blow drier. The

samples for SEM micrograph analysis were etched using electrolytic etching of copper and copper alloys. Table 3.2 shows the compositions, preparation, and use of the etchant.

Table 3.2: The compositions, preparation, and use of the etchant.

Composition	Preparation for the etchant	Etching the samples
1000 ml water, 240g sodium thiosulfate, 30g citric acid, 24g lead acetate	The individual chemicals were mixed in order given in the composition column. Each chemical was allowed to dissolve before adding next. The solution was left to age for 24 hours in a dark bottle before use.	The samples were immersed in the etchant until the surface is colored.
5 ml acetic acid (glacial), 10 ml HNO_3, 30 ml H_2O	The individual chemicals were mixed in order given in the composition column and used.	Voltage range: 0.5-1, current density: 0.2-0.5 A/cm², and the etching time: 5-15 s.

3.8 Metallography analysis

3.8.1 Light optical microscopy

The etched samples were analyzed for morphology and matrix features by obtaining optical photomicrographs from each sample. The analysis were done using Leica DM6000M microscope and Leica DFC490 camera coupled with Leica Application Suite version 4.8.0 (Build: 154) software(see appendix A).

3.8.2 SEM

The observations of morphologies, sizes, microstructural characteristics, and analysis of chemical compositions for different samples were done using a Carl Zeiss Sigma Field Emission Scanning Electron Microscope (FESEM) equipped with an Oxford X-act detector for Energy Dispersive X-ray Spectroscopy (EDS), the apparatus is shown in Figure 3.7.

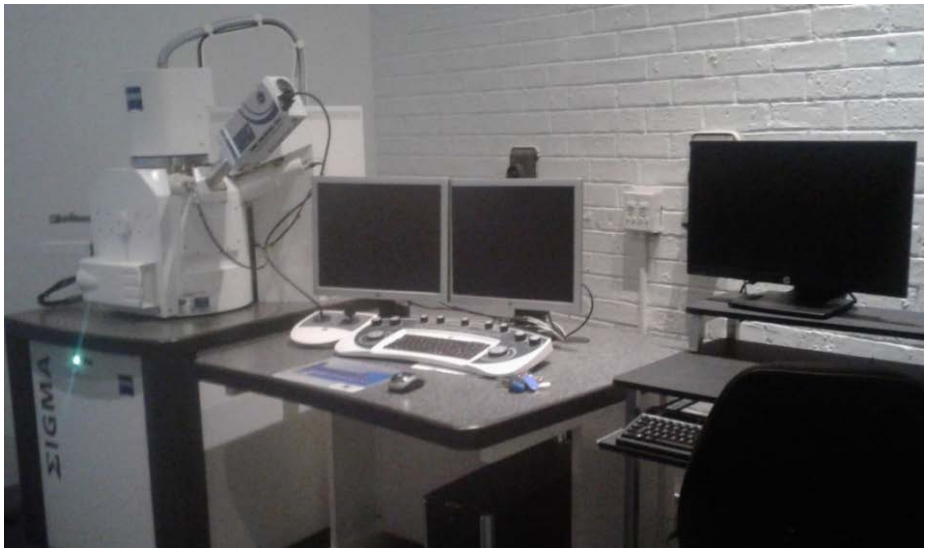


Figure 3.7: Carl Zeiss FESEM.

3.9 Hardness measurements

The polished samples were measured for hardness using the Vickersmicro-hardness tester FM-700 (presented in Figure 3.8). A load of 100 gf was applied on the samples and the indentation lasted for 10 s. The indentation resulted in a diamond shape that was measured to determine the hardness of the material. The test was performed multiple times to have a better representative.



Figure 3.8: Vickers micro-hardness tester.

3.10 Corrosion measurements

3.10.1 The electrochemical cell

The electrochemical cell consisted of a cylindrical glass electrochemical cell, with holes for the working electrode, reference electrode, counter electrode, and thermometer. It was suitable for the three-electrode system. The counter electrode used was graphite, the reference electrode used was silver/silver chloride in 3M KCL solution, and the working electrode was the prepared samples from the HVOF coating and sintering processes. The cylindrical glass electrochemical cell also contained the water jacket placed around the cell to allow for heating the system to a desired temperature. A water bath was used to heat the water. A rubber band was used to demarcate the area of the sample surface to expose the surface in the corrosive environment. The corrosion test solution used was 2M H_2SO_4 which was prepared using analytical grade chemical and distilled water. The electrochemical measurements were made at different temperature, ranging from (25-65°C ±1°C). The temperature was kept constant in the water bath and measured with the thermometer in the electrochemical cell. The Figure 3.9 below shows the electrochemical cell used.

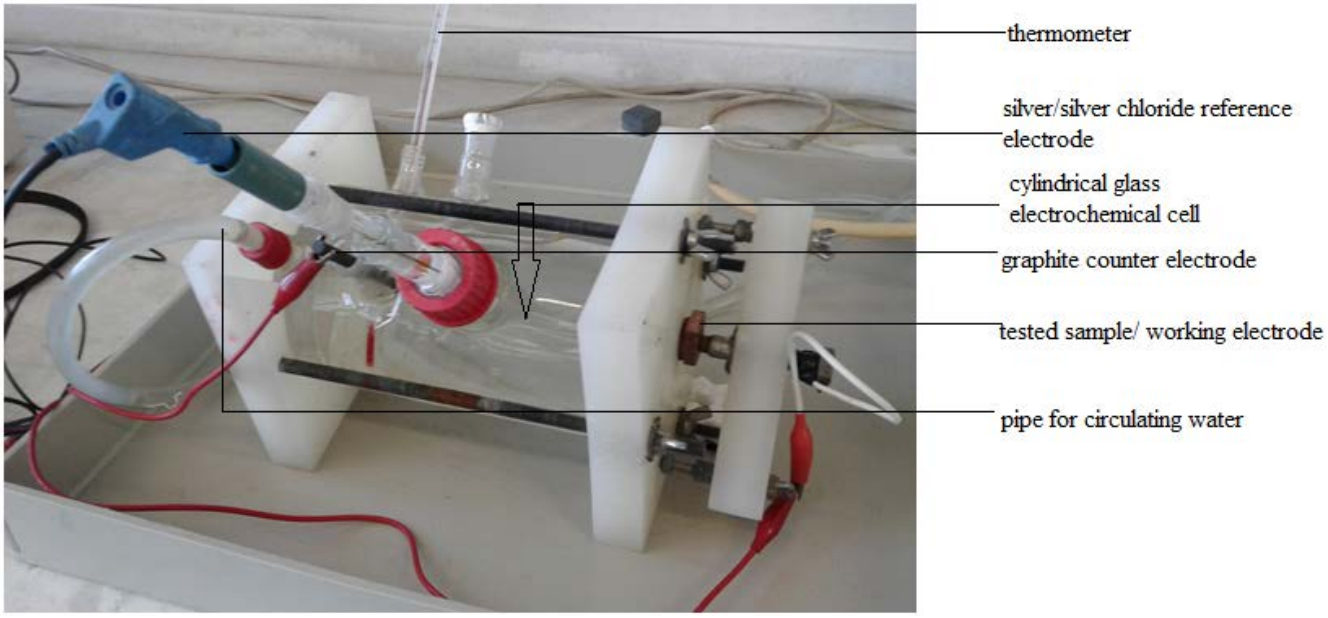


Figure 3.9: The electrochemical cell.

3.10.2 Electrochemical measurements

Electrochemical measurements were carried out using a computer controlled PGSTAT302 Autolab potentiostat using NOVA software Version 1.11. All tests were carried out in triplicate for a good reproducibility.

3.10.3 Potentiodynamic polarisation

Corrosion rates of the samples with varying ruthenium content were determined using the electrochemical corrosion testing method. The potentiodynamic polarisation characteristics were investigated in a 2M H_2SO_4 solutions at different temperatures. The solution was neither aerated nor deaerated, it was left as is. The potentiostatic pulse testing was used to study the corrosion rates of some of the spark plasma sintered alloy. The polarisation curves were obtained at a scan rate of 0.1m V/s, starting from – 1000 mV to 1200 mV. The corrosion rates were calculated using the corrosion potential, corrosion current and corrosion current density from the polarisation curves obtained from the electrochemical experiments. The electrolyte and samples were replaced after every test before performing the next test. The overall setting for the experiment and the equipment used are shown in Figure 3.10.

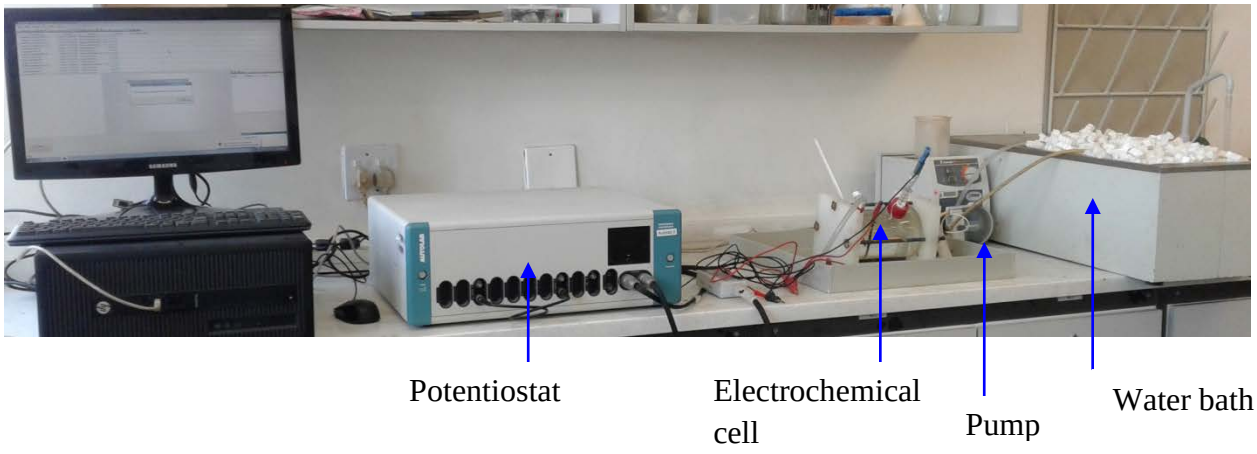


Figure 3.10: The overall setting for the experiment and the equipment used.

3.10.4 Corrosion rate calculations

Corrosion rate was determined using the Faraday's law stated in equation 13.

$$CR\ (mm/yr) = \frac{k \times i_{corr} \times E_w}{\rho} \quad \text{.....13}$$

Where:

CR = the corrosion rate in millimetre per year

K = 0.00327 (mm g/µA cm yr)

i_{corr} = corrosion current density (µA/cm^2)

E_w = equivalent weight (g)

ρ = density (g/cm^3)

The corrosion current density was calculated using the following equation 14.

$$i_{corr} = \frac{I_{corr}}{A} \quad \text{.....14}$$

Where:

I_{corr} = total current (µA)

A = exposed specimen area (cm^2)

The total current was calculated using equation 15.

$$I_{corr} = \frac{B}{R_p} \quad \text{..... 15}$$

Where:

B = Stern-Geary constant (V)

R_p = polarisation resistance (ohm)

$$B = \frac{b_a \times b_c}{2.303(b_a + b_c)} \quad \text{..... 16}$$

Where:

b_a = slope of the anodic Tafel region (V/decade)

b_c = slope of the cathodic Tafel region (V/decade)

The Tafel slopes, b_a and $b_{c,}$ were directly extracted from Autolab Nova software for each potentiodynamic curve by choosing two point on the linear Tafel region of each slop which were at least a decade in current apart.

Chapter 4 : Results

4.1 Introduction

Different copper samples were prepared using various processes. These processes included HVOF, CSC, SPS, electroplating, as well as combination of these processes to create either a coating or a copper alloy as explained in Chapter 3. All these samples were analysed, first, to determine their porosity, microstructure, elemental compositions, and their elemental distribution (mostly focusing on ruthenium and copper). Thereafter the samples were analysed for hardness when load was applied. Finally the electrochemical characteristics where exposed to a corrosive medium to analyse the corrosion resistance. The results will discuss the effect that ruthenium will have on the different surfaces. For the microstructures the changes will be revealed by etching the sample, and the hardness will be measured by the diamond indentations. As for the electrochemical measurement, the shift in the corrosion current density and corrosion potentials will be of focus.

4.2 As-received copper

The following section will be looking at the properties of the as-received copper to set a basis for comparison with the other samples when changes in the surfaces are made. It will illustrate its microstructure, its behaviour in the corrosive environment and its hardness measurements.

4.2.1 Micrographs

The microstructure of the as-received copper is shown in Figure 4.1.

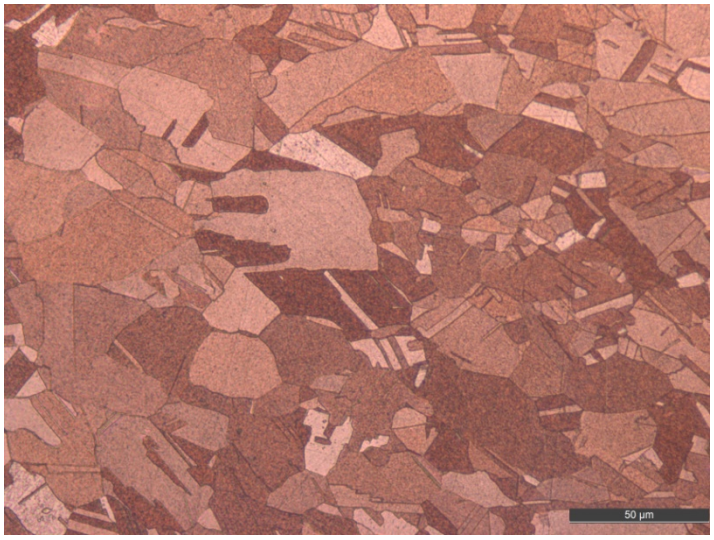


Figure 4.1: The optical micrograph of as-received copper (oxygen free), etched with Beraha's lead sulfide (PbS) reagent.

The image shows the copper grain structure and size appearing in different shades. The copper micrograph presented in Figure 4.1 was obtained after grinding and polishing using Saphir 520 automatic grinding machine. The grinding was done using AKA-Largan disk, and the polishing was done using 1 µm polishing disk. The polished sample was etched using Beraha's leas sulphide etchant to reveal grains. It shows well defined grain boundaries with equiaxed, recrystallized grains containing twinned areas.

4.2.2 Electrochemical results

The calculation of the corrosion rates was carried out by measuring the Tafel slope from the potentiodynamic curves. Figure 4.2 shows the potentiodynamic polarisation curves for as-received copper, exposed to 2M sulphuric acid solution at 25, 45, and 65°C. Each curve represents the average values at each point of the three repeated measurements in similar conditions. This was done for all the temperatures. The figure shows the shift of the corrosion potential and corrosion current density at the different temperatures that were being investigated.

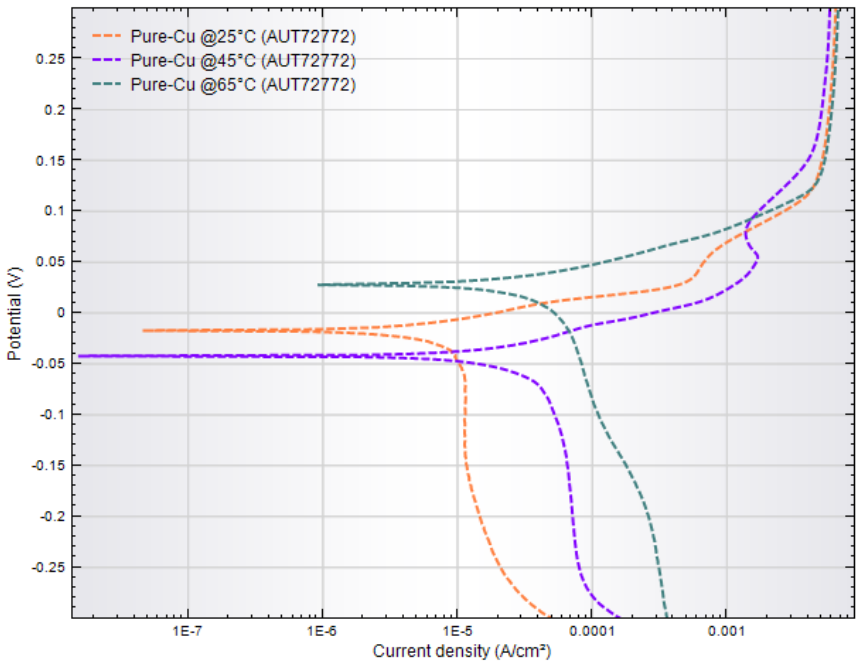


Figure 4.2: Potentiodynamic polarisation curves of as-received copper exposed to 2M sulphuric acid solution at 25, 45, and 65°C.

The measurements were made to establish a baseline for comparison to the coatings and the alloys that were formed to improve the corrosion resistance of the copper . The as-received copper at 25°C had the lowest corrosion current density, followed by copper and 45°C and

lastly that at 65°C. The values obtained from the graphs are presented in Table 4.1, which was used to calculate the corrosion rates.

Table 4.1: Calculated corrosion rate of as-received copper at 25, 45, and 65°C respectively.

	Icorr (A)	Icorr (µA)	Icorr (µA/cm^2)	CR (mmpy)
As-received Cu at 25°C	$6{,}74\times10^{-6}$	6,74	13,41	0,16
As-received Cu at 45°C	$9{,}63\times10^{-6}$	9,63	19,15	0,22
As-received Cu at 65°C	$3{,}34\times10^{-5}$	33,47	66,58	0,77

4.2.3 Average hardness

The hardness measurements of the as-received copper were done using Vickers hardness measurements. A load of 100gf was applied and the average hardness is plotted in Figure 4.3 with the deviation of these hardness values. The hardness values were similar, resulting in a small deviation. The average hardness of the as-received copper will be compared with the copper-ruthenium alloys.

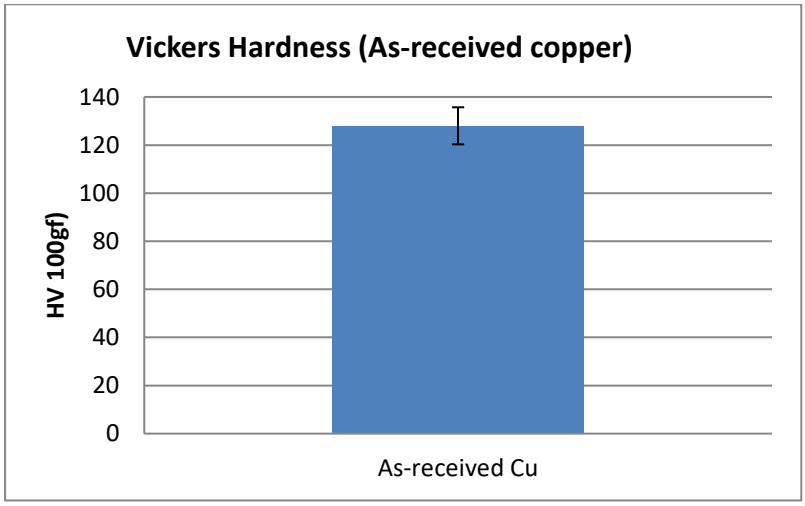


Figure 4.3: The average hardness of the as-received copper.

4.3 HVOF

The surface properties of the coatings will be investigated, as well as the area between the coating and the substrate, the ruthenium distribution, and impurities where applicable. The characterisation was done with an optical microscope, SEM, Vickers hardness, and a potentiostat.

4.3.1 Optical microscopy images

During the HVOF coating process, different ruthenium contents were introduced on the copper surface. The images in Figure 4.4 are presenting the optical micrograph (cross sections) of these different samples. All the images were captured under 50× magnification. The target concentrations for ruthenium in each sample were 0, 0.5, 1, and 2% respectively.

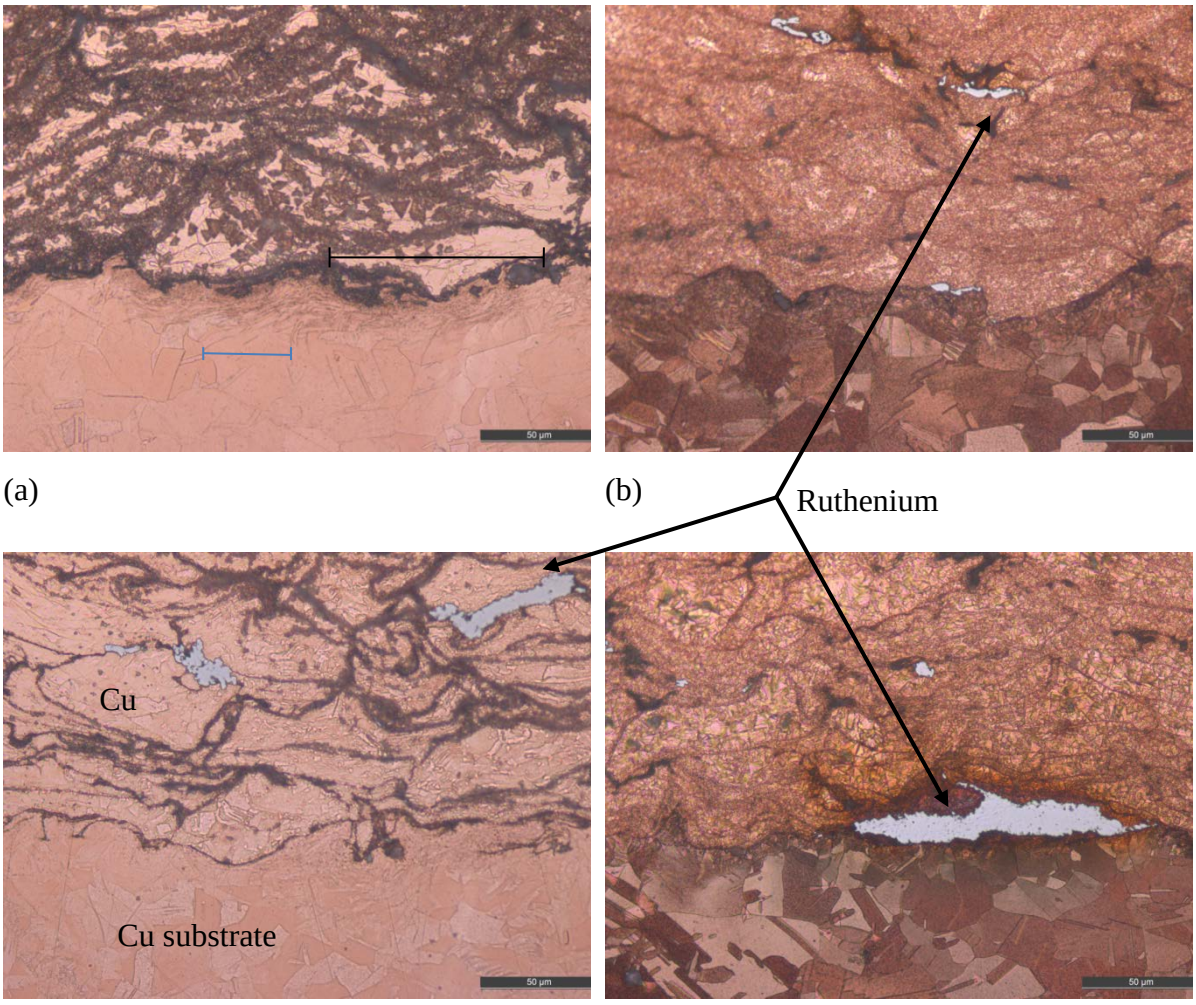


Figure 4.4: HVOF optical micrographs of (a) 0%Ru, (b) 0.5%Ru, (c) 1%Ru, and (d) 2%Ru.

The optical images show the distribution of ruthenium in small regions of the cross sections for the samples that contained ruthenium. The areas analysed in these images show that as the concentration of ruthenium was increased on the surface, more ruthenium islands were found in the cross sections. The HVOF-0%Ru coating had no ruthenium, and the image also show no other elements were visible on the cross section of the sample. Small islands of ruthenium are visible on the HVOF-0.5%Ru coating, and they grow larger as you move to HVOF-1%Ru and HVOF-2%Ru coated sample.

The splat sizes were considerably larger than the grain size of the substrate material as highlighted in Figure 4.4 (a) for the 0% Ru sample. This was also true for the rest of the HVOF coated samples. The presence of ruthenium in the coating did not result in any visible change in the splat size and shape. All the coatings showed dark spots, most of which surrounds these splats. This is assumed to be the pores created when the HVOF coatings were applied, or the effect of the etching process where some particles were corroded.

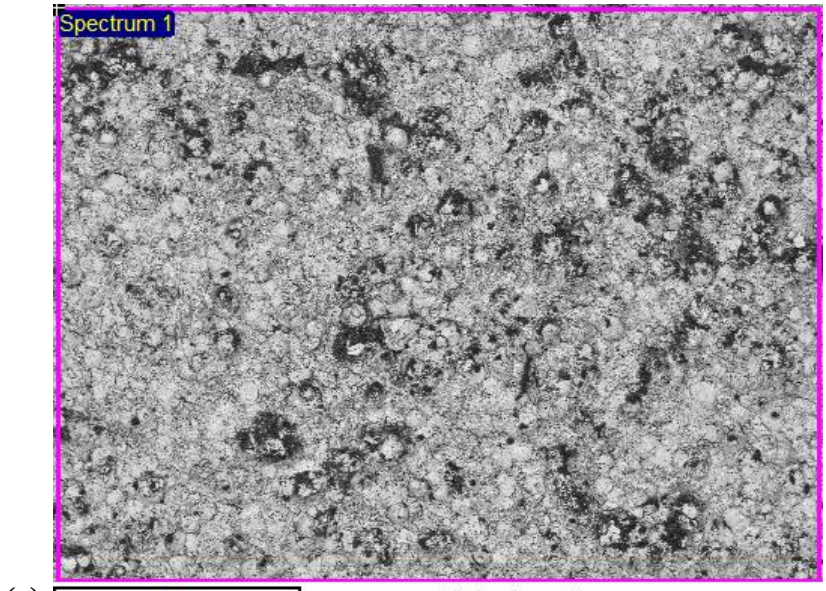
4.3.2 SEM EDS results

The SEM was used to analyse the surfaces and cross-sections of all the samples. The surface analysis investigated the elements on the surface, their distribution, and estimations of elemental compositions in different regions of the sample. The cross-section looked at the coating thickness, the porosity of the coating, and the adhesion of the coating to the substrate. The cross-sectioned samples were first etched prior to the analysis. The backscatter electron detector was used together with the EDS detector.

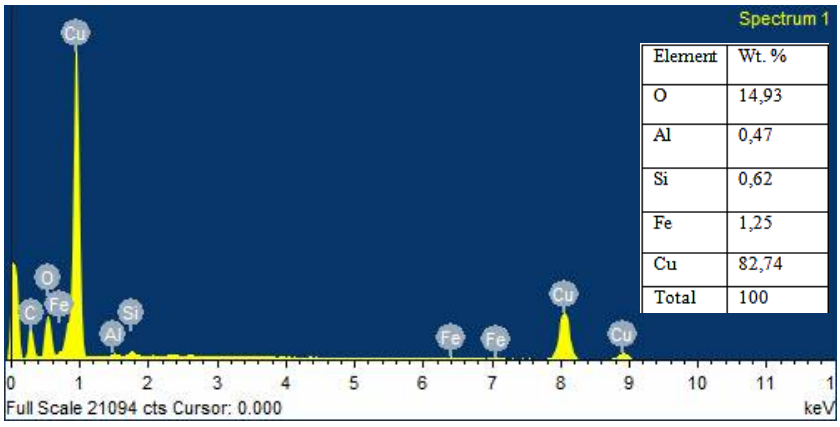
4.3.2.1 HVOF-0%Ru

4.3.2.1.1 Surface

Figure 4.5 (a) and (b) show SEM micrographs of the surface of the coating taken with the BSE detector and the EDS spectrum chemical analysis for the selected area. The estimated average weight percentages of detected elements are also shown. This served as a representative composition of the coating.



(a)



(b)

Figure 4.5: (a) Back-scatter electron image of area analysed (b) EDS spectrum with elemental weight percentages of the HVOF-0%Ru coated sample.

The EDS spectrum in Figure 4.5 (b), shows three different peaks of copper and other elements that were also detected on the surface. The surface of the HVOF-0%Ru coating showed some contaminants. These were Al, Si, and Fe. The presence of oxygen suggested that there was oxidation process taking place.

4.3.2.1.1 Cross section

The micrograph of the cross section of the HVOF-0%Ru coating shows the distinct regions of the coating and the substrate. The thickness of the coating was measured. The integrity of the coating was investigated by inspecting the adhesion of the coating to the substrate, and determining the extent of the inclusions, most of which were alumina from the sand blasting stage as shown in Figure 4.6 (a). The inclusions can contribute positively or negatively to the strength of the coating. The average thickness of the HVOF-0%Ru sample was found to be

379 µm. Figure 4.6 (b) is the representation of the etched cross section of the HVOF-0%Ru coating at higher magnification.

(a)

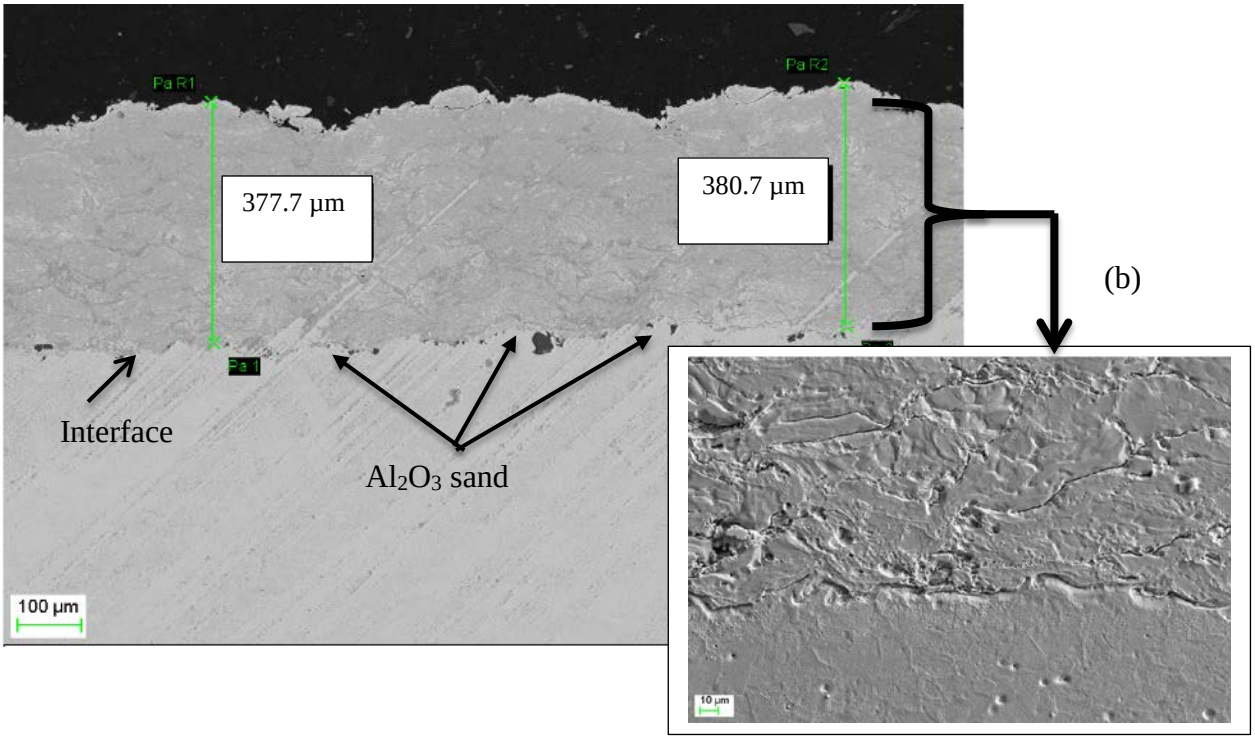


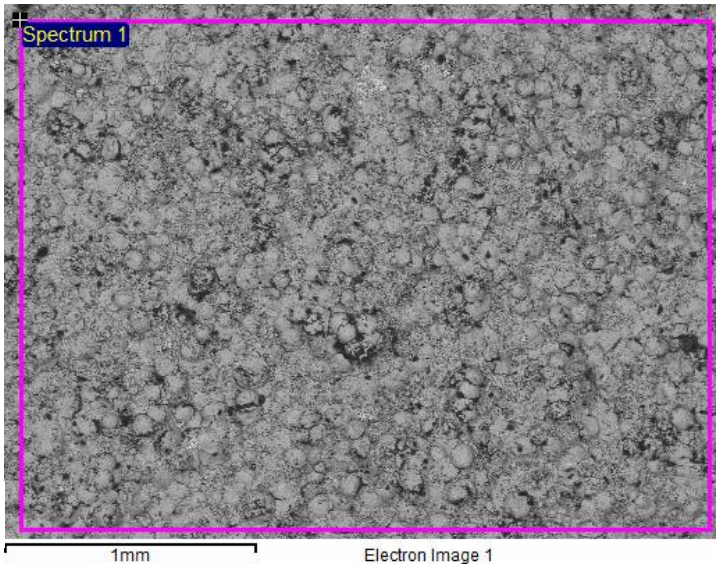
Figure 4.6: SEM micrograph of the cross-section of HVOF-0%Ru coating, (a) measurements of the coating thickness, and (b) the etched coating interface at higher magnification.

4.3.2.2 HVOF-0.5%Ru

4.3.2.2.1 Surface

The SEM micrograph shown in Figure 4.7 (a) shows the surface of the coating, and (b) the EDS spectrum obtained from the selected area with the quantified analysis in weight percent. This analysis showed 0.42wt% Ru on the surface of the coating, which was close to the expected 0.5 wt% Ru. However, there were contaminants, Al_2O_3 and Si, similar to those detected in HVOF-0%Ru sample.

(a)



(b)

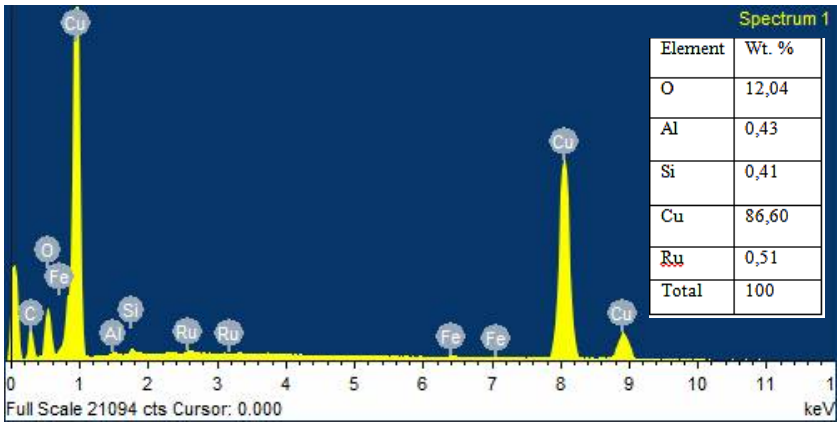


Figure 4.7: SEM micrograph taken with a back-scattered electron detector (a) of the top surface of the coating, and (b) the EDS spectrum of the coating with elemental weight percentages.

4.3.2.2.2 Cross section

The micrograph of the cross section of the HVOF-0.5%Ru coating showed an estimated coating thickness, of approximately 370 µm. The coating-substrate interface also shows bits of aluminium sand that remained on the substrate surface after it was used for grit blasting the copper surface prior to coating.

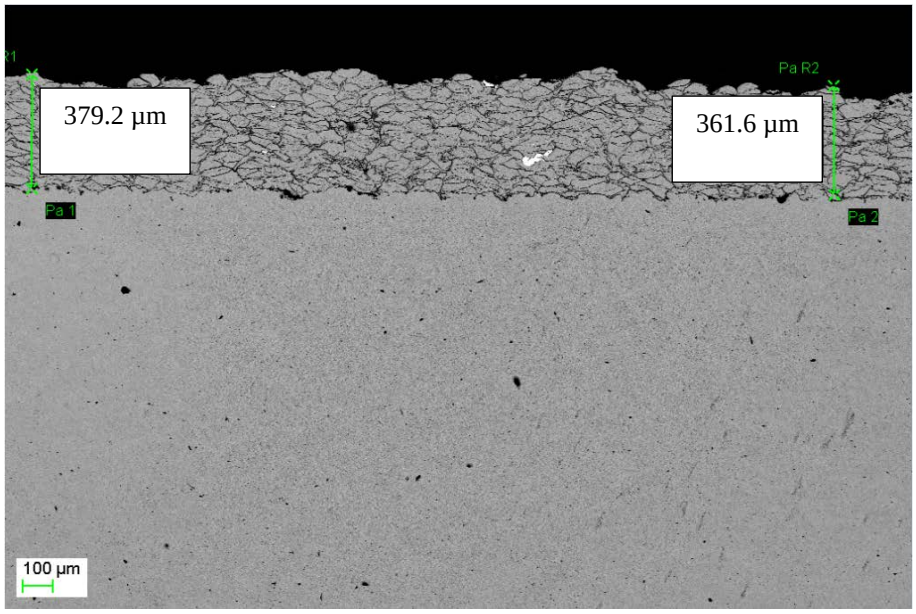


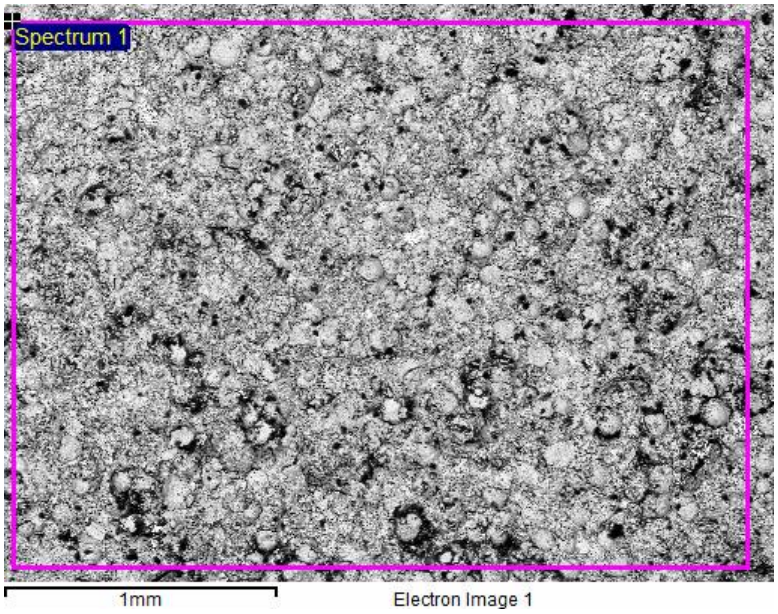
Figure 4.8: SEM micrograph of the cross section of HVOF-0.5%Ru coating and estimated measurements of the coating thickness.

4.3.2.3 HVOF-1%Ru

4.3.2.3.1 Surface

An EDS analysis was performed on the area shown in figure 4.9 (a). The results of this analysis are shown in figure 4.9 (b), containing average compositions of elements detected on the surface, and also producing the spectrum for those elements. This surface also contained contaminants similar to those of the first two coated samples (Fe, Si, and Al), but it also had sulphur as one of the contaminants.

(a)



(b)

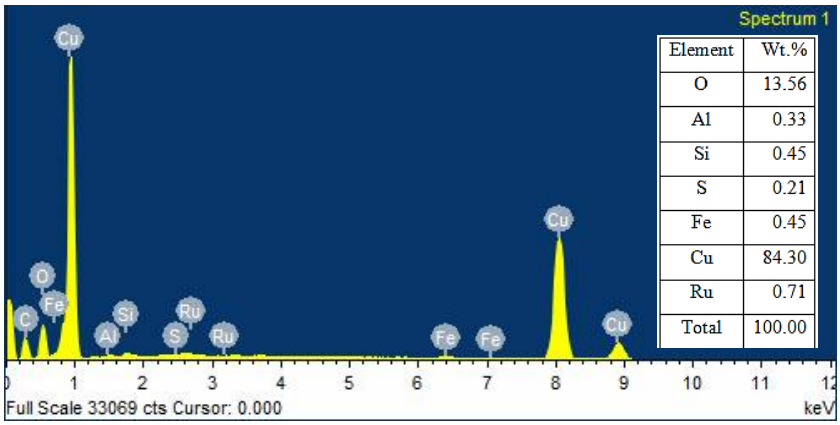


Figure 4.9: (a) The SEM image of the top surface of the HVOF-1%Ru coating, and (b) results of the EDS analysis with average compositions of the elements.

4.3.2.3.2 Cross section

The SEM image of the cross section of the HVOF-1%Ru coating is shown Figure 4.10 (a). A higher magnification view of this coating is shown in Figure 4.10 (b). From this image two different shades can be spotted. The grey shade is copper, and the white shades are the ruthenium. The EDS analysis was made in one of the white shade to prove it is ruthenium, and the results are presented in the spectrum in Figure 4.10 (c). The coating thickness was measured and approximated to be 470 µm.

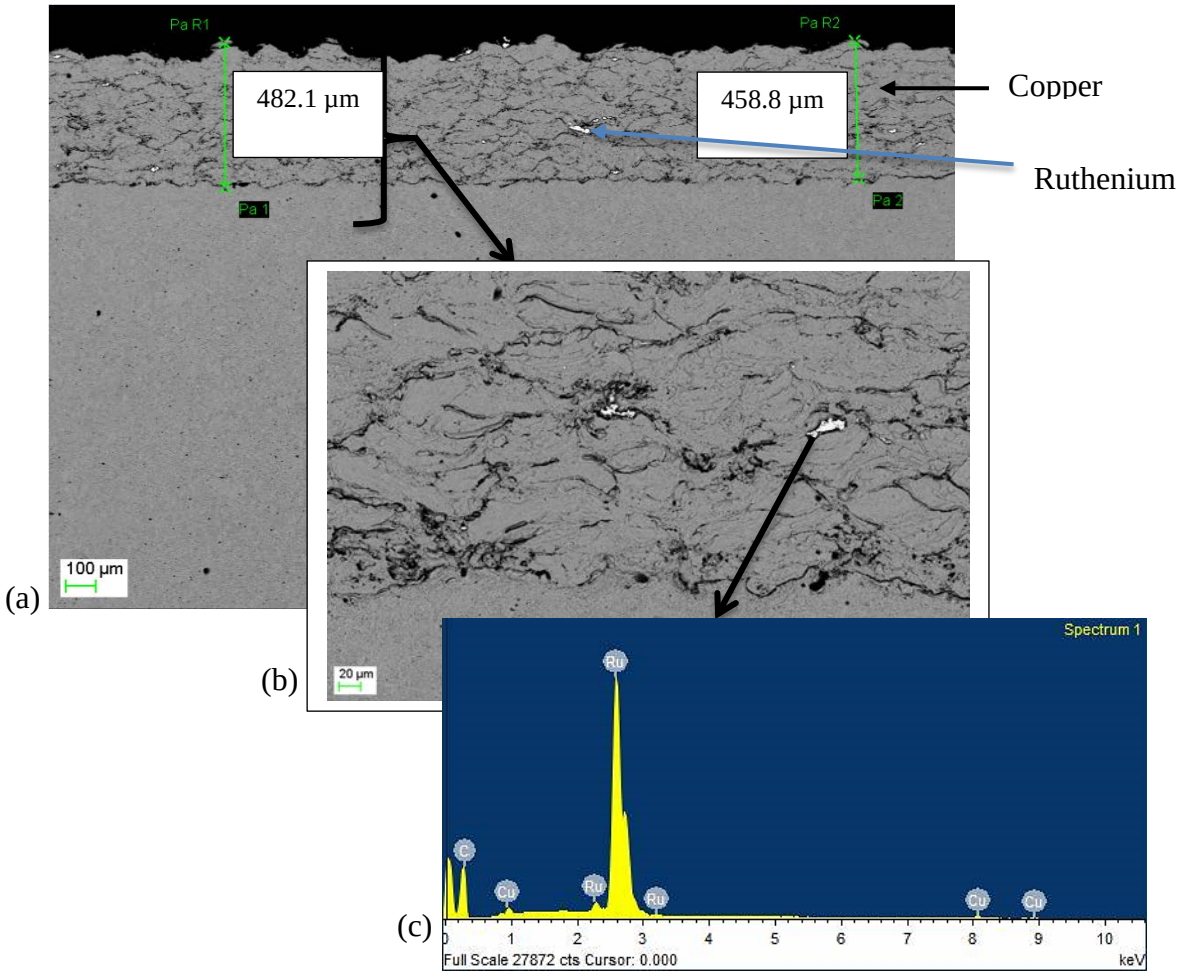


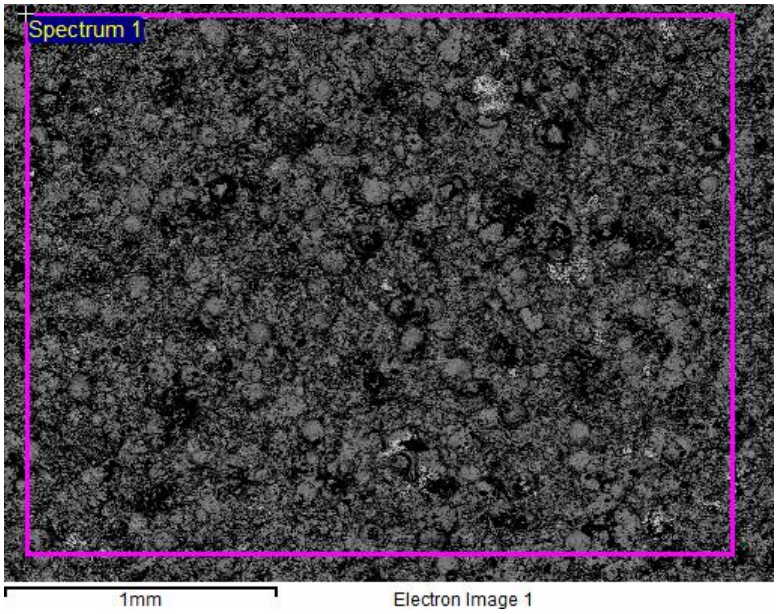
Figure 4.10: SEM images of the cross section of the HVOF-1%Ru sample (a) estimated coatingthickness, (b) the coating at a higher magnification, and (c) the EDS of the ruthenium island in the coating.

4.3.2.4 HVOF-2%Ru

4.3.2.4.1 Surface

The top surface of the HVOF-2%Ru in Figure 4.11(a) was analysed using the SEM and a backscatter electron detector. The results of the analyses are shown in Figure 4.11(b), which is presented with an EDS spectrum. The spectrum also outlines the averaged elemental weight percentages. The area selected is assumed to be the representative sample of the entire HVOF-2%Ru coating.

(a)



(b)

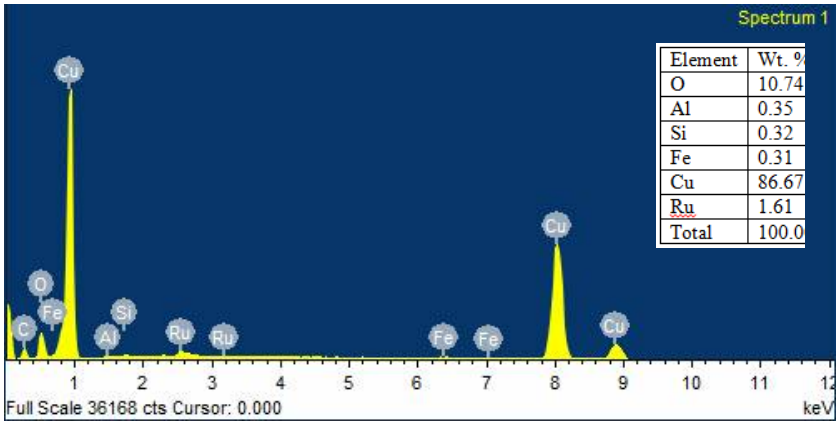


Figure 4.11: SEM micrograph of (a) the top surface of the HVOF-2%Ru coating, and (b) the results of the EDS analysis performed on the coating surface in (a) and the averaged elemental compositions detected.

4.3.2.4.2 Cross section

The SEM micrograph of the cross-section of the HVOF-2%Ru coating is shown in Figure 4.12. As in the previous coatings, it also measures the approximate thickness of the coating, which was found to have an average of 380 µm.

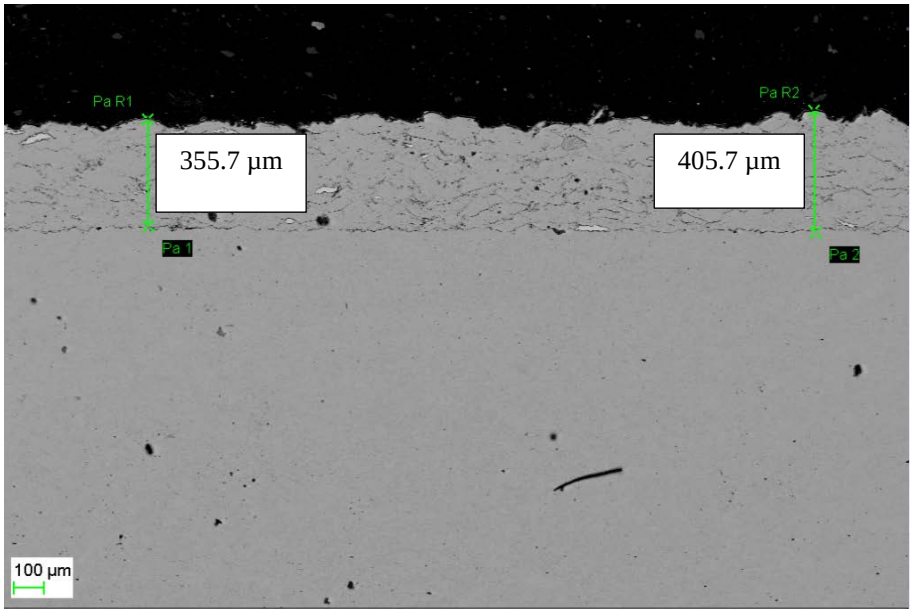


Figure 4.12: SEM micrograph of the cross-section of the HVOF-2%Ru coating, showing measurements of the coating thickness.

4.3.2.5 The comparison of all the HVOF coating element maps

The top surfaces of the coatings were evaluated with a Carl Zeiss Sigma Field Emission Scanning Electron Microscope (FESEM) equipped with an Oxford x-act detector for Energy Dispersive X-ray Spectroscopy (EDS). The equipment was used to determine copper and ruthenium elemental maps. These results are shown in Figure 4.13, where copper is represented by green and ruthenium by yellow. The ruthenium maps show an increase in ruthenium concentrations on the coating surface, which corresponds to the increasing overall ruthenium content.

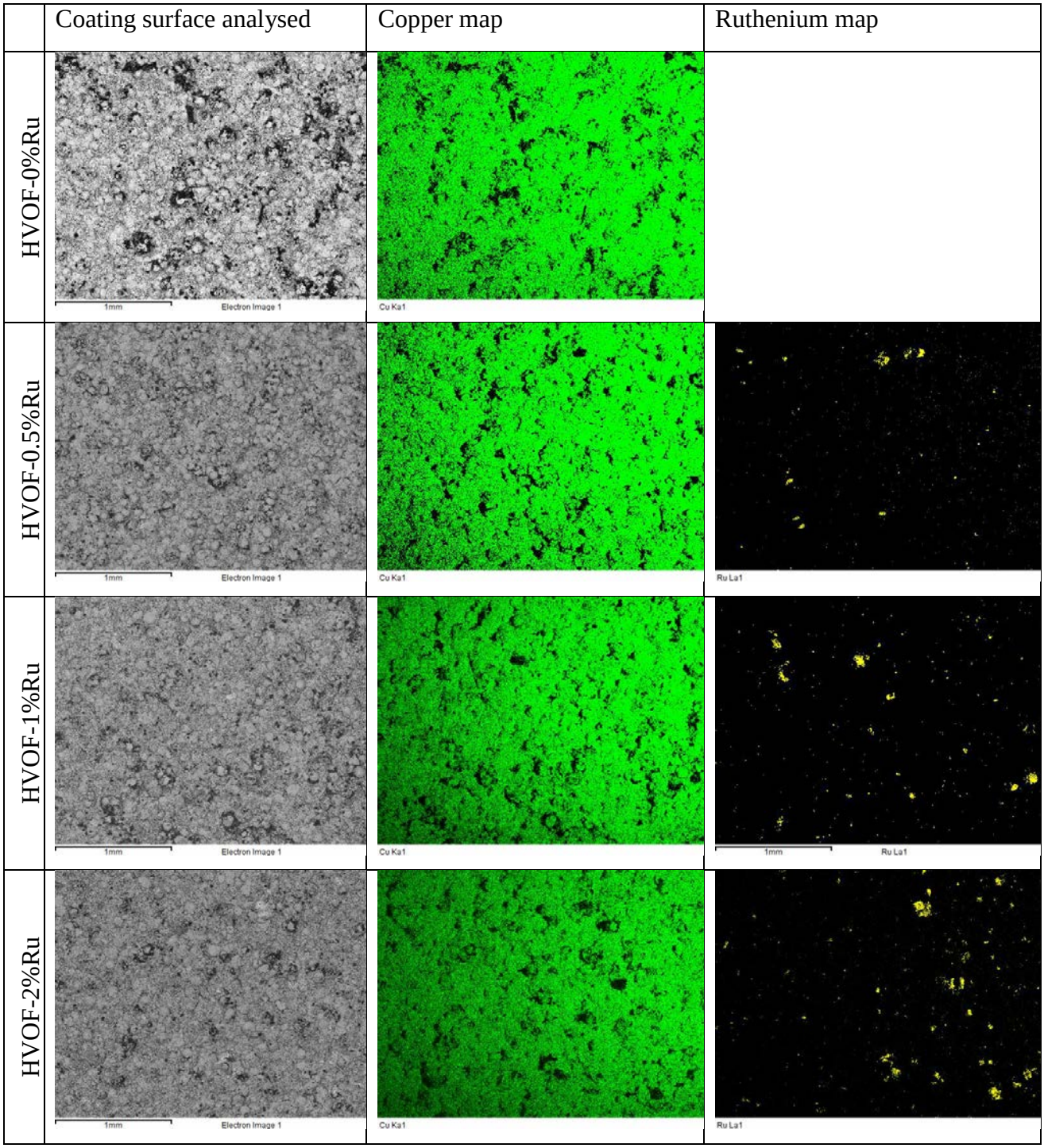


Figure 4.13: The SEM EDS elemental maps (copper (green) and ruthenium (yellow)) of the HVOF coating surfaces.

4.3.3 Hardness results

The Vickers micro hardness of all the coatings were measured and are presented in Figure 4.14. The graph shows an increase in hardness for the coated region and lower hardness values for the substrate. The as-received copper had almost similar hardness values to that of the substrates of the coatings.

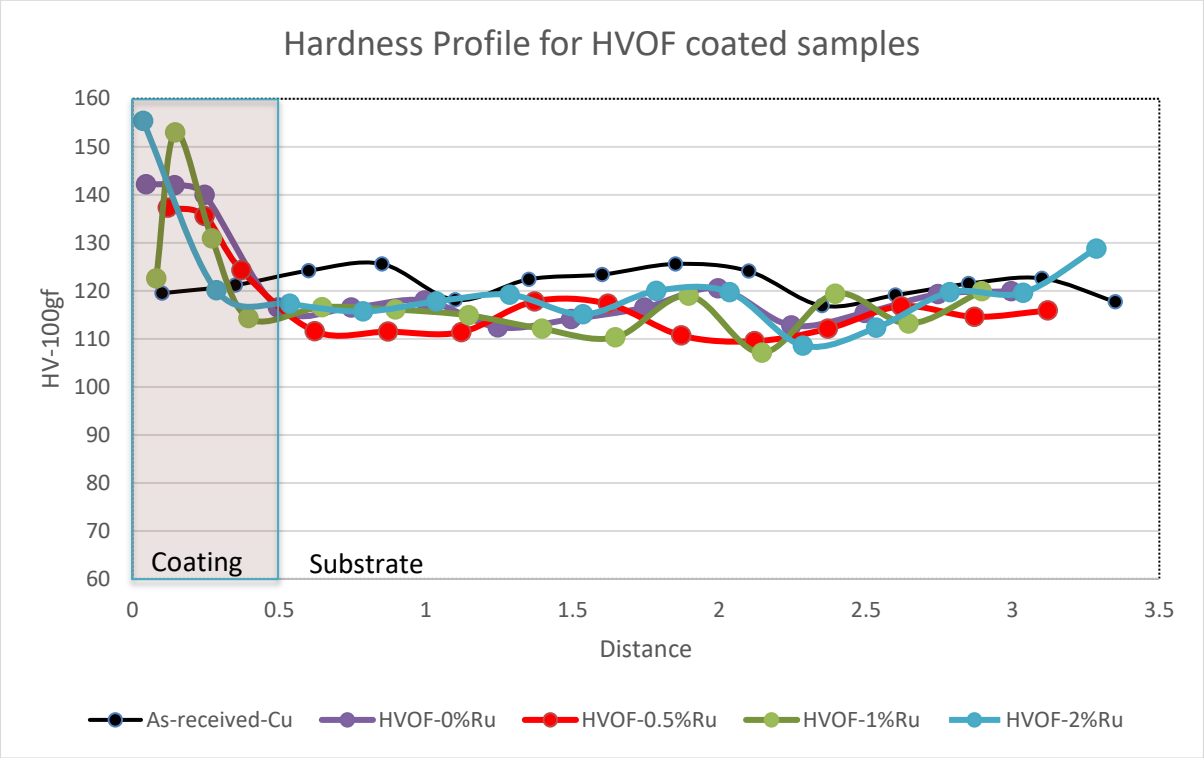


Figure 4.14: Hardness profile of all the HVOF coated samples compared to that of as-received copper.

4.3.4 Electrochemical results

The corrosion characteristics of the HVOF coatings and the as-received copper were determined by performed in 2M sulphuric acid at 45 and 65°C after 45 min exposure, and linear polarisation curves were produced. The corrosion potential and corrosion current densities were determined and was used in the comparison of the different responses of the coatings, as shown in Figure 4.15 for the 45°C environment.

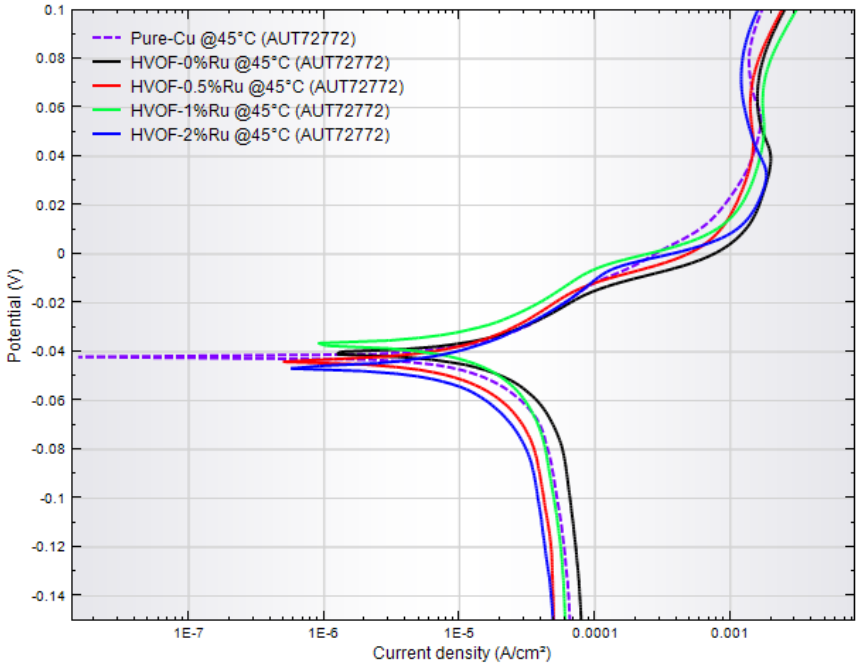


Figure 4.15: Linear polarisation potentiodynamic curves of HVOF coated copper and the as-received copper exposed to 2M H_2SO_4 at 45˚C.

The corrosion characteristics of the HVOF coatings were also determined in 2M sulphuric acid at 65°C. Figure 4.16 shows the comparison of linear polarisation curves of the HVOF coatings to the as-received copper. The as-received copper is presented by the dotted curve and the coatings by the solid curves.

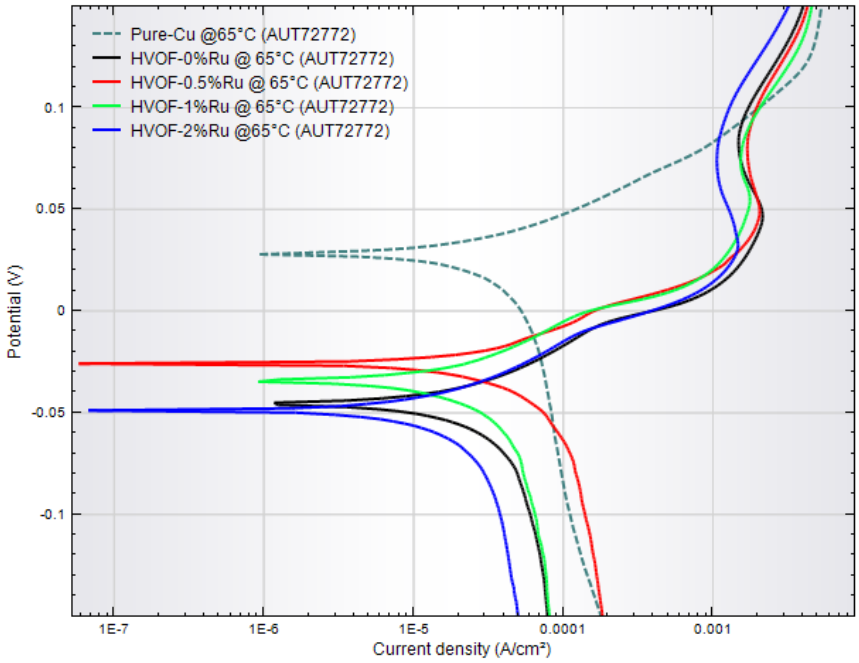


Figure 4.16: Linear polarisation potentiodynamic curves of HVOF coated copper and the as-received copper exposed to 2M H_2SO_4 at 65˚C.

4.3.4.1 The corrosion results

The section will show the corrosion rates of different coatings and compare the results to the as-received copper. The corrosion rates were calculated using the polarisation resistance technique, by determining the polarisation resistance at the corrosion potential and converting that to the corrosion current density, and then corrosion rate. The corrosion rates are shown in Table 4.2 and 4.3, and these results were also presented in Figure 4.17.

Table 4.2: Corrosion rate calculations for the HVOF coated samples measured at 45°C in 2M H_2SO_4.

	Icorr(A)	Icorr (µA)	icorr (µA/cm^2)	CR (mmpy)
As-received Cu	$9{,}63\times10^{-6}$	9,63	19,15	0,22
HVOF-0%Ru	$1{,}1\times10^{-5}$	11,02	21,92	0,25
HVOF-0.5%Ru	$9{,}57\times10^{-6}$	9,57	19,04	0,22
HVOF-1%Ru	$1{,}1\times10^{-6}$	11,02	21,92	0,25
HVOF-2%Ru	$4{,}77\times10^{-6}$	4,77	9,49	0,11

Table 4.3: Corrosion rate calculations for the HVOF coated samples measured at 65°C in 2M H_2SO_4.

	Icorr (A)	Icorr (µA)	icorr (µA/cm^2)	CR (mmpy)
As-received Cu	$3{,}34\times10^{-5}$	33,47	66,58	0,77
HVOF-0%Ru	$1{,}22\times10^{-5}$	12,27	24,40	0,28
HVOF-0.5%Ru	$2{,}12\times10^{-5}$	21,20	42,17	0,49
HVOF-1%Ru	$1{,}25\times10^{-5}$	12,57	25,94	0,29
HVOF-2%Ru	$5{,}24\times10^{-5}$	5,24	10,43	0,12

The coated samples showed a constant corrosion rate, but a significant increase at 0.5wt% Ru. At 65°C the corrosion rates were slightly higher, but not for the 2wt% Ru coating, where the corrosion rate almost remained constant.

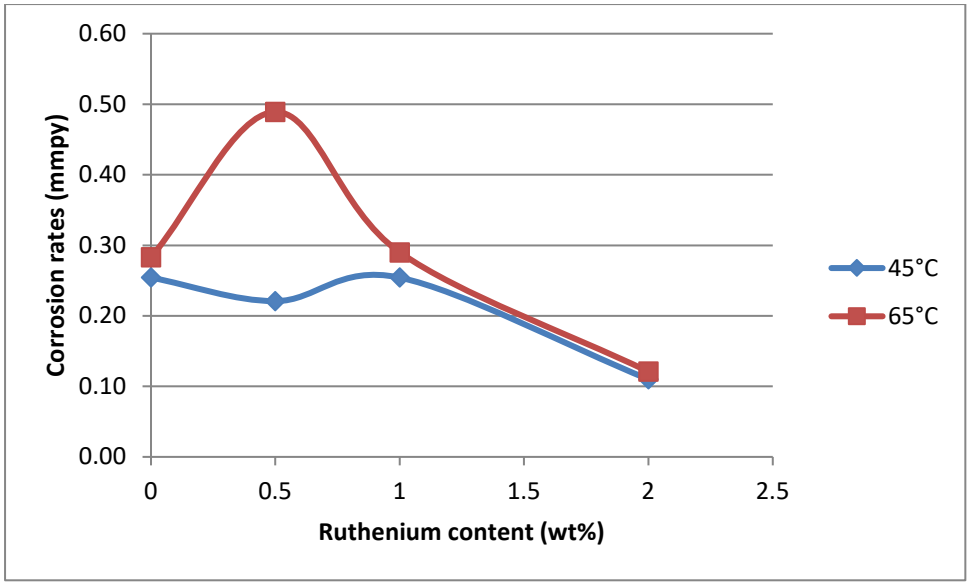


Figure 4.17: Corrosion rate as a function of ruthenium concentration in the HVOF coatings exposed to 2M H_2SO_4.

4.4 CSC

The section will look at all the cold sprayed copper coatings, comparing their characteristics and surface properties to that of as-received copper. The main focus will be on the ruthenium distributions, the adhesion of the coating to the substrate, and the effect of the increase in the ruthenium content, and their response when exposed to corrosive environment. Hardness measurements of the coatings will also be shown. The optical microscope, SEM, Vickers hardness, and potentiostat were used in gathering data.

4.4.1 Optical micrographs

The cross-sections of the CSC were mounted, ground, polished, and etched for optical analysis. Figure 4.18 shows the optical micrograph cross-sections taken for the CSC coatings, with different ruthenium contents as labelled. The target concentrations for ruthenium in each sample were 0, 0.5, 1, and 2% respectively. The images show formation of corrosion products on the surface that formed after etching and discontinuity of the coating.

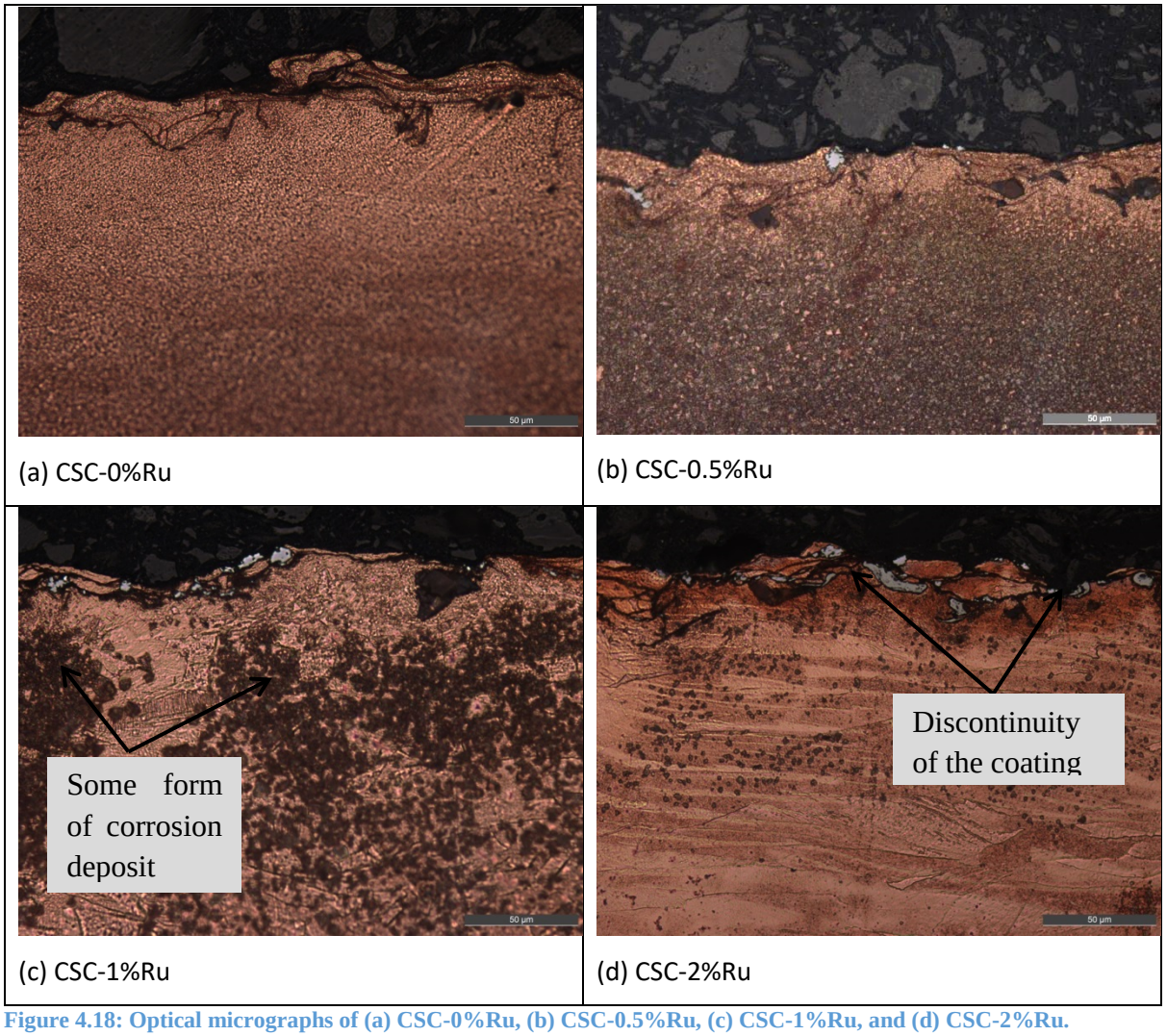


Figure 4.18: Optical micrographs of (a) CSC-0%Ru, (b) CSC-0.5%Ru, (c) CSC-1%Ru, and (d) CSC-2%Ru.

4.4.2 SEM EDS results

A more detailed study of the CSC coatings was made using the FESEM with EDS analysis. The study was used to observe the chemical compositions, porosities, and the thickness of the coating. The ruthenium distribution in the coatings, and the adhesion of the coating to the substrate was investigated. The cross-sectioned samples were first etched prior to the analysis.

4.4.2.1 CSC-0%Ru

4.4.2.1.1 Surface

The coating surfaces was analysed to determine the distribution of the ruthenium, and if the extent of contaminants on the surface of the coating. The top surface of the CSC-0%Ru coating was analysed from the area shown in Figure 4.19(a) by using the SEM and a backscatter electron detector. The results of the analyses are presented in an EDS spectrum shown in Figure 4.19(b), which also outlines the averaged elemental weight percentages.

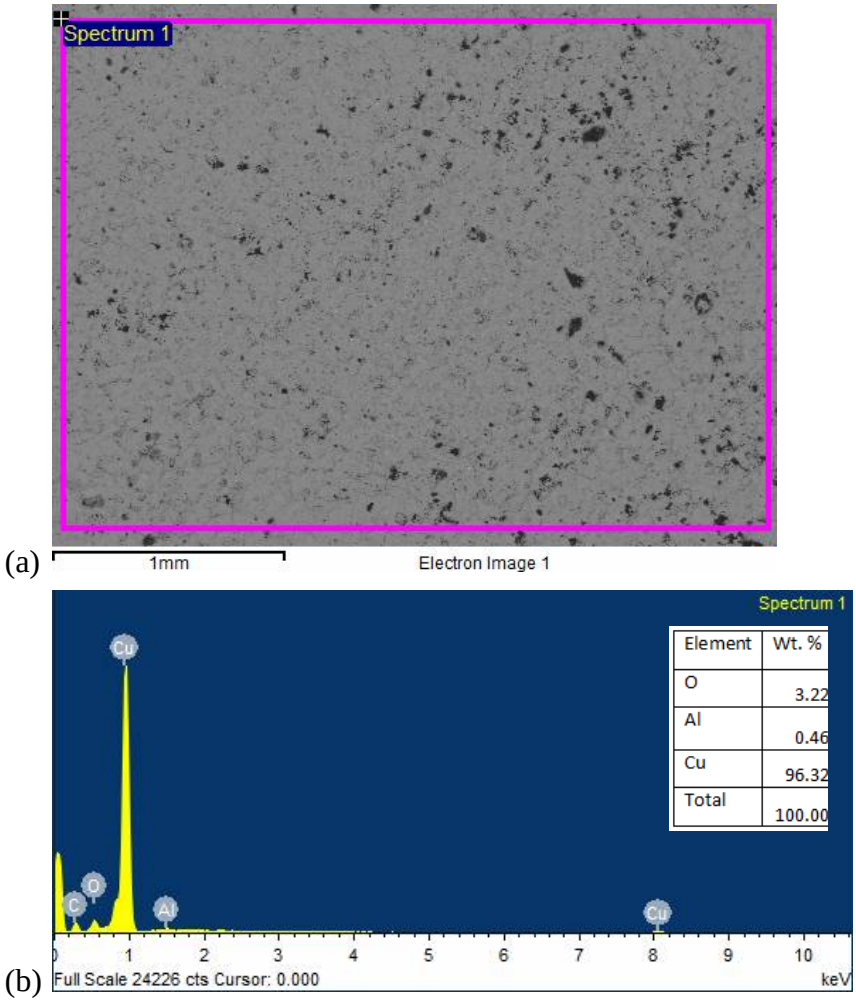


Figure 4.19: The SEM micrograph taken with a back-scattered electron detector (a) and the EDS spectrum with elemental weight percentages (b) of the CSC-0%Ru coating.

4.4.2.1.2 Cross section

The backscattered SEM image of the CSC-0%Ru coating is shown in Figure 4.20. The image was taken after grinding, polishing, and electro etching of the sample. The image was taken at high magnification due to the thin coating thickness. The coating showed poor adhesion to the substrate. The etching process had also removed some of the lose particles in the coating. The thickness of the coating was approximated as shown in Figure 4.20.

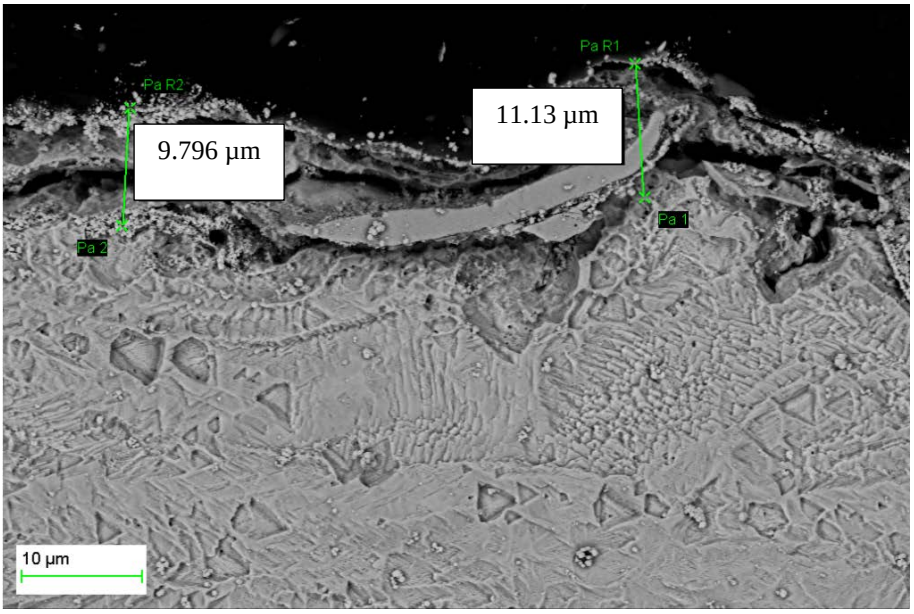


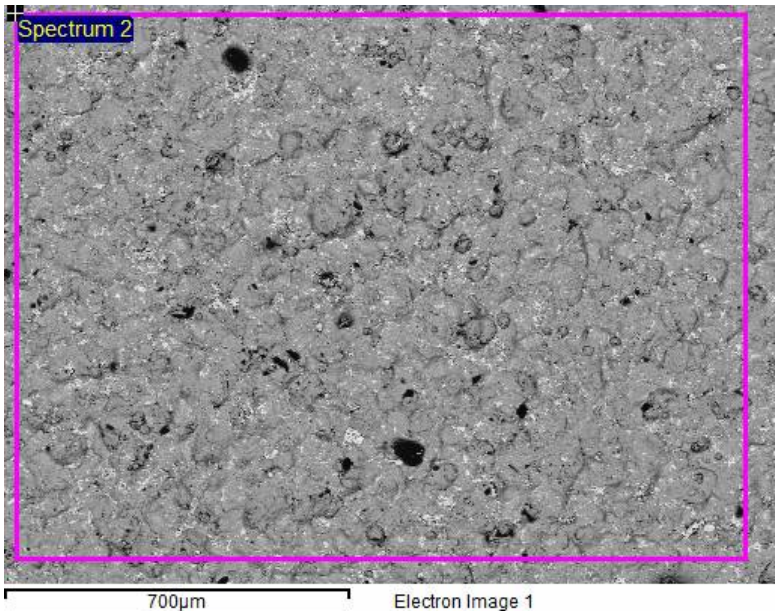
Figure 4.20: SEM micrograph of the cross section of CSC-0%Ru coated coating taken using a backscattered detector.

4.4.2.2 CSC-0.5%Ru

4.4.2.2.1 Surface

The SEM micrograph in Figure 4.21(a) shows the top surface of the CSC-0.5%Ru coating. The area selected was analysed using the EDS, and the results of this analysis is shown in Figure 4.21(b). The chemical analysis results are also shown in Figure 4.21. The EDS results detected a high concentration of ruthenium (7.55 wt.%) compared to the 0.5 wt.% that was intended. This could have been due to the poor mixing of the two powders prior to the coating process. The surface shows black dots that appear to be pores. The pores can be assumed to have formed when the gas was escaping from the coating.

(a)



(b)

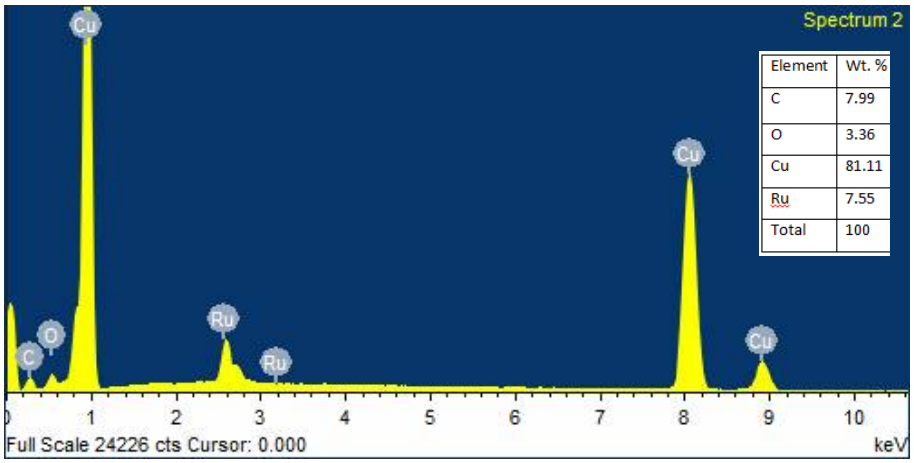


Figure 4.21: SEM micrograph taken with a back-scattered electron detector (a) of the top surface of the CSC-0.5%Ru coating, and (b) the EDS spectrum of the coating with elemental weight percentages.

4.4.2.2.2 Cross section

The micrograph of the cross section of the CSC-0.5%Ru coating in Figure 4.21 was taken using the back-scatter detector in the SEM. The coating thickness was measured. The thickness of this coating was observed to be uneven with different coating thickness along the substrate.

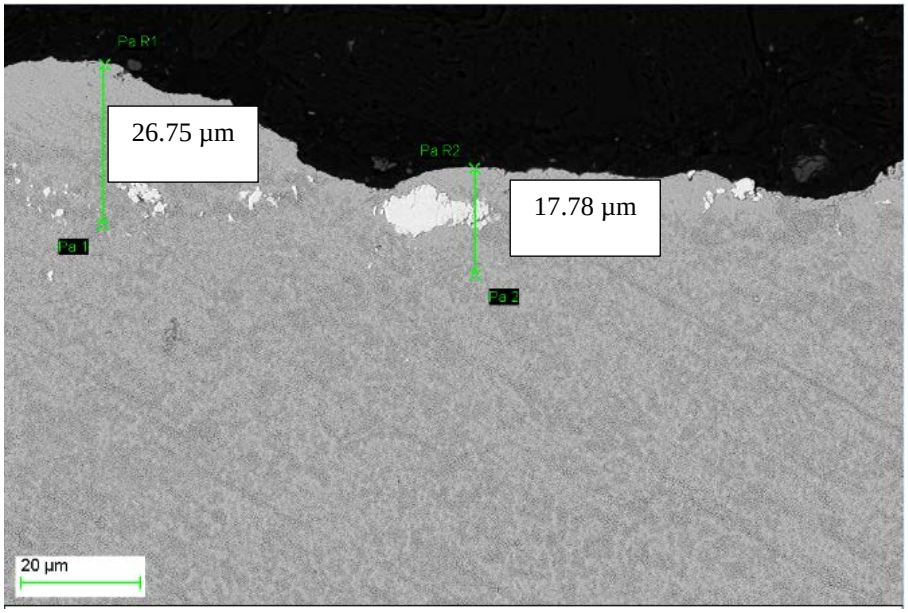


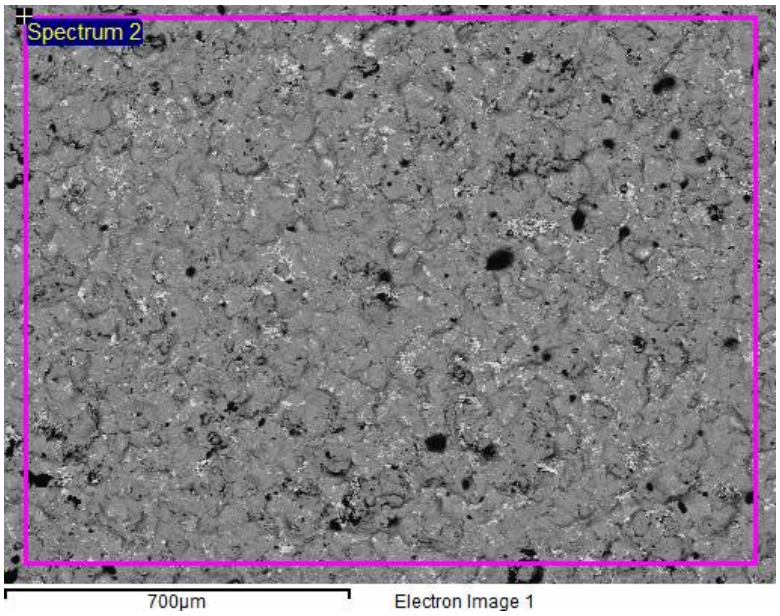
Figure 4.22: the back-scattered SEM micrograph of the cross section of CSC-0.5%Ru coating which was not etched.

4.4.2.3 CSC 1%Ru

4.4.2.3.1 Surface

The top surface micrograph of the CSC-1%Ru coating shown in Figure 4.23 (a) is the area that was used to perform the EDS analysis of the coating, and the results of this analysis are presented in Figure 4.23(b).

(a)



The EDS was performed to detect the composition of ruthenium that was added to the copper surface. Two ruthenium peaks are observed in the spectrum, and they are high compared to those found in high oxygen fuel thermal sprayed coatings. The ruthenium composition detected in the CSC-1%Ru was very high, 6.79% more than what was expected. This outcome has been affected by the coating process used.

(b)

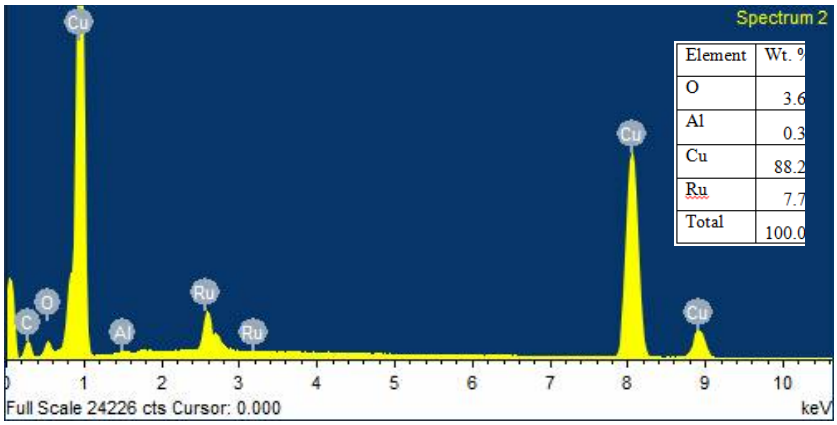


Figure 4.23: (a) SEM image of the top surface of the CSC-1%Ru coating, and (b) results of the EDS analysis over the area with averaged elemental compositions.

4.4.2.3.2 Cross section

The following image in Figure 4.24 shows the cross section of the CSC-1%Ru coating after polishing and electro-etching. The coating thickness was roughly measured. The coating also show different shades which were analysed with EDS. The coating of the CSC-1%Ru copper had poor adhesion. From the image in Figure 4.24 it can be seen that the coating, although still intact, were pealing off from the substrate.

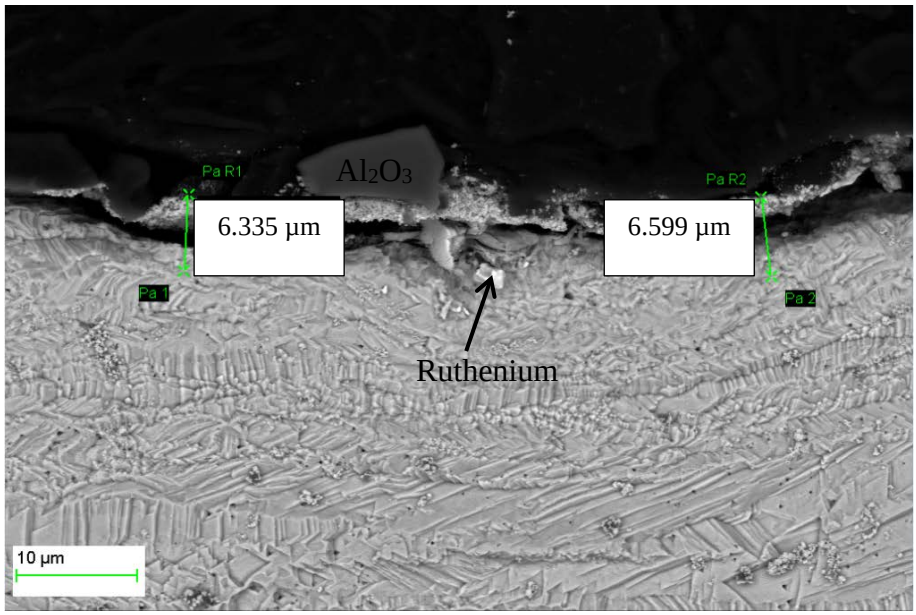


Figure 4.24: SEM micrograph of the cross section of CSC-1%Ru coating taken by the back-scattered detector.

4.4.2.4 CSC 2%Ru

4.4.2.4.1 Surface

The top surface of the CSC-2%Ru was analysed using EDS analysis technique on the area selected in Figure 4.26(a). The analysis results are shown in Figure 4.26(b) containing average compositions and the spectrum of elements detected on the surface. From the spectrum, about 17wt% Ru was detected instead of 2wt% Ru which was intended. This was unexpected. It is assumed that there was inhomogeneity that resulted from the thermal spraying stage since copper and ruthenium have different densities.

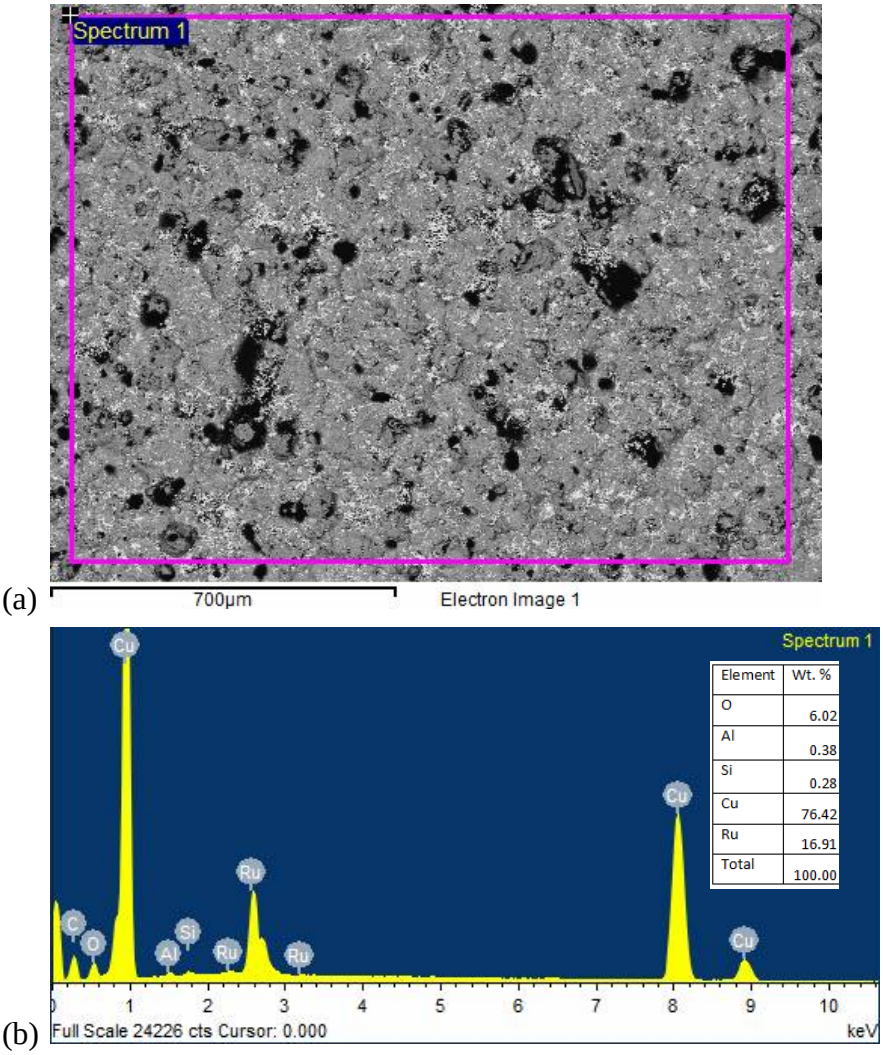


Figure 4.25: SEM micrograph taken with a back-scattered electron detector (a) of the top surface of the CSC-2%Ru coating, and (b) the EDS spectrum of the CSC-2%Ru coating with elemental weight percentages.

4.4.2.4.2 Cross section

Figure 4.26 is the micrograph of the cross-section of the CSC-2%Ru coating. Prior to capturing the image, the sample was ground, polished, and electro-etched to reveal the coating and substrate grain structure. The area selected had an uneven surface, which appeared to be curvaceous at higher magnifications. The thickness of the coating was roughly estimated. The coating adhesion to the substrate was poor, resulting in pores along the coating-substrate boundary as well as in the coating.

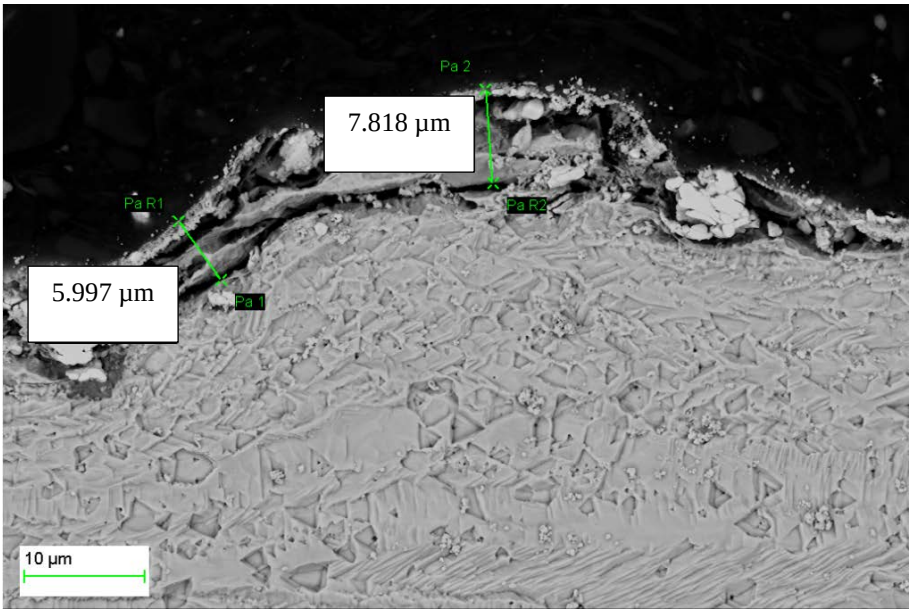


Figure 4.26: SEM micrograph of the cross section of CSC-2%Ru coating and estimated measurements of the coating thickness.

4.4.2.5 The comparison of all the CSC coating element maps

The field emission electron microscope with EDS was used to evaluate the surfaces of all the cold sprayed coatings. The main focus was on the distribution pattern of copper and ruthenium, which were presented as elemental maps. The results of the analysis are shown in Figure 4.27. In the maps, copper is represented by green and ruthenium by yellow. The ruthenium maps show an increase in the ruthenium concentrations and cluster on the coating surface which corresponds to the increase in ruthenium content.

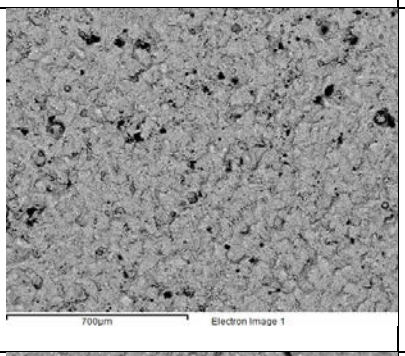
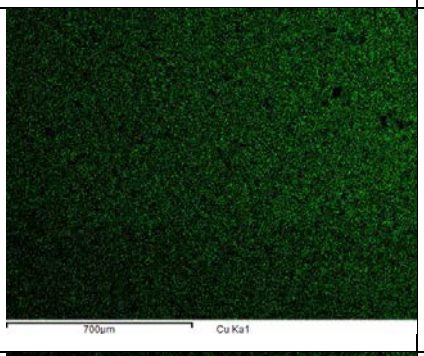
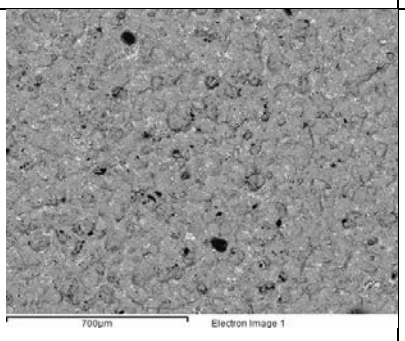
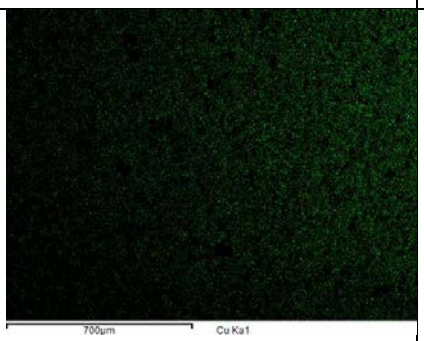
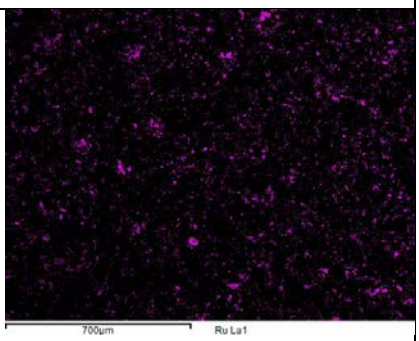
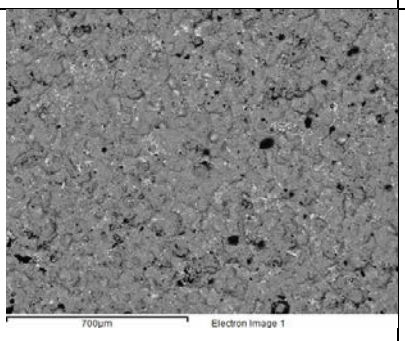
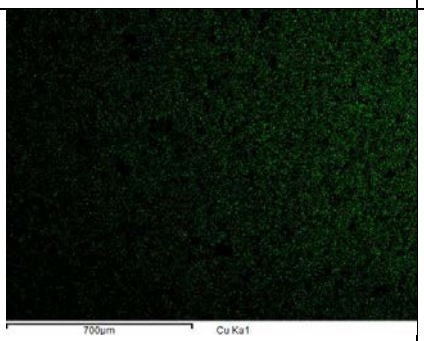
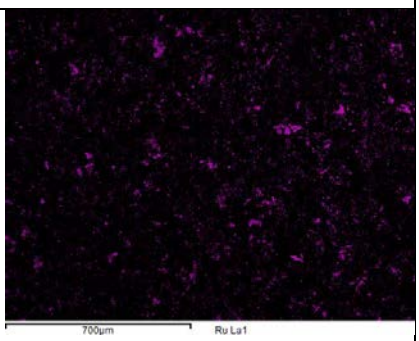
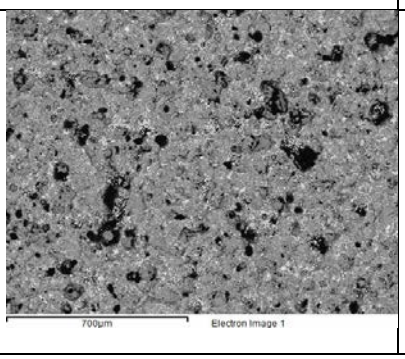
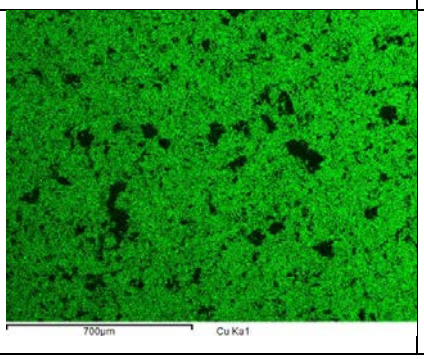
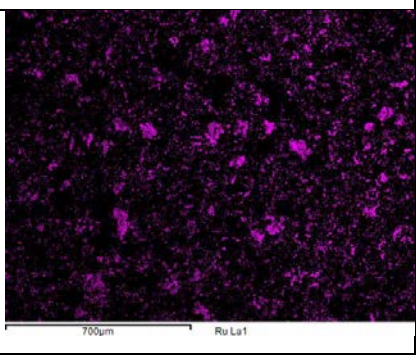
	Coating surface analysed	Copper map	Ruthenium map
CSC-0%Ru			
CSC-0.5%Ru			
CSC-1%Ru			
CSC-2%Ru			

Figure 4.27: SEM EDS elemental maps of the CSC coating surfaces representing copper (green) and ruthenium (yellow).

4.4.3 Hardness results

The Vickers micro hardness of all the CSC was measured, and the averaged hardness was plotted together with that of as received copper in Figure 4.28. The hardness values were measured using 10 gf indentation load. The variability of the data is also indicated in the graph by the error bars.

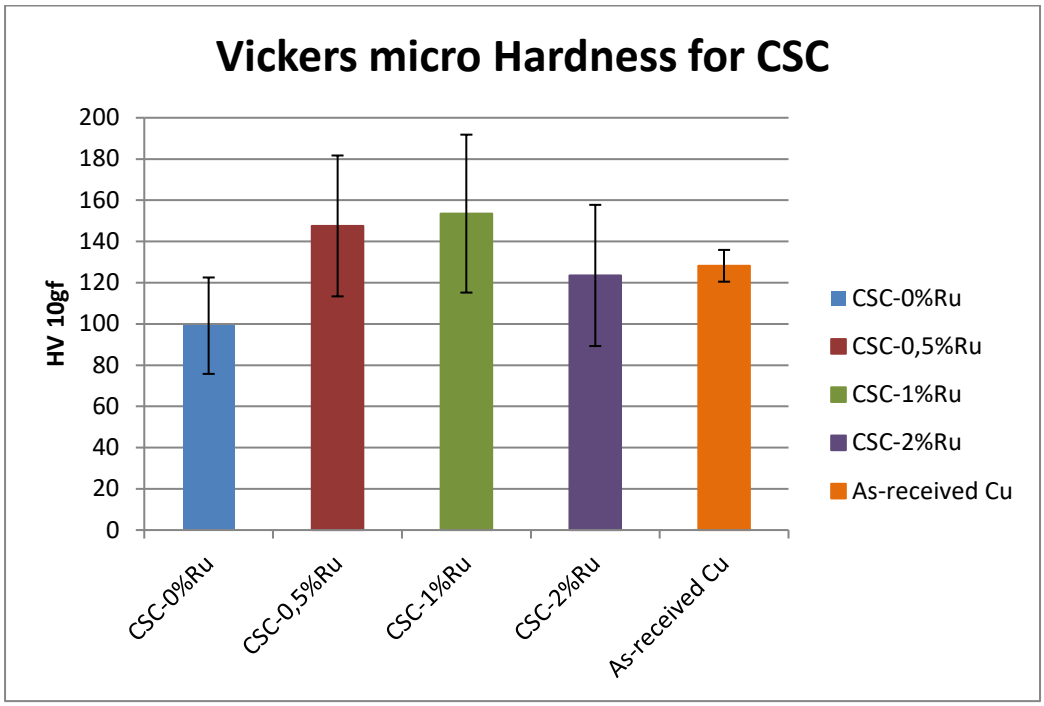


Figure 4.28: The average Vickers hardness of all the CSC coating compared to that of as-received copper.

4.4.4 Electrochemical results

The corrosion characteristics of CSC coatings were determined in 2M sulphuric acid environment at 45 and 65°C. The coatings were exposed to the acidic environment for 45 minutes, keeping the temperature constant throughout the experiment. The produced linear polarisation curves where used to measure the corrosion potential and current density. The coatings responded differently to the environment. To increase precision of the results, the experiments where repeated three times for good reproducibility. Figure 4.29 is showing the comparison of the coatings and the as-received copper at 45°C and Figure 4.30 shows the comparison at 65°C. The as-received copper is represented by the dotted line, and all the CSC coatings as solid lines.

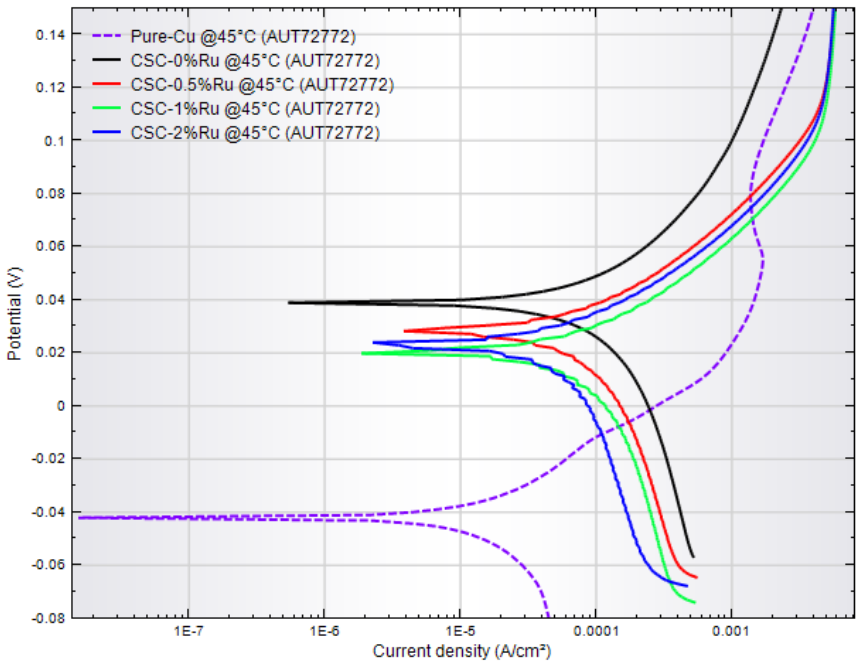


Figure 4.29: Potentiodynamic polarisation curves of CSC coating and as-received copper exposed to 2M H_2SO_4 at 45˚C.

The corrosion characteristics of the CSC coatings determined in 2M H_2SO_4 at 65°C is shown in Figure 4.30.

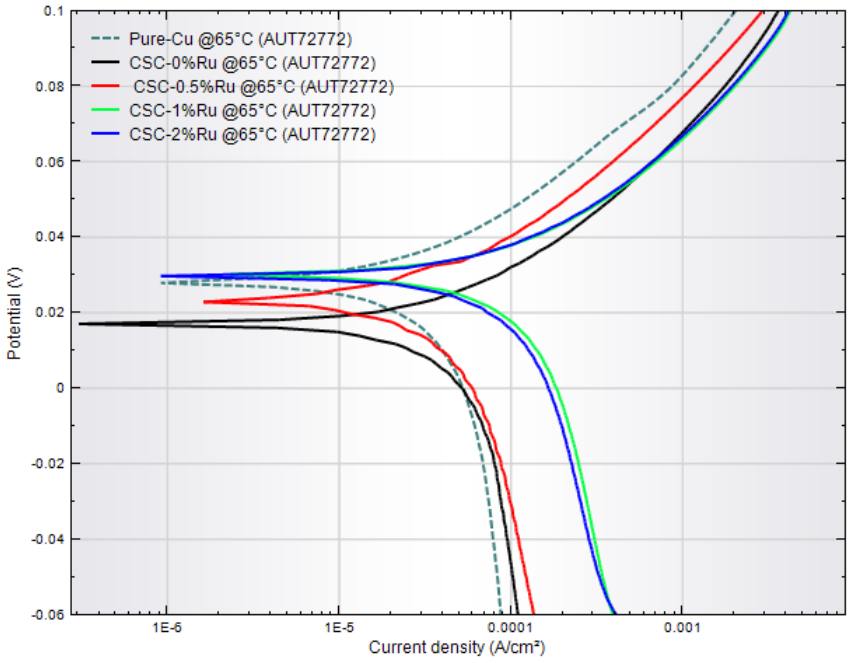


Figure 4.30: Potentiodynamic polarisation curves of CSC coating and as-received copper exposed to 2M H_2SO_4 at 65˚C.

4.4.4.1 The corrosion results

The polarisation resistance and corrosion potential values used in the corrosion rate calculations were taken from the potentiodynamic curves to determine the effect of coating the copper. Table 4.4 and 4.5 show the calculated corrosion rates. A graphical presentation of these corrosion rates are shown in Figure 4.31.

Table 4.4: Calculated corrosion rates for the CSC coatings at 45°C in 2M H_2SO_4.

	Icorr (A)	Icorr (µA)	icorr (µA/cm^2)	CR (mmpy)
As-received Cu	$9{,}62\times10^{-6}$	9,63	19,15	0,22
CSC-0%Ru	$2{,}73\times10^{-5}$	27,36	54,43	0,63
CSC-0.5%Ru	2.43×10^{-5}	24.34	48.43	0.56
CSC-1%Ru	$2{,}36\times10^{-5}$	23.63	47.00	0.54
CSC-2%Ru	$2{,}14\times10^{-5}$	21,43	42,49	0,49

Table 4.5: Calculated corrosion rates for the CSC coatings at 65°C in 2M H_2SO_4.

	Icorr (A)	Icorr (µA)	icorr (µA/cm^2)	CR (mmpy)
As-received Cu	$3{,}34\times10^{-5}$	33,47	66,58	0,77
CSC-0%Ru	$2{,}12\times10^{-5}$	21,27	42,31	0,49
CSC-0.5%Ru	$1{,}98\times10^{-5}$	19,86	39,52	0,46
CSC-1%Ru	$2{,}96\times10^{-5}$	29,63	58,94	0,68
CSC-2%Ru	$2{,}80\times10^{-5}$	28,04	55,79	0,65

Figure 4.31 displays the corrosion rates measured from the CSC coated copper with different ruthenium content. At 45°C there was a steady change in corrosion rate, there CR decreased with increase in ruthenium content. At 65°C the corrosion rates are increasing, with the highest rate at 1%Ru. The corrosion rate for the coating containing no ruthenium was found to be higher at 45°C than at 65°C. This is assumed to be due to the rate of formation of the copper oxide protective film. At lower temperatures the reaction kinetics are slower compared to higher temperatures. At high temperature the surface corroded, but enough oxides formed to protect the coating, and lower the corrosion rate.

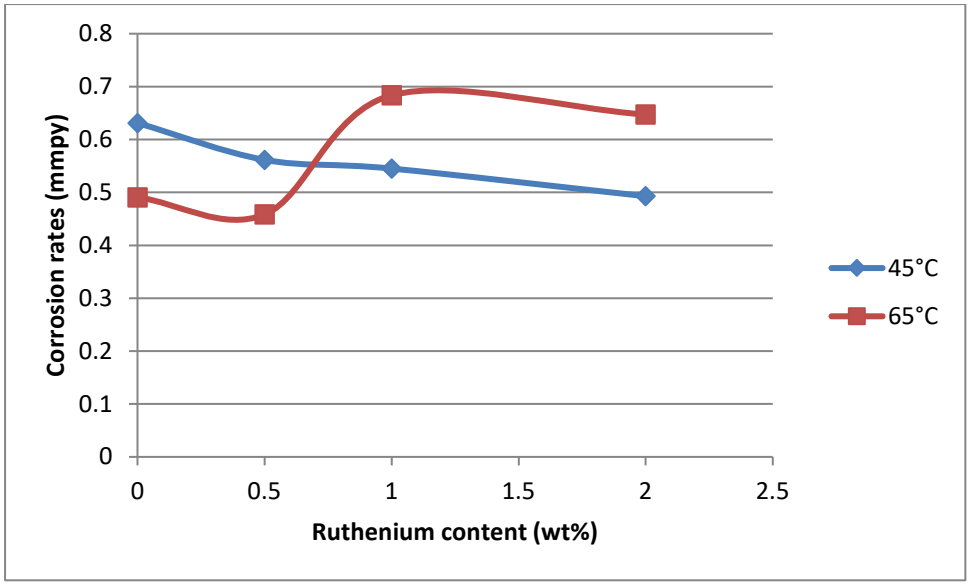


Figure 4.31: Corrosion rate as a function of ruthenium concentration in the CSC coatings exposed to in 2M H_2SO_4.

4.5 SPS

The section will look at all spark plasma sintered copper alloys. It will focus on different properties of the alloy, like corrosion resistance and hardness, and compare them to the as-received copper. The section will investigate the effect of ruthenium in the grain structure and sizes, and the mechanism of corrosion of the alloys when exposed to corrosive environment. Corrosion rate calculations will also be presented.

4.5.1 Optical micrographs

The alloys were sectioned and mounted, ground, polished and etched for optical analysis. Figure 4.32 is showing the result of the analysis of the alloys with different ruthenium concentrations as labelled. All the images were captured at 50× magnification.

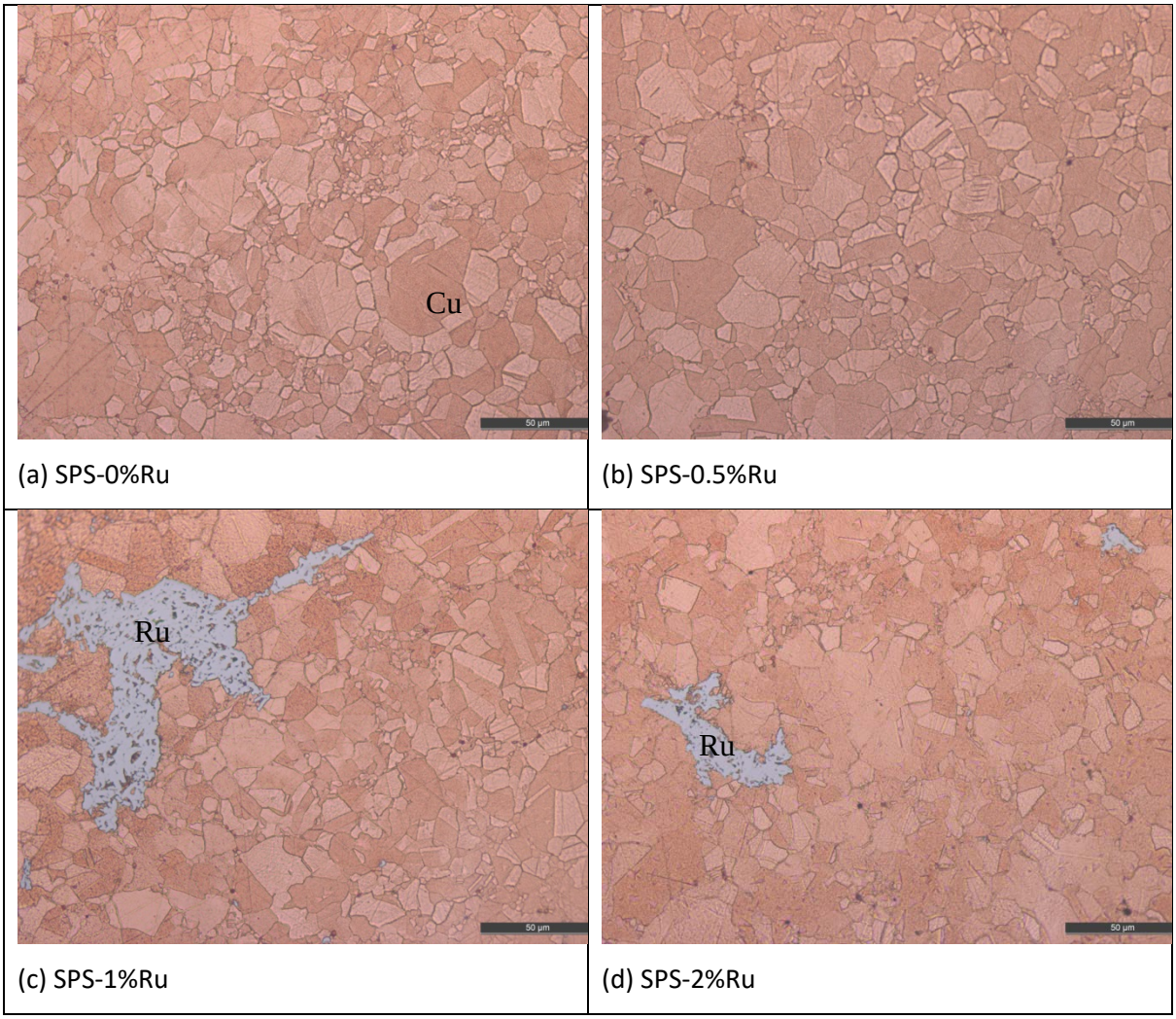


Figure 4.32: Optical micrographs of (a) SPS-0%Ru, (b) SPS-0.5%Ru, (c) SPS-1%Ru, and (d) SPS-1%Ru etched with Beraha's lead sulfide (PbS).

4.5.2 SEM EDS results

Further analyses of the alloy were made using SEM. The back-scattered electron detector of the SEM was used. The distribution of ruthenium in the alloy, the effect on grain size, and the corrosion mechanism were investigated.

4.5.2.1 SPS-0%Ru

The alloy was mounted, ground, polished and electro-etched. The SEM micrograph shown in Figure 4.33(a) of the SPS-0%Ru alloy was obtained using a backscattered detector. The image was further studied under higher magnification, Figure 4.33(b), and from this image it shows pits that could have resulted from etching. The EDS analysis was made on the alloy, and the results are shown in Figure 4.33(c).

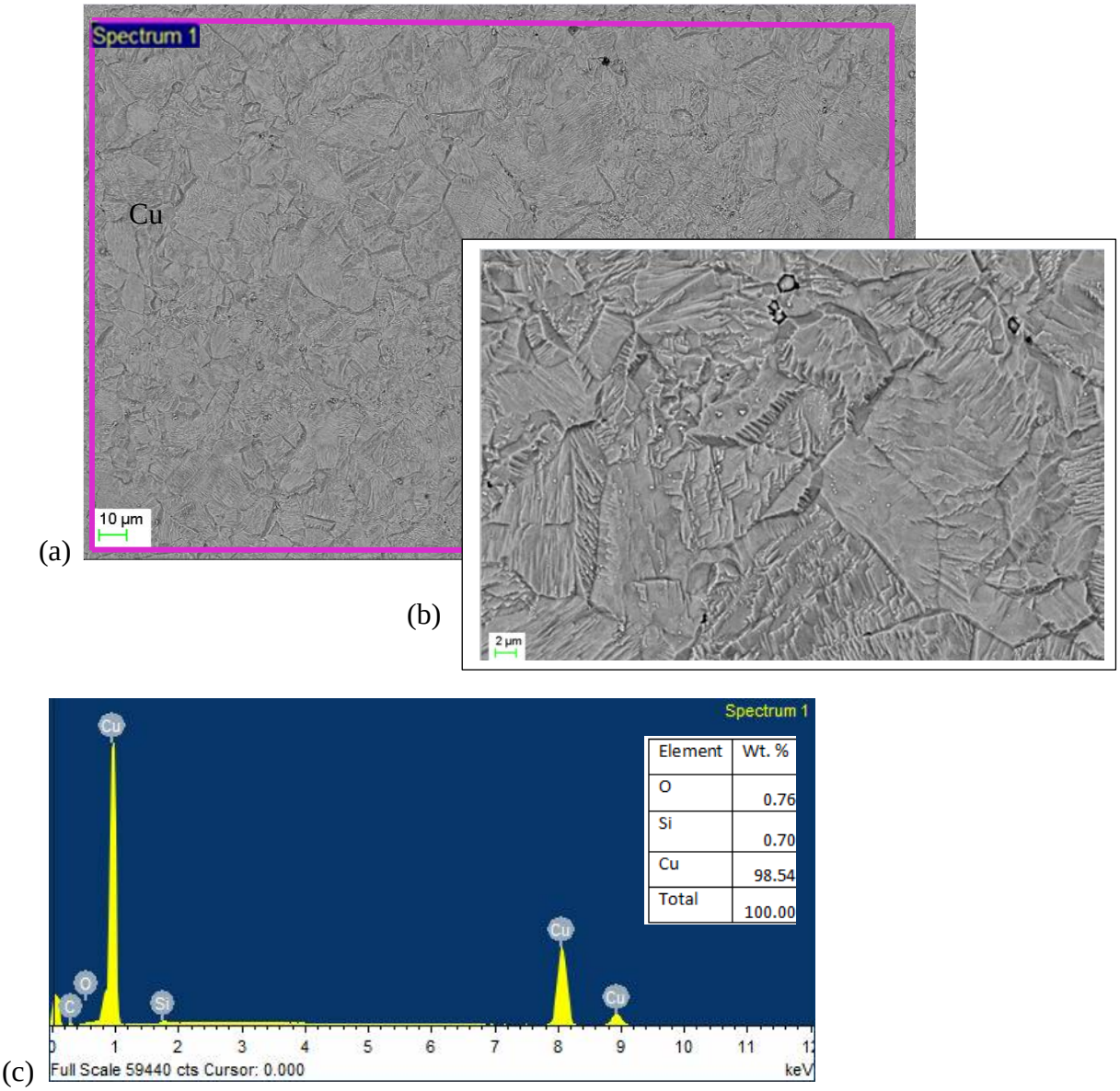


Figure 4.33: SEM micrograph of the SPS-0%Ru alloy taken with a backscattered electron detector (a), and (b) is showing the alloy at higher magnification, and (c) is the results of the EDS analysis of the alloy.

4.5.2.2 SPS -0.5%Ru

The SPS-0.5%Ru alloy was prepared for SEM analysis by mounting, grinding, polishing, and electro-etching. A selected area on the alloy was analysed, and an image in Figure 4.34(a) was produced. The micrograph of the alloy showed two different regions. A lighter region comprised of ruthenium, and a darker region, which was copper. These two regions were also captured at a higher magnification, Figure 4.34(b), and an EDS analysis was performed on the lighter region to validate the assumption that it was ruthenium. The results of this analysis is shown in an EDS spectrum in Figure 4.34(c).

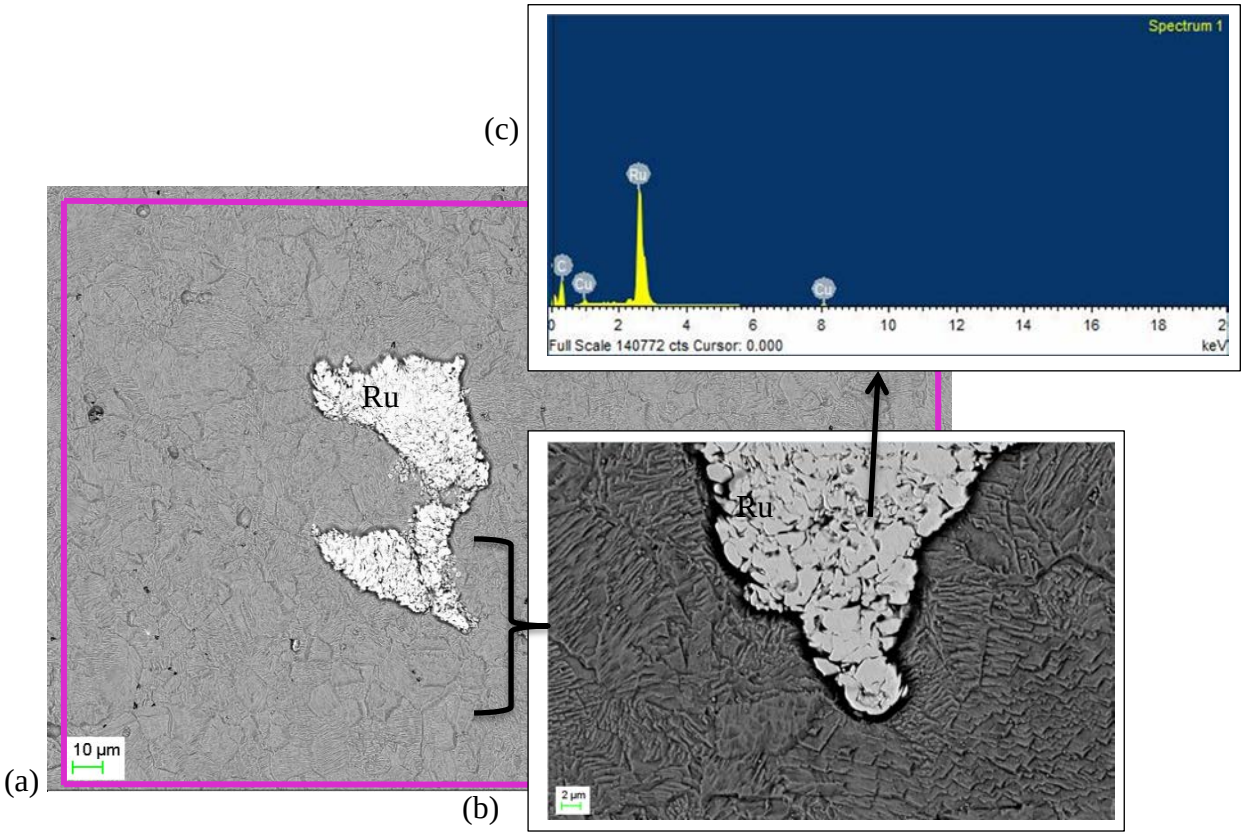


Figure 4.34: SEM micrograph of (a) the SPS-0.5%Ru alloy, (b) the alloy at higher magnification, and (c) the EDS results of the analysis shown as a spectrum.

The overall EDS analysis of the area shown in Figure 4.34(a) was also conducted, and the results (EDS spectrum) of this analysis are shown in Figure 4.35, with the weight percentages of all detected elements.

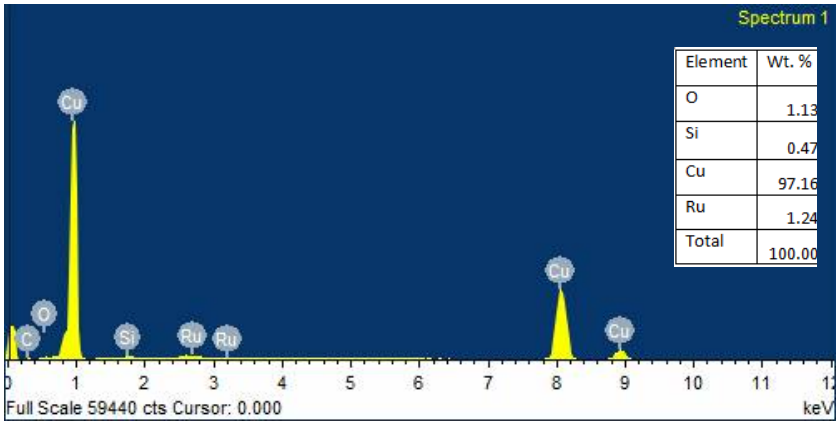
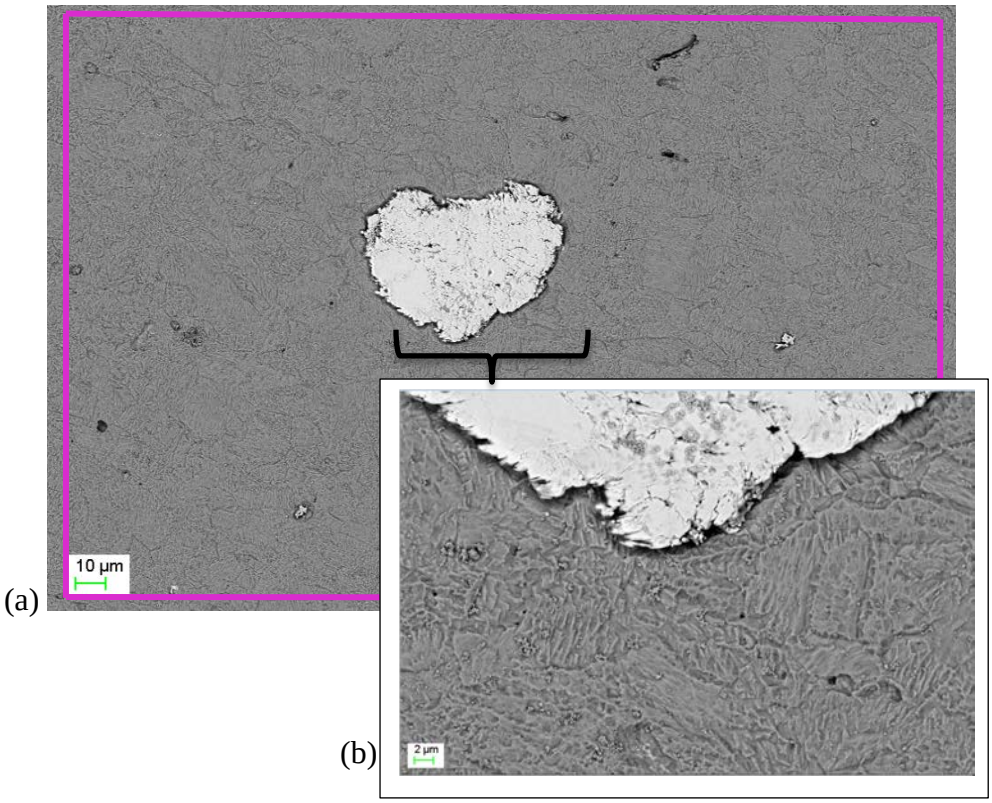


Figure 4.35: EDS spectrum of the SPS-0.5%Ru alloy showing the chemical compositions.

4.5.2.3 SPS 1%Ru

The SPS-1%Ru alloy was studied with theback-scattered electron detector of the SEM and EDS analysis was performed. Prior to the analysis, the sample was ground, polished and electro-etched. The micrograph Figure 4.36 (a) is showing the area of the SPS-1%Ru that was analysed, and Figure 4.36(b) is showing a magnified image of the alloy for a closer look of the

surface. The results to the analysis made in Figure 4.36(a) are shown in Figure 4.36(c), which is an EDS spectrum, also outlining compositions of the elements detected.



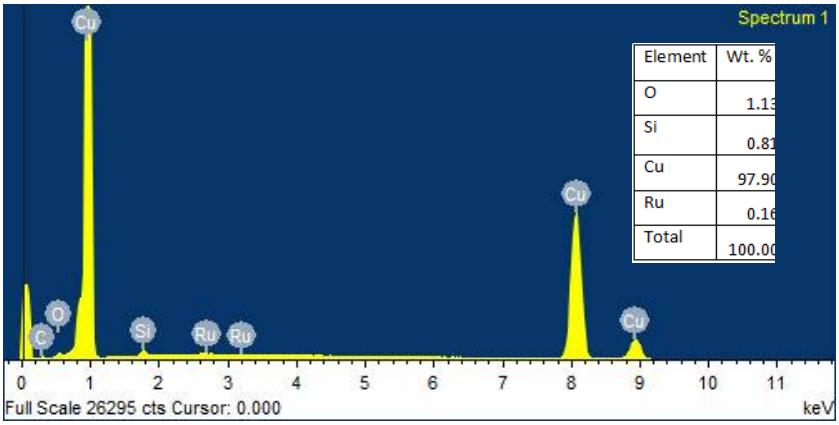


Figure 4.36: SEM image, taken with a back-scattered detector, of (a) the SPS-1%Ru alloy, and (b) the same alloy at higher magnification, with(c) the EDS spectrum of the SPS-1%Ru alloy with elemental weight percentages.

4.5.2.4 SPS 2%Ru

The micrograph shown in Figure 4.37 is of the SPS-2%Ru alloy after it was mounted, ground, polished and electro-etched to reveal the alloy surface characteristics, the same area at higher magnification is shown in Figure 4.37 (b). The alloy was scanned by an Oxford x-act detector for Energy Dispersive X-ray Spectroscopy, as shown in Figure 4.38.

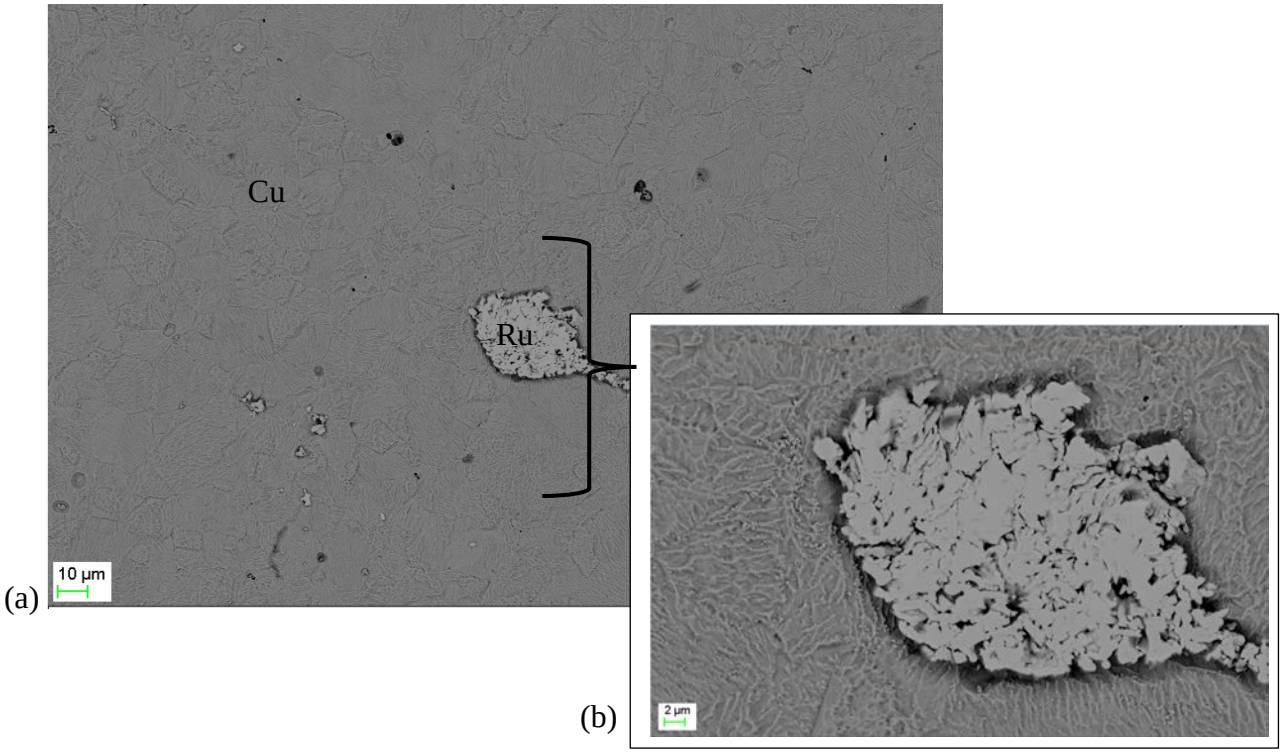


Figure 4.37: SEM image, taken with a back-scattered detector, of (a) the SPS-2%Ru alloy, and (b) the same alloy at higher magnification.

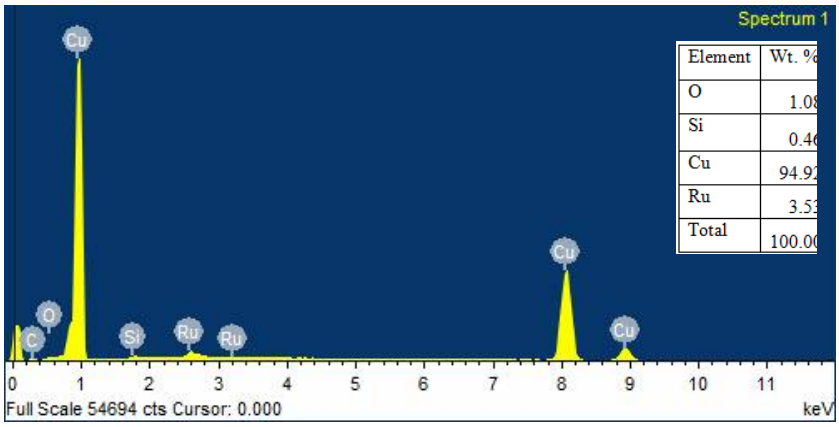


Figure 4.38: EDS spectrum of the SPS-2%Ru alloy with elemental weight percentages.

4.5.3 Hardness results

The Vickers micro hardness measurements of the SPS alloys were measured on the polished sample. A load of 100gf was used for indentations during the measurement. The averaged hardness was plotted in Figure 4.39. The hardness of the alloys was compared to the as-received copper. The error bars are also indicated on the graph to show data variability.

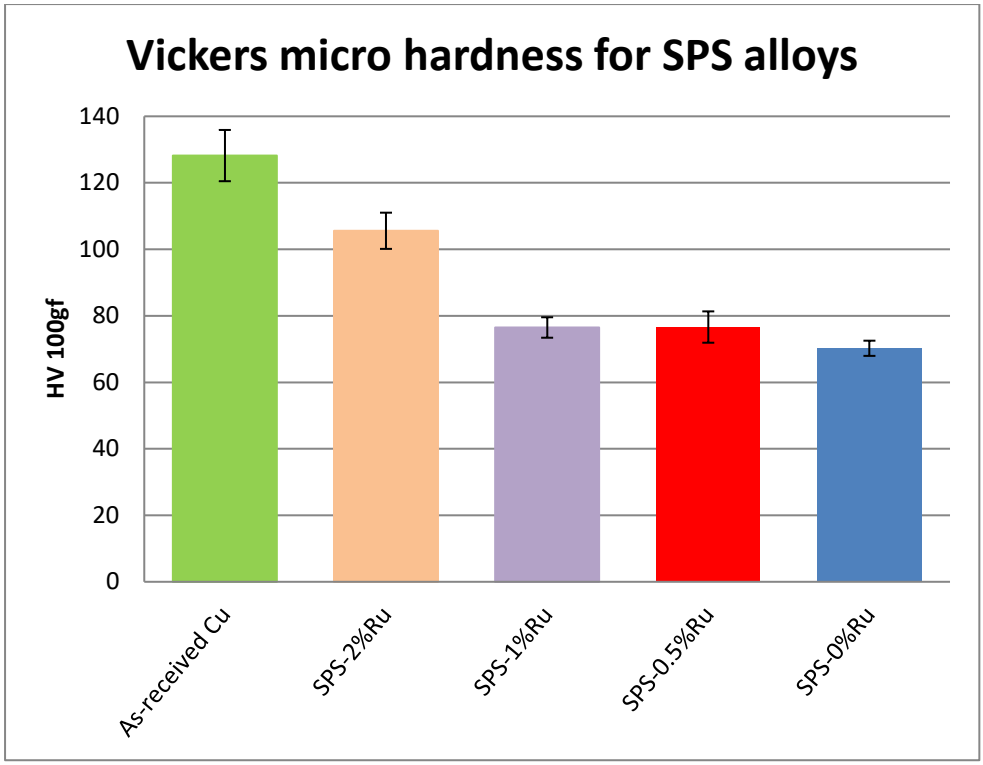


Figure 4.39: The average Vickers hardness of all the SPS alloys compared to that of as-received copper.

4.5.4 Electrochemical results

The corrosion characteristics of the alloys were determined in 2M sulphuric acid at 45 and 65°C. The alloys were exposed in this condition for 45 min prior to the scan. The results of the experiments were recorded as linear polarisation curves. From the curves, corrosion current density and potential for different alloys were determined. Figure 4.40 and 4.41 show the comparison of the potentiodynamic curves between the alloys and as-received copper at 45 and 65°C respectively.

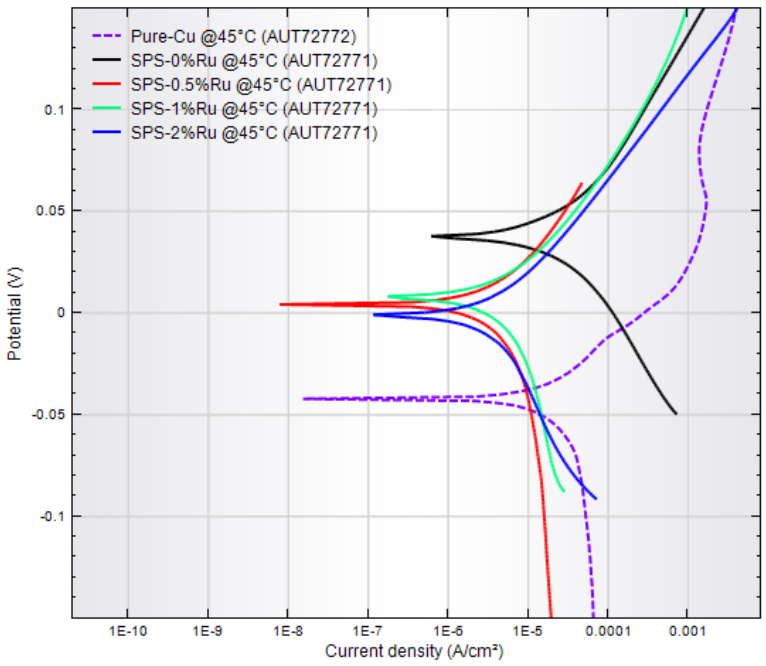


Figure 4.40: Linear polarisation potentiodynamic curves for SPS alloys and as-received copper in 2M H_2SO_4 at 45˚C.

The graph shown in Figure 4.41 is showing the corrosion characteristics of the alloys in 2M H_2SO_4 at 65°C.

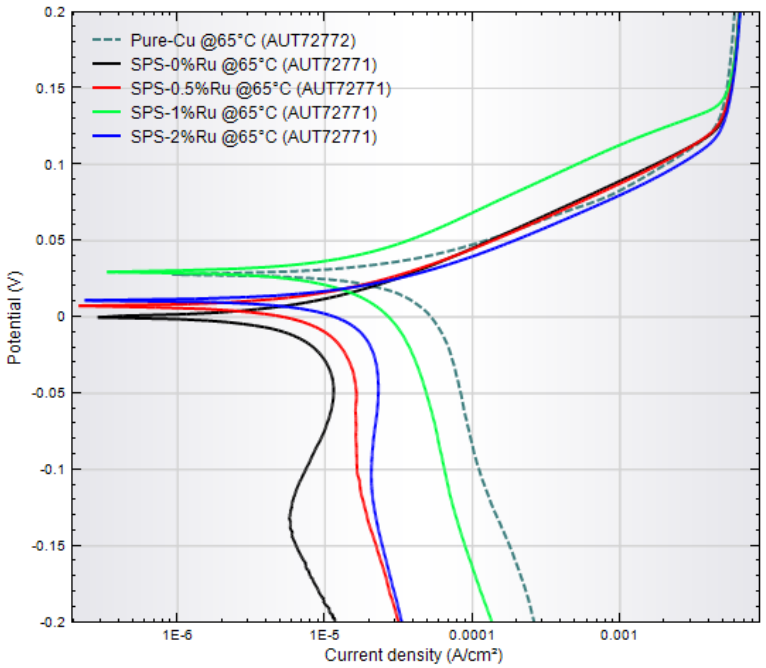


Figure 4.41: Linear polarisation potentiodynamic curves for SPS alloys and as-received copper in 2M H_2SO_4 at 65˚C.

The potentiodynamic curves shown in Figure 4.41 are the results of the alloys being exposed in 2M sulphuric acid at 65°C for a longer time. The potentiostatic pulse corrosion test was done with exposure time of 1 hour 30 min, with a pulse after 45 min. The experiment was done to

determine the corrosion characteristics of the alloy when exposed for longer in the acidic environment.

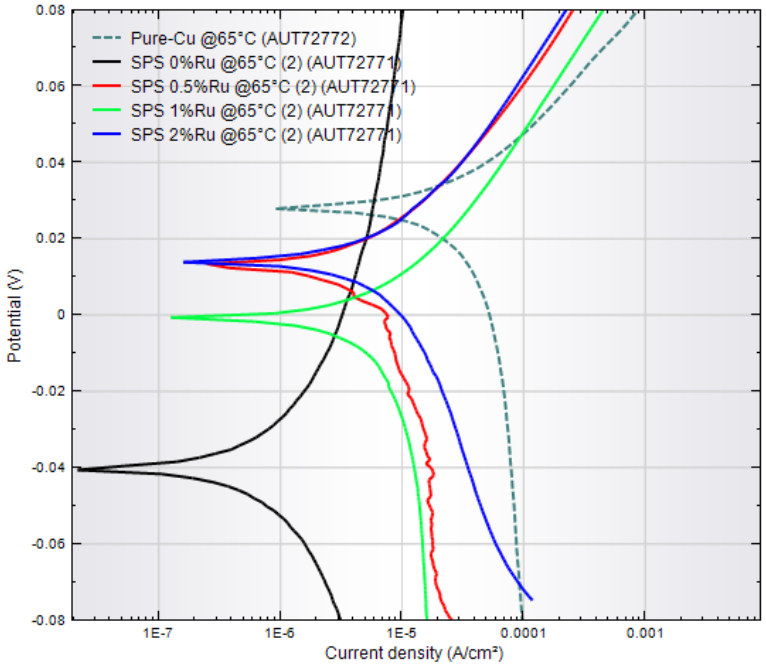


Figure 4.42: Linear polarisation potentiodynamic curve of SPS alloys exposed in 2M H_2SO_4 at 65˚C for 1hr30min.

4.5.4.1 Corrosion results

Corrosion rate calculations of the alloys are shown in this section. The corrosion rates were calculated by determining the polarisation resistance at the corrosion potential and converting that to the corrosion current density, and then corrosion rate. The results of the corrosion rates were compared to the as-received copper. Table 4.6, 4.7, and 4.8 are showing these results. A graphical presentation of the results is shown in Figure 4.43 showing the change in corrosion rates with increase in ruthenium content in the alloy.

Table 4.6:Corrosion rate calculations for the SPS alloys and as-received copper measured in 2M H_2SO_4 at 45°C.

	Icorr (A)	Icorr (µA)	icorr (µA/cm^2)	CR (mmpy)
As-received Cu	$9{,}63\times10^{-6}$	9,63	19,15	0,22
SPS -0%Ru	$3{,}05\times10^{-6}$	3,05	6,06	0,07
SPS -0.5%Ru	$6{,}83\times10^{-7}$	0,68	1,36	0,02
SPS -1%Ru	$1{,}09\times10^{-6}$	1,09	2,16	0,03
SPS -2%Ru	$9{,}98\times10^{-7}$	0,99	1,97	0,02

Table 4.7: Corrosion rate calculations for the SPS alloys and as-received copper measured in 2M H_2SO_4 at 65°C.

	Icorr (A)	Icorr (µA)	icorr (µA/cm^2)	CR (mmpy)
As-received Cu	$3{,}34\times10^{-5}$	33,47	66,58	0,77
SPS-0%Ru	$2{,}22\times10^{-6}$	2,22	4,41	0,05
SPS -0.5%Ru	$2{,}34\times10^{-6}$	2,34	4,66	0,05
SPS-1%Ru	$2{,}99\times10^{-6}$	2,99	5,96	0,07
SPS -2%Ru	$3{,}00\times10^{-6}$	3,00	5,97	0,07

Table 4.8: Corrosion rate calculations for the SPS alloys exposed for 1 h 30 min and the as-received copper measured in 2M H_2SO_4 at 65°C.

	Icorr (A)	Icorr (µA)	icorr (µA/cm^2)	CR (mmpy)
As-received Cu	$3{,}34\times10^{-5}$	33,47	66,58	0,77
SPS -0%Ru	$1{,}90\times10^{-7}$	0,19	0,38	0,01
SPS -0.5%Ru	$1{,}82\times10^{-6}$	1,82	3,62	0,04
SPS -1%Ru	$1{,}68\times10^{-6}$	1,68	3,34	0,04
SPS -2%Ru	$2{,}21\times10^{-6}$	2,21	4,40	0,05

The measured corrosion rates of the SPS alloys are shown in Figure 4.43. These corrosion rates are considerably lower compared to the pure copper. There is a slight increase in corrosion rates of the alloy with an increase in ruthenium content. At 65°C the resultant corrosion rates of the SPS alloys were lower than at 65°C after 45 min. The corrosion rates of the alloys at 45 min gives the idea of the kind of corrosion attack suffered by the alloys at the first circle of the SPS samples. It can be observed that at 45°C the coating with no ruthenium resulted in a higher corrosion rate compared to the coating with no ruthenium at 65°C. This can be accounted for by the difference in the reaction kinetics and the rate of protective oxides formation at the two temperatures. At 65°C the corrosion products that formed served as a protective film.

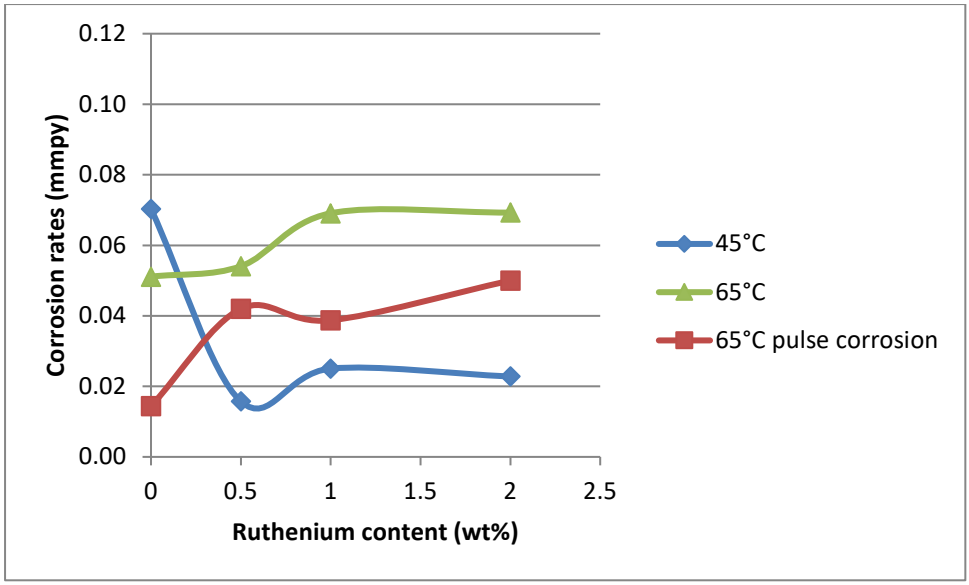


Figure 4.43: Corrosion rate as a function of ruthenium concentration in the SPS alloys exposed to 2M sulphuric acid.

To clearly compare the corrosion characteristics of the SPS alloys exposed to sulphuric acid at 65°C for different durations, the graph in Figure 4.44 was generated. From the figure, the first run represents the corrosion rates of the SPS alloy after 45 min, and second run represents the corrosion rates of the SPS alloys after 90 min exposure time.

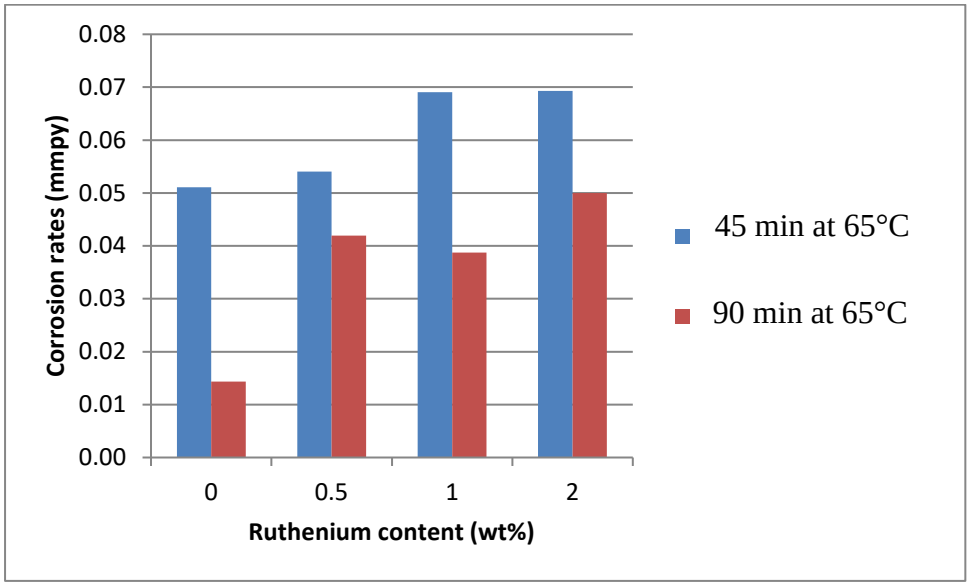


Figure 4.44: Comparison of corrosion rates of the SPS alloys that were exposed for different durations (45 min and 90 min) in 2M H_2SO_4 at 65°C.

4.5.4.2 Corrosion mechanism of the SPS alloys

This section will be exploring the corrosion mechanism of the SPS alloys, and a close study of the effect of ruthenium and the role it plays when added to the alloy. After performing the corrosion test, the samples were cleaned using ultrasonic cleaner. The solution used to clean was acetone at a temperature of 35°C. This was done to remove all the corrosion products that had formed during corrosion. The corrosion products were removed so they do not interfere with the alloy surface analysis. The back-scattered and secondary detectors were used in the SEM analysis. The analysis shows the alloy sample right after corrosion, the area that was exposed to the acidic environment, the area where the rubber band had been placed to control the area exposed, and lastly, the area of the alloy that was not exposed to the acid. The main focus was on the corroded area. The section will also show magnified images to increase the visibility of the corroded alloy and investigate the type of corrosion propagation that had occurred.

The corroded SPS-0%Ru alloy was analysed using SEM and Figure 4.45, showing the distinctive corroded, affected band, and alloy area. The corroded area is showing some pits, and the scratches from polishing.

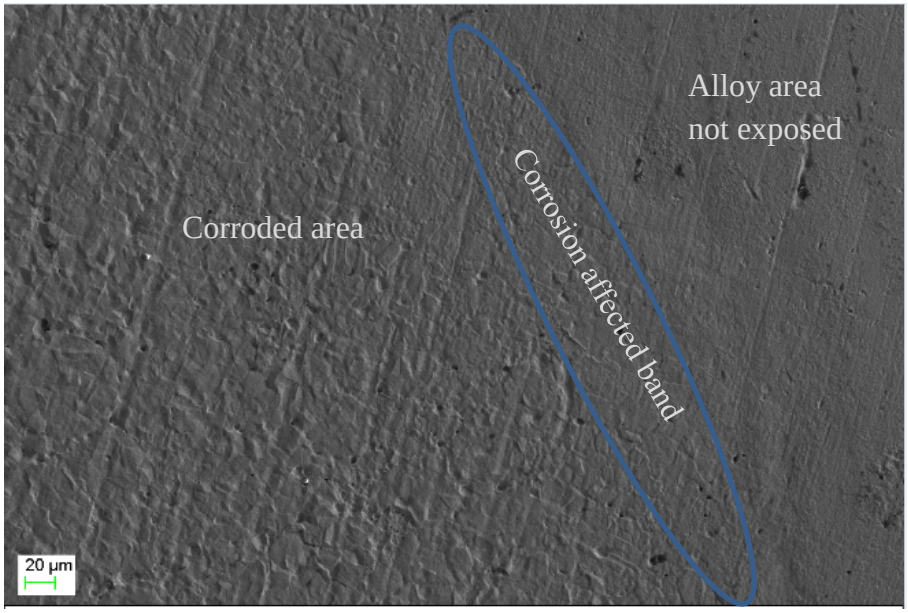


Figure 4.45: SEM micrograph of corroded SPS-0%Ru alloy analyzed after ultrasonic cleaning.

The corroded area which appeared to have pits was magnified to gather more details, and the images produced are shown in Figure 4.46 (a) and (b). The images only show pits, which

suggest that pitting corrosion had occurred. The pits appear to have mostly attacked the alloy along the grain boundaries.

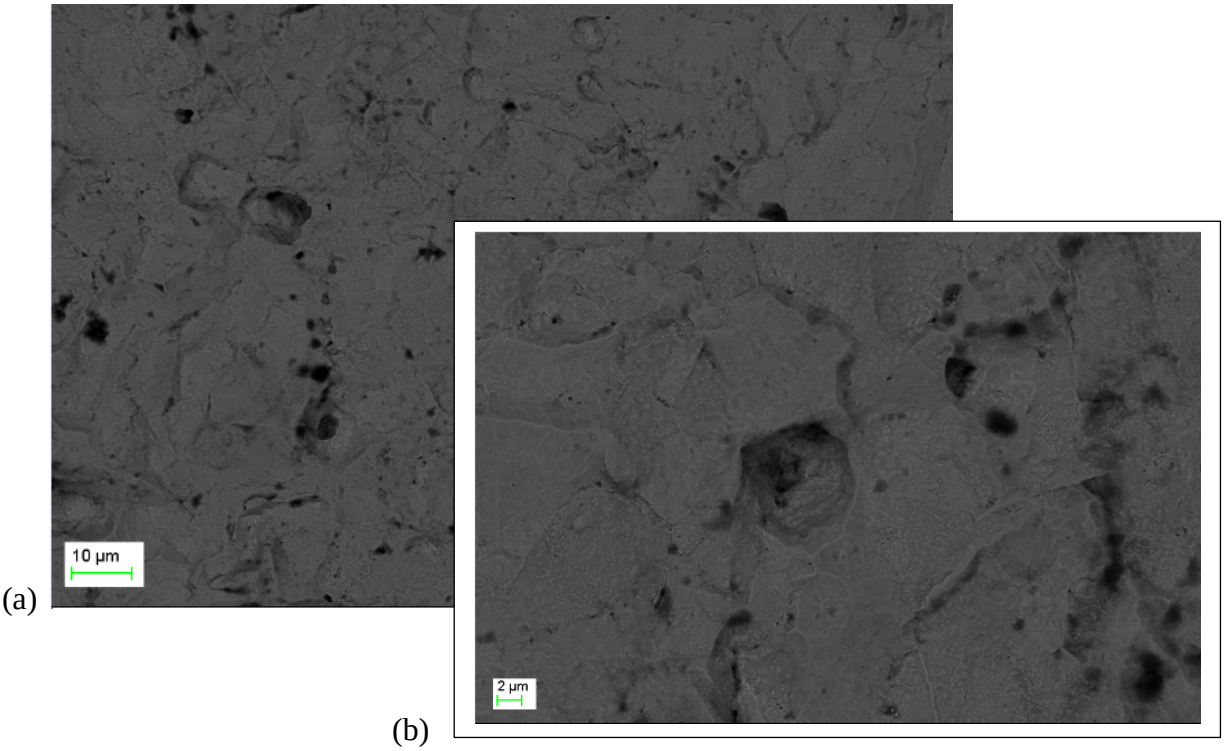


Figure 4.46: The SEM images taken by BSD and SE detectors showing the pits that formed by corrosion

The SEM image shown in Figure 4.47 is showing an SEM image of the corroded SPS-0.5%Ru alloy taken with the secondary electron detector.

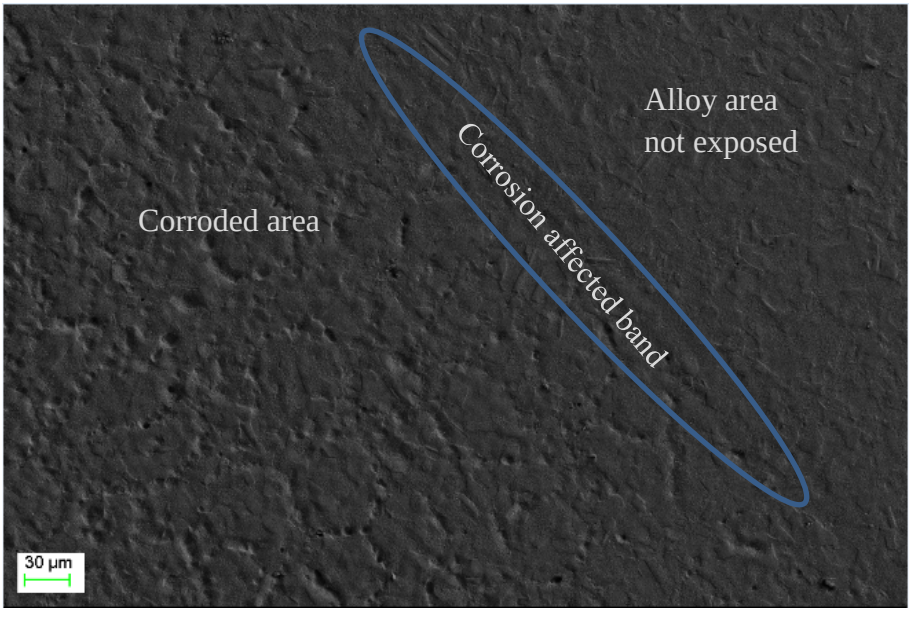


Figure 4.47: SEM micrograph of corroded SPS-0.5%Ru alloy taken by the secondary electron detector.

More analyses were made on the corroded area of the SPS-0.5%Ru alloy using SEM, which produced the micrographs shown in Figure 4.48 (a) and (b). Figure 4.48(b) is at higher

magnification compared to (a). The alloy appears to have pits of different depths. There was a minor corrosion effect on the ruthenium in the alloy.

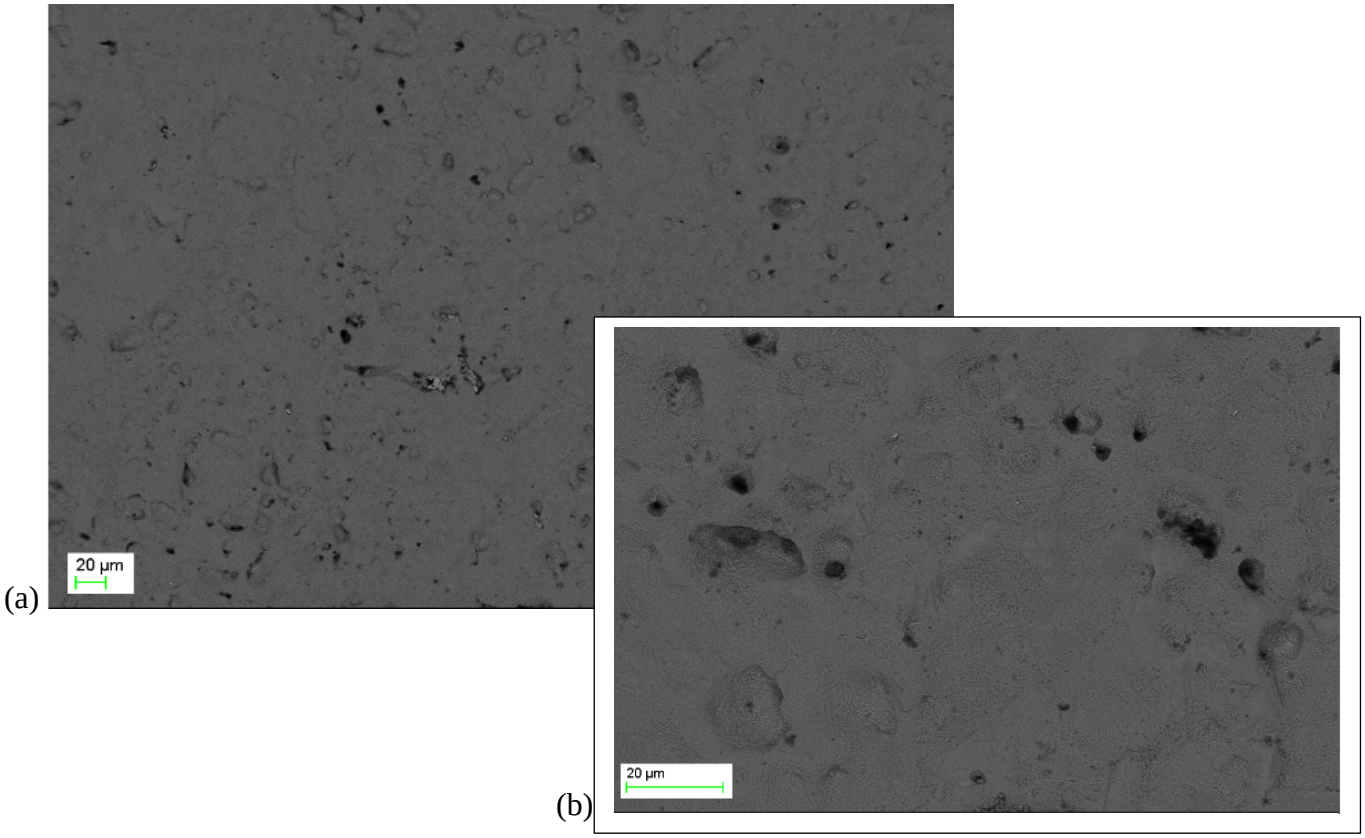


Figure 4.48: SEM micrographs of SPS-0.5%Ru alloy taken by the BSD and SE detectors under different magnifications.

The BSD and SE SEM micrographs shown in Figure 4.49 are showing the ruthenium in the alloy after corrosion. The images show ruthenium protruding over the alloy surface since it was left un-attacked during the corrosion process.

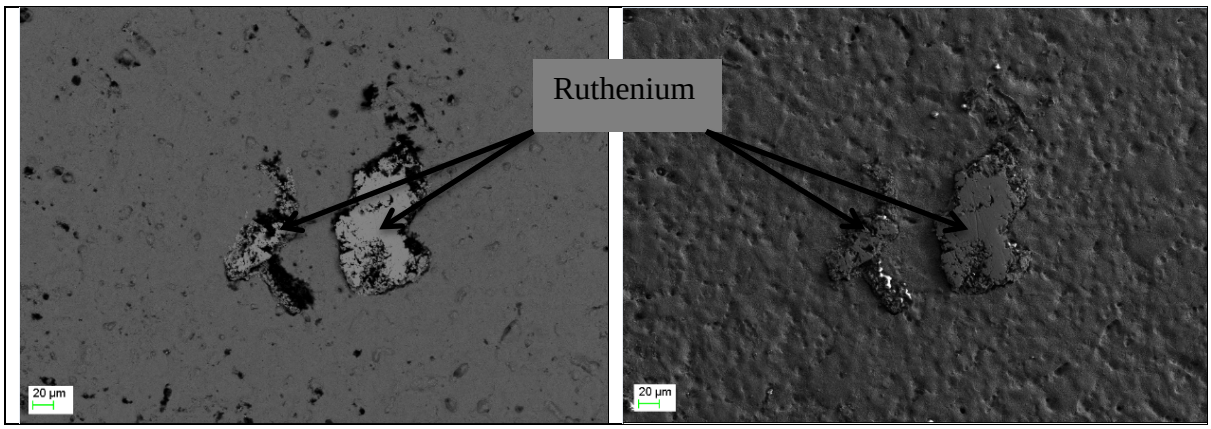


Figure 4.49: the SEM micrograph of SPS-0.5%Ru alloying showing the area with ruthenium which was not corroded.

The SEM micrograph shown in Figure 4.50 is of the SPS-1%Ru alloy that was corroded and cleaned using acetone and an ultrasonic cleaner to reveal the corrosion damage to the alloy.

The micrograph shows two areas of the sample, where it corroded and where it was not exposed to the corrosive environment and did not corrode. In between the two areas it shows possible crevice corrosion that had occurred under the silicon rubber ring. The corrosion affected band is the part of the alloy that had a rubber band, which was used to control the area of the alloy that needed to be exposed to the corrosive environment. The ruthenium was not affected by the corrosion process.

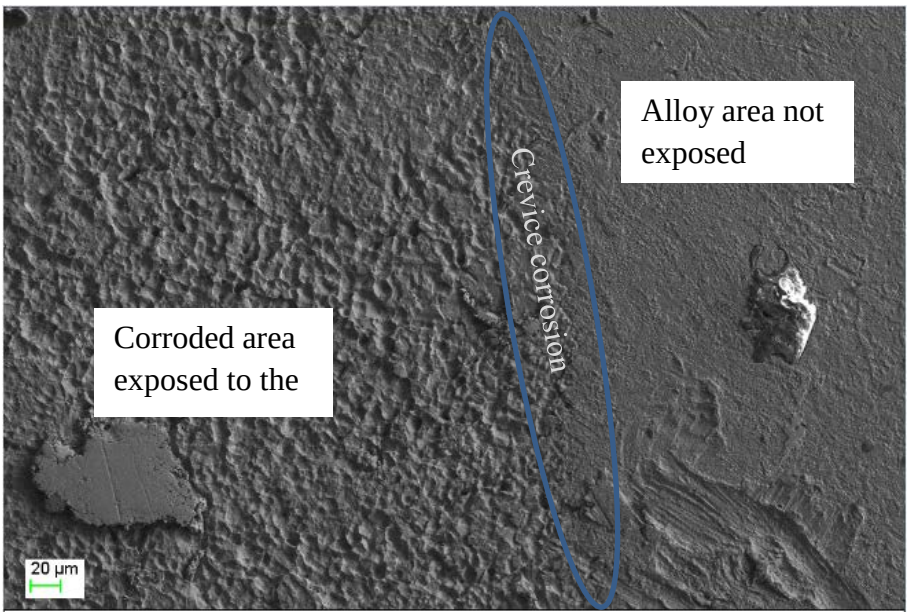


Figure 4.50: SEM image of the corroded SPS-1%Ru alloy after cleaning in acetone using an ultrasonic cleaner.

The SEM micrograph shown in Figure 4.51 (a) and (b) was taken from the corroded area of the SPS-1%Ru alloy in the region of a ruthenium island. The ruthenium in the alloy was barely affected by the corrosion process, and only the copper part of the alloy was corroded. The pits on the alloy were propagating through the grains and did not follow the grain boundaries.

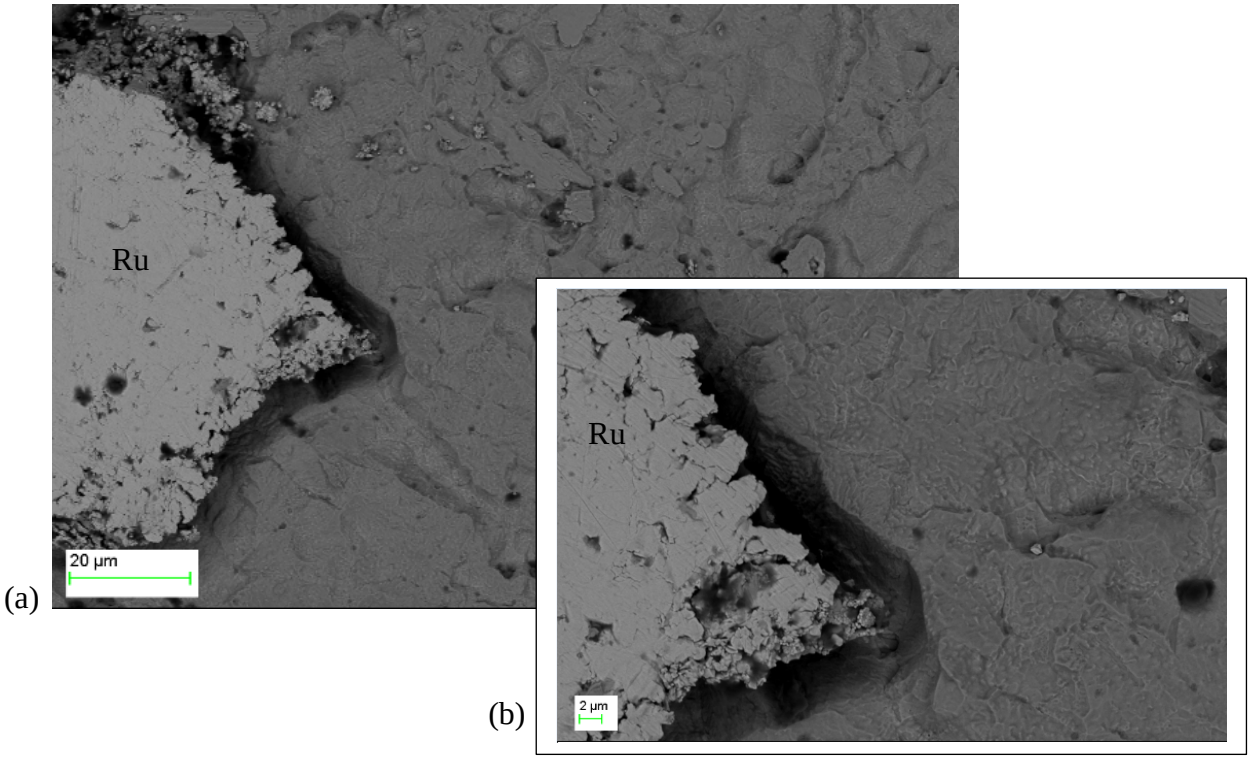


Figure 4.51: SEM micrographs of the corroded SPS-1%Ru alloying at different magnifications showing the area around ruthenium and the pits that had formed on the alloy.

The SEM micrograph shown in Figure 4.52 is of the corroded SPS-2%Ru alloy. This micrograph contains three distinctive regions, the one that the alloy was corroded and not corroded, and the one with corrosion affected band. The ruthenium was not affected by the corrosion process.

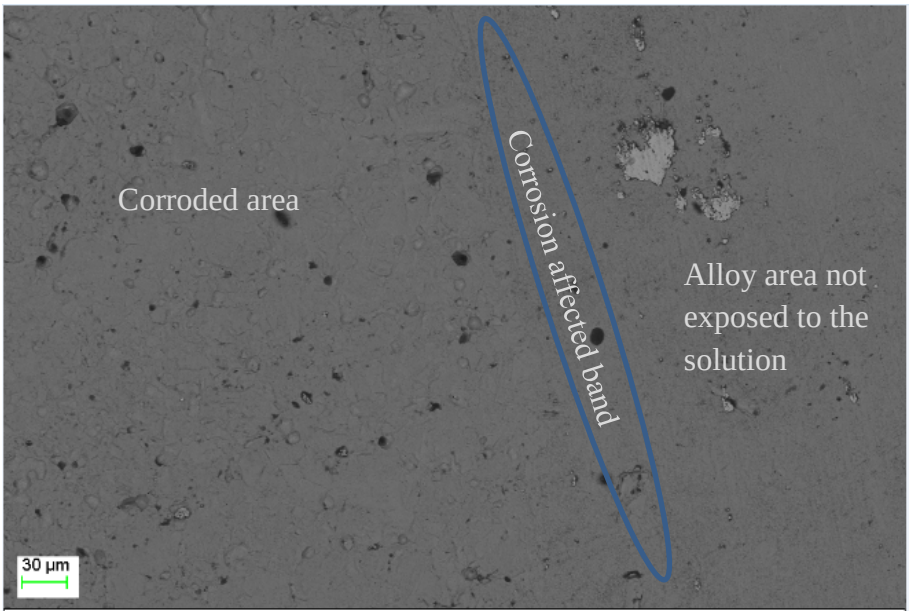


Figure 4.52: SEM image of the corroded SPS-2%Ru alloy after cleaning in acetone using an ultrasonic cleaner.

The micrographs shown in Figure 4.53 were taken by BSD and SE electron detectors in the SEM from the corroded area of the SPS-2%Ru alloy. The alloy had the highest content of ruthenium. The mode of corrosion attack in this alloy was pitting corrosion. The pits were observed to initiate around the grain boundaries. Figure 4.53 (b) and (c) are showing the pits going through the grain boundary in the alloy.

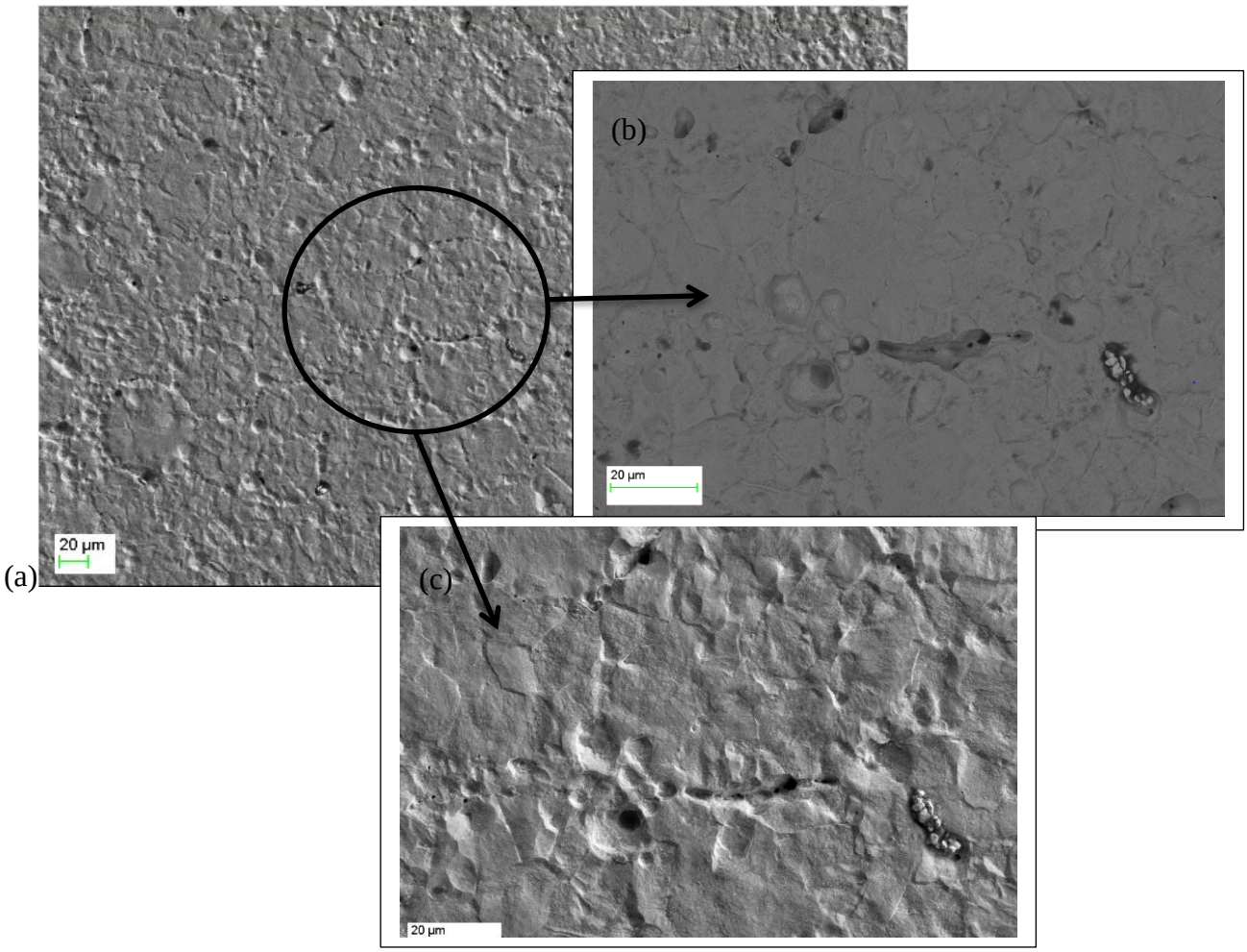


Figure 4.53: BSD and SE SEM micrographs of the SPS-2%Ru alloy showing the pits growing around the grain boundaries.

4.6 Electroplating (Electroplated samples-EPS)

Electroplating has been one of the methods used to add the ruthenium to the copper surface for corrosion resistance improvement. A pulse plating technique was used for the application of the ruthenium coating. In doing so, the current and time of plating were varied to get the optimum coating to expose in the subsequent corrosion tests and analyses. A preliminary study was conducted to choose the best plating time and current. The electroplating process optimisation results are shown first. .

4.6.1 Experimental design

This shows the experimental design process followed, varying the plating current and time. The optimum batch will be the one that produce a ruthenium coating with the best adhesion properties over the entire copper surface, and with minimum impurities on the surface of the coat. The experimental procedure was followed as stated in section 3.6. for the pulse plating method.

Table 4.9: Parameters (current and time) that were changed for the experimental design of the pulse plating method.

Current	Current density (A/cm^2)	Time (min)
1.5 A	0.16	30
		45
		60
2.0 A	0.22	30
		45
		60

4.6.2 Microscopic visual examination Results

The preliminary study of the plating was conducted, following the experimental design, and the results are shown in Figure 4.54. The minor flaws of the coatings, like coating pealing of, substrate not covered, and coatings peeling off, are also pointed out in the micrographs in the figure.

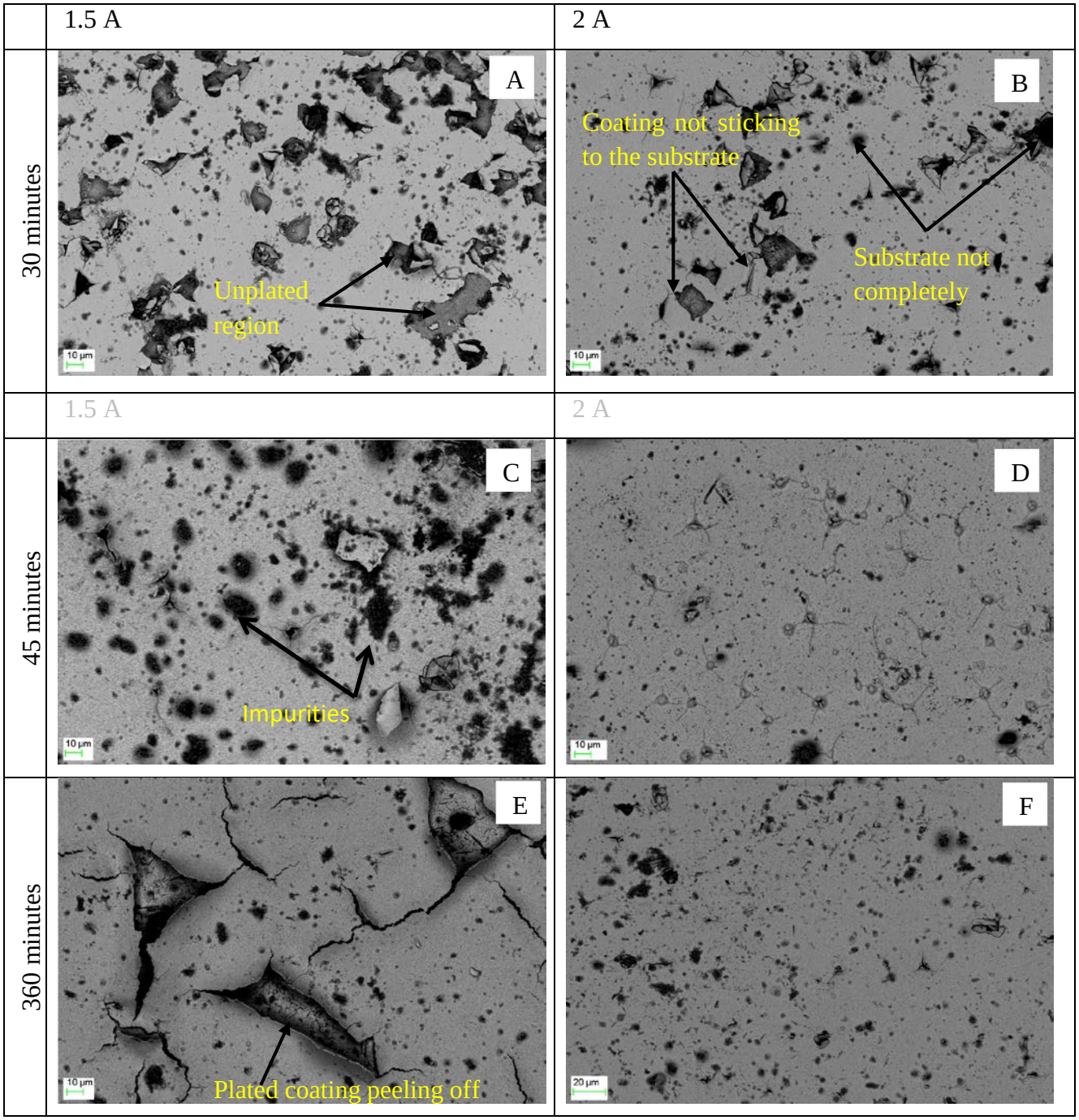


Figure 4.54: SEM micrographs showing the results of the preliminary study conducted to chose the best plating parameters.

From all the microstructural visual examination presented in Figure 4.54, it was concluded that the samples plated at 1.5 A and 2.0 A for the duration of 45 minutes were the once to be used in the following tests. This is because they are the once that produced better coatings compared to all the other electroplated copper samples. There was very little peeling off of the coating and had almost covered the entire surface of the substrate. The ruthenium electroplated copper will be referred to as EP-1.5A for the one created by plating using 1.5 A plating current, and EP-2A for the one formed by using 2 A plating current.

4.6.3 SEM EDS results

Further analyses were made on the chosen set of ruthenium electroplated copper coating. Henceforth it should be noted that the mentioning of electroplated samples referred to are those obtained from 45 min plating time only. The analyses were performed using the SEM, with secondary and back-scattered electron detectors, and also using the EDS.

4.6.3.1 The 1.5 A plated copper sample before and after corrosion in 2M H_2SO_4.

4.6.3.1.1 Surface analyses

The SEM micrographs shown in Figure 4.55 were taken from the 1.5 A ruthenium electroplated copper, comparing the surface appearance before and after corrosion in 2M sulphuric acid. The different surfaces are also accompanied by the EDS spectrum scanned from each respective surface area.

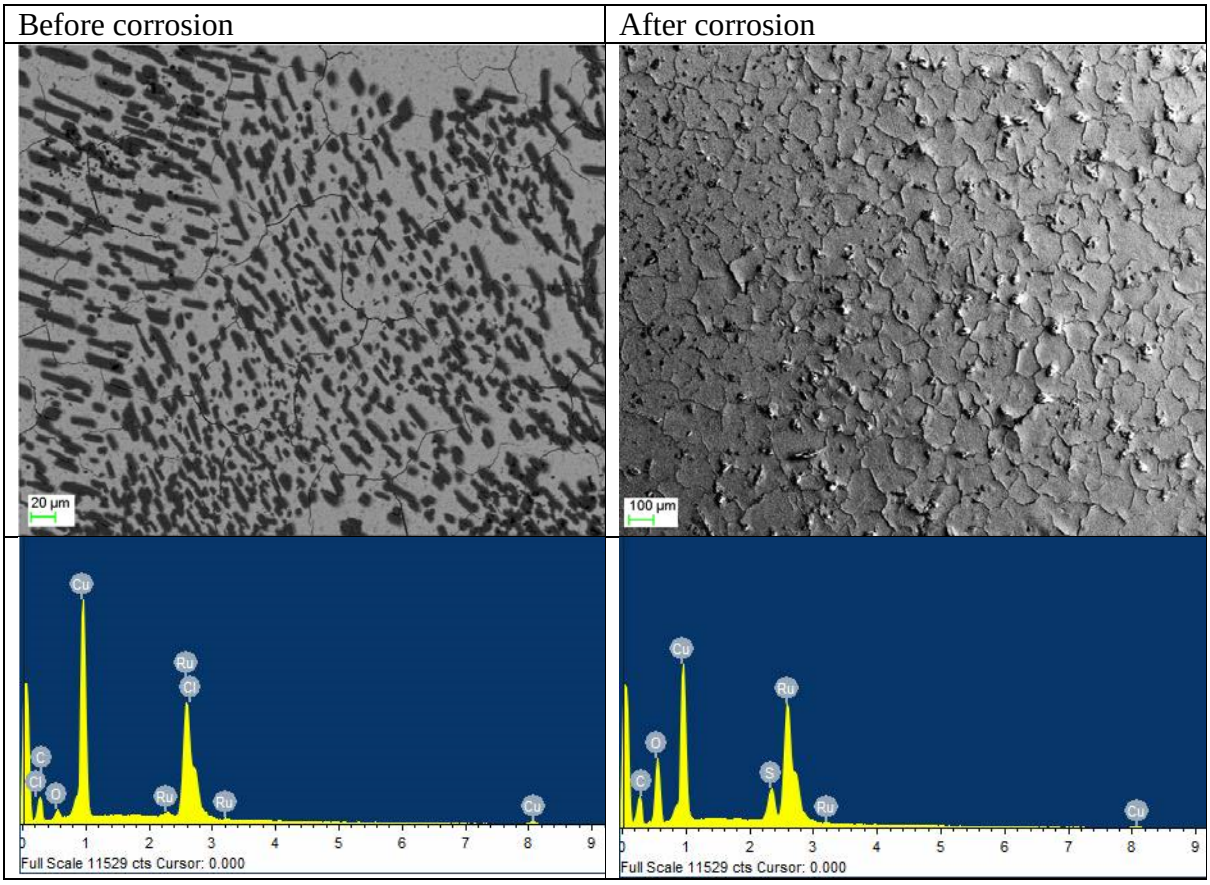


Figure 4.55: SEM micrographs of 1.5 A plated copper, comparing the surface appearance before and after corrosion and their respective EDS spectrum scanned from each surface.

To further study the electroplated coating surface after corrosion, an image in Figure 4.56 was obtained under high magnification. This was done in order to show the detailed changes in the surface area. The light grey area of the image is the ruthenium coating, and the dark grey area is ruthenium oxide that formed during corrosion process. There also is an area in this image

that shows some wrinkling of the surface coating which is shaped like cracks. An EDS analysis was done on the wrinkled area, and the results of this analysis is shown by the EDS spectrum in Figure 4.56(b) with elemental composition.

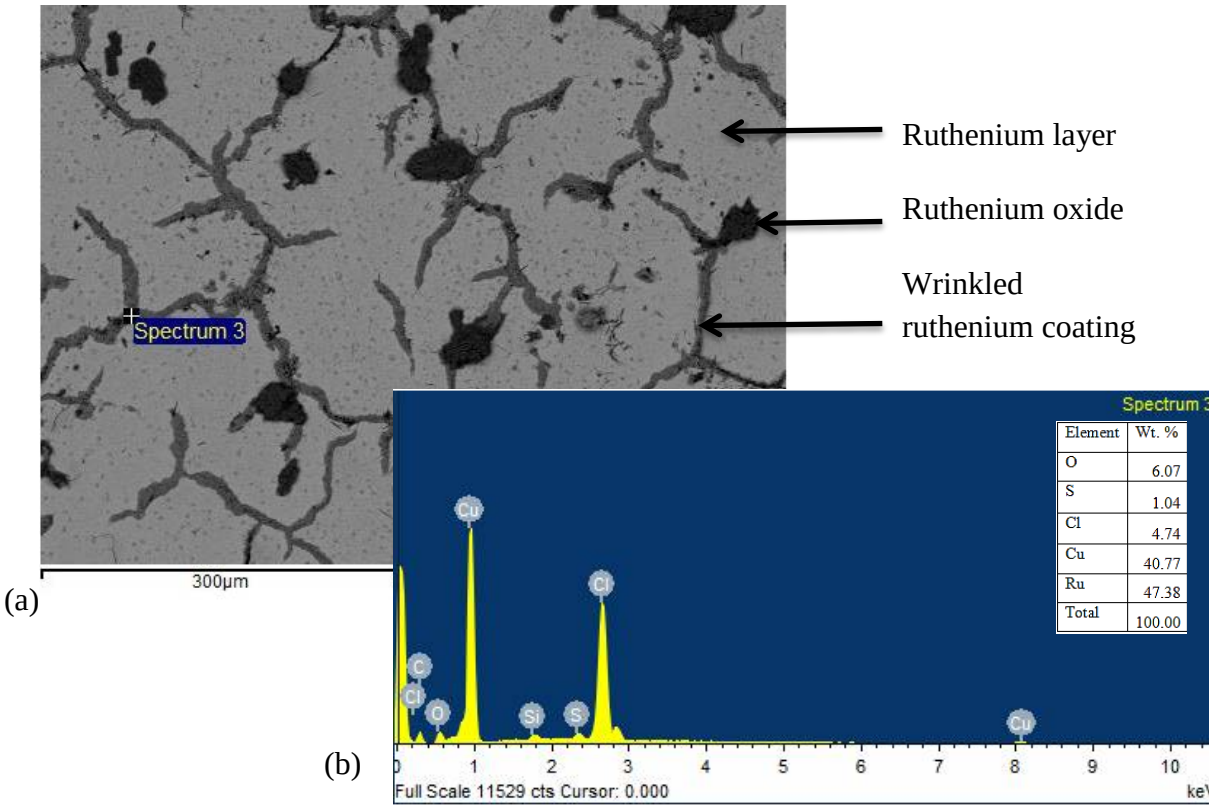


Figure 4.56: SEM micrograph showing the corroded EP-1.5 A ruthenium electroplated copper, and (b) is the results of EDS analysis made on the crack of the coating after corrosion.

4.6.3.1.2 Cross section analyses

The cross section of the ruthenium electroplated copper, EP-1.5A, was ground and polished then analysed using SEM. The result of the analysis is shown in Figure 4.57 (a) and EDS spectrum in (b). The EDS analysis was taken, and elemental composition of Ru and Cu detected on the coating were 40.8% and 42.1% respectively.

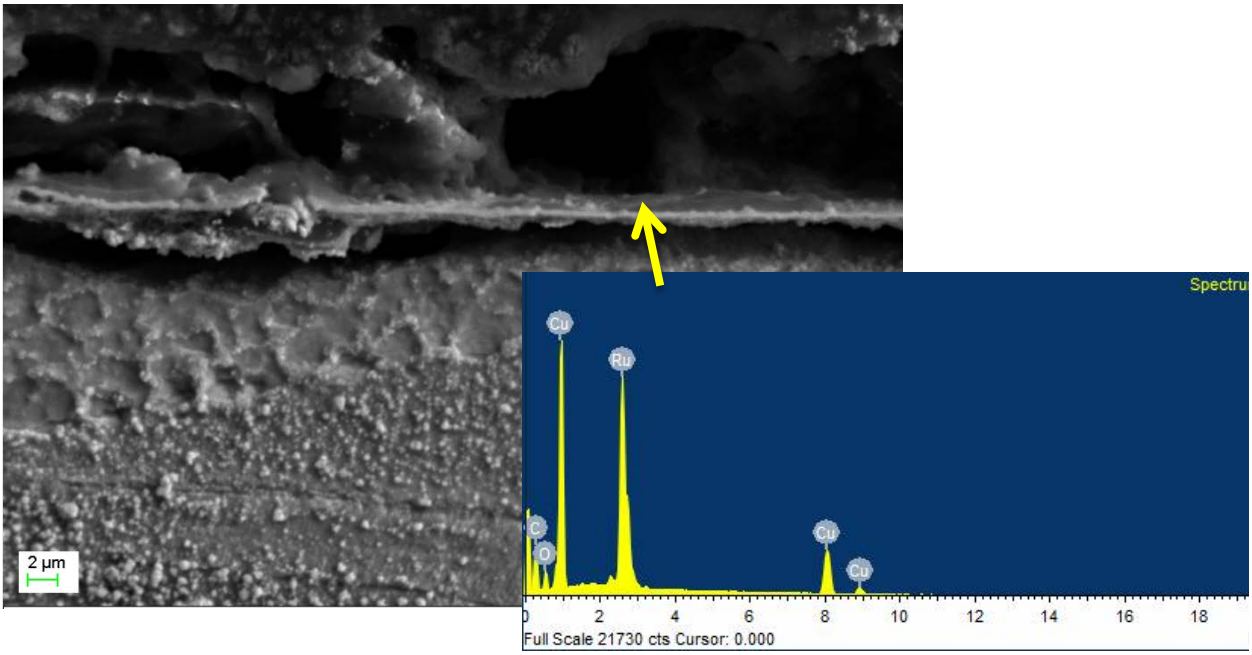


Figure 4.57: The cross section micrograph of 1.5 A plated copper and the EDS spectrum scanned on the coating.

4.6.3.2 The 2 A plated copper sample before and after corrosion in 2M H_2SO_4.

4.6.3.2.1 Surface analyses

An EDS analysis was performed on the surface of EP-2A copper, before and after corrosion in 2M sulphuric acid, is shown in Figure 4.58. The results of this analysis are shown by the respective EDS spectra. The corroded sample had cracks and secondary phase products formed on its surface. It also contained sulphur, as detected by EDS.

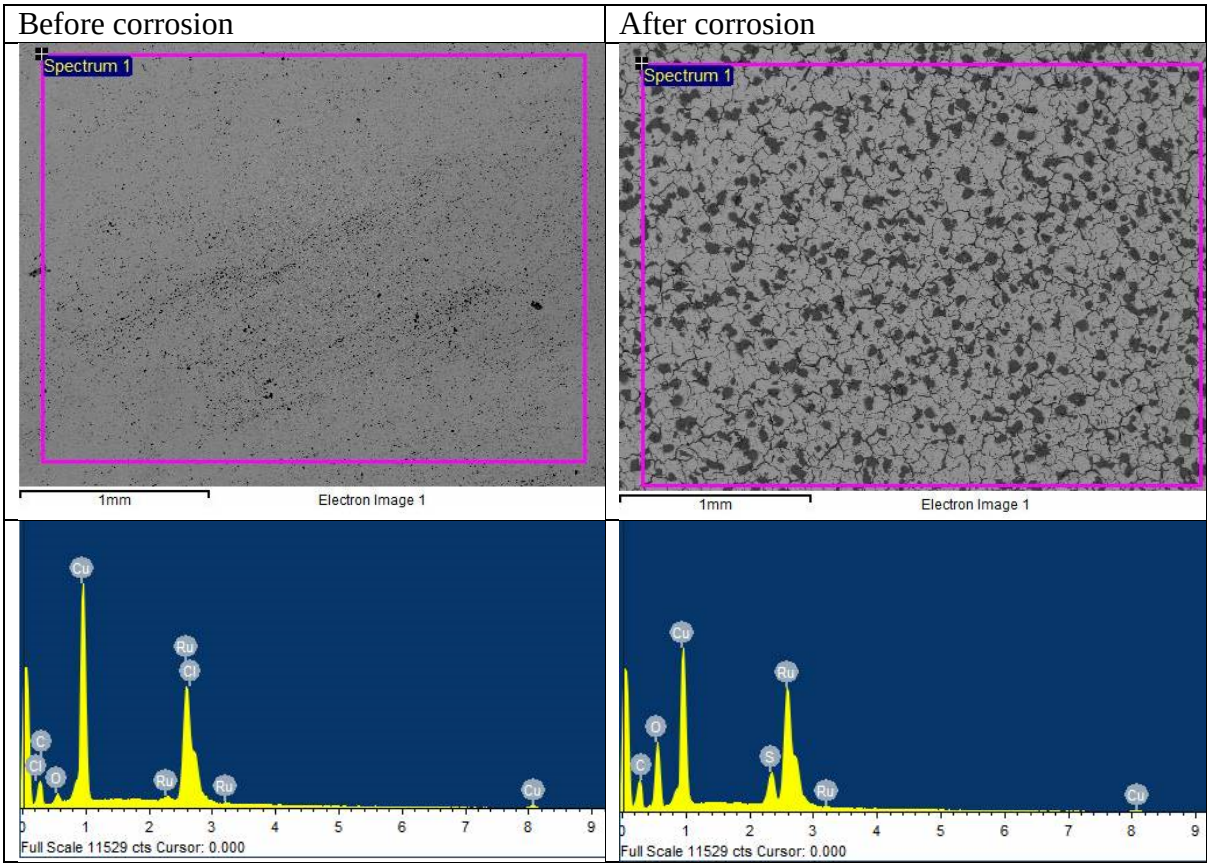


Figure 4.58: The 2.0 A plated copper sample, before and after corrosion in 2M sulphuric acid, with their EDS spectrum scanned on the surface of the sample.

The corroded EP-2A copper was further studied under high magnification to show the detailed changes in the surface area. The surface in Figure 4.59 is showing different areas. Some had cracks, some with precipitates, and the rest was the ruthenium layer coated. All these areas were scanned to get the EDS spectrum with elemental compositions of those areas. The EDS results are also shown in Figure 4.59 (a), (b), and (c). The light grey area of the image is the ruthenium coating, and the dark grey area is ruthenium oxide that formed during corrosion process.

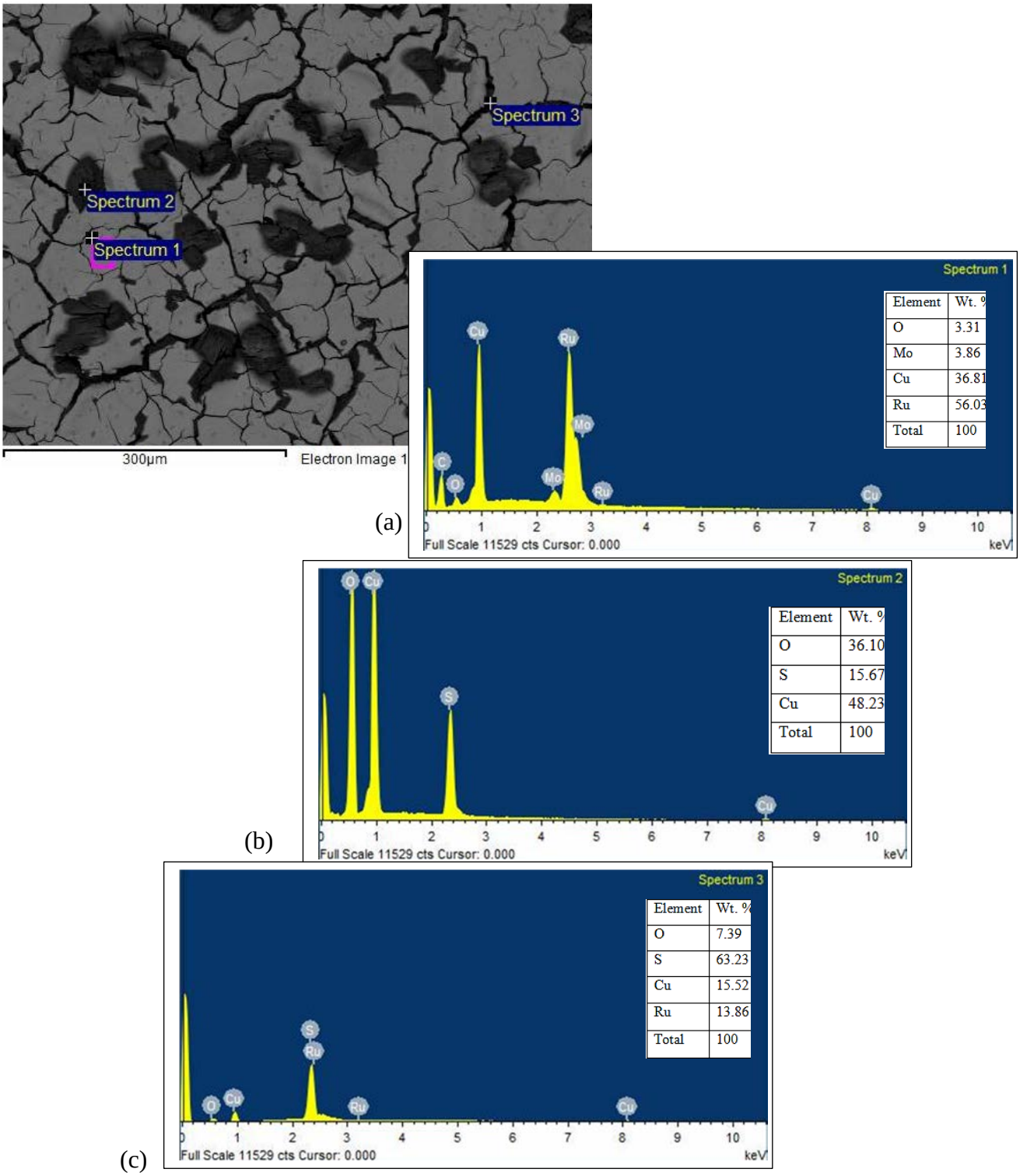


Figure 4.59: SEM micrograph of the corroded EP-2A copper sample showing different phases which were analyzed by EDS producing EDS spectrum in a, b, and c.

4.6.3.2.2 Cross section analyses

The SEM image of the cross-section of the EP-2A copper is shown in Figure 4.60. To prepare the sample, it was ground, polished, and electro-etched. Alongside the image, there is an EDS spectrum that was generated by analysing the area of the coating indicated. The EDS detected 45.9% Ru and 49.2% Cu to be the composition of the coat. The layer of the coating was too thin to analyze just the coating, but also some of the neighbouring copper from the substrate. An estimation of the coating thickness was approximated to be 1.5 µm.

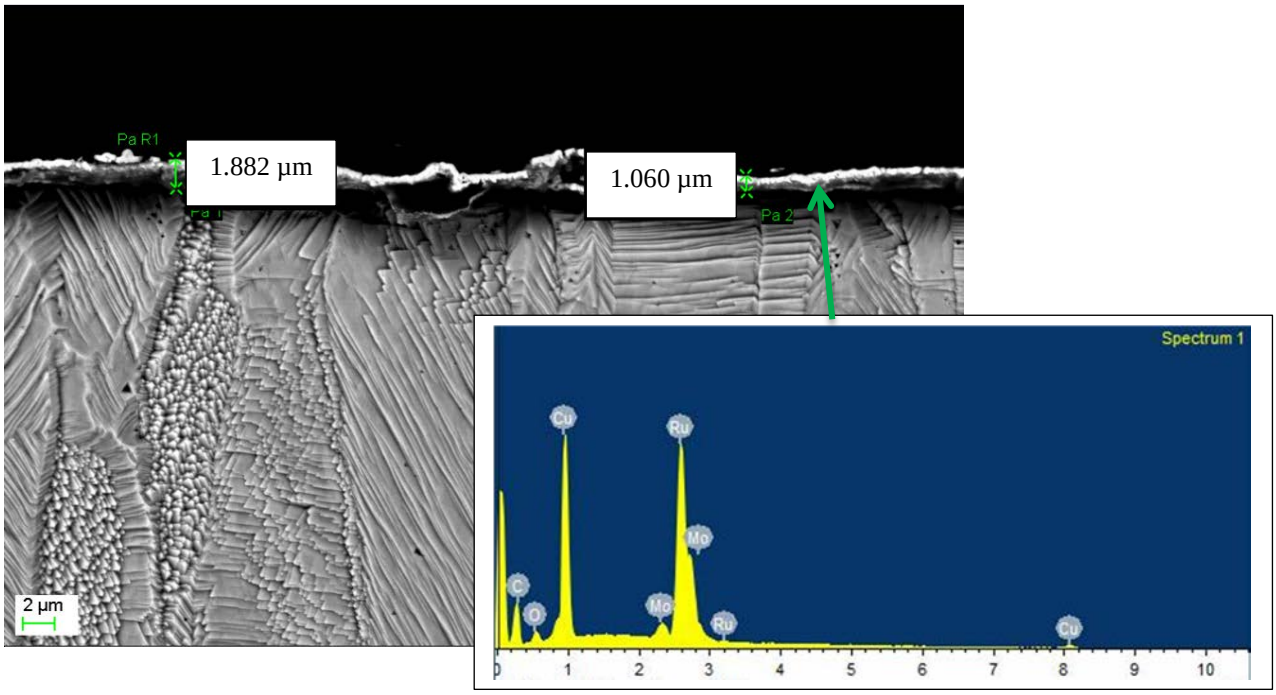


Figure 4.60: SEM image taken by BSD electron detector showing cross sections of the EP-2A ruthenium plated copper.

4.6.4 Hardness results

Figure 4.62 is showing the average micro Vickers hardness measured for all the ruthenium electroplated copper and comparing it to the as-received copper. A 5 gf load was used for the hardness measurements. It should be noted that there was an anvil effect since the coating layer was too thin. The hardness measured was almost that of the substrate copper. The error bars are also indicated in each bar.

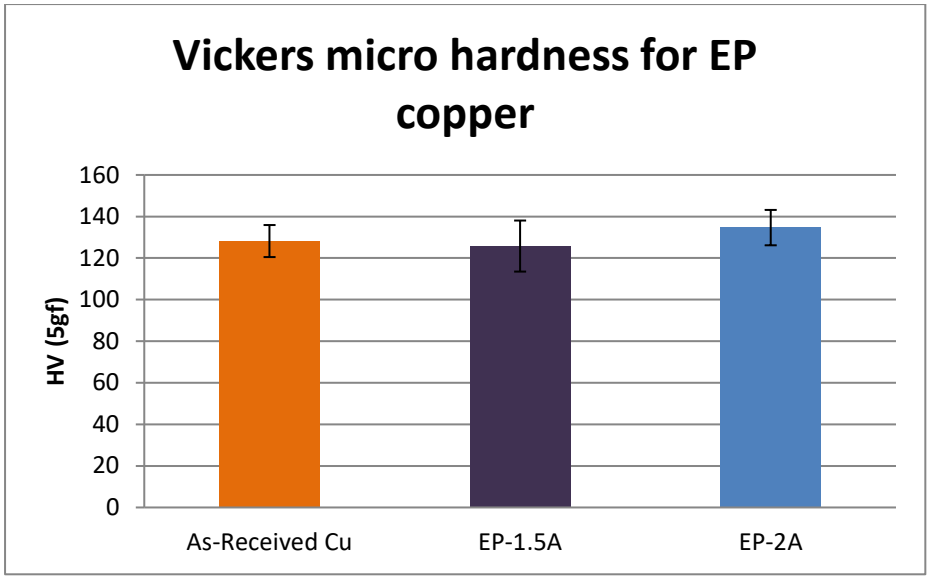


Figure 4.61: Average Vickers hardness for all ruthenium electroplated copper samples compared to as-received Cu.

4.6.5 Electrochemical results

The section shows the corrosion characteristics of the ruthenium electroplated copper . This was investigated in 2M sulphuric acid environment at 45 and 65°C. The samples were exposed in this environment for the duration of 45 min. The results of the experiment were recorded as potentiodynamic curves, which were used to measure the corrosion current density and potential. Each experiment was repeated thrice for good reproducibility. The results were also compared to the as-received copper to investigate the corrosion improvement that could have been achieved by electroplating copper. The addition of ruthenium into the copper surface was aimed to decrease the corrosion current density.

Figure 4.63 is showing the comparison of linear polarisation potentiodynamic curves of the ruthenium electroplated copper samples and as-received copper in 2M sulphuric acid environment at 45°C.

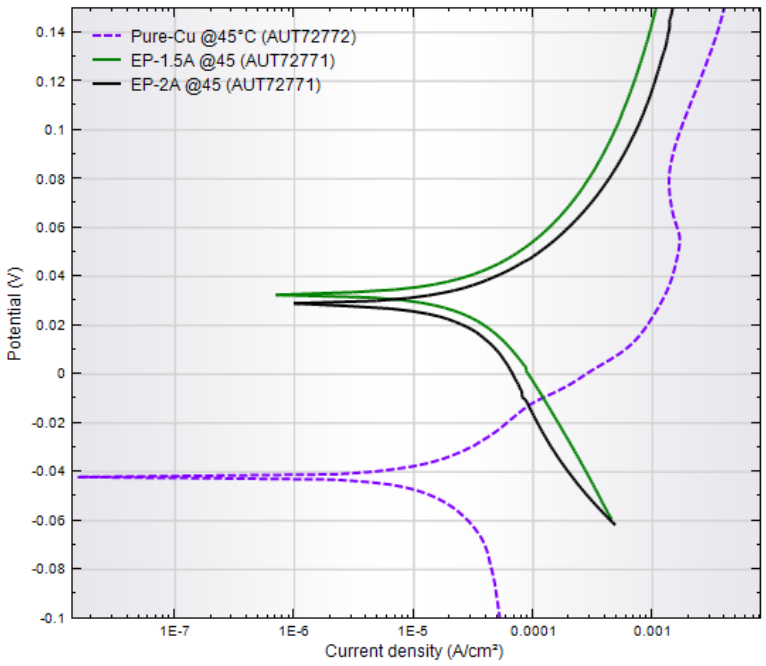


Figure 4.62: Potentiodynamic polarisation curves of all EP copper samples and as-received copper exposed to 2M H_2SO_4 at 45°C.

Linear polarisation curves shown in Figure 4.64 is the corrosion response of all ruthenium electroplated copper samples and as-received copper in 2M sulphuric acid environment at 65°C.

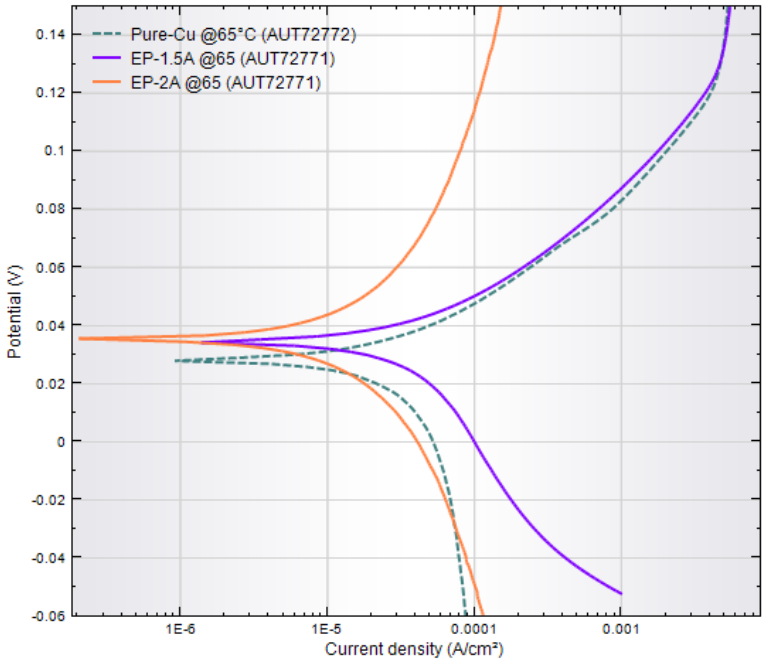


Figure 4.63: Potentiodynamic polarisation curves of all EP copper samples and as-received copper exposed to 2M H_2SO_4 at 65°C.

4.6.5.1 Corrosion results

The section will show the corrosion rate calculations for the ruthenium electroplated copper using the polarisation resistance technique. The values needed for calculation were extracted from the graphs. Table 4.10 and 4.11 are showing the corrosion rate calculations, and Figure 4.65 is a graphical presentation of the corrosion rates calculated. The calculations were done for all the temperatures.

Table 4.10: Calculated corrosion rates for the ruthenium electroplated and as-received copper at 45°C.

	Icorr (A)	Icorr (µA)	icorr (µA/cm^2)	CR (mmpy)
As-received Cu	9.63×10^{-6}	9.63	19.15	0.22
EP-1.5 A	7.94×10^{-6}	7.94	15.80	0.18
EP-2.0 A	9.77×10^{-6}	9.77	19.43	0.23

Table 4.11: Calculated corrosion rates for the ruthenium electroplated and as-received copper at 65°C.

	Icorr (A)	Icorr (µA)	icorr (µA/cm^2)	CR (mmpy)
As-received Cu	3.34×10^{-5}	33.47	66.58	0.77
EP-1.5 A	1.03×10^{-5}	10.32	20.53	0.24
EP-2.0 A	2.75×10^{-6}	2.75	5.46	0.06

Figure 4.65 is the graphical presentation of effect of plating current on the resultant corrosion rate of the ruthenium plated copper.

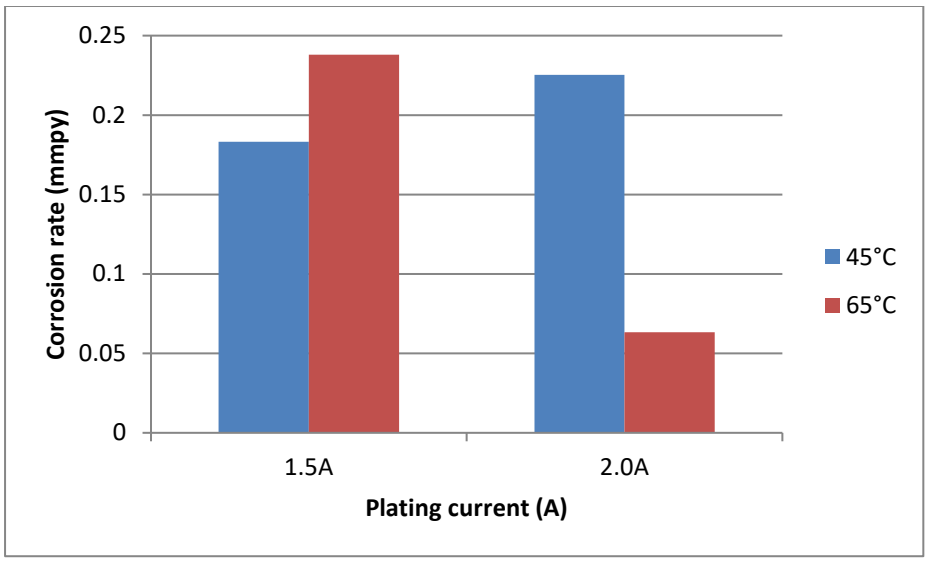


Figure 4.64: Corrosion rate as a function of plating current.

4.7 EPP (Electroplated powders)

This section will show another method that was explored to add ruthenium to copper surface to improve its corrosion resistance in sulphuric acid environment. The method used was electroplating of copper powder. This is similar to the pulse electroplating process that was done in section 4.6. Hence the plating parameters used (plating current and time) were the same as those approved in the previous sections, which were 45 min for both 1.5 and 2 A plating current. The corrosion current density for the powders is however different from the copper slabs used in section 4.6. The coated powders will be used for coating using high oxygen fuel spray, and for creating an alloy using spark plasma sintering method..

Similarly, a preliminary study will be done to find the optimum method to be used for plating which must result in more ruthenium plated on the copper powders. The choice is narrowed down to either using 1.5 A or 2 A plating current. The microscopic visual examinations were also conducted to reach to a conclusion.

4.7.1 Ruthenium powder

The micrograph in Figure 4.66 is showing the cross section of the copper powder. The powder was mixed with polyfast resin and mounted, and then it was ground, polished and etched. This image will be used for reference to see the difference that occurs after electroplating using ruthenium solution. It is expected that after electroplating there will be ruthenium layer that will have formed around the copper powder.

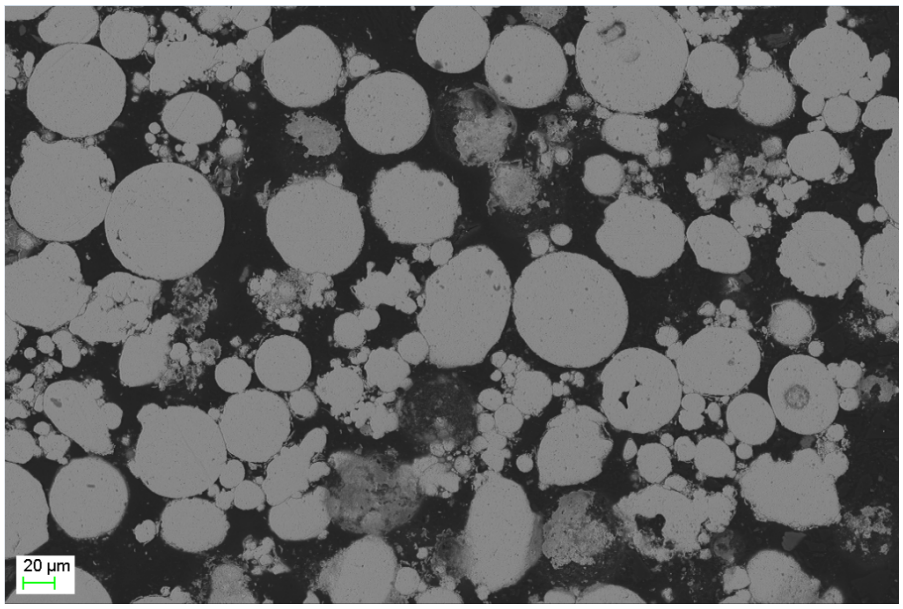


Figure 4.65: SEM micrograph of the cross-section of copper powder

4.7.1.1 Electroplating powders using 1.5 A plating current

The electroplating experiment was conducted, and the electroplated powders were analysed and is shown in Figure 4.67. The EDS analysis made showed the results in a form of a spectrum. From the elemental composition, there was no ruthenium detected.

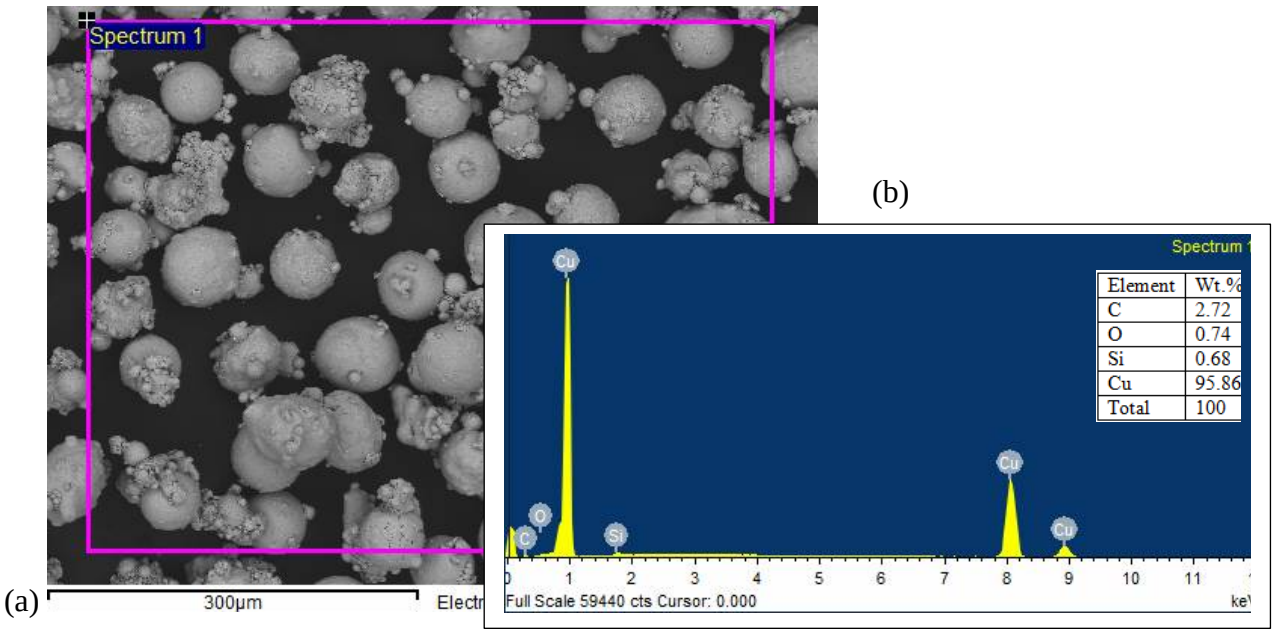
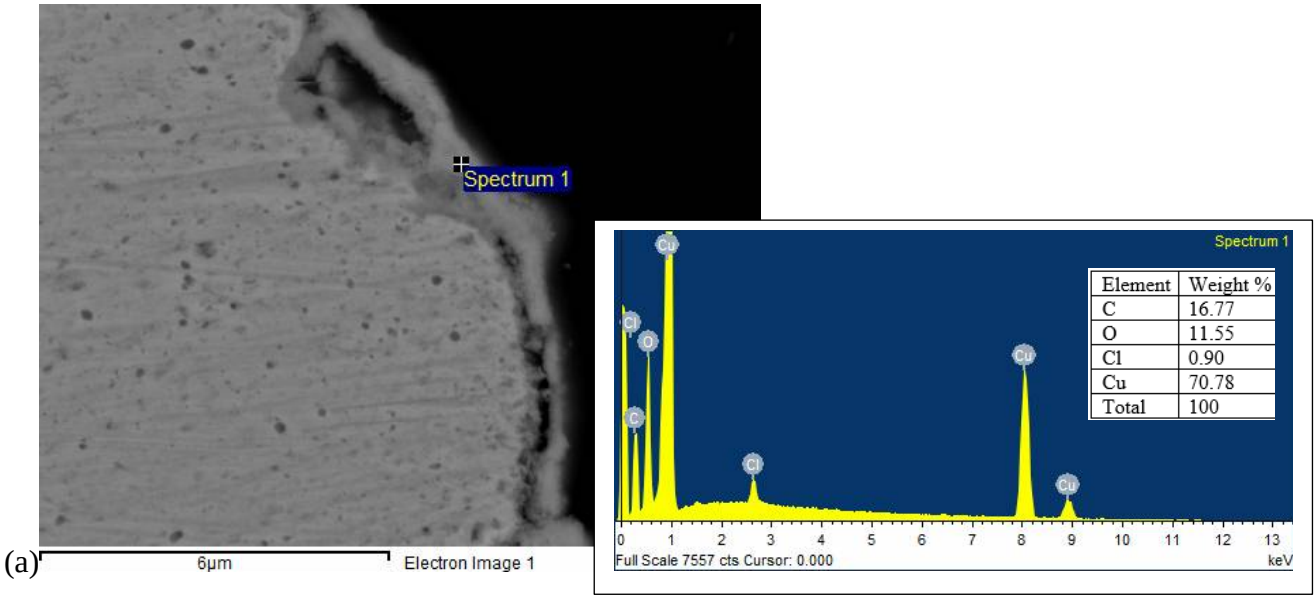


Figure 4.66: SEM micrograph of the electroplated copper powder using 1.5 A plating current, and (b) is the EDS spectrum obtained after the EDS analysis over the selected area in (a).

Further study was conducted on a single powder grains for a clearer analysis. This was to show the coating film that had formed after electroplating, and analysis were made on this film. The results of this analysis showed that the film that had formed around the powder had no ruthenium detected in it. It is therefore assumed that the 1.5 a plating current plated very little ruthenium which was hardly detected by the EDS analysis technique.



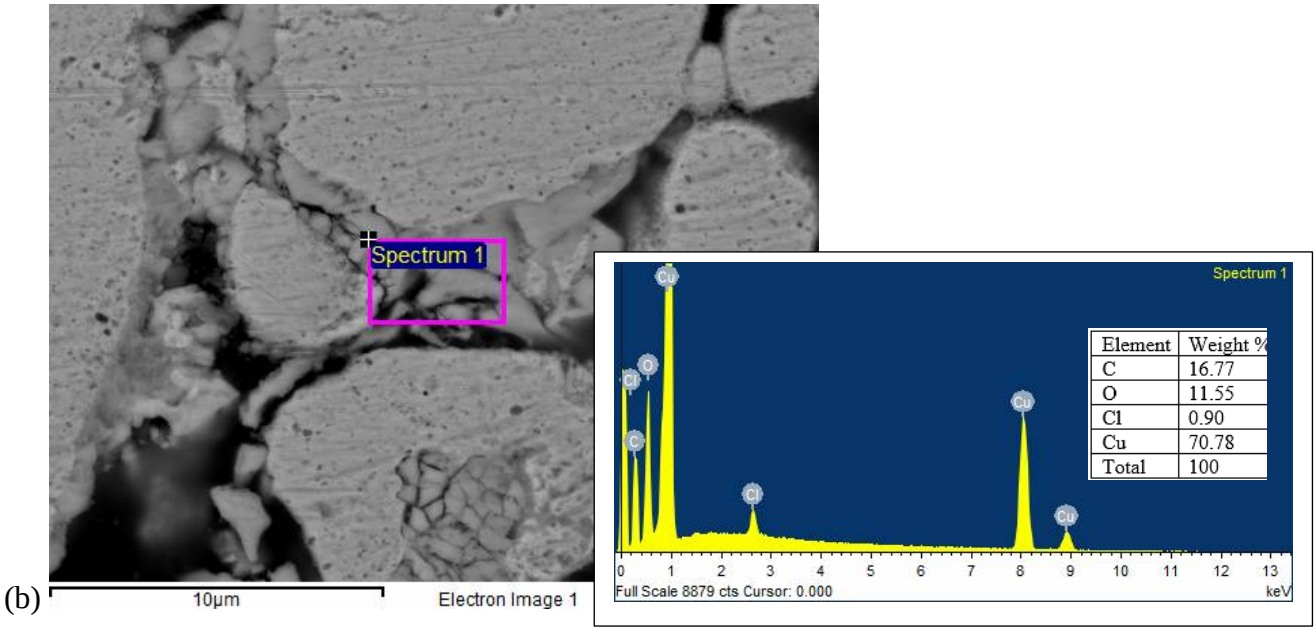


Figure 4.67: SEM micrographs showing the film around the cross section of the plated copper powder which was analyzed and the results are shown by the EDS spectrum alongside the micrograph.

4.7.1.2 Electroplating powders using 2 A plating current

Some of the powders were electroplated using 2 A plating current and the results of this analysis are shown in Figure 4.68. An EDS analysis was made over a range of powder grains, and the results of this analysis are shown by the EDS spectrum in Figure 4.68 (b). The elemental compositions shown in the EDS spectrum had shown that there was about 0.66 weight percent ruthenium detected from the powders.

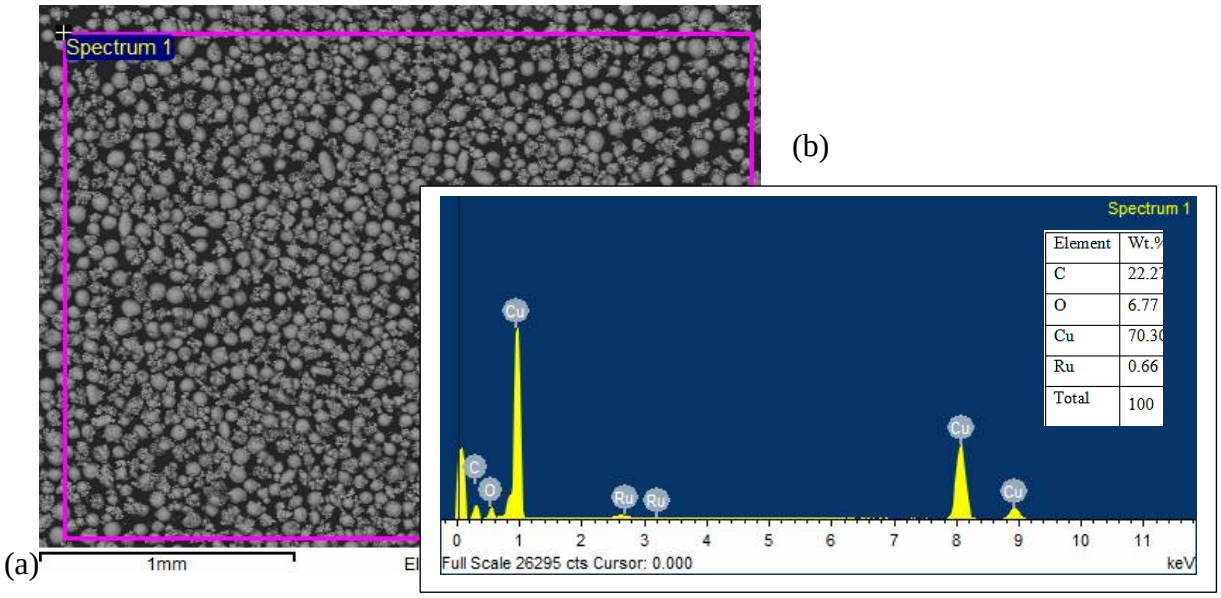
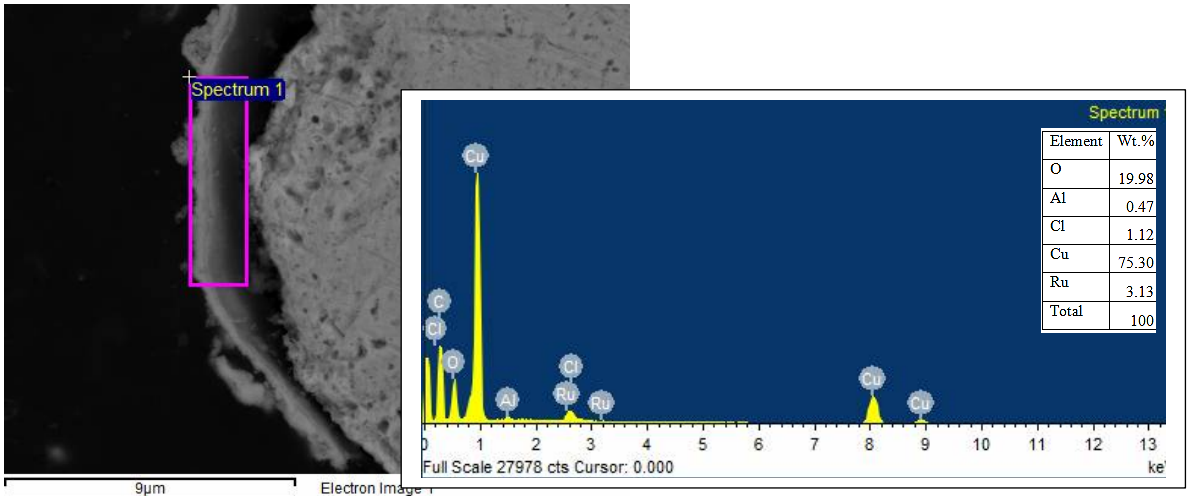


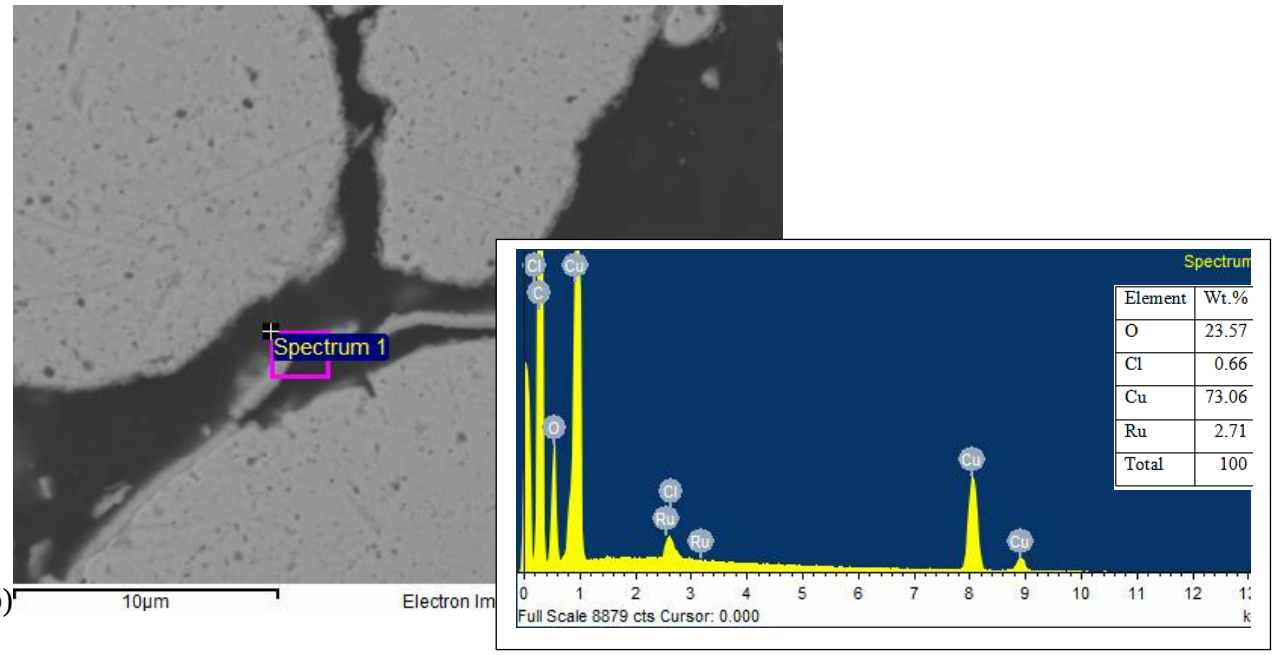
Figure 4.68: SEM micrograph of the electroplated copper powder using 2 A plating current, and (b) is the EDS spectrum obtained after the EDS analysis over the selected area in (a).

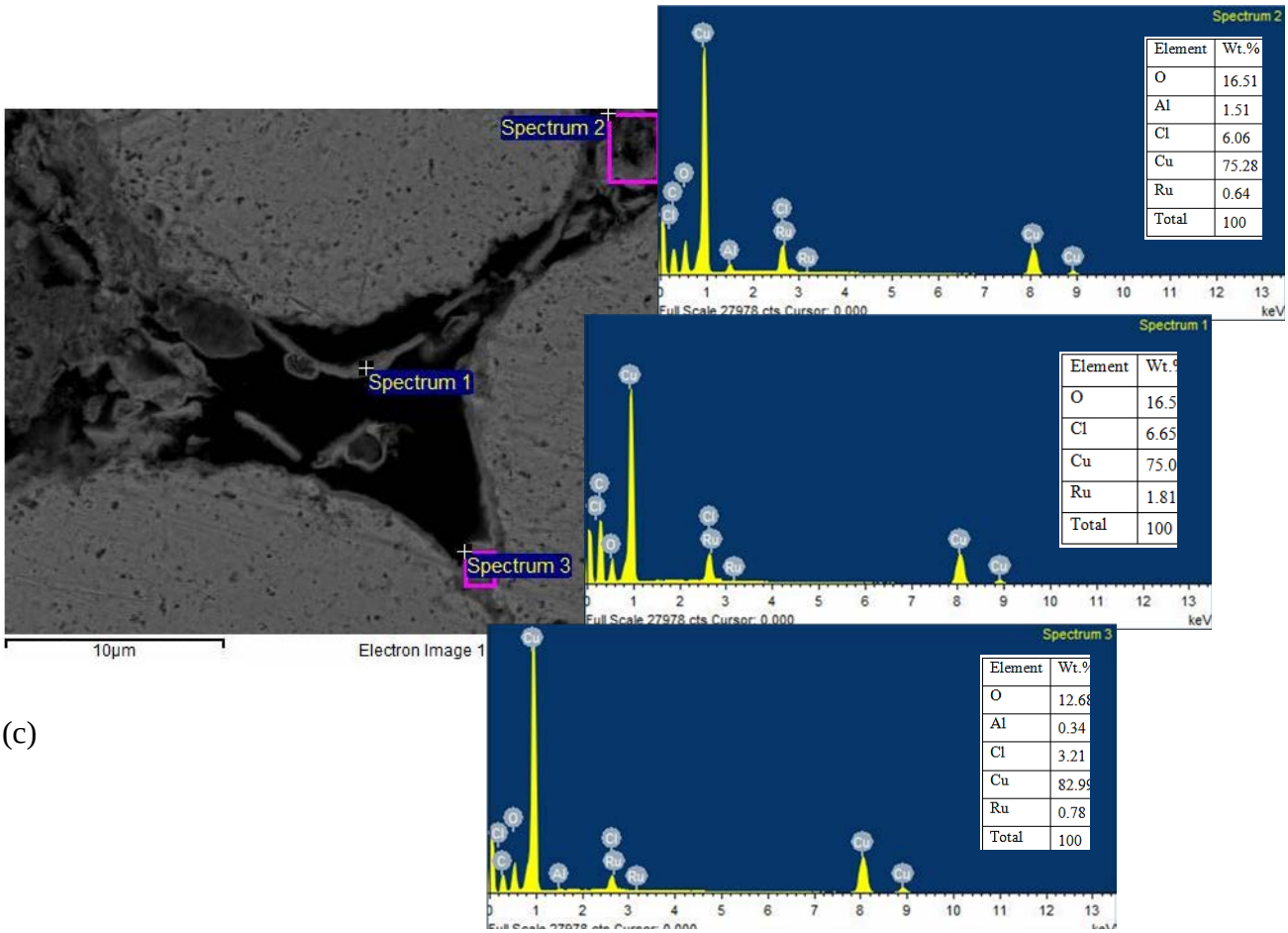
The electroplated powder was mounted, grinded, polished and etched to reveal the powder ruthenium coating. EDS analysis were made on the plated film of different copper powder grains at different positions and the results are shown in Figure 4.70 (a) to (c). A lot of the powder films were analyzed to validate the presence of ruthenium in these films. In all the analyses made, there was a certain amount of ruthenium that was detected.

(a)



(b)





(c)

Figure 4.69: SEM micrographs showing the film around the cross section of the plated copper powder which was analyzed and the results are shown by the respective EDS spectrum alongside the micrograph.

4.8 EPP-HVOF

The 2 A electroplated powder from the previous section 4.7 was used to coat the copper substrate using HVOF coating method. In this section, the coatings from this process will be referred to as EPP-HVOF. The section will also focus on the ruthenium distribution in the coating, and the corrosion characteristics of the coated copper.

4.8.1 SEM EDS results

The scanning electron microscope was used to analyse the cross section of the EPP-HVOF coated copper. The average coating thickness of this sample was measured to be 300 µm. The chemical composition of this coating was measured by the EDS spectrum. Figure 4.71 is showing the results to this analysis. The analyses show about 0.6 weight percent ruthenium detected, and also there were some impurities associated with the coating. The light grey spots

on the coating were not ruthenium as observed in previous sections, but some impurity. There was cobalt, chromium and tungsten, which are assumed to have entered the coat during the HVOF coating process.

.

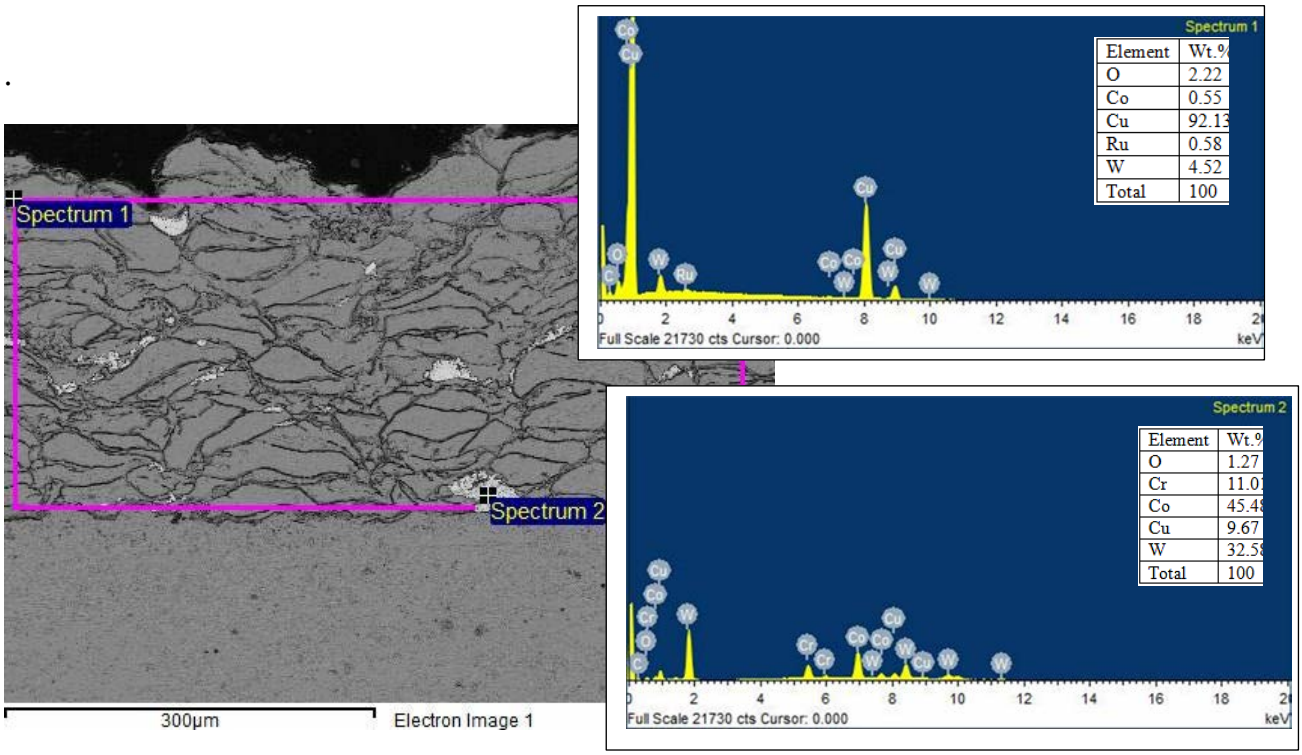


Figure 4.70: SEM micrograph showing the cross section of the EPP-HVOF coated copper, and the EDS spectrum of the analysis made from the selected areas in the micrograph.

4.8.3 Hardness results

The bar graph shown in Figure 4.72 is the Vickers micro hardness profile of the EPP-HVOF coated copper comparing it to that of as-received copper. The hardness measurements were done using 100 gf indentation loads.

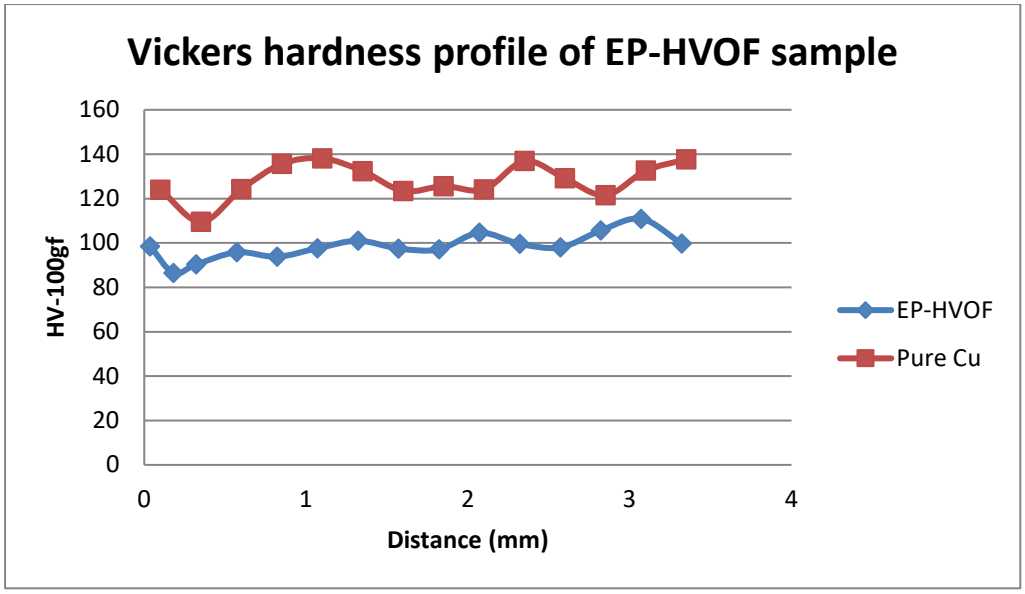


Figure 4.71: Vickers hardness profile for the EPP-HVOF coated copper.

4.8.4 Electrochemical results

To evaluate the effectiveness of the coating in reducing the corrosion rate, the EPP-HVOF corrosion characteristics had to be determined. An experiment was conducted in 2M sulphuric acid at 45 and 65°C for duration of 45 minutes. Figure 4.73 shows the results of the experiment as potentiodynamic polarisation curves for EPP-HVOF and comparing them to the as-received copper which was exposed to the same conditions. The coated copper is represented by solid lines and as-received copper by dotted lines.

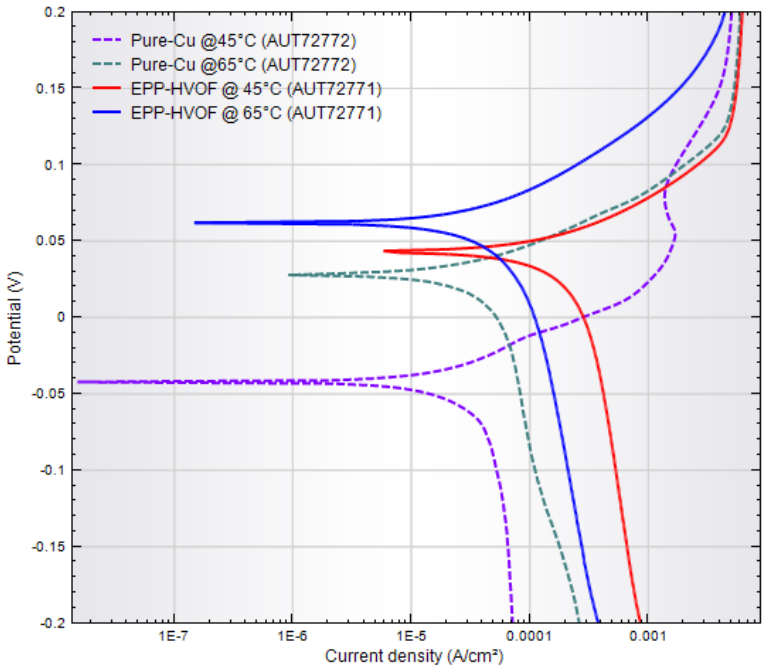


Figure 4.72: Potentiodynamic polarisation curves of EPP-HVOF coated copper and as-received copper exposed to 2M H_2SO_4 at 45 and 65°C.

4.8.4.1 Corrosion results

The section shows the corrosion rates calculation for all the EPP-HVOF copper coatings and the as-received copper. The corrosion potential, corrosion current and polarisation resistance values used for the corrosion calculations were extracted from the polarisation curves.

Table 4.12: Calculated corrosion rates of EPP-HVOF coated copper compared to as-received copper at 45 and 65°C in 2M sulphuric acid.

Sample	Temp	Icorr (A)	Icorr (µA)	icorr (µA/cm^2)	CR (mmpy)
As-received Cu	45°C	9.62×10^{-6}	9.62	19.15	0.22
EP-HVOF		3.3×10^{-5}	33.01	65.67	0.76
As-received Cu	65°C	3.34×10^{-5}	33.47	66.58	0.77
EP-HVOF		9.67×10^{-6}	9.67	19.24	0.22

A graphical presentation of the corrosion rates of as-received copper compared to EPP-HVOF coated copper is showed in Figure 4.74.

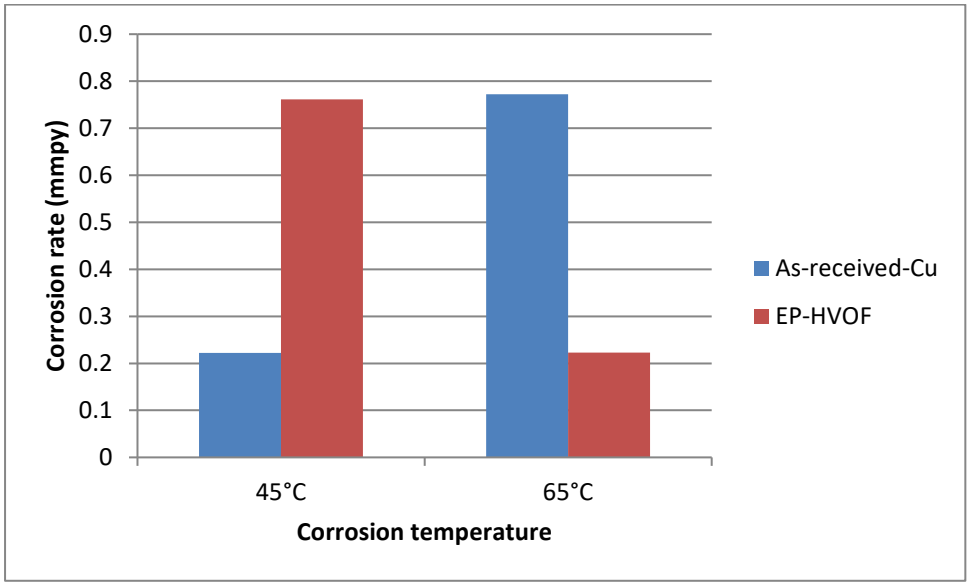


Figure 4.73: Comparison of the corrosion rates between as-received copper and EPP-HVOF coated copper at 45 and 65°C.

4.9 EP-SPS

The 2 A electroplated powder was used to make an alloy using spark plasma sintering process. In this section, the resultant alloy will be referred to as EP-SPS. The focus will be on ruthenium distribution in the alloy and corrosion improvement achieved when compared to as-received copper.

4.9.1 SEM EDS results

The scanning electron microscope was used in analysing the property of the EP-SPS copper alloy. The chemical composition of the alloy was analysed, and the distribution of the elements detected on the alloy was investigated. Prior to the analysis, the alloy was mounted, grinded, polished and etched. Figure 4.75 is showing the SEM micrographs taken by BSD and SE electron detectors and the EDS spectrums of the denoted areas in the magnified micrograph. The cobalt, tungsten, chromium, and nickel were impurity elements detected in the alloy from the EDS analysis. The impurities are assumed to have entered the alloy through contaminated equipment used to create the alloy.

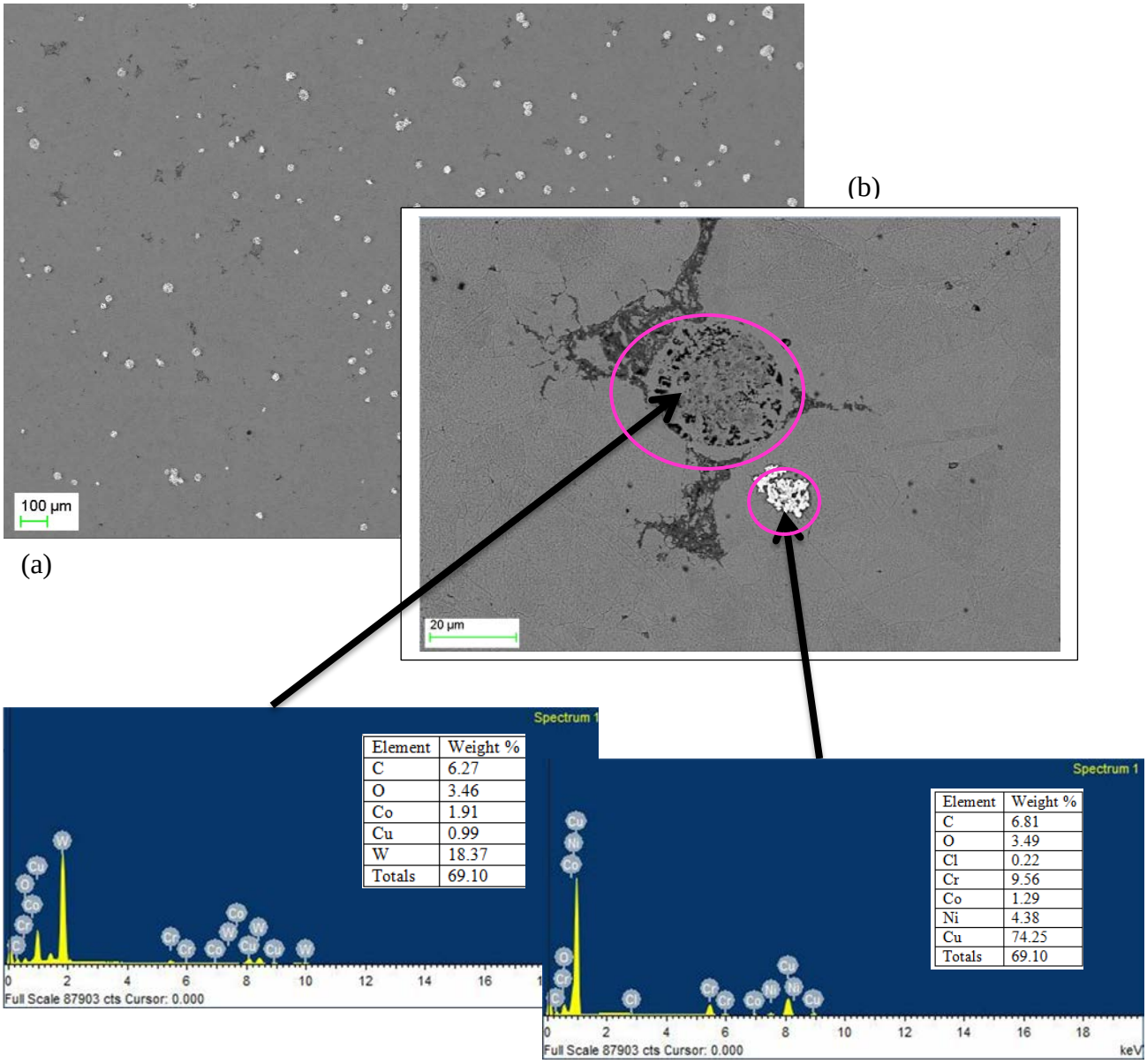


Figure 4.74: SEM micrograph of the EP-SPS alloy, (b) is the magnified alloy micrograph showing the EDS spectrum of particular futures of interest in the alloy.

4.9.3 Average hardness results

The Vickers micro hardness of the alloy was measured using 100gf indentation load. The results are compared to the average hardness for as-received copper as shown in Figure 4.76.

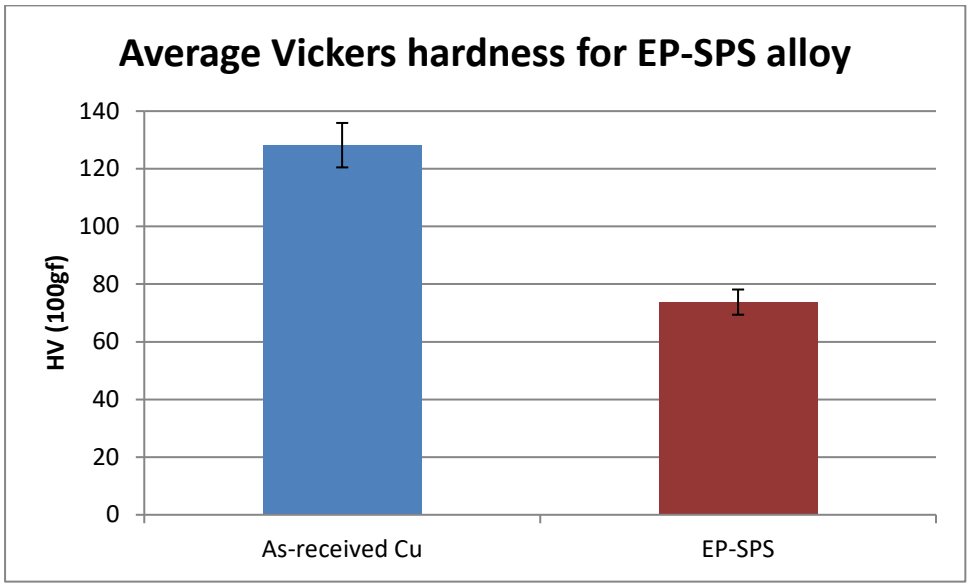


Figure 4.75: Average Vickers hardness for EP-SPS alloy compared to as-received copper

4.9.4 Electrochemical results

Figure 4.78 shows the potentiodynamic polarisation curves for EP-SPS alloy exposed to 2M sulphuric acid for 45 minutes at 45 and 65°C. The curves were compared to those received for as-received copper.

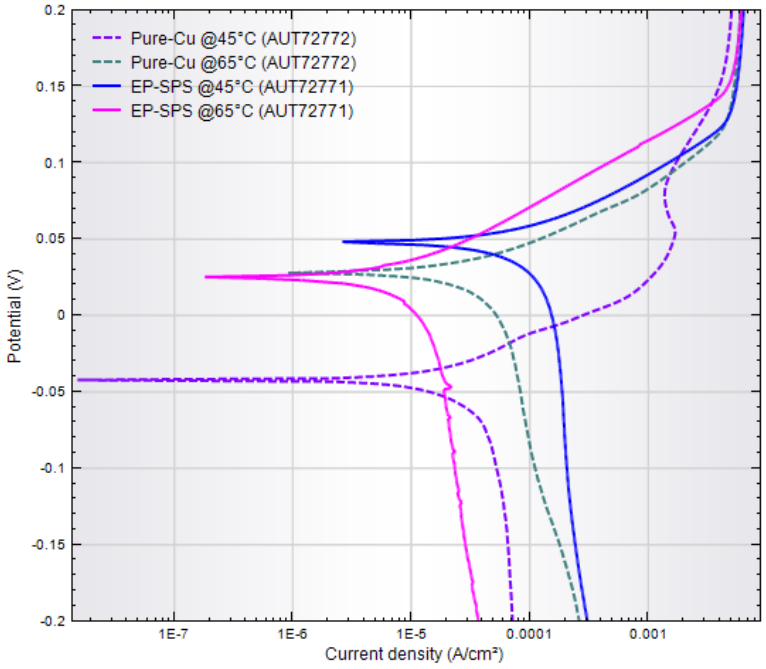


Figure 4.76: Polarisation curve for EP-SPS alloy exposed in 2M sulphuric acid at 45 and 65°C.

4.9.4.1 Corrosion results

Corrosion rates of the alloy were calculated using the information provided by the polarisation curve for EP-SPS alloy. Table 4.13 is showing these corrosion calculations. The corrosion rates calculated in Table 4.13 were also presented in a bar graph shown in Figure 4.78 which shows a clear comparison between the alloy and the as-received copper at 45 and 65°C.

Table 4.13: Corrosion rate calculations for the EP-SPS alloy and as-received copper at 45 and 65°C.

Sample $\times 10^{-6}$	Temp	Icorr (A)	Icorr (µA)	icorr (µA/cm^2)	CR (mmpy)
As-received-Cu	45°C	9.63×10^{-6}	9.63	19.14	0.22
EP-SPS		1.96×10^{-5}	19.58	38.95	0.45
As-received-Cu	65°C	3.35×10^{-5}	33.47	66.58	0.77
EP-SPS		1.76×10^{-6}	1.76	3.50	0.04

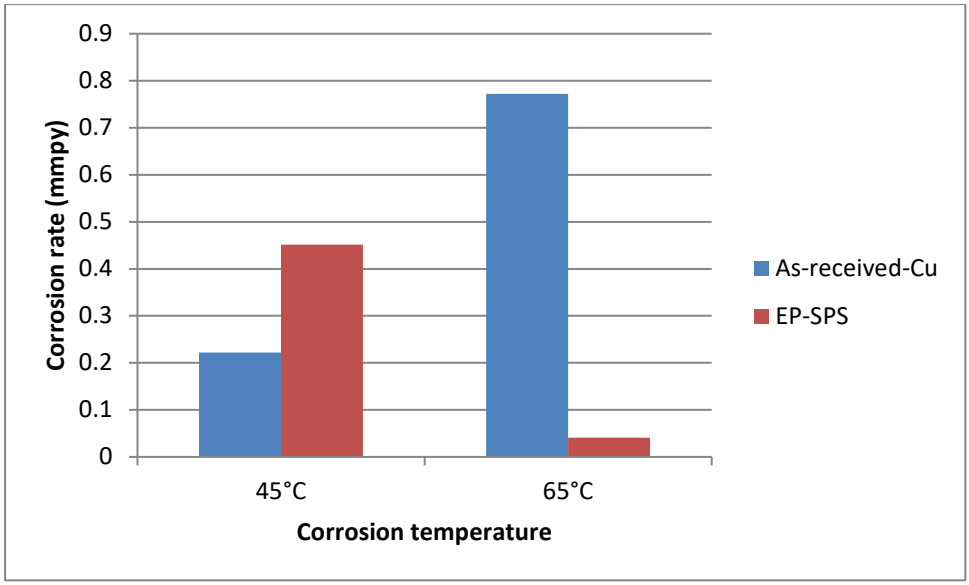


Figure 4.77: Corrosion rate as a function of temperature.

4.10 Summary of results

Chapter 4 has presented all the results of the experiments conducted for this research. It looked into all the different techniques of adding ruthenium to the copper surface and creating an alloy of copper and ruthenium. The other variables studied were ruthenium content and temperature. The main focus was to get a technique that will result in lowering the corrosion rate of the as-received copper. The HVOF produced a good coating with controlled coating thickness. The elemental maps showed that ruthenium distribution on the coating was almost even across the entire surface. The cold sprayed coating did not achieve an improvement in the corrosion resistance when compared to the as-received copper. The cold sprayed coating produced very thin coatings with a lot of breakup along the coating.

The SPS alloys produced lower corrosion rates. The quantity of the ruthenium added to these alloys was very close to the one detected by the EDS analysis. Most of these alloys were affected by pitting corrosion, as shown by the SEM micrographs, which was concentrated along the grain boundaries. The electroplated copper had an interesting outcome. The 2 A plated copper had improved the corrosion resistance of copper in 2M sulphuric acid only at 65°C. The process electroplating the powder was done successfully, but when the subsequent HVOF and SPS processes were applied, very little ruthenium was detected by the EDS. Both the EPP-HVOF and EP-SPS resulted in some contamination, most of which were tungsten, chromium, and nickel.

Chapter 5 : Discussions

5.1 Introduction

The aim of this work was to successfully introduce ruthenium to the copper surface by means of coatings and powder metallurgical techniques. The ruthenium was intended to improve the corrosion resistance of copper. This chapter contain a detailed explanation of the results and comparisons. The coatings were characterised by optical and SEM micrographs as well as EDS analysis. In addition the hardness was determined, as well as the corrosion characteristics through electrochemical potentiodynamic tests.

5.2 As-received copper

The light optical micrographs of as-received copper contained clearly defined grains and grain boundaries. It shows equiaxed, recrystallized grains containing twinned areas.

Current density, according to Faraday's law, is directly proportional to corrosion rate. Ideally, the lowest current density will result in the highest corrosion resistance of the material. Potentiodynamic measurements done for as-received copper showed a positive shift in the current density as the temperature increases. The shift in the corrosion potential also has an effect to the resulting corrosion rate. If the potential moves to more noble regions the corrosion resistance might also improve.

Copper exposed to 2M sulphuric acid showed an increase in current density with increasing temperature. Therefore, the as-received copper had an acceptable corrosion resistance at 25°C, but it became poor at 45 and 65°C. At 25°C the corrosion rate of copper was 0.16 mmpy, and this became 0.22 mmpy at 45°C and 0.77 mmpy at 65°C. The as-received copper results were a baseline to compare with the alloys and coatings that were produced. The Vickers hardness measurements on as-received copper showed an average of 128 HV.

5.3 High velocity oxygen-fuel spray coating

The optical micrograph of the cross section of the coatings showed ruthenium distribution, and the arrangement of the layers or splats of the coating , the existence of pores, and the adhesion quality. The substrate used corresponded to the as-received copper discussed in section 5.2. All the optical images in Figure 4.4 showed dark spots in the coatings. These were concentrated along the splats boundaries and were pores in the coatings. The HVOF spraying process uses oxygen in the application of coatings. It is possible that oxidation of copperoccurred, and some

of the gas gets trapped in the coating could have resulted in the formation of pores on the coating. All the coatings showed good adhesion to the substrate, but at the substrate-coating boundary alumina was found in some areas. As mentioned, the alumina was probably residue from the sandblasting stage.

The surface and cross section analysis of the HVOF-0%Ru coated sample was done to determine the behaviour of this sample when exposed to sulphuric acid environments. As shown in Figure 4.5, the sample surface had contaminants (Al, Si, and Fe), which came into contact with the sample during the HVOF coating process. It is possible that the spraying gun had these elements from the previous powders used. The average thickness of the coating was 379 µm, which was in the range of the desired size (≥ 350 µm). The cross sectional image showed that the HVOF spray process can produce coatings with low porosity, good adhesion, and uniform coating thickness as suggested by Schmid et al. (2004).

The HVOF-0.5%Ru sample contained similar contaminants as those found in HVOF-0%Ru sample. The ruthenium was detected on the sample surface with a concentration of 0.4wt%, which was close to the 0.5wt%, the intended concentration. The average coating thickness was 359 µm. For the HVOF-1%Ru sample, only 0.57 wt% Ru was picked up on the sample surface instead of 1wt% Ru. It had an average coating thickness of 470 µm. To prove the presence of ruthenium in these samples an EDS of the white area in the coating was taken. It proved that the white area in the coatings is the ruthenium. The HVOF-2%Ru coated sample had an average coating thickness of 381 µm, and 1.4wt% Ru instead of the anticipated 2wt%. All the HVOF coatings had good adhesion properties. The orientation of the splats and their sizes did not vary much when ruthenium was added. A good splat-splat bonding was observed in all the coatings.

When comparisons were made among the copper and ruthenium maps reported in Table 4.2, it was observed that the ruthenium density increased with correspondence to the ruthenium content of the made-up powder. The HVOF-0.5%Ru has the least ruthenium content, and its ruthenium map had ruthenium in small dots as compared to that of HVOF-2%Ru, which had small dots and larger ruthenium dots along its surface. The distribution of the ruthenium on the coating surface was almost even in all the samples.

The hardness measurements of all the coated samples showed that the hardness of the coatings increased as compared to the substrate. With reference to Figure 4.14, it was observed that HVOF-2%Ru achieved the highest hardness in the coating, followed by HVOF-1%Ru, and

then HVOF-0.5%Ru, and lastly the HVOF-0%Ru. The hardness decreased into the substrate. These results suggest that the addition of ruthenium in the coatings increased the hardness.

The potentiodynamic curves of the copper and HVOF coated samples in Figure 4.15 and 4.16 were generated when these materials were exposed in 2M sulphuric acid environment at 45 and 65°C. The aim of introducing the ruthenium on to the copper surface was to reduce its corrosion rate. The principle of cathodic protection is based on reduction of corrosion current density by cathodic polarisation. The potential of metals depends on anodic and cathodic electrochemical reactions in an electrolyte solution. The applied ruthenium changes in the copper surface negatively shifts the potential of the copper so the anodic reactions cease and only cathodic reactions occur at the copper surface. The addition of ruthenium was also expected to move the corrosion potential to more noble regions. At 45°C, these parameters did not change much compared to that of as-received copper. The corrosion rate of as-received copper in this environment was recorded to be 0.22 mmpy (refer to table 4.3). The HVOF-2%Ru is the one that achieved the highest corrosion resistance improvement by 50%, followed by HVOF-0.5%Ru. There was a very small shift observed in the corrosion rate of HVOF-1%Ru compared to as-received copper. The corrosion rate of the sample coated with only copper powder (HVOF-0%Ru) increased more than that of as-received copper.

At 65°C, the same test was performed on all the HVOF samples to determine their response in 2M sulphuric acid aqueous environment. An interesting observation was made on the potentiodynamic results obtained at this temperature. The as-received copper curve stands out, with a more positive current potential compared to all the others. For most of the samples, except HVOF-0.5%Ru sample, when ruthenium was added it shifted the corrosion current density to more negative values, resulting in decreased corrosion rate (as tabulated in table 4.4). The corrosion rate of the HVOF coated samples decreased with an increase in ruthenium content as shown in Figure 4.17. The HVOF-2%Ru achieved the highest improvement in corrosion resistance. The corrosion rate of copper was decreased by over 65%. The corrosion rate of HVOF-0.5%Ru slightly increased. This was an unexpected response, which is assumed to be due to possible galvanic action.

5.4 Cold spray coating

The optical micrographs were taken on the cross section of the cold sprayed samples as shown in Figure 4.28. The pictures show contamination between the coating and the substrate, which remained after sand blasting. For those samples with ruthenium additions, the ruthenium was

clearly visible since it is lighter (white) compared to the copper. The images show that the applied coating had a significant number of discontinuities, and the coating thickness could not be controlled. The corrosion deposits were also found on the substrate surface. During the etching process, as the copper cross section was exposed to the etchant, some form of corrosion occurred on the copper substrate. This was the result of the presence of trace oxidants as dissolved oxygen from air. One of the observations made was that the particle near the substrate-coating boundary was more affected and these effects decreased as you move further away from this region. The surface became obscured beneath the corrosion product deposits. More detailed analyses are required to analyse this corrosion occurrence technique.

The surface analysis of the cold sprayed samples showed very little contamination on the surface. Only Si and Al elements were detected. However, these images showed a significant concentration of pores on the surface. The SEM micrographs of the cross sections of the coating showed that the coating was not adhering well to the substrate, even when the sand blasting stage was applied prior to the coating process. The images in Figure 4.20, 4.22, 4.24, and 4.26, not only show that the coating was not well adherent to the substrate, but also that the splat-splat bonds were very week.

The different deposition layers in the coatings can still be distinguished because they did not adhere to each other to form a single coating. Since the cold spraying process is highly dependent on the powder exit velocity for proper intimate contact under high localized pressure for formation of coating onto the substrate, it appears that the velocity used for these coatings was not high enough to achieve this. This could have been caused by the limited pressure available for the machine during the spraying process. The compressor used was an air compressor. The quality of the cold sprayed coatings could be improved by increasing the spray pressure and temperature during coating. The presence of ruthenium in the coatings did not have any visible effect on the adhesion property of the coating.

Considering the elemental maps of ruthenium and copper in Figure 4.27, it is seen that both ruthenium and copper were distributed evenly across the entire surface. The EDS spectrum together with the elemental weight percentages presented in figure 4.19, 4.21, 4.23 and 4.25 shows that the coating surface had higher amounts of ruthenium weight percentages as compared to that used to prepare the coating powders. The coating surface of CSC-0.5%Ru sample had 8 wt%Ru, the CSC-1%Ru sample had 7 wt%Ru, and CSC-2%Ru sample had 15 Wt. %Ru.

The measurements of the coating hardness for all the CSC samples were made and are presented in Figure 4.28. The coatings with ruthenium resulted in increased hardness compared to the as-received copper metal. The CSC-0%Ru coated sample had the lowest hardness, lower than the hardness of copper. This is because it was not hardened by the addition of ruthenium as the other coatings.

The potentiodynamic curves presented in Figure 4.29 and 4.30 show a shift in the corrosion current density and corrosion potential from that of as-received copper as received. At 45°C, the corrosion current shifted to more noble regions but the corrosion current densities increased. The effect of this shift is shown in the corrosion rate calculations shown in Table 4.4. The corrosion rate increased for all the coated samples. This was because the coatings had poor quality caused by the discontinuities in the coating as well as the high porosities of the coatings. Therefore, the acid could the reach and attach the coating and the substrate with ease.

The same effect was observed for the samples exposed at 65°C in the same environment. Although at this temperature, the current density of the coatings did not increase the same way as that in 45°C, it still did not achieve any decrease in corrosion rate of the copper metal (refer to table 4.5). Looking at Figure 4.31, it shows that at 45°C the corrosion rate of the coated samples decreased with an increase in ruthenium content, whereas that at 65°C showed that the corrosion rate decreased with an increase in ruthenium content. This is because at higher temperatures the galvanic actions could have been accelerated while the presence of ruthenium could not counter act the corrosion action.

5.5 Spark plasma sintered alloys

The spark plasma sintered alloys were produced to investigate the improvement in the corrosion resistance of copper in sulphuric acid environments. The grain structure in Figure 4.31 shows that ruthenium additions in the copper alloys resulted in finer grains. The copper (SPS-0%Ru) sintered alloy have more defined grain boundaries compared to the ruthenium alloyed copper samples. The micrographs show very few dark spots of pores on the alloy surface.

It has already been shown from the optical micrographs that the sintered alloys had very low porosities. The SEM images make this fact very clear as shown in Figure 4.33 to 4.37 by the alloy density even at high magnifications. These images show that ruthenium and copper had a fair distribution. The EDS spectrum shows that there were very few contaminants detected

and only silicon was found. This caused the alloy to behave as expected in the acid environment since there will be no side reactions occurring.

The hardness measurements of the alloyed samples shown in Figure 4.39 show a large decrease in the hardness of copper when compared to as-received copper (as received). Although the hardness values were low, there is a trend of hardness increase with increase in ruthenium content as expected. The lowest hardness value measured was 70.2 HV for the SPS-0%Ru alloy which increased to 105.6 HV for the SPS-2%Ru alloy.

The electrochemical result shows that the spark plasma sintered alloys had improved the corrosion resistance as compared to copper (as received) for all the temperatures. At 45°C all the SPS alloys managed to decrease the corrosion density of copper and shifted the corrosion potentials to a nobler region (refer to Figure 4.40). The resultant corrosion rate of the SPS alloys, shown in Table 4.6, decreased compared to copper with more than a 90% decrease. When ruthenium was added the corrosion rate decreased even more. At 45°C, the alloys decreased in corrosion rate as the Ru content in the alloy increased. At 65°C, Figure 4.41 shows the shift in the current density to the more negative region. Since current density is directly proportional to corrosion rate, the corrosion rate of the alloyed samples (Table 4.7) had decreased compared to copper.

The corrosion characteristic of SPS alloys were also taken potentiodynamic pulse corrosion test, where in they were exposed to the 2M sulphuric acid for the duration of 90 min at 65°C with a pulse at 45 min. The samples were exposed into the solution for 45 min prior to the first scan, and after the scan, they remained for another 45 min prior to the second scan. The results from this experiment presented in Figure 4.42 showed a very high decrease in corrosion rate, way much lower than that obtained in the first test (see Table 4.8). The corrosion rate decreased significantly and this effect is assumed to be due to the exposed Ru that was left during the first cycle of the pulse corrosion process that selectively corroded parts with Cu metal. The assumption was made based on the results that Thanjekwayo, (2009) and Potgieter et al., (2014) which affirmed that ruthenium increased the corrosion resistance of hardmetals.

Figure 4.43 shows the trend in the variation of corrosion rate as a function of concentration of ruthenium for the corrosion of SPS alloyed copper samples in 2M H_2SO_4. Although all the sintered alloys had lower corrosion rates compared to copper, at 65°C, the alloys slightly increased in corrosion rate with increase in ruthenium content. When compared with alloys at 65°C as shown in Figure 4.44, it can be seen that regardless of the difference in the corrosion

values, the alloys follow the same trend, increasing in corrosion rate with an increase in ruthenium content.

The corrosion mechanism of the SPS alloys, effect of ruthenium and the role it plays when added to the alloy was also investigated. The SEM images shown in Figure 4.45, 4.47, 4.50, and 4.52 indicated the areas that were corroded, the corrosion affected band, and the alloy area that was not corroded. This study was conducted to show how the SPS alloys achieved the highest corrosion resistance. The alloys were attacked by pitting corrosion as shown by the SEM images taken at high resolution. The corrosion propagated through the grain and also along grain boundaries. The ruthenium in the alloy was left unattacked by corrosion, but parts of the copper corroded. The area around ruthenium was more corroded.

5.6 Electroplating

Copper was successfully electroplated with ruthenium after a preliminary study that was conducted showing the best plating conditions to be 45 minutes for both 1.5 and 2 A plating current (refer to Figure 4.54). Figure 4.55 and 4.58 showed that the coating that was formed wrinkled and cracked after being exposed to sulphuric acid.

There was no corrosion improvement in the ruthenium electroplated copper at 45°C, but at 65°C the EP-2 A decreased the corrosion rate by lowering the corrosion current density of copper. The corrosion mechanism that attacked the EP-1.5 A and EP-2 A was different. The EP-2 A ruthenium plated copper corrosion response is shown in Figure 4.59. When the coating was attacked it cracked and corrosion products and oxides formed. The copper oxide provided a diffusion barrier between the substrate and the acid, causing the film to be more protective and improved corrosion resistance.

Figure 4.56 showed that the EP-1.5 A sample developed wrinkles after corrosion. This is a porous layer that was detached from the substrate in some but was still intact with the overall coating. The corrosion rate in this sample increased because the corrosion was diffusion controlled. Although some corrosion products (Cu_2O and $CuSO_4$) formed, the sulphuric acid could still penetrate beneath the coating and attacked the substrate leading to increased corrosion rates.

Figure 4.57 and 4.61 showed that the ruthenium film coating was very thin. When the hardness measurements were done, it had the anvil effect since the coating layer was too thin. The hardness measured was almost that of the substrate copper. The work done by Zhang et al.

(2015) showed that this effect is experience with decreasing specimen thicknesses. According to Wilburn et al. (2004) the addition of ruthenium in a material will tend to increase its hardness. The same effect was experienced for the ruthenium electroplated copper.

5.7 Electroplated copper powder used in EPP-HVOF and EP-SPS

The copper powder was electroplated and the film formed was shown by the SEM micrographs in Figure 4.68 and 4.70. When EDS analysis were made, only the 2 A plated powder showed ruthenium in the coating. The EPP-HVOF showed significant contaminations. It is possible that these contaminants were collected during the HVOF spraying gun which was used for different samples. Similar contaminants were also found in the EP-SPS alloy. The corrosion rates for the EPP-HVOF were higher than that of the as-received copper in both 45 and 65°C. Figure 4.78 show that the EP-SPS alloy had improved the corrosion resistance at 65°C.

Chapter 6 : Conclusions

Various ways to improve mechanical and corrosion properties of copper surfaces were investigated. To reach these objectives, ruthenium was introduced into the copper surface in different quantities, 0.5, 1, and 2 weight percent, in order to improve its corrosion resistance and serviceability of copper in general. Four major surface coating techniques; High velocity oxygen fuel thermal spray, cold spraying, spark plasma sintering, and electroplating, were involved in attaining the objectives.

The corrosion resistance of copper-ruthenium coatings was investigated in sulphuric acid. The key variables such as ruthenium content, temperature, and ruthenium application technique were studied. Corrosion mechanism, hardness and chemical compositions were determined for all the coatings and the alloys made. From the results obtained in 2M sulphuric acid environment, the following conclusions were made:

The high oxygen fuel spray, spark plasma sintering, and electroplating successfully added ruthenium to the copper surface and achieved certain level of improvement of the corrosion resistance. The SPS alloy achieved the highest corrosion resistance at 65°C when the samples were exposed for 45 and 90 min in the sulphuric acid environment. The HVOF coated copper was the second best method that achieved in reducing the corrosion rate when compared to other methods researched in this work. The corrosion rates tend to decrease with the increase in ruthenium at both 45 and 65°C.

The investigation done during electroplating showed that the ruthenium electroplated copper also enhanced the corrosion resistance of copper when plated using 2 A plating current. The 2A electroplated powders were further processed using the HVOF and sintering technique. Although the electroplating of the powder was done and successfully achieved adding ruthenium to the powder film, the applications that followed did not manage to maintain the ruthenium in the powder film. To improve these results, further studies should be done to investigate ways to make the ruthenium film stick to the powder for longer. There also must be an improvement in avoiding contamination to the electroplated powders.

To improve the ruthenium adherent property to the copper powder, another element can be introduced to be coating binder between copper and ruthenium. One of the elements that can be considered in achieving this is adding nickel between copper and ruthenium. Nickel has a good adhesion property with both copper and ruthenium. Additional benefit to the selection

and use of nickel will be that it is also corrosion resistance in the sulphuric acid environment that the copper-ruthenium alloys and coatings are exposed to.

The cold spray coating process produced poor coatings which caused an increase in the corrosion rate of copper. The coatings had a thin discontinuous layer which allowed the sulphuric acid to reach and attack the substrate. The shape of the powder also could have contributed to the outcome; further studies should also investigate the effect of milling the powder prior to coating. Future work should also look at altering the application technique, for example, increasing coating pressures and speed. There was not a particular trend in corrosion rate of copper that could be followed to show the effect of increase in ruthenium content in the cold sprayed coating.

The hardness measurements conducted showed a decreased in Vickers hardness values obtained for all the coatings and alloys when compared to the as received copper. Another observation made from these measurements was that, for all the alloys and coatings, the Vickers hardness values increased with increase in ruthenium content.

This research has proved that the presence of ruthenium in the copper surface improved the corrosion resistance of copper when exposed in sulphuric acid. The best results were obtained when the high velocity oxygen fuel and spark plasma sintering techniques were applied.

Chapter 7 : References

1. Al Kharaf F.M., Ghayad I.M., and Abdallah R.M., Corrosion inhibition of copper in seawater by 4-Amino-4H-1,2,4-Triazole-3-Thiol, Corrosion Science section, 2013, p 59.
2. Al Shakarji R., He Y., and Simon G., Statistical analysis of the effect of operating parameters on acid mist generation in copper electrowinning, Hydrometallurgy, Volume 106, 2011, p 113–118.
3. Aliya D., Metallographic Sectioning and Specimen Extraction, Metallography and Microstructures, Vol 9, ASM Handbook, ASM International, 2004, p 229–241.
4. Al-Zubidy E.A., and Hummza R.A., Corrosion behaviour of copper and carbon steel in acidic media, Baghdad Science journal, Volume 11, Number 4, 2014, p 1577-1581.
5. Aslin N.J., Stone D., Webb W., Current distribution in modern copper refining, 2007, Retrieved 8 September 2017, from http://www.isakidd.com/EN/Downloads/Technical%20Papers/Current%20Distribution%20in%20Modern%20Copper%20Refining.pdf
6. Aulund R., Spark plasma sintering, Thermal technology LLC, Ceramic industry magazine, 2008.
7. Ayres R.U., Ayres L.W. and Rade I., The life cycle of copper, its co-products and by product, Mining, minerals, and sustainable development, 2002, p 7-10.
8. Babic R., Metikos-Hukovic M., and Jukic A., A study of copper passivity by electrochemical impedance spectroscopy, Journal of the Electrochemical Society, Volume 148, Issue number 4, 2001, p B146-B151.
9. Baeshow A.B., Kadirbayeva A.S., and Jurinov M.J., Dissolution of copper electrode in sulfuric acid at polarisation by industrial alternating current, International Journal of Chemical Science, Volume 12, Number 3, 2014, p 1009-1014.
10. Bartonicek R., Copper corrosion in sulphuric acid at heat transfer, Werkstoffe and corrosion 30, 1979, p 203-210.
11. Beatty R., The elements: Copper, Marshall Cavendish corporation, New York, 2001, p 4-9.
12. Behpour M. and Mohammad N., Inhibiting effects of two derivatives of amino-thiophenol on the corrosion of copper by electrochemical methods, Corrosion science section, Volume 68, Number 12, 2012, p 1119.

13. Besta P., Samolejova A., Janovska K., Lampa M., and Lenort R., Evaluation of benefits resulting from innovation of input raw materials dosing process in sintering, Metalurgija, Volume 51, Number 4, 2012, p 457-460.
14. Beukes N.T. and Badenhorst J., Copper electrowinning technology: forty years of innovation, 2.2 million tonnes of copper annually, The Journal of the South African Institute of Mining and Metallurgy, 2002, p 445-450.
15. Beukes N.T. and Badenhorst J., Copper electrowinning: theoretical and practical design, Hydrometallurgy conference 2009, The Southern African Institute of Mining and Metallurgy, 2009, p 214-229.
16. Biesiekierski A, Ping D.H., Yamabe-Mitarai Y., Wena C., Impact of ruthenium on microstructure and corrosion behavior of b-type Ti–Nb–Ru alloys for biomedical applications, Materials and Design 59, 2014, p 303–309.
17. Caron P., High ɣ solvus new generation nickel-based superalloys for single crystal turbine blade applications, Superalloys, The Minerals, Metals & Materials Society, 2000, p 737-745.
18. Champagne, V.K., The cold spray materials deposition process: fundamentals and applications. Woodhead Publishing and Maney Publishing, CRC press, 2007.
19. Chan R., Arunagiri T.N., Zang Y., Chyan O., Wallace R.M., Kim M.J., and Hurd T.Q., Diffusion studies of copper on ruthenium thin film, Electrochemical and Solid State Letter 7(8), 2004.
20. ChandrasekarM.S., Pushpavanam M., Pulse and pulse reverse plating-Conceptual, advantages and applications, ElectrochimicaActa, Volume 53, Issue 8, 2008,p3313–3322
21. Chen Y., Chen S., and Lei Y., Surface structure and anti-corrosion properties of copper treated by dopamine-assisted-11-mercaptcundecanoic acid film, Corrosion Science section, Volume 68, Number 8, 2012, p 747.
22. Cohen A., Corrosion of copper and copper alloys, Corrosion: Materials, Volume 13A, ASM Handbook, ASM International, 2005, p 125–163.
23. Conradic A., Directorate: Mineral economics, Platinum-Group Metal Mines, Directory D6, 2003.
24. Couto Miguel Pereira de Magalhães e., Cold spray deposition of WC-Co, MSc dissertation, Faculty of Engineering, University of Porto, 2011.
25. Crundwell F.K., Moats M.S., Ramachandran V., Robinson T.G., and Davenport W.G., Extractive metallurgy of nickel, cobalt and platinum group metals, Elsevier, 2011, p 393-532.

26. Damon G.H., and Cross R.C., Controlling factors in anaerated solutions of sulfuric acid, corrosion of copper, Materials Engineering, Volume 7, Reinhold Publishing Corporation, 1936.
27. Darren A.L., and Mallikarjuna N.N., A comprehensive investigation of copper pitting corrosion in drinking water distribution system, Corrosion Science Volume 52, 2010.
28. Davis J.R., Handbook of thermal spray technology, Coating structures, properties, and materials, ASM international, 2004, p 51.
29. Davis R.J., Berndt C., and Lenling W.J., Handbook of Thermal Spray Technology, ASM international, 2004, p 128-130.
30. DioufS., MenapaceC., D'IncauM., Molinari A., and Ischia G., Spark plasma sintering of cryomilled copper powder, Powder Metallurgy, Volume 56, Number 5, 2013, p 420-426.
31. Dodek A., Fajnor P., Liptakova T., Zatkalikova V., Anisimov E., and Vojsovicova M., Corrosion of copper pipes joints in simulated operating conditions, Materials Engineering, Volume 18, 2011, p 140-144.
32. Dunbar W.S., Basics of mining and mineral processing, 2012 Americas school of mines, University of British Columbia, 2012, p 69.
33. Duthil J.P., Mankoswki G., and Glusti A., The synergetic effect of chloride and sulphate on pitting corrosion of copper, Corrosion Science, Volume 38, 1996.
34. Eastwood K.L., and Whebell G.W., Developments in permanent stainless steel cathodes within copper industry, Xstrata technology, 2015.
35. Edwards J., Electroplating: A guide for designers and engineers, The Committee for the Promotion of Electroplating, The Institute of Metal Finishing, UK, 1983, p9,27-32.
36. Fauchais P. L., Heberlein J.V.R., and Boulos M., Thermal Spray Fundamentals: From Powder to Part, Springer Science & Business Media, 2014.
37. Fauchais P.L., Heberlein J.V.R., and Boulos M.I., Thermal spray fundamentals from powder to part, Springer New York Heidelberg Dordrecht London, 2014.
38. Fedrizzi L., Molinari A., DeFlorian F., Tiziani A., and Bonora P. L., Corrosion study of industrially sintered copper alloyed 316L austenitic stainless steel, British Corrosion Journal, Volume 26, Issue 1, 1991, p 46-50.
39. Fink-Jensen P., Hardness testing of organic coatings, International union of pure and applied chemistry, 1964, p 250.
40. Flink R., Laitinen M.I., and Jarvinen P., Industrial coating of metal surfaces, Tikkurila OYJ, industry, 2nd edition, 2011.

41. Fontana Mars G., Corrosion engineering, third edition, McGraw-Hill international editions, 1987.
42. Fraunchais P., and Vardelle A., Thermal sprayed coatings used against corrosion and corrosive wear, University of Limoges, 2012.
43. George M.W., Platinum-Group Metals-2006 mineral year book, U.S. Geological Survey, Science for a changing world, 2007.
44. Gerald V. J., Copper leaching, solvent extraction, and electrowinning technology, Society for Mining, Metallurgy, and Exploration, Inc, 1999, p 179.
45. Govender K., Scenini F., Lyon S. and Sherry A, Influence of Pd and Ru additions on stress corrosion cracking of austenitic stainless steels, Corrosion Engineering, Science and Technology, Volume 47, Number 7, 2012, p 507-515.
46. Grishina E.P, Udalova A.M, and Rumyantsev E.M, Anodic oxidation of copper in concentrated sulfuric acid solution, Russian Journal of electrochemistry, Volume 38, Number 9, 2002, p 1041-1044.
47. Hakamada M., Motomura J., Hirashima F. and Mabuchi M., Preparation of nanoporous ruthenium catalyst and its CO oxidation characteristics, Materials transactions, Volume 53, 2012.
48. Hasan M., High velocity oxy-fuel (HVOF) thermal spray deposition of functionally graded coatings, PhD thesis, Dublin City University 2005.
49. Heath G.R, Heimgartner P., Irons G., Miller R., and Gustatsson S., An assessment of thermal spray coating technologies for high temperature corrosion protection, Material science, 1997.
50. Hilliard H.E, Platinum- group metals, Geological survey mineral resources program, 2000.
51. Hilliard H.E., Platinum–group metals, U.S. geological survey mineral yearbook, 2000, p 59.1-59.6.
52. Jaganraj D., Karthick Y., Chakravarthi S., and Balaji V., A review on study and analysis of nickel coating on solar collector applications, International Journal of Advanced Scientific and Technical Research, Volume 5, Issue 6, 2016, p 228-233.
53. Jehn H., and Zielonka A., Corrosion testing, Research institute for precious metals and chemistry, ASM handbook, Surface engineering, Volume 5, 1994.
54. Kabwe E. and Yiming W., Analysis of copper‘s market and price-focus on the last decade‘s change and its future trend, International Journal of Scientific & Technology Research, Volume 4, October 2015, p 54-61.
55. Kanani N., Electroplating: Basic Principles, Processes and Practice, Elsevier, 2004.

56. Kear G., Barker B.D., and Walsh F.C., Electrochemical corrosion of unalloyed copper in chloride media- a critical review, Corrosion science 46, 2004, p109- 135.
57. King F., and Liljia C., Localised corrosion of copper canisters, Corrosion engineering, science and technology, Volume 49, 2014.
58. King F., Critical review of the literature on the corrosion of copper by water, Integrity corrosion consulting limited, 2009, p 7.
59. Kinnaird J.A., The Bushveld large igneous province, School of Geosciences, University of the Witwatersrand, International Association of Volcanology and Chemistry of the Earth's Interior, 2005.
60. Kordosky G.A, Copper recovery using leach/solvent extraction/electrowinning technology: Forty years of innovation, 2.2 million tonnes of copper annually, The journal of the South African Institute of Mining and Metallurgy, 2002.
61. Leidheiser H., The corrosion of copper, tin, and their alloys, John Wiley & Sons, Inc., New York, 1971.
62. Lekala M. B., van der Merwe J.W., and Pityana S. L., Laser Surface Alloying of 316L Stainless Steel with Ru and Ni Mixtures, International Journal of Corrosion, Volume 2012, 2012, p 1-4.
63. Li C.J., Yong G.Y, and Altun O., Thermal spray coatings for aeronautical and aerospace applications, Aerospace material handbook, 2012.
64. Li W. Y., Zhang D. D., Huang C. J., Yin S., Yu M., Wang F. F., and Liao H. L., Modelling of impact behaviour of cold spray particles: review, Institute of Materials, Minerals and Mining, Surface Engineering ,Volume 30, Number 5, 2014, p299-306
65. Liang D., Sowards J.W., Frankel G.S., Alexandrov B.T., and Lippold J.C., Corrosion resistance of welds in type 304L stainless steel made with a nickel–copper–ruthenium welding consumable, Corrosion Science 52, 2010, p 2439–2451.
66. Lianga C., Mab M., and Zhanga D., Microstructures and tensile mechanical properties of consolidated copper, Materials Research 18(Suppl. 1), 2015, p 158-163
67. Lieser M.J. and Xu J., Composites and future of society: preventing a legacy of costly corrosion with modern materials, Owens corning, 2010, p 2.
68. Liow J.L., Frazer A., He Y., Eastwood K., and Phan C., Acid mist formation in the electrowinning of copper, Chemica, Chemica Melbourne Australia, 2007, p 1373-1380.
69. Lu L., Experimental study of reverse crevice corrosion of copper. Master's thesis. University of Saskatchewan, Canada, 2005.

70. Mak A., Corrosion of steel, aluminium, and copper in electrical applications, General cable, 2013.
71. McCarthy D.L., Creating complex hollow metal geometries using additive manufacturing and metal plating, MSc thesis, faculty of the Virginia Polytechnic Institute and State University, 2012.
72. McGinnity J.J., and Nicol M.J., Sulfuric acid mist: Generation, Suppression, Health Aspects, and Analysis, Mineral processing and extractive metallurgy review 35, 2014, p 149–192.
73. Melciu D., and Maidee N., Pulse-Electroplating: Process parameters and their influence on the formed microstructure, Diploma work No. 161, Department of Materials and Manufacturing Technology, Chalmers university of technology, Gothenburg, Sweden, 2015.
74. Menapace C., Cipolloni G., Hebda M., and Ischia G., Spark plasma sintering behaviour of copper powders having different particle sizes and oxygen contents, Powder Technology 291, 2016, p 170–177.
75. Molina1 A., Torres-Islas A., Serna1 S., Acosta-Flores M., Rodriguez-Diaz R.A., and Colin J., Corrosion, electrical and mechanical performance of copper matrix composites produced by mechanical alloying and consolidation, International Journal of Electrochemical Science, Volume 10, 2015, p 1728-1741.
76. Montay G., Cherouat A., Nussair A., and Lu J., Residual stresses in coating technology, Journal of material science and technology, Volume 20, 2004, p 81.
77. Munir Z.A. and Anselmi-Tamburini U., The effect of electric field and pressure on the synthesis and consolidation of materials: A review of the spark plasma sintering method, Journal of Materials Science, Volume 41, Issue 3, 2006, p 763–777.
78. Nelwalani N.B., Evaluation of erosion-corrosion on ruthenium enriched hard metal coatings, M-Tech dissertation, department of engineering metallurgy, University of Johannesburg, 2014.
79. Neumeier S., Pyczak F., and Goken M., The influence of ruthenium and rhenium on the local properties of the ɣ-and ɣ'-phase in nickel-base superalloys and their consequences for alloy behavior, Superalloys, The Minerals, Metals & Materials Society 2008.
80. Niazi A.R, Shukui L, Yingchun W, Jinxu L, Zhiyu H, and Usman Z., Effect of spark plasma sintering temperature on microstructures and properties of copper-diamond composites, Advanced Materials Research Volume 683, 2013, p 573-576.

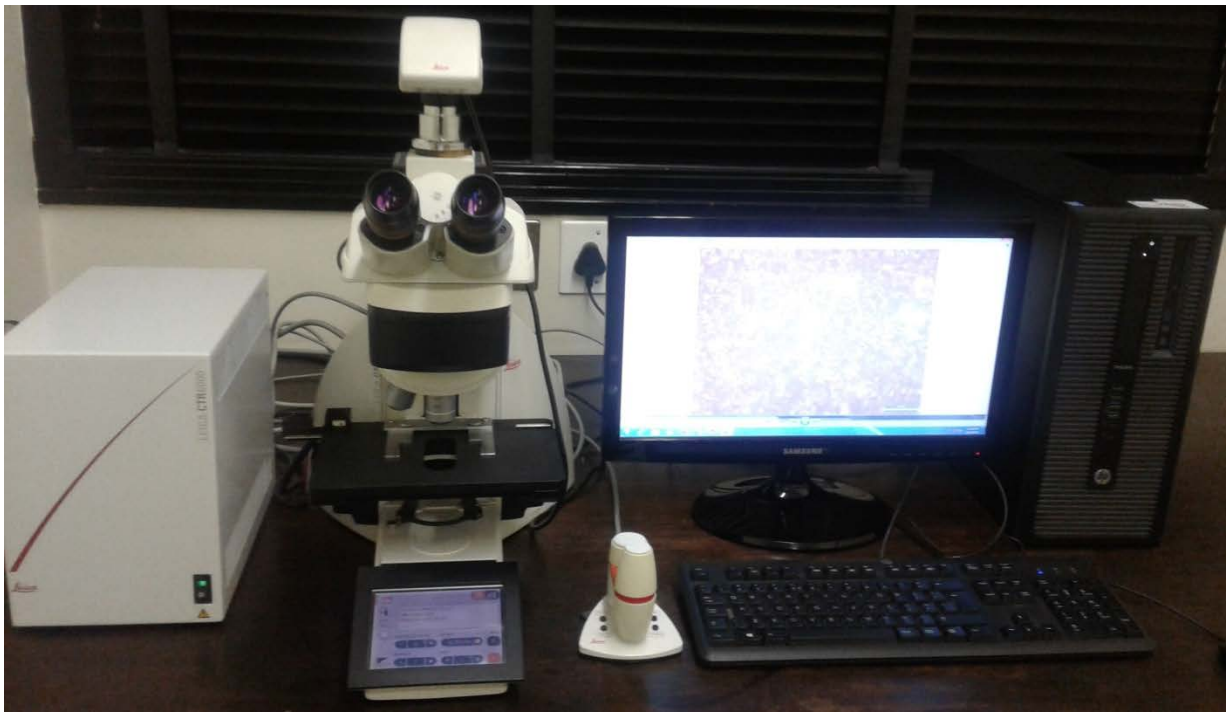
81. Nordlund L., and Virtanen H., Development of permanent cathode technology and related lifecycle solutions, The southern African Institute of Mining and Metallurgy, Base metal conference, 2013, p 89-97.
82. Oksa M., Turunen E., Suhonen T., Varis T., and Hannula S.P., Optimization and characterization of high velocity Oxy-fuel sprayed coatings: Techniques, Materials, and applications.; Coatings, 2011, p 17-47.
83. Olaseinde O.A., van der Merwe J.W., Cornish L.A., Chown L.H., and. Olubambi P.A., Electrochemical studies of Fe-21Cr-1Ni duplex stainless steels with 0.15 wt.% ruthenium at different temperatures, The Journal of The Southern African Institute of Mining and Metallurgy Volume 7A, 2012, p 535-538.
84. Palanna O. G., Engineering Chemistry, Tata McGraw-Hill Education, 2009, p176-194.
85. Pawlowski L., The science and engineering of thermal spray coatings, Second edition, John Wiley & Sons, 2008, p 67.
86. Potgieter J. H., Olubambi P., and Potgieter-Vermaak S. S., The corrosion behaviour of WC-Co-Ru alloys in aggressive chloride media, International Journal of Electrochemistry, Volume 2014, 2014, p 1-11
87. Potgieter J. H., Thanjekwayo N., Olubambi P., Maledi N., and Potgieter-Vermaak S. S., Influence of Ru additions on the corrosion behaviour of WC–Co cemented carbide alloys in sulphuric acid, Int. Journal of Refractory Metals and Hard Materials 29, 2011, p 478–487.
88. Powell C., and Webster P., Copper alloys for marine environments, Copper development association, 2012.
89. Raghu T., Malhotra S. N., and Ramakrishnan P., Corrosion behaviour of sintered austenitic stainless steel filters in sulphuric acid solutions, British Corrosion Journal, Volume 23 , Issue 2, 1988, p 109-116.
90. Rahmouni K., Keddam M., Srhiri A., and Takencuti H., Corrosion of copper in 3% NaCl solution polluted by sulphide ions, Corrosion Science 47, 2005.
91. Rashidi A.M. and Amadeh A., Effect of electroplating parameters on microstructure of nanocrystalline nickel coatings, Journal of Materials Science & Technology, Volume 26, number 1, 2010, p 82-86
92. Saeed A., Unit 4 Metal coating processes, ignou people's university, 2014, p 33-41.
93. Sandenbergh R.F., van der Lingen E., The use of Tafel back extrapolation to clarify the influence of ruthenium and palladium alloying on the corrosion behaviour of titanium in concentrated hydrochloric acid, Corrosion Science 47, 2005, p 3300–3311.

94. Sandoval S.P., Robinson T.G., and Cool P.R., Method and apparatus for electrowinning. copper using the ferrous/ferric anode reaction, US patent 7704354B2, 2010.
95. Schlesinger M. and Paunovic M., Modern Electroplating, fifth edition, John Wiley & Sons inc, 2011.
96. Schmid R.K., Zimmermann H., McCullough R. and Warnecke C., New HVOF developments at sulzermetco, Sulzer technical review 1, 2004.
97. Schmitt G., Global needs for knowledge dissemination, research, and development in materials deterioration and corrosion control, The world corrosion organisation, 2009, p 5.
98. Schneider M., Schroth S., Richter S., Hohn S., Schubert N., and Michaelis A., In-situ investigation of the interplay between microstructure and anodic copper dissolution under near-ECM conditions-Part 2: The transpassive state, Electrochimica Acta, Volume 70, 2012, p 76–83.
99. Shaw B.A. and Kelly R.G., What is corrosion, The electrochemical society interface, 2006, p 24.
100. Sherif E.M. Potgieter J.H., Comins J.D., Cornish L., Olubambi P.A, and Machio C.N., The beneficial effect of ruthenium additions on the passivation of duplex stainless steel corrosion in sodium chloride solutions, Corrosion Science 51, 2009, p 1364–1371.
101. Sherif E.M., Corrosion of Duplex Stainless Steel Alloy 2209 in Acidic and Neutral Chloride Solutions and its Passivation by Ruthenium as an Alloying Element, International Journal of Electrochemical Science, Volume 7, 2012, p 2374 – 2388.
102. Sherif M.E., Corrosion behaviour of copper in 0.50 hydrochloric acid pickling solution and its inhibition by 3-Amino-1,2,4-triazole and 3-Amino-5-mercapto-1,2,4-triazole, International journal of electrochemical science 7, 2012.
103. Stokes J., Production of coated and free-standing engineering components using HVOF (high velocity oxy-fuel process), Dublicity University, school of mechanical and manufacturing engineering, 2003.
104. Stoltenhoff T., Borchers C., Gartner F., and Kreye H., Microstructures and key properties of cold-sprayed and thermally sprayed copper coatings, Surface & Coatings Technology 200, 2006, p 4947–4960.
105. Sule R., Olubambi P.A., Abe B.T., Johnson O.T, Synthesis and characterization of sub-micron sized copper–ruthenium–tantalum composites for interconnection application, Microelectronics Reliability, 2012.

106. Sule R., Olubambi P.A.,Sigalas I., Asante J.K.O., and Garrett J.C., Effect of SPS consolidation parameters on submicron Cu and Cu–CNT composites for thermal management, Powder Technology 258, 2014, p 198–205.
107. Swanson G.D., Precious metals: what are they, why are they used, and how are they managed, Property Professional Volume 18, Issue 2, 2006, p 24-27.
108. Thanjekwayo N.P., The influence of Ru additions on the corrosion behaviour of WC-Co cemented carbide in corrosive media, MSc dissertation, faculty of Engineering and the Built Environment, University of the Witwatersrand, 2009.
109. Van der Lingen E., Sandenbergh R.F., The cathodic modification behaviour of ruthenium additions to titanium in hydrochloric acid, Corrosion Science 43, 2001, p 577-590.
110. Van der Merwe J. and Tharandt D., Corrosion resistance of laser-cladded 304L stainless steel enriched with ruthenium additions exposed to sulphuric acid and sodium chloride media, The Journal of The Southern African Institute of Mining and Metallurgy, Volume 115, 2015, p 409-555.
111. Van der Merwe J., Tharandt D., and MASIU P., Corrosion resistance of laser-cladded 304L stainless steel surfaces enriched with ruthenium additions in sulphuric acid media, The 6th International Platinum Conference, 'Platinum–Metal for the Future', The Southern African Institute of Mining and Metallurgy, 2014, p 219-224.
112. Vastag D., Apostolov S., Hadzistevic M., and Sekulic M., The possibility of copper corrosion protection in acidic media using thiazole derivative, Materials and technology, Volume 47, Issue number 3, 2013, p 329–333.
113. Velasco F., Ibars J.R., Ruiz-Roman J.M., Torralba J.M., and Ruiz-Prieto J.M., Improving the corrosion resistance of powder metallurgy austenitic stainless steels through infiltration, Corrosion Science, Volume 52, Issue number 1, 1962, p 47-52.
114. Villafuerte J., Modern Cold Spray: Materials, Process, and Applications, Springer International Publishing, 2015.
115. Vracar R.Z., Vuckovic N., Kamberovic Z., Leaching of copper (I) sulphide by sulphuric acid solution with addition of sodium nitrate, Hydrometallurgy 70 (2003), p 143.
116. Wagner R., Investigation on copper corrosion in thin films of sulphuric acid, The electrochemical society, Volume 143, 1996, p 139.
117. Wan Y., Wang X., Sun H., Li Y., Zhang K., and Wu Y., corrosion behavior of copper at elevated temperature, International Journal of Electrochemical science, Volume 7, 2012, p 7902-7914.

118. Wang Y.Y., Li C.J, A., Examination of factors influencing the bond strength of high velocity oxy-fuel sprayed coatings, Science direct, Surface Coating Technology 200, 2006, p 2923–2928.
119. Wilburn D.R. and Bleiwas D.I, Platinum-group metals-world supply and demand, U.S geological survey, Science for a changing world, 2004.
120. Wilburn D.R., and Bleiwas D.I., Platinum-Group Metals-World Supply and Demand, U.S. Geological Survey, Science for a changing world, 2004.
121. Wilmot R.E., Corrosion protection of reinforcement for concrete structures, The journal of the southern African institute of mining and metallurgy, 2007, p139.
122. Wong F.S., and Wild S., Prevention of cathode corrosion during electrowinning, U.S patent number 5837123, 1998.
123. Zaafarany A., and Boller H., Corrosion of copper electrode in sodium sulfide solution, Journal of Saudi Chemical Society 14, 2010, p183–189.
124. Zahedipoor A.R., Eslami S.H., Deylami M., Mohaghegh S.S., and Montazeri G.H., Investigation of Producing Chlorine with Electro Dialysis Method and the Effect of Operating Parameters: A Review, Advances in Environmental Biology, 7(14) 2013, p 4589-4594.
125. Zandra W. and O'Hara P.B., Spectroscopic analysis of three anticancer ruthenium (II) complexes and transferrin: No evidence for specific or non-specific binding, Amherst College, 2006.
126. Zhang S., and Zhao D., Advance in materials science and engineering, Aerospace material handbook, 2013, p 282-292.
127. Zhang Y., Dhaigude M., and Wang J., The Anvil Effect in the Spherical Indentation Testing on Sheet Metals, Procedia Manufacturing, Volume 1, 2015, p 828-839.

Appendices



Leica DM6000M light optical microscope